University of Alberta

New Materials and Architectures for Organic Photovoltaics

by

Brian Joseph Worfolk

A thesis submitted to the Faculty of Graduate Studies and Research
in partial fulfillment of the requirements for the degree of

Doctor of Philosophy

Department of Chemistry

Spring 2013
Edmonton, Alberta

Abstract

There are growing demands for energy throughout the world. In order to meet the rising energy pressures of the future, renewable sources are required. One approach to resolve this problem is organic photovoltaics (OPVs), which offers a potential low-cost energy solution for the future. Before this technology is commercially feasible, improvements in efficiency, lifetimes, mechanical stability, and processing are required. This thesis presents an integrative approach to investigating the scalability, lifetime stability, and mechanical properties of OPVs.

A robust spray coating method was developed for high conductivity poly(3,4-ethylenedioxythiophene):poly(p-styrenesulfonate) (PEDOT:PSS) transparent electrodes. Conductivities of >1000 S cm^{-1} are achieved with sheet resistances of 24 ohm sq^{-1} and 74% transmittance, which are amongst the best-reported in the field. OPV devices fabricated with the high conductivity transparent electrodes yielded power conversion efficiencies (PCEs) of 3.2%. Mechanical bending and stretching tests demonstrated that the flexibility of these polymer layers were far superior to that of indium tin oxide (ITO). Collectively, our results illustrate a promising future for the scalable printing of low-cost PEDOT:PSS-based flexible transparent electrodes.

A water-soluble cationic polythiophene derivative was combined with anionic PEDOT:PSS on ITO substrates via electrostatic layer-by-layer (eLbL) assembly. By varying the number of eLbL layers, the electrode's work function was precisely

controlled from 4.6 to 3.8 eV. These polymeric coatings were used as cathodic interfacial modifiers for inverted-mode organic photovoltaics. The PCE of the photovoltaic device was dependent on the composition of the eLbL-assembled interface and permitted fabrication of devices with efficiencies of 5.6%. Notably, these devices demonstrated significant air stability, maintaining 97% of their original PCE after over 1000 h of storage in air.

The optoelectronic and photophysical properties of four regioregular poly[3-(carboxyalkyl)thiophene-2,5-diyl] (P3CAT) with different carboxyalkyl chain lengths (propyl to hexyl) are reported. Each P3CAT is combined with functionalized C_{60} to form the photoactive bulk heterojunction layer for OPV devices. The extent of hydrogen bonding and polymer crystallinity in the films was determined, and the mechanical properties of films suggested that P3CATs were suitable for use in flexible devices. PCEs of up to 2.6% and 1.6% were obtained for devices on glass and plastic substrates, respectively.

Acknowledgements

Firstly, I would like to thank my supervisor, Prof. Jillian Buriak. Her infectious passion for science and innovation has inspired me since the beginning of my degree. Jillian has given me freedom to investigate a number of exciting areas and challenges in materials chemistry. I am especially grateful that Jillian has allowed, and encouraged me to dedicate a portion of my time to developing entrepreneurial skills.

I would like to acknowledge my committee members, Prof. Eric Rivard, Prof. Julianne Gibbs-Davis, and Prof. Karthik Shankar, for their guidance and support throughout my degree. As well, I would like to thank Prof. Timothy Kelly for agreeing to participate in my Ph.D. defence as an external examiner.

I am grateful for the many exceptional collaborators that I have worked with, including: Prof. Michael Brett, Prof. Anastasia Elias, Prof. Mario Leclerc, Prof. David Rider, Dr. Usama Al-Atar, Dr. Serge Beaupré, Dr. Qun Chen, Dr. Michael Fleischauer, Dr. Kenneth Harris, Dr. Tonggang Jiu, Dr. Katie Krause, Dr. Weiwei Li, Dr. Erik Luber, Dr. Sean McClure, Dr. Hosnay Mobarok, Dr. Michael Taschuk, Dr. Jaron Van Dijken, Jennifer Bruce, Bing Cao, Tate Hauger, Joshua LaForge, Abeed Lalany, Peng Li, Fenglin Liu, Kevin Shahbazi, Michael Thomas, Ryan Tucker, and colleagues in the Buriak group. In particular, I am appreciative of the support and guidance of Prof. David Rider, and Dr. Kenneth Harris. These gentlemen helped me get my research started out on the right track, and were always available to discuss

exciting (and not so thrilling) results. And of course I cannot forget to thank my Edmonton friends for making time spent outside the lab both fun and exciting.

I was fortunate to mentor a number of highly motivated high school and undergraduate students, including: Anju Eappen, Jordan Fordyce, Jared Geisinger, David Grewer, Zhiwei He, Grayson Ingram, Byung-Jong Jung, Sam Maloney, and Jeffrey Tait. They all exhibited great enthusiasm for their projects, so early on in their research careers.

Special thanks go to the "lightPower" team of Michael Thomas and Jaron Van Dijken. I learned so incredibly much in the yearlong entrepreneurial roller coaster ride. I would also like to thank the support of TEC Edmonton, and in particular Steve Jakeway and Kyle Kasawski. In addition, I would like to acknowledge the support of Ken Brizel and Rosi Amlani from ACAMP for conference support.

I am appreciative of the dynamic 2011-2012 nanoGroup executive, especially Joshua Siewert and Jocelyn Westwood. We have accomplished some amazing things together.

I would like to acknowledge the helpful support of the Alberta Centre for Surface Engineering and Science (ACSES) for assistance with surface characterization techniques. Prof. Al Meldrum is thanked for access and assistance with solid-state photoluminescence measurements in Chapter 4, and Prof. Jonathon Veinot is acknowledged for access to top-contact evaporator systems.

I would like to acknowledge the following funding agencies which supported me and the research projects that I worked on: Alberta Innovate-Technology Futures,

nanoAlberta, National Sciences and Engineering Research Council of Canada, University of Alberta, National Research Council – National Institute for Nanotechnology, and the Photovoltaics Innovation Network of Canada.

Finally, I would like to thank my parents, Janet Tobin and Brian Worfolk, and my family and friends for supporting and encouraging me throughout my degree.

Table of Contents

List of Tables

List of Figures

List of Equations

$$FF = \frac{V_{MAX}\, J_{MAX}}{V_{OC}\, J_{SC}} \qquad (1.1)$$

$$\eta = \frac{P_{MAX}}{P_{LIGHT}} = \frac{V_{OC}\, J_{SC}\, FF}{P_{LIGHT}} \qquad (1.2)$$

$$V_{OC} = \left(\frac{1}{e}\right)\left(|E^{Donor}HOMO| - |E^{PCBM}LUMO|\right) - 0.3\, V \qquad (1.3)$$

$$\mathrm{FOM} = \frac{\sigma_{DC}}{\sigma_{op}(\lambda)} = \frac{188.5\Omega}{R_{SHEET}\left(T(\lambda)^{-1/2}-1\right)} \qquad (2.1)$$

$$J = \frac{9}{8}\varepsilon_r \varepsilon_0 \mu_{h0} e^{0.89\gamma\sqrt{E}} \frac{V^2}{L^3} \qquad (4.1)$$

List of Symbols and Abbreviations

$(PEDOT:PSS)^{-}Na^{+}$	sodium poly(3,4-ethylenedioxythiophene):poly(*p*-styrenesulfonate)
μ_{h0}	zero-field hole mobility
AFM	atomic force microscope
AM1.5G	air mass 1.5 global
BHJ	bulk heterojunction
bis-PCBA	bis-[6, 6]-phenyl-C_{60}-butyric acid
bPEI	branched poly(ethylenimine)(bPEI)
CAGR	compounded annual growth rate
CIGS	$CuInGaSe_2$
CNT	carbon nanotube
CV	cyclic voltammetry
DC	direct current
DMF	dimethylformamide
DMSO	dimethyl sulfoxide
e	elementary charge
E_0	electronic ground state
E_1	electronic excited state
E	electric field
$E^{Donor}HOMO$	HOMO energy of donor
EG	ethylene glycol
eLbL	electrostatic layer-by-layer
$E^{PCBM}LUMO$	LUMO energy of PCBM
FF	fill factor
FOM	figure of merit
HOMO	highest occupied molecular orbital
HTL	hole transport layer

ICBA	indene-C_{60}-bisadduct
IPA	isopropyl alcohol
IR	infrared
ITO	indium tin oxide
J_{MAX}	maximum current density
J_{SC}	short-circuit current density
J-V	current density – voltage
L	film thickness
LCD	liquid crystal displays
LDA	lithium diisopropylamide
LUMO	lowest unoccupied molecular orbital
NaPSS	poly(sodium 4-styrenesulfonate)
NIR	near infrared
NMR	nuclear magnetic resonance
NW	nanowires
o-DCB	ortho-dichlorobenzene
OLED	organic light emitting diode
OPV	organic photovoltaic
P3(TBP)HT	poly[3-(6-{4-tert-butylpyridiniumyl}-hexyl)thiophene-2,5-diyl]
P3(TBP)HT^{+}Br^{-}	poly[3-(6-{4-tert-butylpyridiniumyl}-hexyl)thiophene-2,5-diyl bromide]
P3AT	poly[3-(alkyl)thiophene]
P3BT	poly(3-butylthiophene)
P3CAT	poly[3-(carboxyalkyl)thiophene-2,5-diyl]
P3CButT	poly[3-(4-carboxybutyl)thiophene-2,5-diyl]
P3CHexT	poly[3-(6-carboxyhexyl)thiophene-2,5-diyl]
P3CPenT	poly[3-(5-carboxypentyl) thiophene-2,5-diyl]
P3CProT	poly[3-(3-carboxypropyl)thiophene-2,5-diyl]
P3HT	poly(3-hexylthiophene)
P3HTb-P3TODT	poly(3-hexylthiophene)-block-poly[3-(2,5,8,11-

	tetraoxadodecane)thiophene]
PAA	poly(acrylic acid)
PAA-HA	poly(acrylic acid)–hyaluronic acid
PAH	poly(allylamine hydrochloride)
PANI	polyaniline
PBDTTPD	poly({4,8-di(2-ethylhexyloxyl)benzo[1,2-b:4,5-b']dithiophene}-2,6-diyl)-alt-({5-octylthieno[3,4-c]pyrrole-4,6-dione}-1,3-diyl)
$PC_{61}BM$ / PCBM	[6,6]-phenyl-C_{61}-butyric acid methyl ester
$PC_{71}BM$	[6,6]-phenyl-C_{71}-butyric acid methyl ester
PCDTBT	poly[N-9''-hepta-decanyl-2,7-carbazole-alt-5,5-(4',7'-di-2-thienyl-2',1',3'-benzothiadiazole)]
PCE	power conversion efficiency
PDDA	poly(diallyldimethylammonium chloride)
PDMS	polydimethylsiloxane
PEDOT:PSS	poly(3,4-ethylenedioxythiophene):poly(*p*-styrenesulfonate)
PEI	poly(ethylenenimine)
PEIE	poly(ethyleninimine ethoxylated)
PEN	poly(ethylene naphthalate)
PET	poly(ethylene terephthalate)
PFN	poly[(9,9-bis(3'-(N,N-dimethylamino)propyl)-2,7-fluorene)-alt-2,7-(9,9–dioctylfluorene)]
PL	photoluminescence
PLED	polymer light emitting diode
P_{LIGHT}	power of light
P_{MAX}	maximum power
PSS	poly(4-styrenesulfonate)
PTB7	poly(thieno[3,4-b]thiophene/benzodithiophene)
PV	photovoltaic
PXT	poly(p-xylylene-α-tetra-hydrothiophenium)
RoC	radius of curvature

R_S	series resistance
R_{SH}	shunt resistance
SAM	self-assembled monolayer
SCLC	space charge limited current
SEM	scanning electron microscope
T	transmission
TEM	transmission electron microscope
TFT	thin film transistor
THF	tetrahydrofuran
UPS	ultraviolet photoelectron spectroscopy
UV	ultraviolet
ν	vibrational energy state
vis	visible
V_{MAX}	maximum voltage
V_{OC}	open-circuit voltage
XPS	X-ray photoelectron spectroscopy
XRD	X-ray diffraction
γ	electric field activation factor
ε_0	permittivity of free space
ε_r	dielectric constant
η	power conversion efficiency
σ_{DC}	direct current conductivity
σ_{op}	optical conductivity

1

General Introduction

1.1 Overview

This thesis investigates new materials and architectures for organic photovoltaics (OPVs). We present an integrated approach investigating different components of OPVs, with goals of improving photovoltaic performance, stability, mechanical properties, and processing.

This first chapter provides a general introduction to semiconducting polymers, the field of OPVs, characterization and components of devices, the market potential and future opportunities. The research chapters delineate the construction of OPVs, starting with spray-coated transparent electrodes (Chapter 2), followed by self-assembled interfacial buffer layers (Chapter 3), and finally, investigation of an approach to control the morphology of photoactive layers (Chapter 4).

1.2 Semiconducting Polymers

A critical discovery enabling organic photovoltaics is semiconducting polymers. The 2000 Nobel Prize in Chemistry was awarded to Alan J. Heeger, Alan G. MacDiarmid and Hideki Shirakawa "for the discovery and development of conductive polymers".[1–4] These can conduct electricity while maintaining the mechanical properties and ease of processing as typical insulating polymers.[3]

The most structurally simple conducting polymer is polyacetylene (PA).[5] PA is a first generation semiconducting polymer, consisting of a carbon backbone with alternating single and double bonds as seen in Figure 1.1A. Along the carbon chain σ-bonds hold the polymer together while carbon-carbon π-bonds enable semiconducting behaviour.[6] In *trans*-polyacetylene there are 4 bands in the band structure as seen in Figure 1.1B. There are σ and σ^* bands from the carbon-carbon bond as well as a π and π^* bands originating from the overlap of adjacent carbon p_z orbitals. The σ and π bands are occupied, while the σ^* and π^* bands are unoccupied. Thus, a band gap exists between the π (highest occupied molecular orbital [HOMO]) and π^* (lowest unoccupied molecular orbital [LUMO]) bands, leading to semiconducting behaviour.[6] PA has limited solubility in organic solvents, limiting its use in solution processed devices.

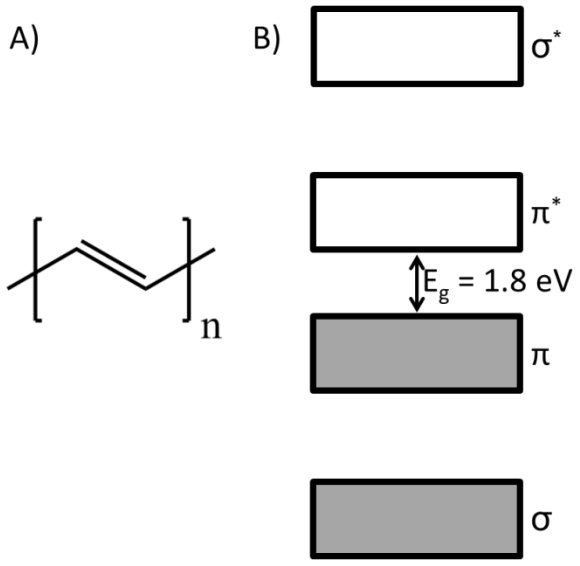

Figure 1.1 A) The chemical structure, and B) the schematic band structure of trans-polyacetylene (PA). The band gap (E_g) of PA is 1.8 eV.[6]

A second generation semiconducting polymer is regioregular poly(3-hexylthiophene) (P3HT). P3HT consists of a thiophene polymer backbone, with

hexyl groups added to improve solubility (Figure 1.2). It can have high carrier mobilities in the head-to-tail arrangement. In films, P3HT forms 2-dimensional lamellae, which are typically oriented normal to the substrate.[7, 8] Alkyl chains interdigitate with one another forming a (100) crystalline plane, while π-π stacking of thiophene rings forms a (010) plane, and facilitates interchain charge transport. P3HT has a band gap of ~2.0 eV.[9] The ultraviolet-visible absorption of P3HT is dependent on a number of factors including: regioregularity, molecular weight, and processing conditions.[8–10] Well-established syntheses and ease of processing have enabled P3HT to become widely used as a standardized donor material for OPVs.[11]

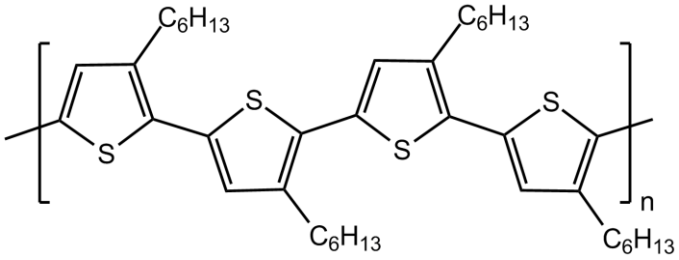

Figure 1.2 Chemical structure of regioregular head-to-tail poly(3-hexylthiophene).

Third generation semiconducting polymers consist of more complex structures with enhanced control over properties.[6] One class includes donor-acceptor copolymers, which has enhanced control of the band gap, and improved stability.[6] This strategy uses electron-rich and electron-deficient moieties as push-pull copolymers.[12] One example, poly[N-9''-hepta-decanyl-2,7-carbazole-alt-5,5-(4',7'-di-2-thienyl-2',1',3'-benzothiadiazole)] (PCDTBT), consists of electron-rich carbazole and electron-deficient dithienyl-benzothiadiazole (Figure 1.3). PCDTBT exhibits remarkable air and thermal stability, the first semiconducting polymer to combine both of these features.[13] The thermal stability is attributed to a deeper HOMO (-5.5

eV below vacuum), making it resistant to oxidation.[13] PCDTBT has also been used as a donor material in OPV devices with an internal quantum efficiency (IQE) approaching 100%. This means that all photons absorbed, result in charges, which are extracted by the electrodes.[14] Continued efforts in designing third generation semiconducting polymers aims to realize high mobility and stability combined with ease of processing.

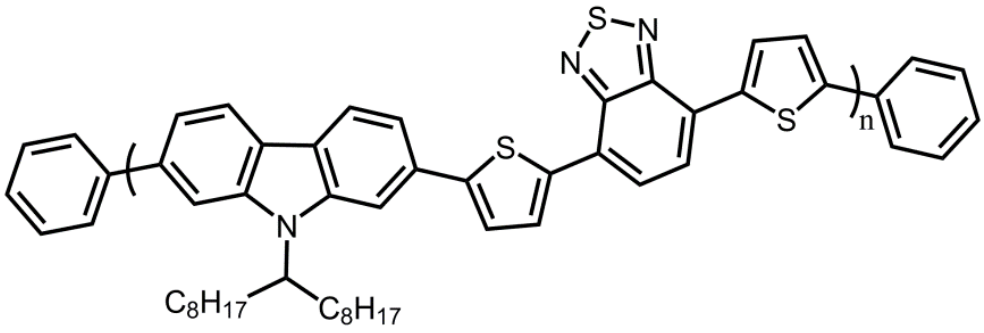

Figure 1.3 The chemical structure of a third generation semiconducting polymer: poly[N-9''-hepta-decanyl-2,7-carbazole-alt-5,5-(4',7'-di-2-thienyl-2',1',3'-benzothiadiazole)] (PCDTBT).

The typical one-dimensional chemical structure of semiconducting polymers leads to anisotropic carrier mobilities.[15] Charges have higher mobility along the backbone of polymers, compared to interchain charge hopping (carriers transported from one polymer chain to another).[16] The extent of π-π intermolecular interactions influences the interchain carrier transport. In order to maximize π-π stacking, the morphology of polymer films can be controlled, which improves carrier mobility. The charge mobilities in polymers can range from 10^{-6} cm^2 V^{-1} s^{-1} for amorphous films to > 1 cm^2 V^{-1} s^{-1} for crystalline morphologies.[17]

Semiconducting polymers can absorb photons, exciting an electron to the π^* band and forming a hole in the π band (if the energy of the photons are greater than the

band gap of the polymer). However, the electron and hole are not free charges, as is the case of bulk inorganic semiconductors. The electron and hole form a bound exciton. In semiconducting polymers, the exciton binding energy is a few tenths of an electron volt, which is much higher than the millielectron volts for bulk inorganic semiconductors.[17–19] Exciton dissociation can occur when the exciton migrates to an interface with lower chemical potential energy, overcoming the exciton binding energy.[18] This facilitates charge transfer from a semiconducting donor polymer to an acceptor-type material (such as buckminsterfullerene, C_{60}).

Semiconducting polymers can be used for similar applications as their inorganic counterparts, including: photovoltaics,[20] lasers,[21] light emitting diodes,[22] and photodiodes.[4] Other areas of application include thin film transistors,[23, 24] supercapacitors,[4, 25] and chemical and biological sensing.[26] The mobilities of semiconducting polymers are typically inferior to most inorganics ($10^2 – 10^3$ cm^2 V^{-1} s^{-1}).[17] However, polymers allow for solution processing, significantly reducing fabrication costs. Another benefit is that they can be used in flexible device applications, enabling flexible electronics such as televisions, cellular phones, and electronic paper.[27]

1.3 Introduction to Organic Photovoltaics

1.3.1 Overview

The advent of semiconducting polymers has allowed for the development of plastic electricity generation, commonly termed organic photovoltaics. Solar energy represents a large, and renewable source of energy. In fact, there is sufficient solar

energy hitting the earth's surface in one hour to provide enough energy to the world, for an entire year.[28] With increasing world population, and increasing economic wealth of developing nations, there is projected to be an unprecedented demand for energy in the future. Conservative models project that energy consumption will double by 2050, and triple by the end of the century.[28] In order to meet future energy demands, large-scale carbon-neutral energy production solutions are required. Given earth's huge solar resource, technologies that can efficiently and inexpensively produce and/or store energy from the sun are of great interest.[28] Organic photovoltaics offer a potential solution to contribute to the energy demands of the future.

Compared to traditional silicon photovoltaics, OPVs have been projected to achieve lower costs of electricity production. This is the result of highly scalable low-temperature solution processing, which is amenable to mass manufacturing via roll-to-roll printing on flexible substrates.[29–31] However, a number of significant challenges remain (low efficiencies and lifetimes), which need to be addressed before OPVs will be able to gain significant market share for utility scale energy production.[32, 33]

1.3.2 Development of Organic Photovoltaics

The photovoltaic effect was first observed by A.E. Becquerel in 1839.[34] From there, the photovoltaic effect has been studied in a number of inorganic semiconductors, resulting in Si p-n junction photovoltaics (first generation),[35] and a number of second generation photovoltaic technologies including: amorphous silicon,[36] CdTe,[37] and $CuInGaSe_2$ (CIGS).[17, 38] C.W. Tang developed an OPV based

on a photoactive bilayer structure of copper phthalocyanine (donor) and perylene tetracarboxylic derivative (acceptor), obtaining a power conversion efficiency (PCE) of 1%.[39] Since Tang's milestone single junction OPV device, a number of advancements have led to increasing PCEs to 10%, obtained by Mitsubishi Chemical in 2011.[40] These include: synthesis of high molecular weight and purity semiconducting polymers,[41, 42] understanding the influence of photoactive layer blend morphology,[43, 44] the use of low band gap polymers,[9, 45] improving device stability,[13, 46, 47] and application of roll-to-roll processing.[48–52] OPVs also include small molecule donors, which have achieved efficiencies of 6.7%.[53] However, this thesis will restrict the discussion to polymer-based OPVs.

The field of OPVs has attracted significant research attention over the past decade. Analysis of the Thomson Reuters Web of Science database searching for topics of "organic photovoltaic*" or "polymer solar cell*" or "plastic photovoltaic*" reveals a growing number of publications in the field as seen in Figure 1.4. Research intensified about a decade ago and in 2011 there were over 1000 publications in the area. The top five countries in terms of papers published are USA, China, South Korea, Germany, and Japan, with over 100 countries producing a least one publication. This data represents a truly global investment and growing effort in the field of OPVs.

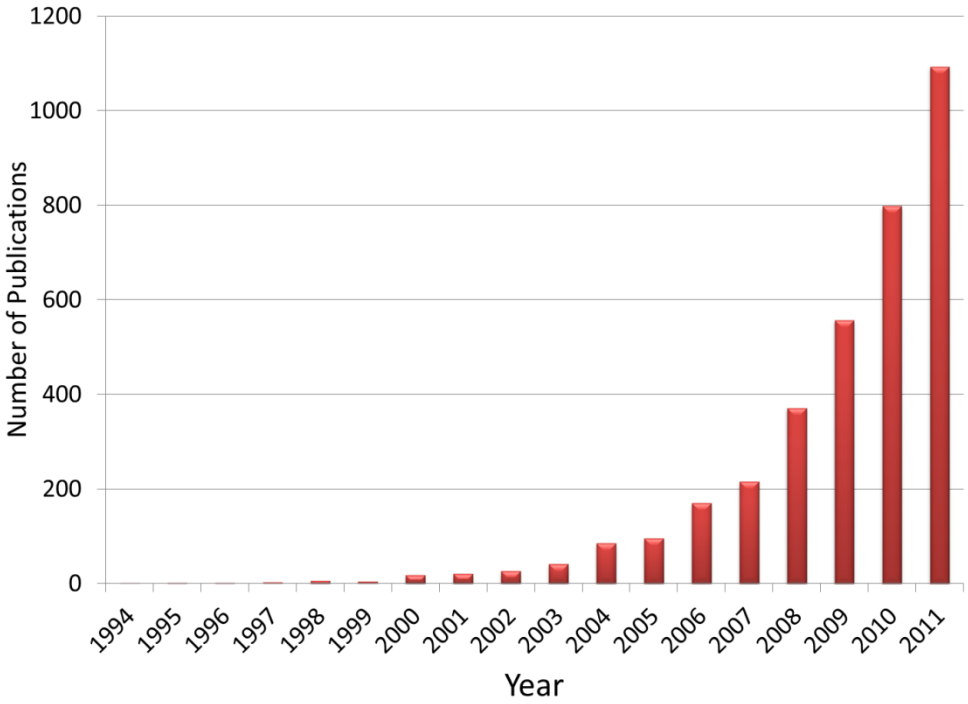

Figure 1.4 The growth of publications in the topic areas of "organic photovoltaic*" or "polymer solar cell*" or "plastic photovoltaic*" compiled from Thomson Reuters Web of Science on December 2nd, 2012.

1.4 Photovoltaic Device Characterization

Photovoltaic devices are tested under simulated solar radiation using a solar simulator. OPVs are typically characterized under air mass 1.5 global (AM1.5G) conditions.[54, 55] This represents light travelling through 1.5x air mass at a solar zenith angle of 48.2°. This represents the yearly average at mid-latitudes of the earth, and corresponds to an integrated power of 100 mW cm^{-2}.[56] Global solar radiation includes both direct and scattered sunlight. Photovoltaic devices are electrically characterized in the dark and under simulated solar light conditions. A source-meter sweeps voltage across the electrodes, while measuring the current. Using this data, a plot similar to Figure 1.5 can be constructed.

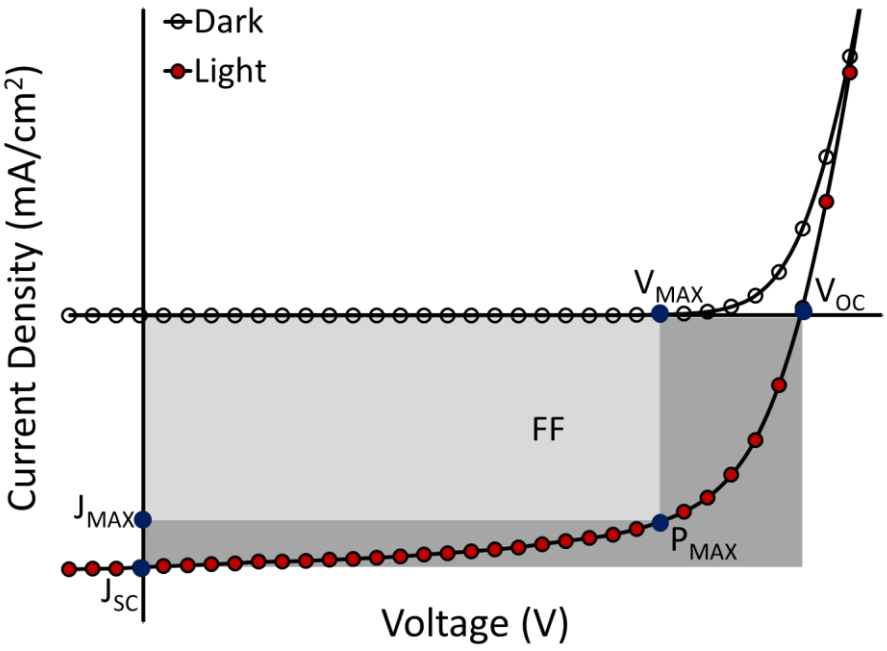

Figure 1.5 The photovoltaic parameters which can be extracted from a current-density-voltage (J-V) plot.

Figure 1.5 shows typical current-density-voltage (J-V) curves of a photovoltaic cell under dark and simulated solar radiation. Key photovoltaic performance parameters can be extracted from the light J-V curves. The open-circuit voltage (V_{OC}) is the potential across the electrodes under zero current or open-circuit conditions. The short-circuit current density (J_{SC}) is the current density at zero voltage. The maximum power (P_{MAX}) point represents the maximum power point along the J-V curve, whereby P=IV. The current density and potential at the P_{MAX} are referred to as the J_{MAX} and V_{MAX}, respectively. The fill factor (FF) is a ratio of the P_{MAX} in the device compared to the theoretical power at the J_{SC} and V_{OC}, and is represented by equation (1.1):

$$FF = \frac{V_{MAX}\, J_{MAX}}{V_{OC}\, J_{SC}} \qquad (1.1)$$

The power conversion efficiency (PCE, η) represents the efficiency of light to current conversion, within the photovoltaic device, as summarized in equation (1.2):

$$\eta = \frac{P_{MAX}}{P_{LIGHT}} = \frac{V_{OC}\, J_{SC}\, FF}{P_{LIGHT}} \qquad (1.2)$$

The P_{LIGHT} is 100 mW cm^{-2} under standard AM1.5G conditions. The FF is controlled by both the series and shunt resistances (R_S, R_{SH}). The R_S and R_{SH} are the inverse slope of the J-V curve at the V_{OC} and J_{SC}, respectively. Ideal photovoltaics would have an R_{SH} of infinity and an R_S of zero, which would confer a FF of 1. These photovoltaic parameters will be discussed in OPV device characterization throughout this thesis.

1.5 Components of Organic Photovoltaics

1.5.1 General Device Architecture & Photocurrent Generation

Organic photovoltaics devices consist of a layered structure, as seen in Figure 1.6. Devices consist of two electrodes: a transparent electrode, such as indium tin oxide (ITO), and a reflective Al, Ag, or Au electrode. The photoactive layer consists of donor (p-type) and acceptor (n-type) materials. The donor material forms a type-II heterojunction (staggered energy levels) with the acceptor as seen in Figure 1.7.

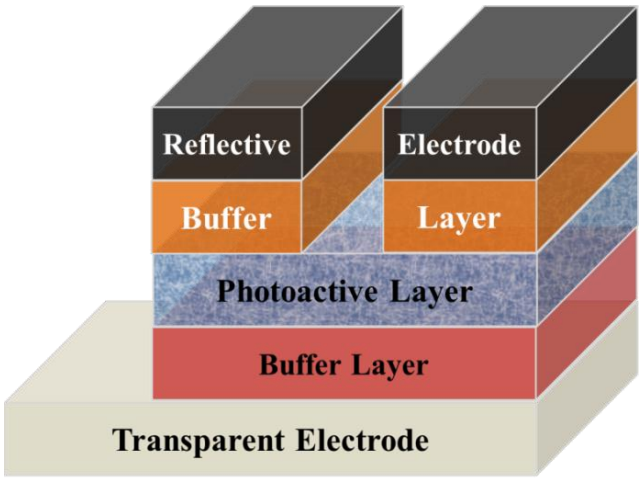

Figure 1.6 Standard OPV device architecture. The transparent electrode is typically supported by a solid substrate such as glass or plastic films.

The donor material absorbs photons of light depending on its band gap. The absorption of a photon excites an electron from the HOMO to the LUMO energy level (π-π^* transition), leaving a hole at the HOMO level. This forms a bound exciton with a relatively large binding energy of ~0.2-0.4 eV.[57, 58] The exciton can be dissociated at a donor-acceptor interface as seen in Step (2) of Figure 1.7. However, excitons in semiconducting polymers typically have short exciton diffusion lengths of ~10 nm.[19] This significantly limits the distance an exciton can travel before recombining, and returning back to the ground state.[17]

After exciton dissociation, the electron and hole can drift and diffuse in the presence of an electric field (from the difference in work function of the two electrodes), depending on the charge carrier mobility of the material towards the interfacial buffer layers.[17, 18, 33] There are usually two interfacial buffer layers, modifying both electrodes, as seen in Figure 1.6. Electrons are transported by the cathodic buffer layer, and holes are transported by the anodic interfacial layer [Step (3) in Figure 1.7]. Electrons are then collected by the cathode, and holes at the

anode, leading to current generation. Each layer of the OPV device will be discussed in more detail below.

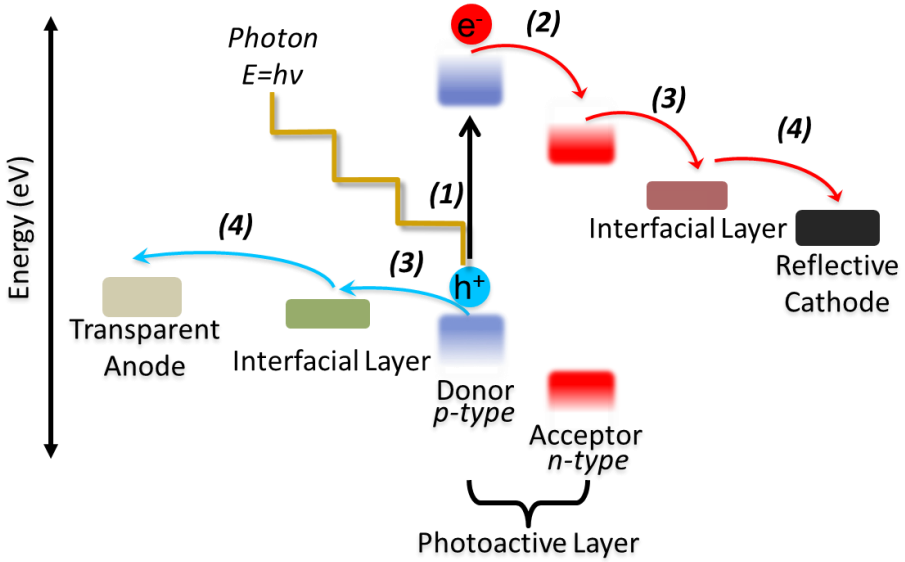

Figure 1.7 Mechanism of charge generation and extraction in OPVs. (1) Absorption of photons by the donor material, creating excitons. (2) Dissociation of excitons. (3) Transport of electrons and holes to the interfacial layers. (4) Collection of electrons and holes at the cathode and anode, respectively. Note: This schematic is simplified to illustrate the electron and hole transport within a device and extraction at the electrodes. The work function of the electrodes can be lower or higher, while still extracting charges. See expanded discussion in Section 1.5.7.

1.5.2 Substrates

OPVs can be fabricated on a range of substrates from glass to plastics, paper, and textiles.[17, 18, 59, 60] Solution processing of subsequent layers allows great versatility in substrate selection. Substrates for OPVs in the device architecture depicted in Figure 1.6, must be highly transparent across the solar spectrum, allowing photons to pass to the photoactive layer. Back-illuminated OPVs have also been reported, where light would enter the top of the device in Figure 1.6.[51, 61, 62] In this case the substrate is not required to be transparent. The transparent electrode is coated on top of the devices,

which usually consists of poly(3,4-ethylenedioxythiophene):poly(4-styrenesulfonate) (PEDOT:PSS) and a metal grid.[51, 61, 62] Back-illuminated OPVs are beneficial in module fabrication, as only the last-deposited layer (transparent electrode) is required to be patterned.[51]

To fabricate OPVs on a variety of materials, the surface chemistry of the substrate can be tuned, enhancing the adhesion of subsequent films.[63, 64] One example is the use of polydopamine to form a hydrophillic surface on polydimethylsiloxane (PDMS) substrates, as seen in Figure 1.8.[64] This enables great adhesion of spray-deposited Ag nanowires (NWs) forming reversibly stretchable transparent electrodes.[64]

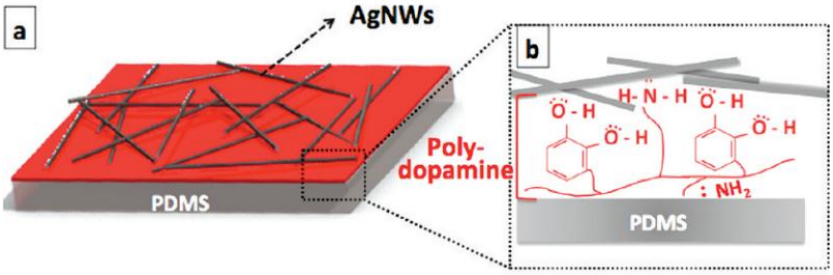

Figure 1.8 Schematic of A) spray-deposited Ag NWs on dopamine-modified PDMS films, and B) the polydopamine interaction with Ag NWs and the PDMS surface. Reprinted with permission from reference [64]. Copyright © 2012 American Chemical Society.

1.5.3 Transparent Electrodes

The next layer in typical OPV device architectures is the transparent electrode. Transparent electrodes have high transmissivity with low sheet resistances, which are often conflicting properties. The most common material used as transparent electrodes in OPVs is indium tin oxide (ITO). The properties of ITO are sensitive to processing conditions, but films typically have low resistivity (10^{-4} Ω cm), and high

transmissivity in the visible region (>80%).[65, 66] ITO is a doped n-type semiconductor with an optical band gap of 3.6 eV.[66–68] ITO can be prepared by a number of vacuum deposition techniques, but is commonly deposited with magnetron reactive sputtering using a In_2O_3 target with 10 wt.% SnO_2.[69, 70] Electron conduction in ITO arises from oxygen vacancies in the lattice, as well as the substitution of Sn^{4+} for In^{3+} providing an extra electron for conduction.[71] ITO has a work function of 4.3-4.8 eV depending on atomic stoichiometry and surface cleaning treatments.[67, 68] When using ITO as a transparent electrode in optoelectronic devices, an oxygen plasma is used to remove carbon contamination. The plasma also improves hole-injection by increasing the work function and favourable wettability for coating subsequent layers.[67, 72, 73] However, the declining reserves of indium in the earth's crust introduce significant cost variability.[65] One of the unique properties of OPVs is the ability to create flexible modules.[74–76] ITO supported plastic films exhibit limited flexibility, and are prone to cracking with repeated flexing to small radii of curvature and low strain as seen in the optical image in Figure 1.9.[77–81] The image shows cracks in ITO on polyethylene terephthalate (PET) substrates under 2.5% strain. These cracks are concomitant with a sharp increase in the ITO film resistance.[79]

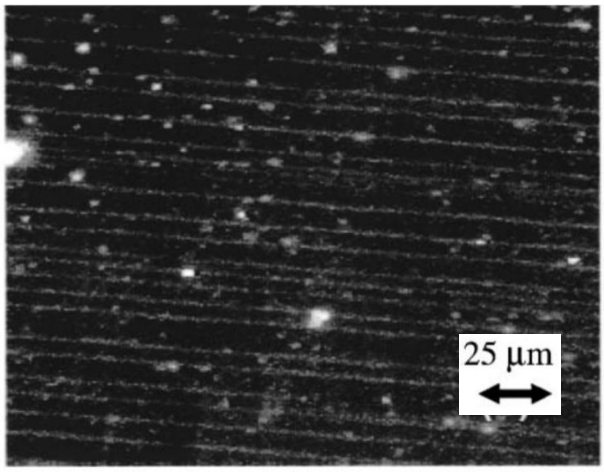

Figure 1.9 Optical image of ITO coated polyethylene terephthalate (PET) at a minimal 2.5% strain. Reprinted with permission from reference [79]. Copyright © 2000 American Institute of Physics.

There has been considerable interest in the literature evaluating alternatives to ITO transparent electrodes. Some of these include nanomaterials (Ag, and Cu nanowires[NWs]),[82, 83] conducting carbon allotropes (carbon nanotubes [CNTs], graphene)[84, 85], and conducting polymers.[86, 87]

Metals (Ag, Cu, Au) are known to be highly conductive, but are also reflective. To circumvent the high reflectivity, thin metal films or nanowire meshes have been used to form highly transparent and low resistance electrodes.[88–94] Ligands can solubilize metal nanowires, enabling scalable solution processing through spray-coating,[64, 95] Meyer rod coating,[82] and inexpensive roll-to-roll coating techniques.[96] Metal nanowire mesh films allow essentially all light to pass through 'holes' in the film, while forming a conductive network. The properties of these NW mesh films are highly dependent on the density of metal NWs, whereby higher density films are conductive but have reduced transmission. Careful tuning is required to form a percolation network, without sacrificing film transmission.[82, 97]

Yi Cui and coworkers used Ag NWs to coat PET substrates as seen in Figure 1.10.[82] Films were deposited with a Meyer rod and had sheet resistances of 20 Ω □$^{-1}$ with 80% transmissivity, which are in the same range as ITO.[82] Transmittance values are typically reported as specular. However, NW meshes can scatter light and have significantly higher diffuse transmittance. In OPVs diffuse light can be collected by the photoactive layer, making it a useful parameter to study.

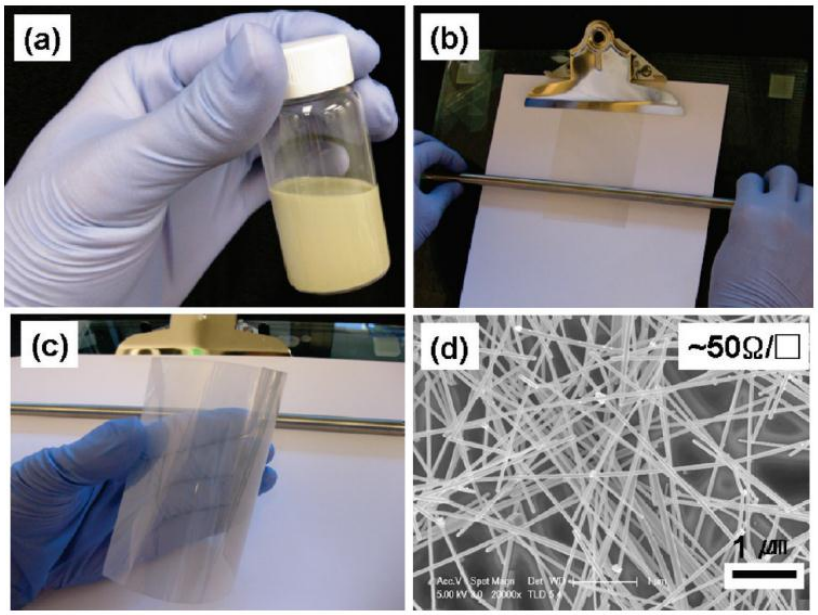

Figure 1.10 A) Ethanol solution of Ag NWs. B) Meyer rod coating of Ag NW films. C) Ag NW films on PET. D) Scanning electron microscope image of a Ag NW film with a sheet resistance of ~50 Ω □$^{-1}$. Reprinted with permission from reference [82]. Copyright © 2012 American Chemical Society.

The ligands on metal NWs allow solution processing. But, the organic coatings significantly increase resistance of the films. Ligands prevent conduction across junctions resulting in >10^9 increase in resistance compared to a single NW.[82] Annealing films at 200 °C is required to remove the ligand coating on glass substrates.[98] However, this temperature is not compatible to processing on plastic substrates. Several strategies have emerged to process Ag NW films on plastic

substrates including: galvanic displacement forming gold-coated Ag NWs,[82] applying mechanical pressure to as-deposited films,[98, 99] and plasmonic welding.[100] Plasmonic welding was applied to Ag NW films, which selectively heats up and epitaxially joins NW junctions as seen in Figure 1.11.[100] The localized heating does not affect underlying plastic substrates, and is amenable to low-cost roll-to-roll processing.

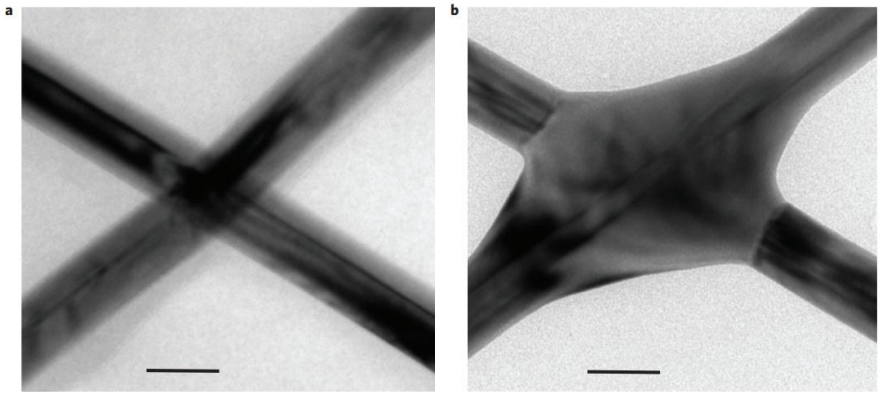

Figure 1.11 Transmission electron microscope image of a Ag NWs junction A) before, and B) after plasmonic welding. The scale bar is 5 nm. Reprinted with permission from reference [100]. Copyright © 2012 Macmillan Publishers Limited.

CNTs and graphene have been applied as transparent electrodes for OPV devices.[101–104] Carbon nanotubes have great potential as a transparent electrode, as a result of high mobilities > 10^5 cm^2 V^{-1} s^{-1}, and high transmittance in thin films.[105] However, it is difficult to obtain high purity, monodisperse CNTs, limiting the commercial applicability of transparent CNT films.[96] Another challenge is dispersing CNTs in solution. Several strategies have been developed including the use of surfactants to solubilize CNTs in water,[106] and the addition of chemical functional groups to improve solubility.[107] Upon formation of a dispersible CNT ink, films can be fabricated using similar methods as used for Ag NW meshes.[96] Marks and coworkers fabricated CNT transparent electrodes with a sheet resistance of 150 Ω □$^{-}$

^{1} and 80% transmission as seen in Figure 1.12.[108] CNT films have a relatively flat transmission spectra, making them appear light grey, with superior colour neutrality compared to ITO.[96] A major limiting factor for CNT transparent electrodes are high sheet resistances. Considering the above CNT film of 150 $\Omega\ \square^{-1}$, the sheet resistance would have to decrease an order of magnitude at 80% transmission to replace ITO. The theoretical conductivity of CNTs is 9×10^{4} S cm^{-1}.[109] If this level of conductivity can be achieved, CNT films will beat the performance metrics of ITO, and be an ideal transparent electrode for OPVs.

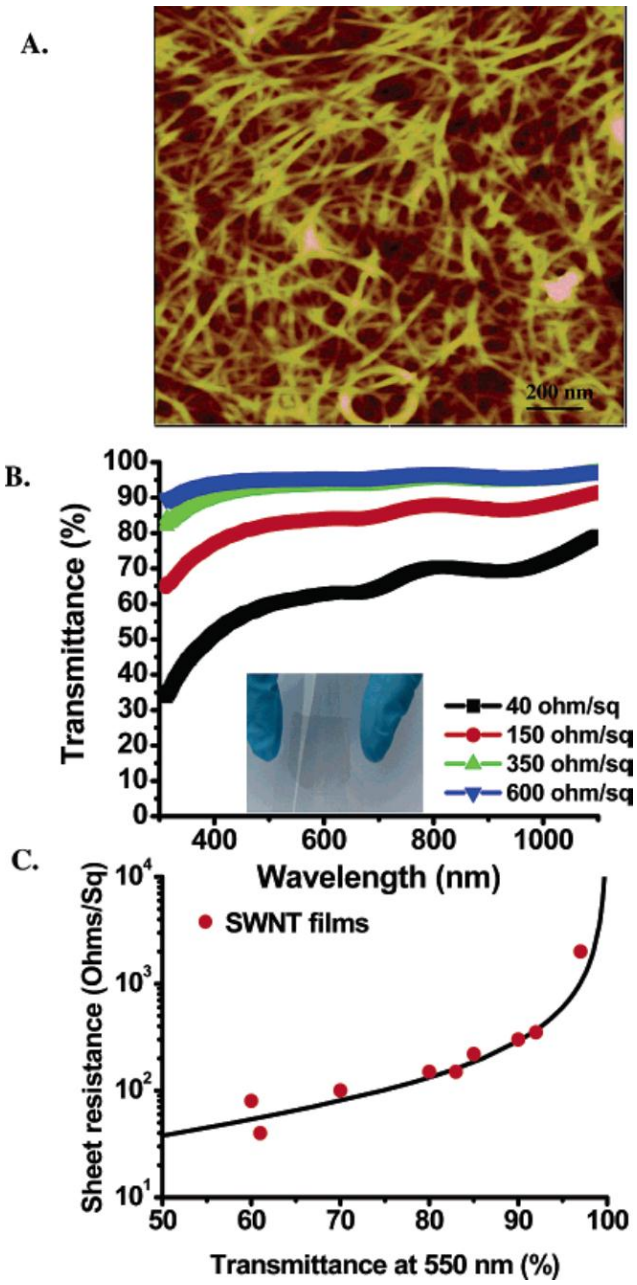

Figure 1.12 A) Atomic force microscope image of a CNT film. B) The transmittance of CNT films ranging from 40-600 Ω □$^{-1}$. The inset shows a CNT film on PET with a sheet resistance of 120 Ω □$^{-1}$. C) The relationship between the sheet resistance and transmittance of CNT films. Reprinted with permission from reference [108]. Copyright © 2006 American Chemical Society.

Conducting polymers have the potential to replace ITO transparent electrodes as a result of better mechanical properties for flexible and stretchable applications,[110, 111] and reduced fabrication costs driven by scalable solution processing.[51] However,

conducting polymers are more resistive than ITO. This has motivated the field to look for polymer conductivity enhancements. Two conducting polymers have emerged as candidates for transparent electrodes: polyaniline (PANI) and poly(3,4-ethylenedioxythiophene) (PEDOT). PEDOT is often charge stabilized by poly(4-styrenesulfonate) (PSS) forming a PEDOT:PSS blend (Figure 1.13). The monomer (EDOT) can undergo oxidative polymerization in the presence of water soluble PSS. H.C. Stark commercialized PEDOT:PSS, and it is commercially available as a colloidal solution.[96]

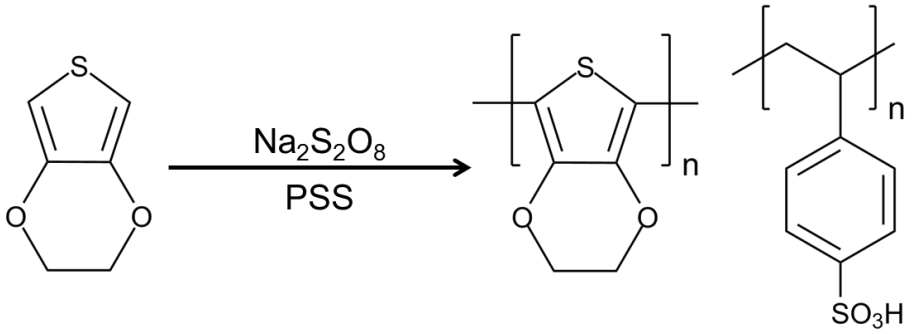

Figure 1.13 The oxidative polymerization of PEDOT:PSS.

PEDOT:PSS has a conductivity < 1 S cm^{-1} which is considerably too low for transparent electrode applications.[112–114] However, a number of additives have been used to significantly increase the conductivity of PEDOT:PSS films including: solvents,[112, 113, 115–117] fluorosurfactants,[86, 118, 119] and ionic liquids.[120, 121] These additives can act as dopants or affect the morphology of PEDOT:PSS films (by removing excess PSS and extending the polymer conjugation length.[113, 122] For example, a dilute H_2SO_4 treatment led to an enhancement from 0.3 S cm^{-1} to 3065 S cm^{-1}.[123] This is one of the best conductivities reported for PEDOT:PSS, to date and resulted in sheet resistances of 39 Ω $□^{-1}$ with 80% transmittance. OPV devices using

the high conductivity PEDOT:PSS electrode achieved 87% of the PCE compared to the ITO-based devices. Although the properties of PEDOT:PSS are approaching that of ITO, some have identified stability issues when films of PEDOT:PSS are exposed to air, humidity and UV light.[90, 124–127]

None of the emerging transparent electrode technologies have yet to match the electrical and optical properties of ITO. However, considering the energy used to make the material, and fabricate films, ITO represents 74% of the embedded energy of OPV modules, as seen in Figure 1.14A. This is in contrast to the 7%, 7%, and 10% embedded energy for Ag NWs, CNTs, and PEDOT:PSS, respectively.[128] Using any of these transparent electrodes would have shorter energy payback times. Most of the emerging transparent electrodes discussed herein are lower-cost than ITO, as seen in Figure 1.14B. Single walled carbon nanotubes (SWCNTs), are currently more expensive than ITO electrodes, due to difficulties in obtaining high yield and purity. PEDOT:PSS is the least expensive transparent electrode with a minimum 50x cost reduction per square meter of printed film.[128] Taking the embedded energy, cost, and flexibility into account, PEDOT:PSS and Ag NWs have the potential to be implemented as transparent electrodes in OPV modules. It will not be long before alternatives gain industrial and market acceptance.

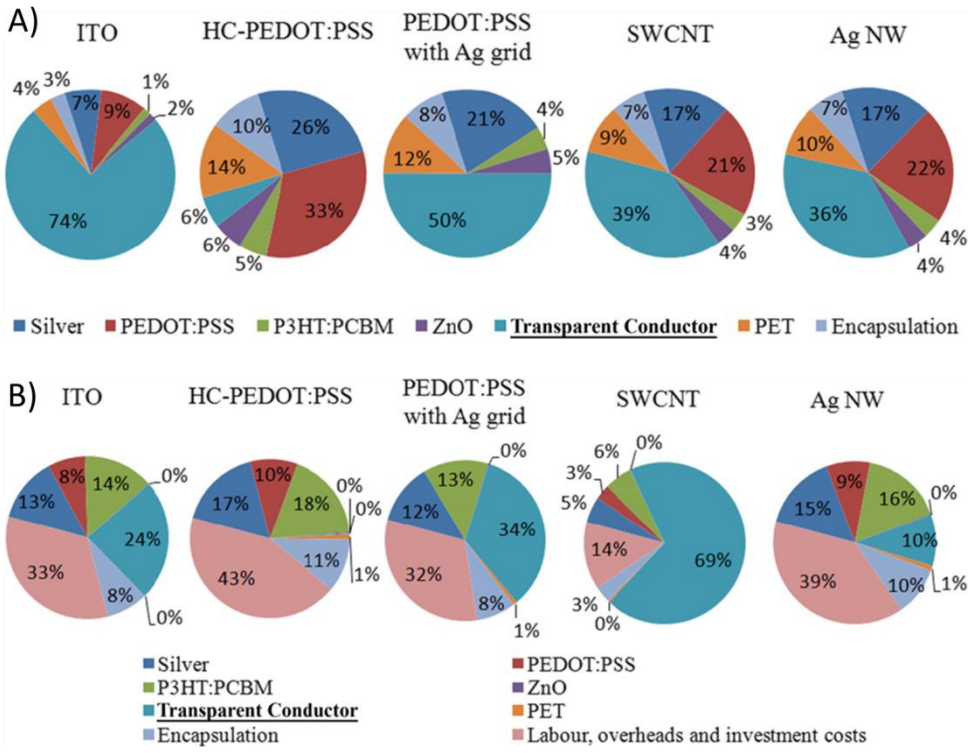

Figure 1.14 A) A comparison of the embedded energy in OPV modules using different transparent electrodes. B) The minimum costs of OPV modules per m^2 using different transparent electrodes. Reprinted with permission from reference [128]. Copyright © 2011 Elsevier.

1.5.4 Anodic Interfacial Buffer Layers

Interfacial buffer layers modify OPV electrodes as seen in Figure 1.6. These layers have a number of functions, which affect both the photovoltaic performance and stability of OPVs. These functions include: tuning the interfacial energy level alignment between the photoactive layer and the electrode, electron or hole blocking, controlling the surface properties of the subsequent layer (photoactive layer),[124] improving stability,[129] and defining the polarity or charge selectivity of the device.[130]

OPVs can operate in both forward- and inverted-mode as seen in Figure 1.15. This defines the electrode where electrons and holes are extracted. In the forward-mode of operation, holes are extracted by the transparent anode and electrons by the

reflective top cathode (Figure 1.16). The opposite occurs in inverted-mode; electrons are extracted by the transparent cathode and holes by the reflective top anode. The polarity of the device is defined by the work function of the interfacial buffer layers. In forward-mode, ITO is modified with a high work function buffer layer, reducing the hole extraction barrier, enabling preferential hole collection. In inverted-mode, ITO is modified with a low work function material, reducing the electron extraction barrier. By simply raising or lowering the work function of the buffer layer on ITO, the polarity of the device can be switched. The proper top buffer layer and electrode must also be selected to ensure extraction of the opposite charge carrier. For example as seen in Figure 1.16, in forward-mode, a lower work function top buffer layer and electrode are selected (LiF/Al), and in inverted-mode, a higher work function top buffer layer and electrode are chosen (V_2O_5/Ag). A primary advantage of the inverted-mode architecture is significantly improved stability and lifetimes of OPV modules. This is primarily explained by the selection of a higher work function metal (Ag, Au) as the top anode, which improves resistance to oxidation.[131, 132]

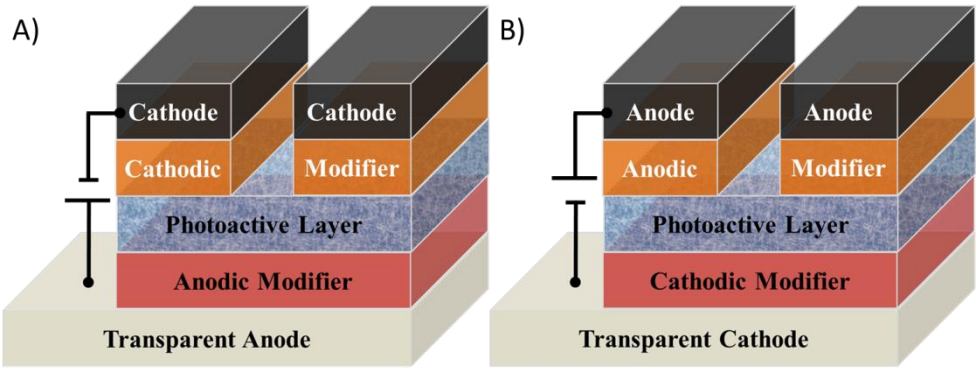

Figure 1.15 OPV device architecture for A) forward- and B) inverted-modes.

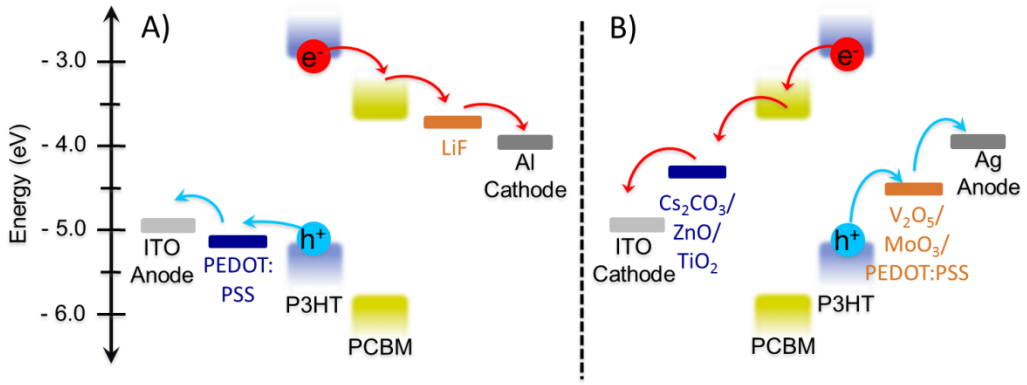

Figure 1.16 A) Forward- and B) inverted-modes of operation for OPVs. The photoactive layer consists of poly(3-hexylthiophene) (P3HT) and [6,6]-phenyl-C_{61}-butyric acid methyl ester ($PC_{61}BM$).

One of the most common anodic interfacial layers is PEDOT:PSS. The chemical structure is presented in Figure 1.13. PEDOT:PSS has been used as an anodic modifying layer in organic light emitting diodes (OLEDs) and OPVs. PEDOT:PSS has been shown to improve hole extraction, prevent electron leakage, provide a smoother electrode surface, and improve ohmic contact.[133–137] These attributes have made PEDOT:PSS an ubiquitous anodic buffer layer in both forward- and inverted-mode OPVs. However, PEDOT:PSS has been shown to be a major contributor to the degradation of OPVs.[138] Studies have shown that acidic (pH ~1) PEDOT:PSS solutions can etch ITO,[137, 139] excess poly(sodium 4-styrenesulfonate) (NaPSS) can migrate within the device,[140] and the hygroscopicity of PEDOT:PSS can accelerate the oxidation of the cathode.[141]

Another organic approach is the use of carboxylated polythiophenes as the anodic buffer layer. We developed a technique for the self-assembly of poly[3-(5-carboxypentyl) thiophene-2,5-diyl] (P3CPenT) into nanowires as shown in Figure 1.17.[124] The P3CPenT NWs increased the work function of ITO electrodes and provided great interfacial energy alignment, since the optoelectronic properties of

P3HT and P3CPenT are nearly identical.[124] In addition, films of P3CPenT NWs decreased the interfacial surface energy, allowing a more favourable morphology of the subsequent film: the photoactive layer.[124] These attributes led to an increase in the power conversion efficiency of OPV devices compared to PEDOT:PSS buffer layers.

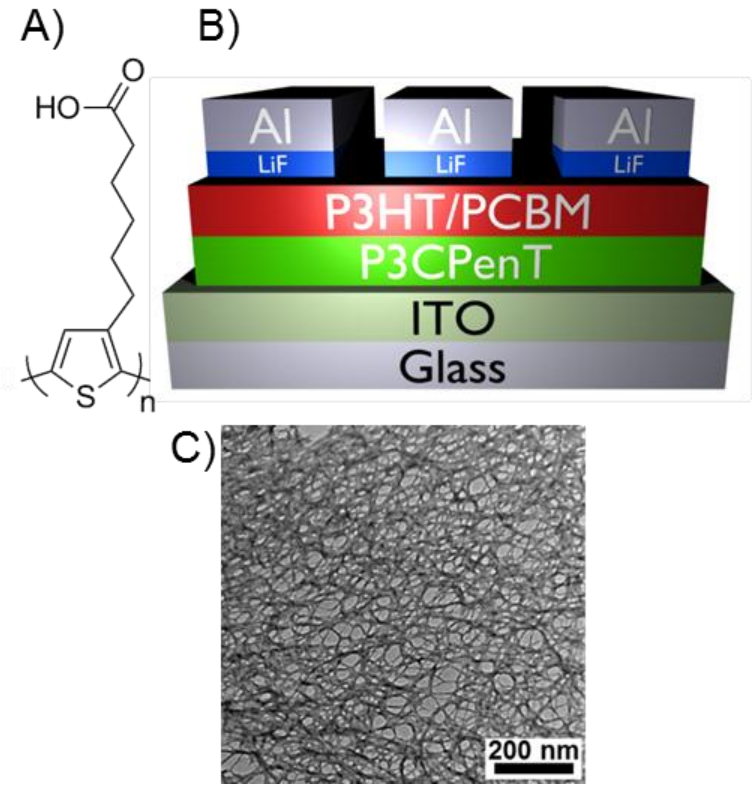

Figure 1.17 A) Chemical structure of poly[3-(5-carboxypentyl)thiophene-2,5-diyl] (P3CPenT) used to self-assemble nanowires for use as the anodic buffer layer in OPVs. B) The device architecture of plastic solar cells consisting of: ITO/P3CPenT/P3HT:PCBM/LiF/Al. C) Transmission electron microscope image of P3CPenT NWs. Reprinted with permission from reference [124]. Copyright © 2012 The Royal Society of Chemistry.

Metal oxides have also been extensively investigated as the anodic buffer layer for OPVs. Examples include NiO,[137, 142–144] WO_3,[145, 146] MoO_3,[147–150] IrO_x,[151] V_2O_5,[152] and Cu_2O.[153] Metal oxides have been prepared a number of ways including: from solution through sol-gel chemistry,[148] synthesized via dispersible nanoparticles,[153]

acidified aqueous dispersions,[147] metal-organic precursor decomposition,[142, 154] and under vacuum by thermal evaporation.[150, 152] NiO shows particularly beneficial properties as an anodic buffer layer. NiO is highly transparent in thin films, allowing photons to pass to the photoactive layer for harvesting. As seen in Figure 1.18, p-type NiO shows great energy level alignment with P3HT to transport holes, while the conduction band is high enough to block electrons.[137] Metal oxides offer tunable electronic properties with doping and stoichiometry, stability towards oxidation, and improved electrical stability as anodic interfacial buffer layers.[149, 154]

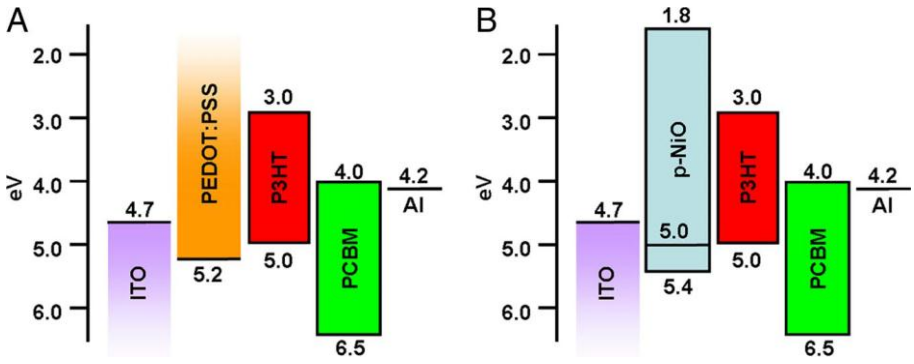

Figure 1.18 Energy level diagrams for OPV devices with A) PEDOT:PSS and B) p-type NiO as the anodic interfacial layers. Energies are referenced to vacuum. Reprinted with permission from reference [137]. Copyright © 2008 The National Academy of Sciences of the USA.

1.5.5 Cathodic Interfacial Layers

Cathodic buffer layers decrease the electron extraction energy barrier, block holes, prevent recombination, modify the surface chemistry affecting the next deposited layer, and can stabilize the performance of OPVs.[155] In the forward-mode of operation cathodic buffer layers modify the top reflective electrode (commonly Al), where in inverted-mode these layers modify the transparent electrode. When used in forward-mode of operation this layer also serves to protect the underlying photoactive layer from hot metal atoms deposited by thermal evaporation.[156–158]

A large variety of materials have been investigated as cathodic interfacial materials including: low work function metals (Ca, Ba, Mg),[155, 159] alkali metal compounds (LiF, Cs_2CO_3, CsF, CsCl),[160–166] metal oxides (TiO_2, ZnO),[167–171] and polymers.[129, 172–183] Low work function metals can make ohmic contact between the photoactive layer and the cathode. However, they are sensitive to water, degrading OPV performance when stored under ambient conditions.[130, 155, 184] LiF has been extensively used as a cathodic interfacial material in OLEDs and OPVs. Typically a very thin ~0.9 nm layer is thermally evaporated onto devices. This layer forms an ohmic contact between the cathode and photoactive layer, through the formation of a dipole, which lowers the energetic barrier for electron extraction.[164, 185, 186] Low work function metals, LiF, CsF, and CsCl have typically been used as anodic modifiers in the forward-mode of operation for OPVs.

In inverted-mode OPVs Cs_2CO_3, metal oxides and polymers have been investigated to modify the transparent electrode (usually ITO). One of the first cathodic interfacial buffer layers for inverted-mode OPVs was Cs_2CO_3. Yang and coworkers reported a work function decrease from 4.5 eV to 3.1 eV by modifying ITO with a thin annealed film of Cs_2CO_3 (Figure 1.19), enabling ohmic contact with the photoactive layer.[166] Annealing at 170 °C decomposes Cs_2CO_3 to form n-doped Cs_2O. Cs_2O on ITO forms an interfacial dipole as depicted in Figure 1.19B. The dipole moment is directed towards vacuum, and its magnitude is relative to the work function shift.[187] In addition, Cs_2O reduces the interfacial surface energy, and leads to improved morphology of the subsequent photoactive layer.[188]

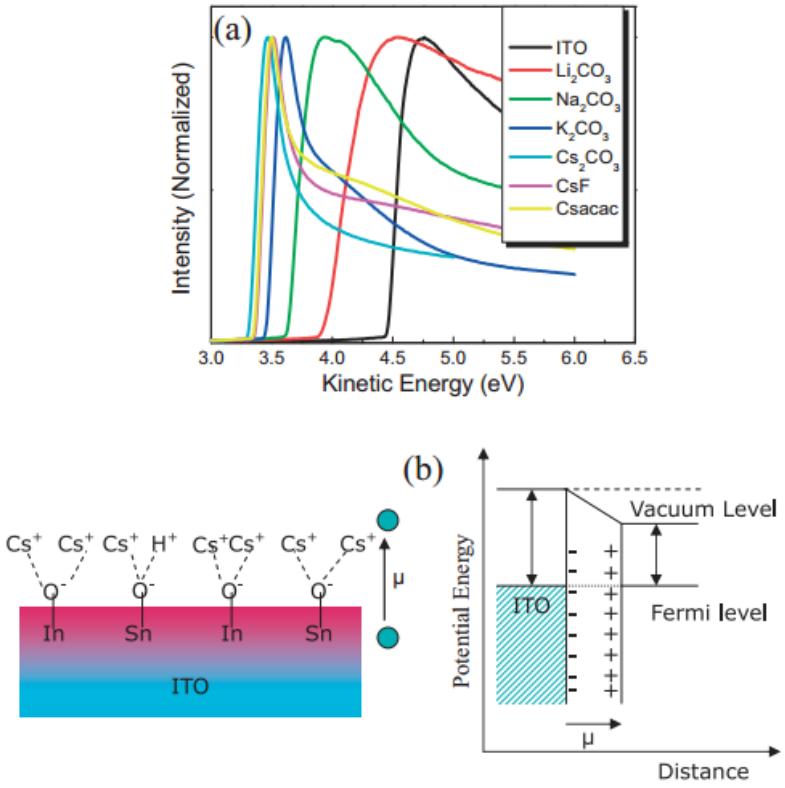

Figure 1.19 A) Ultraviolet photoemission spectroscopy (UPS) of different buffer layers on ITO. B) Schematic for the mechanism of work function decrease via dipole formation on ITO and the corresponding energy level diagram. Reprinted with permission from reference [187]. Copyright © 2008 WILEY-VCH Verlag GmbH & Co.

N-type metal oxides such as TiO_2 and ZnO are commonly used as cathodic modifiers in both forward- and inverted- modes of OPVs. They are non-toxic and transparent across the visible and NIR spectrum and have suitable conduction band energies to match fullerene acceptors.[130] In addition, their deep valence bands are able to block holes, making them highly electron selective. These materials have also been used as optical spacers in OPVs, helping to redistribute light intensity.[155, 170, 189] One disadvantage of these metal oxides is the requirement for high temperature (>300 °C) annealing to produce crystalline, high mobility films.[130, 190, 191] However, sol-gel solution processing has been developed, decreasing the annealing temperatures to < 200 °C.[167, 191] TiO_2 and ZnO can be modified by self-assembled

monolayers (SAMs), which can further tune the work function via dipole formation, and can alter the interfacial surface energy. Carboxylic acid-modified fullerenes have been used to form SAMs on ZnO.[192] These SAMs were shown to passivate surface trap states in ZnO, improve electron extraction, and optimize the photoactive layer morphology.[192–194]

Semiconducting organic small molecules and polymers have also been used as cathodic interfacial modifiers, and will be discussed in Chapter 3.

A myriad of cathodic interfacial modifiers have been developed offering a range of tunability in optical and electronic properties, work functions, and interfacial surface energies to match the required properties of the photoactive layer. These layers play a major role in both the photovoltaic performance and stability of OPVs. However, much of the research to date has focused on modifying ITO transparent electrodes. With a number of emerging substitutes to ITO, cathodic interfacial buffer layers on alternative transparent electrodes should be examined.

1.5.6 Photoactive Layers

The photoactive layer is responsible for the absorption of photons, and the formation of charge carriers, which are then transported through the interfacial layers and extracted by the electrodes (Figure 1.7). The photoactive layer of OPVs consists of two semiconducting components: a p-type donor and an n-type acceptor. One of the most common donor/acceptor combinations is regioregular poly(3-hexylthiophene) and [6,6]-phenyl-C_{61}-butyric acid methyl ester ($PC_{61}BM$), respectively. The chemical structures of both are presented in Figure 1.20. The donor material is responsible for the majority of the absorption, creating excitons. Excitons

can be dissociated at a donor-acceptor interface.[195] The n-type semiconductor accepts electrons, which are then transported to the cathode, while holes are transported through the donor material to the anode. Excitons have a diffusion length of ~10 nm.[19] Meaning that if an exciton does not reach a donor/acceptor interface within 10 nm, the exciton will recombine, and the charge carriers will be lost. This limits the domain sizes within the photoactive layer.

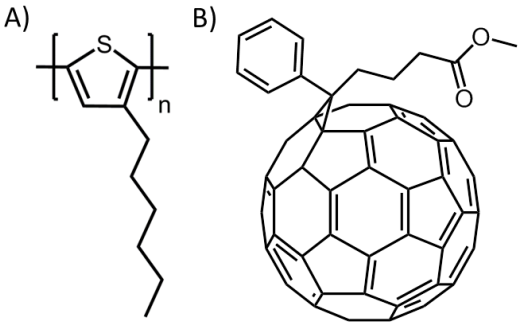

Figure 1.20 Chemical structure of A) P3HT and B) $PC_{61}BM$.

One of the first OPV devices consisted of a bilayer photoactive layer, as schematically depicted in Figure 1.21A.[39] This architecture limits the donor material thickness to ~20 nm, in order to efficiently dissociate excitons. However, such thin films are not able to absorb a significant portion of photons. Thus in bilayer architectures, the exciton dissociation competes with photon absorption, leading to limited photovoltaic performance.[20] Heeger and coworkers, and Friend and coworkers discovered that by blending the donor and acceptor materials together, it was possible to form a bicontinuous interpenetrating network of both components, termed a bulk heterojunction (BHJ) (Figure 1.21B).[41, 42, 44] The controlled formation of a BHJ led to high interfacial area between donor and acceptor components with a

domain size of ~20 nm. This enabled thicker photoactive layers on the order of 100-220 nm, significantly increasing photon absorption.[17]

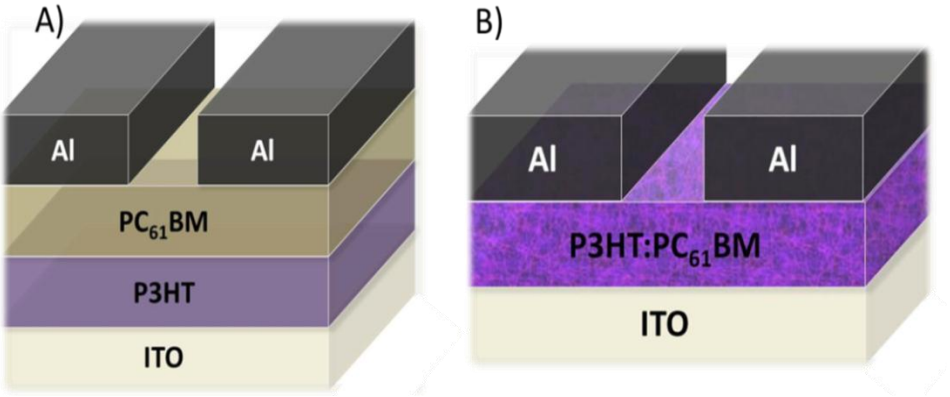

Figure 1.21 A schematic of A) a bilayer and B) a bulk heterojunction photoactive layer.

The photoactive layer is typically deposited by spin-coating, but there are a number of scalable deposition methods being developed including: spray-coating,[95, 196] ink jet printing,[197, 198] and traditional roll-to-roll methods.[48, 50, 61, 199–202] Since solution processing is one of the major advantages of OPVs, the materials selected for the photoactive layer should be highly soluble, enabling scalable processing techniques.

Poly(3-hexylthiophene) is a donor semiconducting polymer, commonly used in the photoactive layer of OPVs.[11] Highly regioregular head-to-tail P3HT can be synthesized via both the McCollough and Rieke routes, as seen in Figure 1.22.[203, 204] The McCollough route involves Kumada coupling to alkylate 3-bromothiophene and subsequent bromination in acetic acid. The one-pot polymerization involves metalation with lithium diisopropylamide (LDA) at the 5-position, conversion with $MgBr_2 \bullet Et_2O$, and polymerization using a $NiCl_2$dppp catalyst.[204][55] Rieke's method

uses activated zinc to form the reactive thiophene precursor. Polymerization is performed using $NiCl_2$dppp at -78 °C.[203]

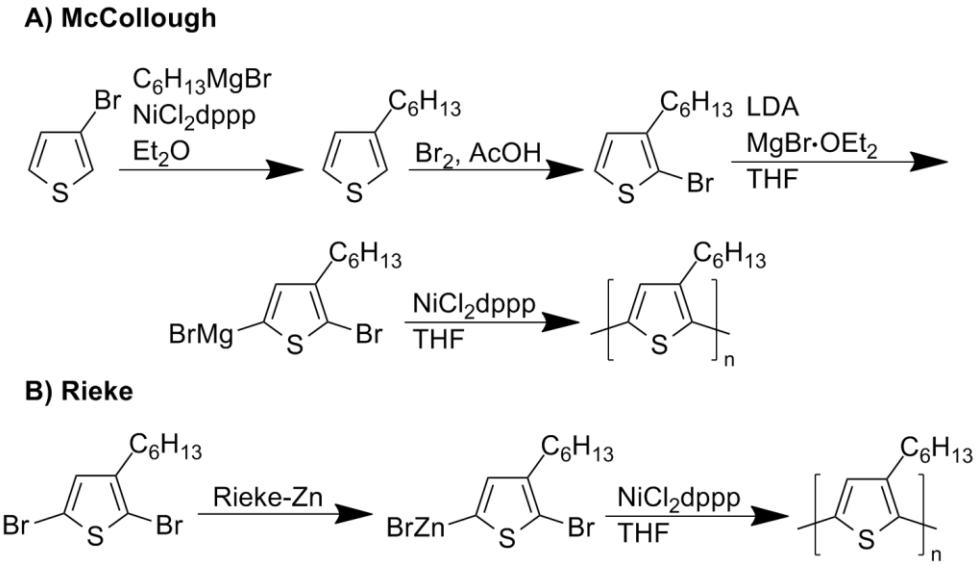

Figure 1.22 Synthesis of regioregular P3HT via the A) McCollough[204] and B) Rieke routes.[203]

P3HT has a band gap of ~ 2.0 eV, which defines the portion of the solar spectrum in which photons can be absorbed. As seen in Figure 1.23 the box representing the absorption range of P3HT is fairly limited. Lower energy photons in the NIR are not absorbed by P3HT, limiting the potential photocurrent. A strategy to circumvent this problem is to reduce the band gap of the donor polymer. Recently, the synthesis of low band gap polymers has been the subject of intensive research.[9, 12] Promising low band gap polymers are shown in Figure 1.24, and include: poly[N-9''-hepta-decanyl-2,7-carbazole-alt-5,5-(4',7'-di-2-thienyl-2',1',3'-benzothiadiazole)] (PCDTBT),[13, 205] poly({4,8-di(2-ethylhexyloxyl)benzo[1,2-b:4,5-b']dithiophene}-2,6-diyl)-alt-({5-octylthieno[3,4-c]pyrrole-4,6-dione}-1,3-diyl) (PBDTTPD),[206–208] and poly[[4,8-bis[(2-ethylhexyl)oxy]benzo[1,2-b:4,5-b']dithiophene-2,6-diyl][3-fluoro-2-[(2-ethylhexyl)carbonyl]thieno[3,4-

b]thiophenediyl]] (PTB7).[182, 209, 210] These polymers have lower band gaps than P3HT, and have all achieved power conversion efficiencies (PCEs) in excess of 7% in single junction OPVs (Table 1.1).

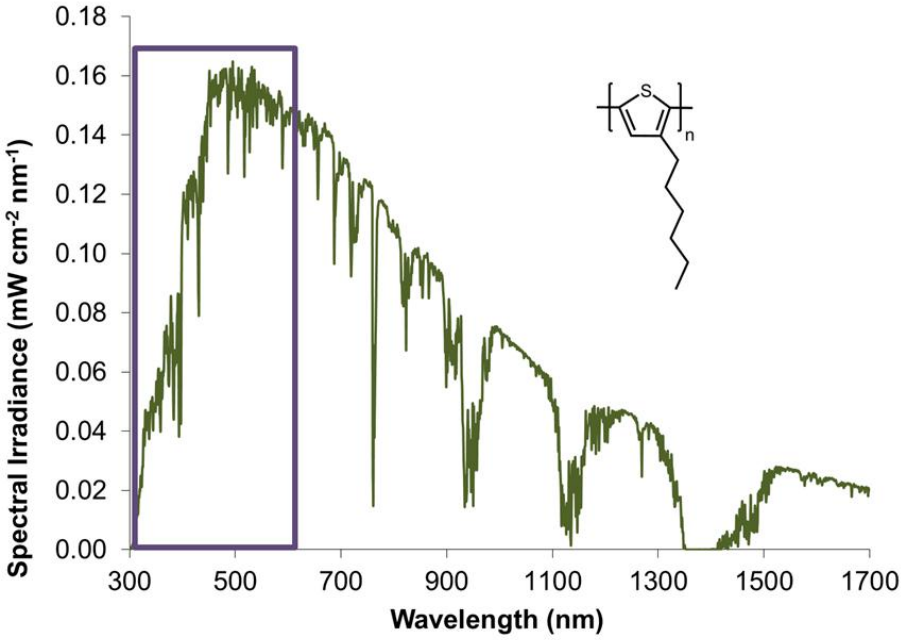

Figure 1.23 The AM1.5G 100 mW cm^{-2} solar spectrum with a box enclosing the absorption range of P3HT (chemical structure in inset). Spectral data was obtained from the American Society for Testing and Materials (ASTM).

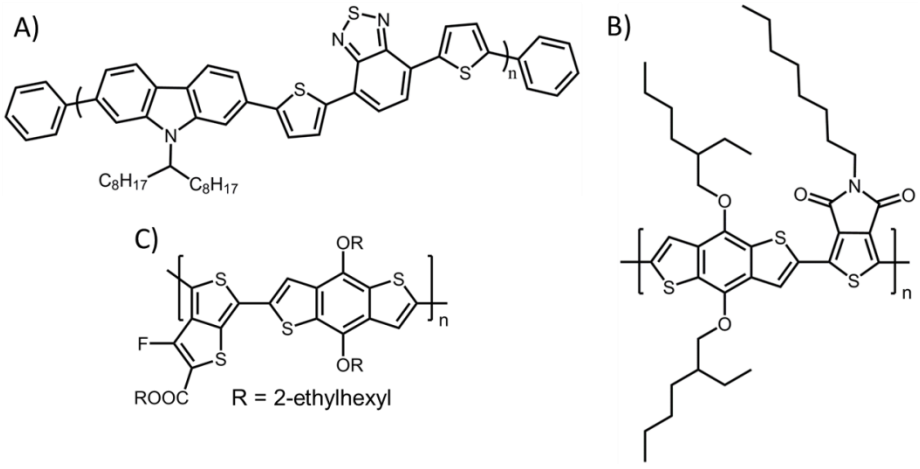

Figure 1.24 The chemical structures low band gap polymers: A) PCDTBT, B) PBDTTPD, and C) PTB7.

Important factors when selecting a donor polymer for high efficiency OPVs include: band gap, HOMO and LUMO energy levels, good hole mobility, and high solvent solubility. As previously mentioned, the band gap defines the absorption range, which affects the short-circuit current density (J_{SC}). The open-circuit voltage (V_{OC}) is related to the energetic offset between the E^{Donor}HOMO and E^{PCBM}LUMO, as depicted in Figure 1.25. Larger energetic offsets will have increased open-circuit voltages as seen in equation (1.3):

$$V_{OC} = \left(\frac{1}{e}\right)(|E^{Donor}HOMO| - |E^{PCBM}LUMO|) - 0.3\,V \qquad (1.3)$$

where e represents the elementary charge, and a $PC_{61}BM$ LUMO of -4.3 eV.[211] The donor:acceptor LUMO-LUMO energy difference must be greater than 0.3 eV to efficiently dissociate excitons.[211] The low band gap polymers all have larger E^{PCBM}LUMO - E^{Donor}HOMO values than P3HT, which increase their V_{OC} in OPV devices.[211] A V_{OC} of 0.6 V is typical for P3HT:$PC_{61}BM$ OPVs, but can be improved to > 0.9 V when using PBDTTPD.[208, 212]

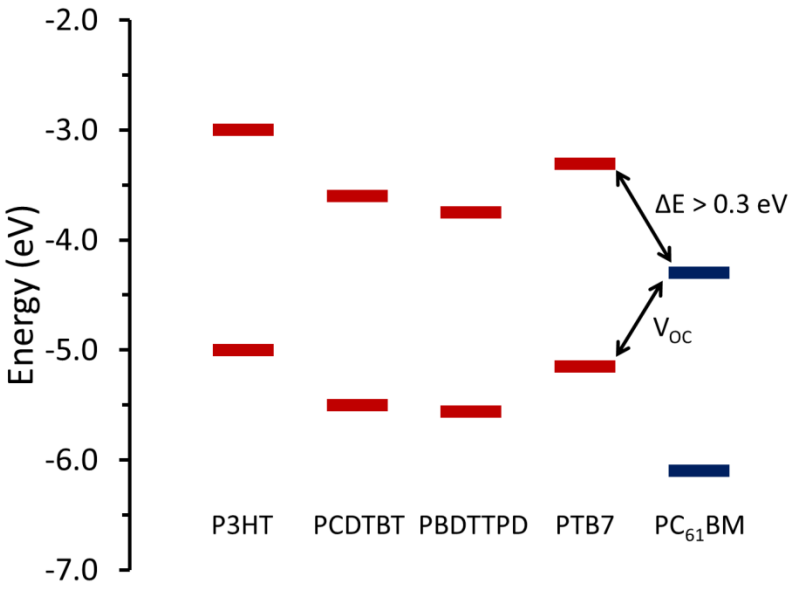

Figure 1.25 Band energy diagram of: P3HT, PCDTBT, PBDTTPD, PTB7 donors, and $PC_{61}BM$ acceptor relative to vacuum.

Fullerenes are the most common acceptor used in OPV devices. This is a result of high electron affinity and mobility, and the ability to accept multiple electrons. Fullerene was discovered in 1985, and the Nobel Prize in Chemistry was awarded to Robert Curl, Harold Kroto, and Richard Smalley in 1996 for its discovery.[213] Fullerene is made on a "large" scale by the arc vaporization of graphite, which was developed in 1990.[214]. This has allowed further synthetic modification and functionalization of fullerenes for a range of properties and applications.[215] Fullerene has limited solubility in organic solvents. Organic functional groups can be added to fullerenes to increase solubility, and tune their optoelectronic properties.[215] [6,6]-phenyl-C_{61}-butyric acid methyl ester ($PC_{61}BM$) is a functionalized fullerene, soluble in organic solvents, with widespread use in OPV devices. The chemical structure can be seen in Figure 1.20B. More recently [6,6]-phenyl-C_{71}-butyric acid methyl ester ($PC_{71}BM$) has been used as an acceptor, because of its stronger visible absorption (Figure 1.27A).[216, 217] Both $PC_{61}BM$ and $PC_{71}BM$ are synthesized following the same

procedure as seen in Figure 1.26.[217, 218] The reaction forms a number of multiadduct products, which are separated with silica gel chromatography.

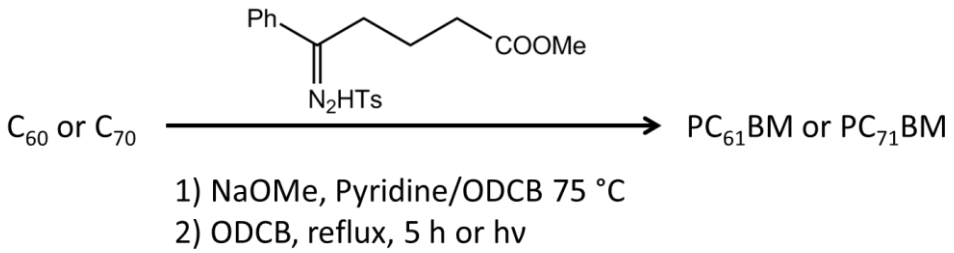

Figure 1.26 The synthesis of $PC_{61}BM$ and $PC_{71}BM$.

Although P3HT:$PC_{61}BM$ is the standard photoactive layer for OPVs, this combination exhibits poor band alignment, limiting the V_{OC}.[11] Bisadduct fullerenes such as indene-C_{60}-bisadduct (ICBA), and bis-[6,6]-phenyl-C_{60}-butyric acid methyl ester (bis-PCBM), can improve the energetic alignment by increasing the LUMO energy level (see Figure 1.25 and Figure 1.27 for reference and chemical structures). For example, ICBA (shown in Figure 1.27B) has a 0.17 eV increase in the LUMO which increases the V_{OC} by 0.2 V OPV devices compared to $PC_{61}BM$, as seen in Table 1.1.[219] Bis-PCBM OPV devices have a similar effect whereby the LUMO energy level is 0.1 eV higher than $PC_{61}BM$, which is enough to improve the V_{OC} by 0.08 V.[220]

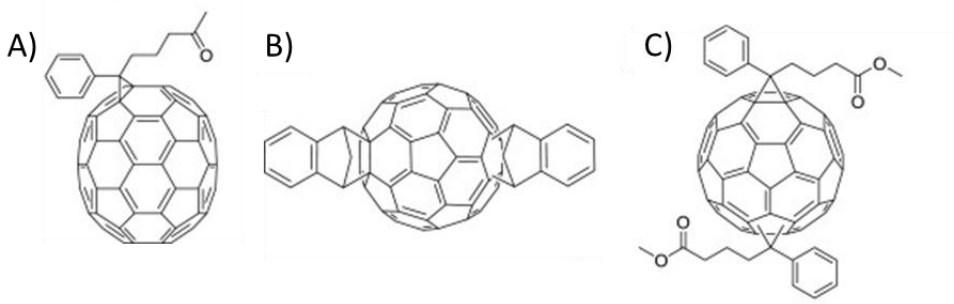

Figure 1.27 Chemical structures of fullerene electron acceptors: A) $PC_{71}BM$, B) ICBA, and C) bis-PCBM.

Table 1.1 Summary of the photovoltaic performance of the photoactive materials discussed.

Photoactive Components	J_{SC} (mA cm^{-2})	V_{OC} (V)	FF	PCE (%)	Reference
P3HT:$PC_{61}BM$	10.6	0.64	0.55	3.7	[220]
P3HT:$PC_{71}BM$	12.2	0.72	0.68	4.5	[220]
P3HT:ICBA	12.1	0.84	0.72	7.3	[219]
P3HT:bisPCBM	9.1	0.72	0.68	4.5	[220]
PCDTBT:$PC_{71}BM$	11.4	0.91	0.66	7.1	[205]
PBDTTPD:$PC_{61}BM$	10.9	0.93	0.70	7.1	[208]
PTB7:$PC_{71}BM$	17.5	0.75	0.70	9.2	[182]

There has been considerably less research on new acceptors compared to the myriad of donor polymers available. In developing the next generation of organic acceptors the following should be considered: range of light absorption, molar extinction coefficient, electron mobility, solubility, and thermal stability.[215]

The morphology of the photoactive layer is critical to maximizing light absorption, exciton dissociation, limiting recombination, and efficient charge transport. Control over the morphology of the BHJ is important in optimizing the performance of OPVs. Loos and coworkers investigated the effect of different processing conditions on the morphology of the photoactive layer, as characterized with transmission electron microscopy (TEM) (Figure 1.28).[221] After spin-coating, the blend film has not reached thermodynamic equilibrium.[221] Thus, additional post-processing steps can improve blend morphology. Thermal annealing the deposited film for 20 minutes at 130 °C improves the polymer crystallinity. As seen in Figure 1.28B, crystalline P3HT nanowires (NWs) are formed (white phase contrast).

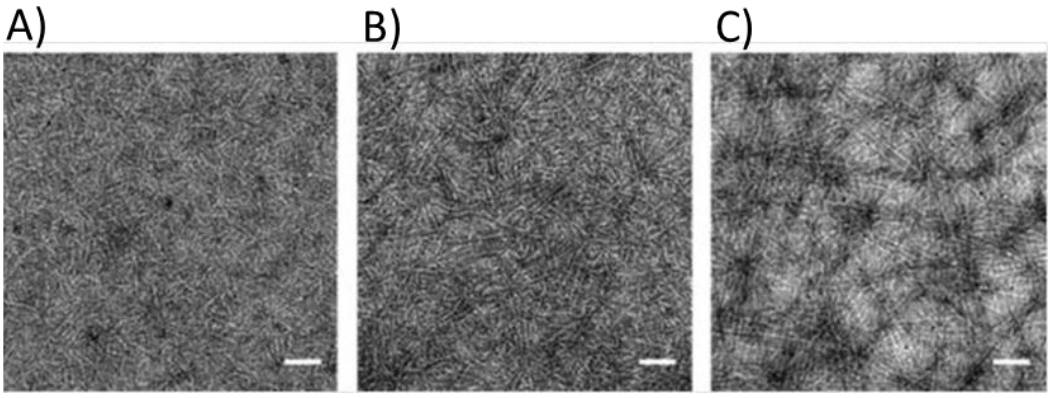

Figure 1.28 Bright-field transmission electron microscope (TEM) images of a 50 nm BHJ of P3HT:$PC_{61}BM$ after A) spin-coating, B) thermal annealing at 130 °C for 20 minutes, and C) solvent assisted annealing for 3 hours. The scale bar is 200 nm. Reprinted with permission from reference [221]. Copyright © 2009 American Chemical Society.

A similar result is obtained with solvent assisted annealing, which consists of placing wet P3HT:$PC_{61}BM$ films in a closed Petri dish for 3 hours. This allows the ortho-dichlorobenzene solvent to slowly evaporate from the films. From Figure 1.28C, we once again see crystalline P3HT NWs. OPV devices almost doubled in power conversion efficiency for both thermal annealing and solvent assisted annealing treatments. Both the J_{SC} and the fill factor improved. The J_{SC} increase is attributed to enhanced hole mobility in the crystalline P3HT NWs. The higher FF indicates improved morphology: better percolation pathways and fewer trap sites.[221] Further discussion on controlling and stabilizing the BHJ morphology of OPV devices can be found in Chapter 4.

Low band gap donor and fullerene acceptor materials with high mobilities and appropriate offsetting of energy levels maximize the short-circuit current density and open-circuit voltage. The photoactive layer should have high interfacial area between the donor and acceptor with ideal morphology consisting of domain sizes of ~20

nm, while providing bicontinuous pathways for charge extraction which results in higher power conversion efficiencies.

1.5.7 Reflective Electrodes

Reflective electrodes are the top contact in OPVs as depicted in Figure 1.6. Ideal top electrodes make ohmic contact with the photoactive layer,[222] and are reflective. This allows light which has not been absorbed by the photoactive layer to be reflected for a second opportunity for absorption. Higher work function metals such as Ag, and Au (anode) are used for inverted-mode, while a lower work function metal like Al (cathode) is used for forward-mode OPVs.

The electrode work function should be close in energy to the appropriate photoactive layer component. For example, the anode work function should match the HOMO energy of the donor, and the cathode work function should have similar energy as the LUMO of the acceptor, in order to maximize the V_{OC}. Electrodes with higher and lower work functions (~ 1 eV difference) can still extract charges, but will have smaller open-circuit voltages. The V_{OC} is very sensitive to the E^{Donor}HOMO and E^{PCBM}LUMO offset, while significantly less susceptible to the work function of the electrodes. This is due to Fermi level pinning of the anode to the donor, and cathode to the acceptor, which minimizes the effect of different metal work function contacts. In addition, the relative work functions of the anode and cathode are important. In order to maximize the V_{OC} there should be a large energetic offset between the anode and cathode work functions. This helps to improve charge extraction, by increasing the drift mobility of charge carriers. In the ideal case, the electrode work functions should be close in energy to the appropriate photoactive

layer component, while maximizing their relative energetic position with respect to each other.

Top electrodes are typically deposited via thermal evaporation of the metal under vacuum.[223] However, some solution processes have been developed. These include: slot-die coating,[61] screen printing,[224] spin-coating PEDOT:PSS,[225] and spray-coating PEDOT:PSS.[226] In fact, Jen and coworkers used PEDOT:PSS as both the transparent and top electrodes.[226] This opens the potential for all-organic OPVs, however, PEDOT:PSS has poor reflectivity limiting the photovoltaic performance.[226]

1.5.8 Tandem Organic Photovoltaics

Tandem OPVs consist of two photoactive layers stacked on top of each other (Figure 1.29). Requirements for high efficiency polymer tandem photovoltaics include: two donors with complementary absorption, efficient recombination layer, and orthogonal solubilities of adjacent layers.[227] When two donor polymers are selected with different absorption ranges, a larger portion of solar radiation can be absorbed. The recombination layer is located between the two photoactive layers. The purpose of this layer is to efficiently collect electrons from one sub-cell and holes from the other photoactive layer. This layer should form ohmic contact with each of the sub-cells.[227] Orthogonal solubilities of adjacent layers are required to prevent the dissolution of previously cast films. Although challenging for a minimum of 6 layers, solution processed polymer tandem photovoltaics have been fabricated, obtaining 6% efficiency.[169, 228]

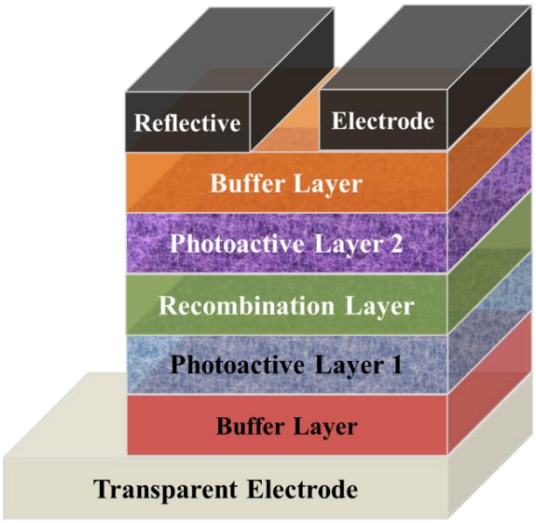

Figure 1.29 Schematic of tandem OPV devices.

The serial connection of two photoactive layers leads to a sum of individual open-circuit voltages, while the short-circuit current density is limited to the sub-cell with the higher fill factor.[229, 230] The J_{SC} is dependent on the recombination efficiency of the interlayer. If one of the photoactive layers is providing an excess of charge carriers, they will not be collected. This results in overall J_{SC} losses.[229]

A high efficiency polymer tandem OPV was reported by Yang and coworkers in 2012.[231] This device combines P3HT with the low band gap polymer: poly{2,6'-4,8-di(5-ethylhexylthienyl)benzo[1,2-b;3,4-b]dithiophene-alt-5-dibutyloctyl-3,6-bis(5-bromothiophen-2-yl)pyrrolo[3,4-c]pyrrole-1,4-dione} (PBDTT-DPP) (Figure 1.30A). PBDTTT-DPP has a band gap of 1.44 eV, enabling complementary absorption to P3HT as seen in Figure 1.30B.[231] The inverted-mode tandem OPV consisted of a P3HT:ICBA bottom cell and PBDTT-DPP:$PC_{70}BM$ as the top photoactive layer. A certified tandem device obtained a power conversion efficiency of 8.62%.[231] Multi-junction OPVs are more difficult to fabricate with solution processing, and have higher material costs. However, theory predicts that optimized tandem OPVs have

the potential to obtain almost 15% efficiency, which would present a strong case for commercialization.[232]

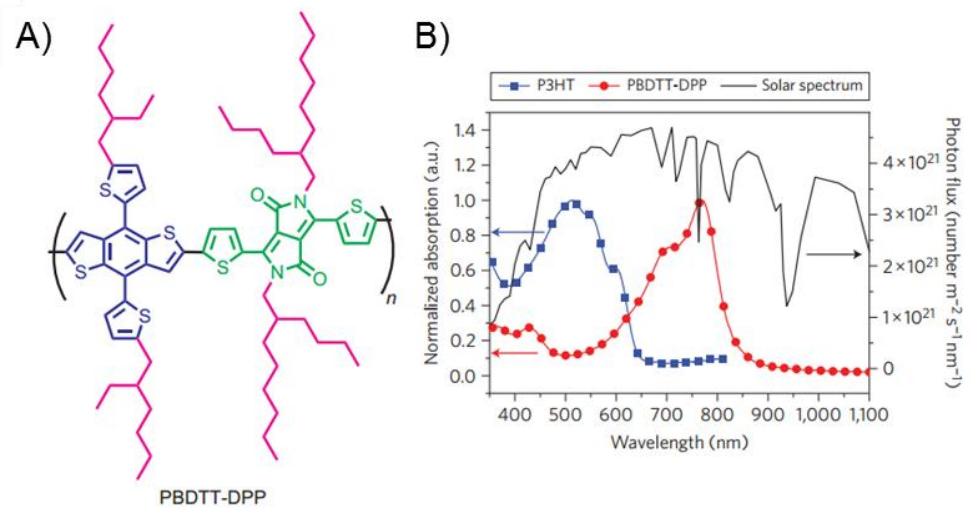

Figure 1.30 A) The chemical structure of PBDTT-DPP, and B) the UV absorption of P3HT and PBDTT-DPP plotted with the solar radiation spectrum. Reprinted with permission from reference [231]. Copyright © 2012 Macmillan Publishers Limited.

1.6 Market and Future of Organic Photovoltaics

1.6.1 Market Analysis of Organic Photovoltaics

The ability to print OPVs on lightweight, flexible substrates, opens up new potential products and markets, which traditional photovoltaic technologies cannot compete.[29, 30] The ability to tune the colour of OPVs and printing on fabrics adds aesthetic appeal and a closer integration of consumers with their power sources.[59, 233] Flexible and mechanically robust OPVs may find application in portable consumer electronics, reducing or potentially eliminating the need to charge devices.[59] Other applications include off-grid power, outdoor recreation, lightweight power for the

military, building integrated photovoltaics, and the potential for lowlight and indirect power applications.[59]

Krebs and coworkers projects a 500 million $US market by 2018 with the main applications in consumer electronics and residential building applications.[32] This is backed by an industrial market report by IDTechEx, which projects a 630 million $US market by 2022.[234] The projected market segments of OPVs are presented in Figure 1.31. Consumer electronics, and products designed for developing countries are the first major sectors for OPVs. One example of an OPV integrated product for developing countries is an OPV powered LED lamp used in the "Lighting Africa" initiative.[235] Mature applications for OPVs include residential, commercial, industrial, military and emergency applications.[32, 234] In the 2012 Nanomarkets assessment of the OPV market, they state that a big breakthrough in reduction of costs, increase in efficiency and lifetimes, are required before commercialization is feasible.[236]

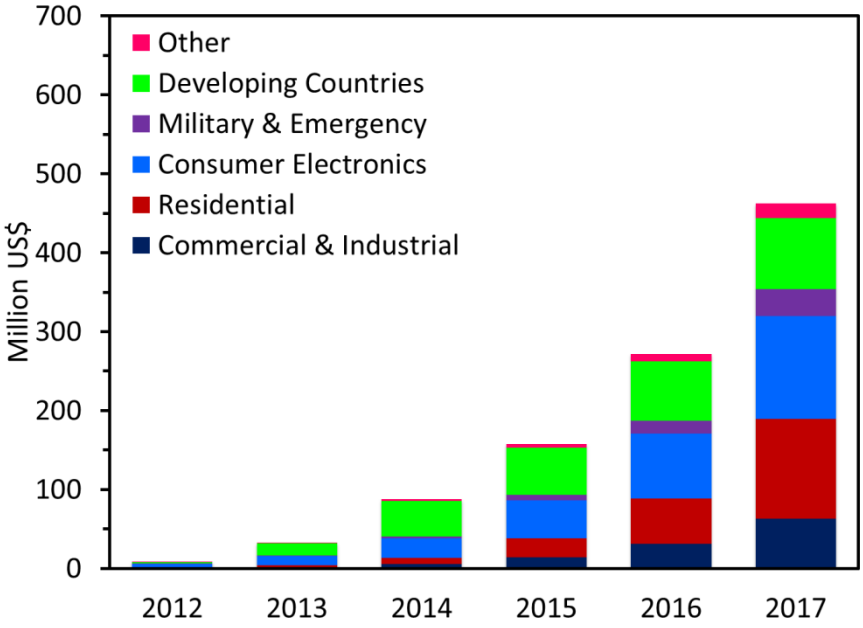

Figure 1.31 The projected market segments of OPVs. Data was extracted from Nanomarkets[237] and Krebs and coworkers.[32]

1.6.2 Future of Organic Photovoltaics

OPVs have the potential to produce cost effective electrical power from solar radiation.[41, 51, 61, 238, 239] To encourage widespread commercial acceptance, flexible OPVs should be efficient, mechanically robust, lightweight, and fabricated with techniques scalable for mass manufacturing.[48, 51] A combination of all these factors has yet to be achieved, limiting the current commercial success of the technology. The scalability of OPVs, has yet to overcome limitations in efficiencies and lifetimes compared to other photovoltaic systems.

Theory predicts that, single junction organic photovoltaics may be able to achieve power conversion efficiencies of 10-20%.[211, 240] In addition, a study has demonstrated projected lifetimes of 7 years,[47] with OPV modules encapsulated in glass. While work in improving the synthesis of high molecular weight semiconducting polymers aims to provide economical and environmentally friendly

coupling polymerizations.[241] There is considerable fundamental research still occurring in this field, which are leading to daily reports of new materials and architectures for OPVs. If 10% modules and lifetimes in excess of 10 years are achieved, there will be considerable applications for this technology.[30, 32]

1.7 Organization of Thesis

This thesis presents an integrative approach to improving the mechanical properties and stability of high efficiency organic photovoltaics with the use of new semiconducting polymers and device architectures. The thesis is organized to "build-up" OPV devices starting with the transparent electrode.

Transparent conductors have utility in a number of applications including electrodes for OPVs. A scalable spray-coating method for PEDOT:PSS transparent electrodes on glass and plastic substrates is developed in Chapter 2. This fabrication method leads to low sheet resistance films with high transparency, and have superior mechanical properties compared to ITO. Chapter 2 was reproduced in part with permission from:

a) J.G. Tait, B.J. Worfolk, S.A. Maloney, T.C. Hauger, A.L. Elias, J.M. Buriak, K.D. Harris, *Sol. Energy Mater. Sol. Cells.* **2013**, *110*, 98-106. Copyright © 2013 Elsevier.

A new architecture for cathodic interfacial buffer layers is introduced in Chapter 3. Using water-soluble polymers, stable and high efficiency inverted-mode organic photovoltaics are achieved. The chapter discusses stability and degradation issues of

OPVs, as well as electrostatic layer-by-layer assembly, which is used to fabricate cathodic interfacial films. Chapter 3 was reproduced in part with permission from:

a) B.J. Worfolk, T.C. Hauger, K.D. Harris, D.A. Rider, J.A.M. Fordyce, S. Beaupré, M. Leclerc, J.M. Buriak, *Adv. Energy Mater.* **2012**, *2*, 361-368. Copyright © 2012 Wiley-VCH Verlag GmbH & Co.

b) D.A. Rider, B.J. Worfolk, K.D. Harris, A. Lalany, K. Shahbazi, M.D. Fleischauer, M.J. Brett, J.M. Buriak, *Adv. Funct. Mater.* **2010**, *20*, 2404-2415. Copyright © 2010 Wiley-VCH Verlag GmbH & Co.

c) Q. Chen, B.J. Worfolk, T.C. Hauger, U. Al-Atar, K.D. Harris, J.M. Buriak, *ACS Appl. Mater. Interfaces* **2011**, *3*, 3962-3970. Copyright © 2011 American Chemical Society.

In Chapter 4, carboxylated polythiophenes are introduced into the bulk heterojunction photoactive layer of OPVs. This enables morphological control of the photoactive layer through the use of hydrogen bonding. The effect of hydrogen bonding on the mechanical properties of the photoactive layer is discussed. Strategies for controlling and stabilizing the morphology, as well as the use of hydrogen bonding in the photoactive layer are outlined. Chapter 4 was reproduced in part with permission from:

a) B.J. Worfolk, D.A. Rider, A.L. Elias, M. Thomas, K.D. Harris, J.M. Buriak, *Adv. Funct. Mater.* **2011**, *21*, 1816-1826. Copyright © 2011 Wiley-VCH Verlag GmbH & Co.

b) B.J. Worfolk, W. Li, P. Li, T.C. Hauger, K.D. Harris, J.M. Buriak, *J. Mater. Chem.* **2012**, *22*, 11354-11363. Copyright © 2012 The Royal Society of Chemistry.

Chapter 5 summarizes the research in each chapter, and discusses future research directions.

1.8 References

[1] A.J. Heeger, A.G. MacDiarmid, H. Shirakawa, *The Nobel Prize in Chemistry 2000: Conductive Polymers*, Stockholm, Sweden: Royal Swedish Academy Of Sciences, Stockholm, Sweden **2000**.

[2] H. Shirakawa, *Angew. Chem. Int. Ed.* **2001**, *40*, 2574.

[3] A. MacDiarmid, *Rev. Mod. Phys.* **2001**, *73*, 701.

[4] A.J. Heeger, *Angew. Chem. Int. Ed.* **2001**, *40*, 2591.

[5] C. Chiang, C. Fincher, Y. Park, A.J. Heeger, H. Shirakawa, E. Louis, S. Gau, A. MacDiarmid, *Phys. Rev. Lett.* **1977**, *39*, 1098.

[6] A.J. Heeger, *Chem. Soc. Rev.* **2010**, *39*, 2354.

[7] I. McCulloch, M. Heeney, C. Bailey, K. Genevicius, I. Macdonald, M. Shkunov, D. Sparrowe, S. Tierney, R. Wagner, W. Zhang, M.L. Chabinyc, R.J. Kline, M.D. McGehee, M.F. Toney, *Nat. Mater.* **2006**, *5*, 328.

[8] Y. Kim, S. Cook, S.M. Tuladhar, S.A. Choulis, J. Nelson, J.R. Durrant, D.D.C. Bradley, M. Giles, I. McCulloch, C.-S. Ha, M. Ree, *Nat. Mater.* **2006**, *5*, 197.

[9] E. Bundgaard, F.C. Krebs, *Sol. Energy Mater. Sol. Cells* **2007**, *91*, 954.

[10] P. Schilinsky, U. Asawapirom, U. Scherf, M. Biele, C.J. Brabec, *Chem. Mater.* **2005**, *17*, 2175.

[11] M.T. Dang, L. Hirsch, G. Wantz, *Adv. Mater.* **2011**, *23*, 3597.

[12] P.-L.T. Boudreault, A. Najari, M. Leclerc, *Chem. Mater.* **2011**, *23*, 456.

[13] S. Cho, J.H. Seo, S.H. Park, S. Beaupré, M. Leclerc, A.J. Heeger, *Adv. Mater.* **2010**, *22*, 1253.

[14] S.H. Park, A. Roy, S. Beaupré, S. Cho, N. Coates, J.S. Moon, D. Moses, M. Leclerc, K. Lee, A.J. Heeger, *Nat. Photonics* **2009**, *3*, 297.

[15] A. Moliton, R.C. Hiorns, *Polym. Int.* **2004**, *53*, 1397.

[16] H. Sirringhaus, P.J. Brown, R.H. Friend, M.M. Nielsen, K. Bechgaard, B.M.W. Langeveld-Voss, A.J.H. Spiering, R.A.J. Janssen, E.W. Meijer, P. Herwig, D.M. de Leeuw, *Nature* **1999**, *401*, 685.

[17] B. Kippelen, J.-L. Brédas, *Energy Environ. Sci.* **2009**, *2*, 251.

[18] A. Mayer, S. Scully, B. Hardin, M. Rowell, M. McGehee, *Mater. Today* **2007**, *10*, 28.

[19] Y. Liu, M.A. Summers, C. Edder, J.M.J. Fréchet, M.D. McGehee, *Adv. Mater.* **2005**, *17*, 2960.

[20] S. Günes, H. Neugebauer, N.S. Sariciftci, *Chem. Rev.* **2007**, *107*, 1324.

[21] M.D. McGehee, A.J. Heeger, *Adv. Mater.* **2000**, *12*, 1655.

[22] A.P. Kulkarni, C.J. Tonzola, A. Babel, S.A. Jenekhe, *Chem. Mater.* **2004**, *16*, 4556.

[23] H.E. Katz, *Chem. Mater.* **2004**, *16*, 4748.

[24] C.D. Dimitrakopoulos, P.R.L. Malenfant, *Adv. Mater.* **2002**, *14*, 99.

[25] K. Wang, J. Huang, Z. Wei, *J. Phys. Chem. C* **2010**, *114*, 8062.

[26] B. Adhikari, S. Majumdar, *Prog. Polym. Sci.* **2004**, *29*, 699.

[27] B.J. Schwartz, *Annu. Rev. Phys. Chem.* **2003**, *54*, 141.

[28] N.S. Lewis, D.G. Nocera, *Proc. Natl. Acad. Sci. U.S.A.* **2006**, *103*, 15729.

[29] C.J. Brabec, J.A. Hauch, P. Schilinsky, C. Waldauf, *MRS Bull.* **2005**, *30*, 50.

[30] C.J. Brabec, *Sol. Energy Mater. Sol. Cells* **2004**, *83*, 273.

[31] N. Espinosa, M. Hösel, D. Angmo, F.C. Krebs, *Energy Environ. Sci.* **2012**, *5*, 5117.

[32] T.D. Nielsen, C. Cruickshank, S. Foged, J. Thorsen, F.C. Krebs, *Sol. Energy Mater. Sol. Cells* **2010**, *94*, 1553.

[33] H. Spanggaard, F.C. Krebs, *Sol. Energy Mater. Sol. Cells* **2004**, *83*, 125.

[34] A. Becquerel, *C. R. Acad. Sci.* **1839**, *9*, 561.

[35] D.M. Chapin, C.S. Fuller, G.L. Pearson, *J. Appl. Phys.* **1954**, *25*, 676.

[36] A. Slaoui, R.T. Collins, *MRS Bull.* **2007**, *32*, 211.

[37] T. Aramoto, S. Kumazawa, H. Higuchi, T. Arita, S. Shibutani, T. Nishio, J. Nakajima, M. Tsuji, A. Hanafusa, T. Hibino, K. Omura, H. Ohyama, M. Murozono, *Jpn. J. Appl. Phys.* **1997**, *36*, 6304.

[38] K. Ramanathan, M.A. Contreras, C.L. Perkins, S. Asher, F.S. Hasoon, J. Keane, D. Young, M. Romero, W. Metzger, R. Noufi, J. Ward, A. Duda, *Prog. Photovoltaics Res. Appl.* **2003**, *11*, 225.

[39] C.W. Tang, *Appl. Phys. Lett.* **1986**, *48*, 183.

[40] M.A. Green, K. Emery, Y. Hishikawa, W. Warta, E.D. Dunlop, *Prog. Photovoltaics Res. Appl.* **2012**, *20*, 12.

[41] G. Yu, J. Gao, J.C. Hummelen, F. Wudl, A.J. Heeger, *Science* **1995**, *270*, 1789.

[42] J.J.M. Halls, C.A. Walsh, N.C. Greenham, E.A. Marseglia, R.H. Friend, S.C. Moratti, A.B. Holmes, *Nature* **1995**, *376*, 498.

[43] H. Hoppe, M. Niggemann, C. Winder, J. Kraut, R. Hiesgen, A. Hinsch, D. Meissner, N.S. Sariciftci, *Adv. Funct. Mater.* **2004**, *14*, 1005.

[44] C.Y. Yang, A.J. Heeger, *Syn. Met.* **1996**, *83*, 85.

[45] N. Blouin, A. Michaud, D. Gendron, S. Wakim, E. Blair, R. Neagu-Plesu, M. Belletête, G. Durocher, Y. Tao, M. Leclerc, *J. Am. Chem. Soc.* **2008**, *130*, 732.

[46] F.C. Krebs, H. Spanggaard, *Chem. Mater.* **2005**, *17*, 5235.

[47] C.H. Peters, I.T. Sachs-Quitana, J.P. Kastrop, S. Beaupré, M. Leclerc, M.D. McGehee, *Adv. Energy Mater.* **2011**, *1*, 491.

[48] F.C. Krebs, M. Jørgensen, K. Norrman, O. Hagemann, J. Alstrup, T.D. Nielsen, J. Fyenbo, K. Larsen, J. Kristensen, *Sol. Energy Mater. Sol. Cells* **2009**, *93*, 422.

[49] M. Manceau, D. Angmo, M. Jørgensen, F.C. Krebs, *Sol. Energy Mater. Sol. Cells* **2011**, *12*, 566.

[50] F.C. Krebs, T. Tromholt, M. Jørgensen, *Nanoscale* **2010**, *2*, 873.

[51] F.C. Krebs, *Sol. Energy Mater. Sol. Cells* **2009**, *93*, 1636.

[52] F.C. Krebs, S.A. Gevorgyan, J. Alstrup, *J. Mater. Chem.* **2009**, *19*, 5442.

[53] Y. Sun, G.C. Welch, W.L. Leong, C.J. Takacs, G.C. Bazan, A.J. Heeger, *Nat. Mater.* **2012**, *11*, 44.

[54] C.J. Chen, *Physics of Solar Energy*, John Wiley & Sons, Inc., Hoboken, NJ, USA **2011**.

[55] F.C. Krebs, *Polymer Photovoltaics: A Practical Approach*, SPIE Press **2008**.

[56] V. Shrotriya, G. Li, Y. Yao, T. Moriarty, K. Emery, Y. Yang, *Adv. Funct. Mater.* **2006**, *16*, 2016.

[57] E.M. Conwell, *Syn. Met.* **1996**, *83*, 101.

[58] L.J.A. Koster, V.D. Mihailetchi, P.W.M. Blom, *Appl. Phys. Lett.* **2006**, *88*, 093511.

[59] V. Shrotriya, *Nat. Photonics* **2009**, *3*, 447.

[60] M.C. Barr, J.A. Rowehl, R.R. Lunt, J. Xu, A. Wang, C.M. Boyce, S.G. Im, V. Bulović, K.K. Gleason, *Adv. Mater.* **2011**, *23*, 3499.

[61] F.C. Krebs, *Org. Electron.* **2009**, *10*, 761.

[62] B. Zimmermann, M. Glatthaar, M. Niggemann, M.K. Riede, A. Hinsch, A. Gombert, *Sol. Energy Mater. Sol. Cells* **2007**, *91*, 374.

[63] P.J. Hotchkiss, S.C. Jones, S.A. Paniagua, A. Sharma, B. Kippelen, N.R. Armstrong, S.R. Marder, *Acc. Chem. Res.* **2012**, *45*, 337.

[64] T. Akter, W. Soo Kim, W.S. Kim, *ACS Appl. Mater. Interfaces* **2012**, *4*, 1855.

[65] T. Minami, *Semicond. Sci. Technol.* **2005**, *20*, S35.

[66] O. Mryasov, A. Freeman, *Phys. Rev. B* **2001**, *64*, 233111.

[67] K. Sugiyama, H. Ishii, Y. Ouchi, K. Seki, *J. Appl. Phys.* **2000**, *87*, 295.

[68] Y. Park, V. Choong, Y. Gao, B.R. Hsieh, C.W. Tang, *Appl. Phys. Lett.* **1996**, *68*, 2699.

[69] S. Ray, R. Banerjee, N. Basu, A.K. Batabyal, A.K. Barua, *J. Appl. Phys.* **1983**, *54*, 3497.

[70] M. Bender, W. Seelig, C. Daube, H. Frankenberger, B. Ocker, J. Stollenwerk, *Thin Solid Films* **1998**, *326*, 72.

[71] N. Balasubramanian, A. Subrahmanyam, *J. Phys. D: Appl. Phys.* **1989**, *22*, 206.

[72] K.H. Lee, *J. Appl. Phys.* **2004**, *95*, 586.

[73] C.C. Wu, C.I. Wu, J.C. Sturm, A. Kahn, *Appl. Phys. Lett.* **1997**, *70*, 1348.

[74] C. Lungenschmied, G. Dennler, H. Neugebauer, S.N. Sariciftci, M. Glatthaar, T. Meyer, A. Meyer, *Sol. Energy Mater. Sol. Cells* **2007**, *91*, 379.

[75] Y. Galagan, J.-E. J.M. Rubingh, R. Andriessen, C.-C. Fan, P. W.M. Blom, S. C. Veenstra, J. M. Kroon, *Sol. Energy Mater. Sol. Cells* **2011**, *95*, 1339.

[76] G.P. Kushto, W. Kim, Z.H. Kafafi, *App. Phys. Lett.* **2005**, *86*, 093502.

[77] Y. Leterrier, L. Médico, F. Demarco, J.-A.E. Månson, U. Betz, M.F. Escolà, M. Kharrazi Olsson, F. Atamny, *Thin Solid Films* **2004**, *460*, 156.

[78] D.S. Hecht, R.B. Kaner, *MRS Bull.* **2011**, *36*, 749.

[79] D.R. Cairns, R.P. Witte, D.K. Sparacin, S.M. Sachsman, D.C. Paine, G.P. Crawford, R.R. Newton, *Appl. Phys. Lett.* **2000**, *76*, 1425.

[80] Z. Chen, B. Cotterell, W. Wang, *Eng. Fract. Mech.* **2002**, *69*, 597.

[81] Z. Chen, *Thin Solid Films* **2001**, *394*, 201.

[82] L. Hu, H.S. Kim, J.-Y. Lee, P. Peumans, Y. Cui, *ACS Nano* **2010**, *4*, 2955.

[83] A.R. Rathmell, B.J. Wiley, *Adv. Mater.* **2011**, *23*, 4798.

[84] Z. Wu, Z. Chen, X. Du, J.M. Logan, J. Sippel, M. Nikolou, K. Kamaras, J.R. Reynolds, D.B. Tanner, A.F. Hebard, A.G. Rinzler, *Science* **2004**, *305*, 1273.

[85] J. Wu, M. Agrawal, H.A. Becerril, Z. Bao, Z. Liu, Y. Chen, P. Peumans, *ACS Nano* **2010**, *4*, 43.

[86] M. Vosgueritchian, D.J. Lipomi, Z. Bao, *Adv. Funct. Mater.* **2011**, *22*, 421.

[87] R. Po, C. Carbonera, A. Bernardi, F. Tinti, N. Camaioni, *Sol. Energy Mater. Sol. Cells* **2012**, *100*, 97.

[88] B. O'Connor, C. Haughn, K.-H. An, K.P. Pipe, M. Shtein, *Appl. Phys. Lett.* **2008**, *93*, 223304.

[89] R.B. Pode, C.J. Lee, D.G. Moon, J.I. Han, *Appl. Phys. Lett.* **2004**, *84*, 4614.

[90] W. Cai, X. Gong, Y. Cao, *Sol. Energy Mater. Sol. Cells* **2010**, *94*, 114.

[91] J.-Y. Lee, S.T. Connor, Y. Cui, P. Peumans, *Nano Lett.* **2008**, *8*, 689.

[92] A.R. Rathmell, S.M. Bergin, Y.-L. Hua, Z.-Y. Li, B.J. Wiley, *Adv. Mater.* **2010**, *22*, 3558.

[93] P.E. Lyons, S. De, J. Elias, M. Schamel, L. Philippe, A.T. Bellew, J.J. Boland, J.N. Coleman, *J. Phys. Chem. Lett.* **2011**, *2*, 3058.

[94] D. Zhang, R. Wang, M. Wen, D. Weng, X. Cui, J. Sun, H. Li, Y. Lu, *J. Am. Chem. Soc.* **2012**, *134*, 14283.

[95] S.-I. Na, B.-K. Yu, S.-S. Kim, D. Vak, T.-S. Kim, J.-S. Yeo, D.-Y. Kim, *Sol. Energy Mater. Sol. Cells* **2010**, *94*, 1333.

[96] D.S. Hecht, L. Hu, G. Irvin, *Adv. Mater.* **2011**, *23*, 1482.

[97] L. Hu, H. Wu, Y. Cui, *MRS Bull.* **2011**, *36*, 760.

[98] T. Tokuno, M. Nogi, M. Karakawa, J. Jiu, T.T. Nge, Y. Aso, K. Suganuma, *Nano Res.* **2011**, *4*, 1215.

[99] S. De, T.M. Higgins, P.E. Lyons, E.M. Doherty, P.N. Nirmalraj, W.J. Blau, J.J. Boland, J.N. Coleman, *ACS Nano* **2009**, *3*, 1767.

[100] E.C. Garnett, W. Cai, J.J. Cha, F. Mahmood, S.T. Connor, M. Greyson Christoforo, Y. Cui, M.D. McGehee, M.L. Brongersma, *Nat. Mater.* **2012**, *11*, 241.

[101] R. Ulbricht, S.B. Lee, X. Jiang, K. Inoue, M. Zhang, S. Fang, R.H. Baughman, A.A. Zakhidov, *Sol. Energy Mater. Sol. Cells* **2007**, *91*, 416.

[102] R.C. Tenent, T.M. Barnes, J.D. Bergeson, A.J. Ferguson, B. To, L.M. Gedvilas, M.J. Heben, J.L. Blackburn, *Adv. Mater.* **2009**, *21*, 3210.

[103] Y. Zhu, Z. Sun, Z. Yan, Z. Jin, J.M. Tour, *ACS Nano* **2011**, *5*, 6472.

[104] H.A. Becerril, J. Mao, Z. Liu, R.M. Stoltenberg, Z. Bao, Y. Chen, *ACS Nano* **2008**, *2*, 463.

[105] T. Dürkop, S.A. Getty, E. Cobas, M.S. Fuhrer, *Nano Lett.* **2004**, *4*, 35.

[106] V.C. Moore, M.S. Strano, E.H. Haroz, R.H. Hauge, R.E. Smalley, J. Schmidt, Y. Talmon, *Nano Lett.* **2003**, *3*, 1379.

[107] J. Chen, A.M. Rao, S. Lyuksyutov, M.E. Itkis, M.A. Hamon, H. Hu, R.W. Cohn, P.C. Eklund, D.T. Colbert, R.E. Smalley, R.C. Haddon, *J. Phys. Chem. B* **2001**, *105*, 2525.

[108] J. Li, L. Hu, L. Wang, Y. Zhou, G. Grüner, T.J. Marks, *Nano Lett.* **2006**, *6*, 2472.

[109] L.F.C. Pereira, C.G. Rocha, A. Latgé, J.N. Coleman, M.S. Ferreira, *Appl. Phys. Lett.* **2009**, *95*, 123106.

[110] Z. Chen, B. Cotterell, W. Wang, E. Geunther, S.-J. Chua, *Thin Solid Films* **2001**, *394*, 202.

[111] Y. Zhi-nong, X. Fan, L. Yuqiong, X. Wei, in *Asia Optical Fiber Communication and Optoelectronic Exposition and Conference*, Optical Society of America**2008**, 3.

[112] Y. Xia, J. Ouyang, *ACS Appl. Mater. Interfaces* **2012**, *4*, 4131.

[113] Y.H. Kim, C. Sachse, M.L. Machala, C. May, L. Müller-Meskamp, K. Leo, *Adv. Funct. Mater.* **2011**, *21*, 1076.

[114] L. Groenendaal, F. Jonas, D. Freitag, H. Pielartzik, J.R. Reynolds, *Adv. Mater.* **2000**, *12*, 481.

[115] J.S. Yang, S.H. Oh, D.L. Kim, S.J. Kim, H.J. Kim, *ACS Appl. Mater. Interfaces* **2012**, *4*, 5394.

[116] Y. Xia, J. Ouyang, *J. Mater. Chem.* **2011**, *21*, 4927.

[117] D. Alemu, H.-Y. Wei, K.-C. Ho, C.-W. Chu, *Energy Environ. Sci.* **2012**, *5*, 9662.

[118] D.J. Lipomi, J.A. Lee, M. Vosgueritchian, B.C.-K. Tee, J.A. Bolander, Z. Bao, *Chem. Mater.* **2012**, *24*, 373.

[119] Y. Xia, K. Sun, J. Ouyang, *Energy Environ. Sci.* **2012**, *5*, 5325.

[120] C. Badre, L. Marquant, A.M. Alsayed, L.A. Hough, *Adv. Funct. Mater.* **2012**, *22*, 2723.

[121] M. Döbbelin, R. Marcilla, M. Salsamendi, C. Pozo-Gonzalo, P.M. Carrasco, J.A. Pomposo, D. Mecerreyes, *Chem. Mater.* **2007**, *19*, 2147.

[122] J. Ouyang, Q. Xu, C.-W. Chu, Y. Yang, G. Li, J. Shinar, *Polymer* **2004**, *45*, 8443.

[123] Y. Xia, K. Sun, J. Ouyang, *Adv. Mater.* **2012**, *24*, 2436.

[124] B.J. Worfolk, W. Li, P. Li, T.C. Hauger, K.D. Harris, J.M. Buriak, *J. Mater. Chem.* **2012**, 11354.

[125] M. Jørgensen, K. Norrman, F.C. Krebs, *Sol. Energy Mater. Sol. Cells* **2008**, *92*, 686.

[126] A.M. Nardes, M. Kemerink, M.M. de Kok, E. Vinken, K. Maturova, R.A.J. Janssen, *Org. Electron.* **2008**, *9*, 727.

[127] T. Nagata, S. Oh, T. Chikyow, Y. Wakayama, *Org. Electon.* **2011**, *12*, 279.

[128] C.J.M. Emmott, A. Urbina, J. Nelson, *Sol. Energy Mater. Sol. Cells* **2012**, *97*, 14.

[129] B.J. Worfolk, T.C. Hauger, K.D. Harris, D.A. Rider, J.A.M. Fordyce, S. Beaupré, M. Leclerc, J.M. Buriak, *Adv. Energy Mater.* **2012**, *2*, 361.

[130] H.-L. Yip, A.K.-Y. Jen, *Energy Environ. Sci.* **2012**, *5*, 5994.

[131] S. Hau, H.-L. Yip, A.K.-Y. Jen, *Polym. Rev.* **2010**, *50*, 474.

[132] M.S. White, D.C. Olson, S.E. Shaheen, N. Kopidakis, D.S. Ginley, *Appl. Phys. Lett.* **2006**, *89*, 143517.

[133] L.S. Roman, W. Mammo, L.A.A. Pettersson, M.R. Andersson, O. Inganäs, *Adv. Mater.* **1998**, *10*, 774.

[134] M. Granstr|[ouml]|m, K. Petritsch, A.C. Arias, A. Lux, M.R. Andersson, R.H. Friend, *Nature* **1998**, *395*, 257.

[135] C.J. Brabec, S.E. Shaheen, C. Winder, N.S. Sariciftci, P. Denk, *Appl. Phys. Lett.* **2002**, *80*, 1288.

[136] D.A. Rider, K.D. Harris, D. Wang, J. Bruce, M.D. Fleischauer, R.T. Tucker, M.J. Brett, J.M. Buriak, *ACS Appl. Mater. Interfaces* **2009**, *1*, 279.

[137] M.D. Irwin, D.B. Buchholz, A.W. Hains, R.P.H. Chang, T.J. Marks, *Proc. Natl. Acad. Sci. U.S.A.* **2008**, *105*, 2783.

[138] M. Jørgensen, K. Norrman, F.C. Krebs, *Sol. Energy Mater. Sol. Cells* **2008**, *92*, 686.

[139] M.P. de Jong, L.J. van IJzendoorn, M.J.A. de Voigt, *Appl. Phys. Lett.* **2000**, *77*, 2255.

[140] K. Norrman, N. Larsen, F.C. Krebs, *Sol. Energy Mater. Sol. Cells* **2006**, *90*, 2793.

[141] E. Voroshazi, B. Verreet, A. Buri, R. Müller, D. Di Nuzzo, P. Heremans, *Org. Electron.* **2011**, *12*, 736.

[142] K.X. Steirer, J.P. Chesin, N.E. Widjonarko, J.J. Berry, A. Miedaner, D.S. Ginley, D.C. Olson, *Org. Electron.* **2010**, *11*, 1414.

[143] S.-Y. Park, H.-R. Kim, Y.-J. Kang, D.-H. Kim, J.-W. Kang, *Sol. Energy Mater. Sol. Cells* **2010**, *94*, 2332.

[144] N. Sun, G. Fang, P. Qin, Q. Zheng, M. Wang, X. Fan, F. Cheng, J. Wan, X. Zhao, J. Liu, D.L. Carroll, J. Ye, *J. Phys. D: Appl. Phys.* **2010**, *43*, 445101.

[145] S. Han, W.S. Shin, M. Seo, D. Gupta, S.-J. Moon, S. Yoo, *Org. Electron.* **2009**, *10*, 791.

[146] M. Vasilopoulou, L.C. Palilis, D.G. Georgiadou, P. Argitis, S. Kennou, I. Kostis, G. Papadimitropoulos, N. A. Stathopoulos, A.A. Iliadis, N. Konofaos, D. Davazoglou, L. Sygellou, *Thin Solid Films* **2011**, *519*, 5748.

[147] F. Liu, S. Shao, X. Guo, Y. Zhao, Z. Xie, *Sol. Energy Mater. Sol. Cells* **2010**, *94*, 842.

[148] T. Yang, M. Wang, Y. Cao, F. Huang, L. Huang, J. Peng, X. Gong, S.Z.D. Cheng, Y. Cao, *Adv. Energy Mater.* **2012**, *2*, 523.

[149] J.J. Jasieniak, J. Seifter, J. Jo, T. Mates, A.J. Heeger, *Adv. Funct. Mater.* **2012**, *22*, 2594.

[150] Y. Sun, C.J. Takacs, S.R. Cowan, J.H. Seo, X. Gong, A. Roy, A.J. Heeger, *Adv. Mater.* **2011**, *23*, 2226.

[151] G. Ho Jung, K.-G. Lim, T.-W. Lee, J.-L. Lee, *Sol. Energy Mater. Sol. Cells* **2011**, *95*, 1146.

[152] V. Shrotriya, G. Li, Y. Yao, C.-W. Chu, Y. Yang, *Appl. Phys. Lett.* **2006**, *88*, 073508.

[153] S. Shao, F. Liu, Z. Xie, L. Wang, *J. Phys. Chem. C* **2010**, *114*, 9161.

[154] S. Chen, J.R. Manders, S.-W. Tsang, F. So, *J. Mater. Chem.* **2012**, *22*, 24202.

[155] L.-M. Chen, Z. Xu, Z. Hong, Y. Yang, *J. Mater. Chem.* **2010**, *20*, 2575.

[156] Y. Hirose, A. Kahn, V. Aristov, P. Soukiassian, *Appl. Phys. Lett.* **1996**, *68*, 217.

[157] H. Ishii, K. Sugiyama, E. Ito, K. Seki, *Adv. Mater.* **1999**, *11*, 605.

[158] N. Uyeda, T. Kobayashi, K. Ishizuka, Y. Fujiyoshi, *Nature* **1980**, *285*, 95.

[159] M.O. Reese, M.S. White, G. Rumbles, D.S. Ginley, S.E. Shaheen, *Appl. Phys. Lett.* **2008**, *92*, 053307.

[160] Y. Yi, S.J. Kang, K. Cho, J.M. Koo, K. Han, K. Park, M. Noh, C.N. Whang, K. Jeong, *Appl. Phys. Lett.* **2005**, *86*, 213502.

[161] J. Huang, G. Li, E. Wu, Q. Xu, Y. Yang, *Adv. Mater.* **2006**, *18*, 114.

[162] G.E. Jabbour, B. Kippelen, N.R. Armstrong, N. Peyghambarian, *Appl. Phys. Lett.* **1998**, *73*, 1185.

[163] S.E. Shaheen, G.E. Jabbour, M.M. Morrell, Y. Kawabe, B. Kippelen, N. Peyghambarian, M.-F. Nabor, R. Schlaf, E.A. Mash, N.R. Armstrong, *J. Appl. Phys.* **1998**, *84*, 2324.

[164] J.K. Baral, R. Izquierdo, M. Packirisamy, V.-V. Truong, *Eur. Phys. J. Appl. Phys.* **2011**, *55*, 30202.

[165] G. Li, C.-W. Chu, V. Shrotriya, J. Huang, Y. Yang, *Appl. Phys. Lett.* **2006**, *88*, 253503.

[166] H.-H. Liao, L.-M. Chen, Z. Xu, G. Li, Y. Yang, *Appl. Phys. Lett.* **2008**, *92*, 173303.

[167] Y. Sun, J.H. Seo, C.J. Takacs, J. Seifter, A.J. Heeger, *Adv. Mater.* **2011**, *23*, 1679.

[168] J.-H. Huang, H.-Y. Wei, K.-C. Huang, C.-L. Chen, R.-R. Wang, F.-C. Chen, K.-C. Ho, C.-W. Chu, *Energy Environ. Sci.* **2010**, *3*, 654.

[169] J.Y. Kim, K. Lee, N.E. Coates, D. Moses, T.-Q. Nguyen, M. Dante, A.J. Heeger, *Science* **2007**, *317*, 222.

[170] J.Y. Kim, S.H. Kim, H.-H. Lee, K. Lee, W. Ma, X. Gong, A.J. Heeger, *Adv. Mater.* **2006**, *18*, 572.

[171] H.-L. Yip, S.K. Hau, N.S. Baek, A.K.-Y. Jen, *Appl. Phys. Lett.* **2008**, *92*, 193313.

[172] D.A. Rider, B.J. Worfolk, K.D. Harris, A. Lalany, K. Shahbazi, M.D. Fleischauer, M.J. Brett, J.M. Buriak, *Adv. Funct. Mater.* **2010**, *20*, 2404.

[173] K. Sun, B. Zhao, V. Murugesan, A. Kumar, K. Zeng, J. Subbiah, W.W.H. Wong, D.J. Jones, J. Ouyang, *J. Mater. Chem.* **2012**, *22*, 24155.

[174] C. He, C. Zhong, H. Wu, R. Yang, W. Yang, F. Huang, G.C. Bazan, Y. Cao, *J. Mater. Chem.* **2010**, *20*, 2617.

[175] C. V. Hoven, A. Garcia, G.C. Bazan, T.-Q. Nguyen, *Adv. Mater.* **2008**, *20*, 3793.

[176] J.H. Seo, A. Gutacker, Y. Sun, H. Wu, F. Huang, Y. Cao, U. Scherf, A.J. Heeger, G.C. Bazan, *J. Am. Chem. Soc.* **2011**, *133*, 8416.

[177] T. V. Pho, H. Kim, J.H. Seo, A.J. Heeger, F. Wudl, *Adv. Funct. Mater.* **2011**, *21*, 4338.

[178] H. Kang, S. Hong, J. Lee, K. Lee, *Adv. Mater.* **2012**, *24*, 3005.

[179] T. Shi, X. Zhu, D. Yang, Y. Xie, J. Zhang, G. Tu, *Appl. Phys. Lett.* **2012**, *101*, 161602.

[180] Y.-M. Chang, R. Zhu, E. Richard, C.-C. Chen, G. Li, Y. Yang, *Adv. Funct. Mater.* **2012**, *22*, 3284.

[181] Z. Tang, L.M. Andersson, Z. George, K. Vandewal, K. Tvingstedt, P. Heriksson, R. Kroon, M.R. Andersson, O. Inganäs, *Adv. Mater.* **2012**, *24*, 554.

[182] Z. He, C. Zhong, S. Su, M. Xu, H. Wu, Y. Cao, *Nat. Photonics* **2012**, *6*, 593.

[183] Y. Zhou, C. Fuentes-Hernandez, J. Shim, J. Meyer, A.J. Giordano, H. Li, P. Winget, T. Papadopoulos, H. Cheun, J. Kim, M. Fenoll, A. Dindar, W. Haske, E. Najafabadi, T.M. Khan, H. Sojoudi, S. Barlow, S. Graham, J.-L. Brédas, S.R. Marder, A. Kahn, B. Kippelen, *Science* **2012**, *336*, 327.

[184] S. Cros, M. Firon, S. Lenfant, P. Trouslard, L. Beck, *Nucl. Instrum. Methods Phys. Res., Sect. B* **2006**, *251*, 257.

[185] J. Lee, Y. Park, D.Y. Kim, H.Y. Chu, H. Lee, L.-M. Do, *Appl. Phys. Lett.* **2003**, *82*, 173.

[186] B. Limketkai, M. Baldo, *Phys. Rev. B* **2005**, *71*.

[187] J. Huang, G. Li, Y. Yang, *Adv. Mater.* **2008**, *20*, 415.

[188] Z. Xu, L.-M. Chen, G. Yang, C.-H. Huang, J. Hou, Y. Wu, G. Li, C.-S. Hsu, Y. Yang, *Adv. Funct. Mater.* **2009**, *19*, 1227.

[189] J. Gilot, I. Barbu, M.M. Wienk, R.A.J. Janssen, *Appl. Phys. Lett.* **2007**, *91*, 113520.

[190] S.K. Hau, H.-L. Yip, O. Acton, N.S. Baek, H. Ma, A.K.-Y. Jen, *J. Mater. Chem.* **2008**, *18*, 5113.

[191] A.K.K. Kyaw, X.W. Sun, C.Y. Jiang, G.Q. Lo, D.W. Zhao, D.L. Kwong, *Appl. Phys. Lett.* **2008**, *93*, 221107.

[192] S.K. Hau, Y. Cheng, H. Yip, Y. Zhang, H. Ma, A.K. Jen, *ACS Appl. Mater. Interfaces* **2010**, *2*, 1892.

[193] S.K. Hau, H.-L. Yip, H. Ma, A.K.-Y. Jen, *Appl. Phys. Lett.* **2008**, *93*, 233304.

[194] Y. Zhang, S.K. Hau, H.-L. Yip, Y. Sun, O. Acton, A.K.-Y. Jen, *Chem. Mater.* **2010**, *22*, 2696.

[195] N.S. Sariciftci, L. Smilowitz, A.J. Heeger, F. Wudl, *Science* **1992**, *258*, 1474.

[196] C. Girotto, D. Moia, B.P. Rand, P. Heremans, *Adv. Funct. Mater.* **2011**, *21*, 64.

[197] A. Lange, M. Wegener, C. Boeffel, B. Fischer, A. Wedel, D. Neher, *Sol. Energy Mater. Sol. Cells* **2010**, *94*, 1816.

[198] A. Teichler, R. Eckardt, S. Hoeppener, C. Friebe, J. Perelaer, A. Senes, M. Morana, C.J. Brabec, U.S. Schubert, *Adv. Energy Mater.* **2011**, *1*, 105.

[199] T.R. Andersen, T.T. Larsen-Olsen, B. Andreasen, A.P.L. Böttiger, J.E. Carlé, M. Helgesen, E. Bundgaard, K. Norrman, J.W. Andreasen, M. Jørgensen, F.C. Krebs, *ACS Nano* **2011**, *5*, 4188.

[200] R. Søndergaard, M. Helgesen, M. Jørgensen, F.C. Krebs, *Adv. Energy Mater.* **2010**, *1*, 68.

[201] R. Søndergaard, M. Hösel, D. Angmo, T.T. Larsen-Olsen, F.C. Krebs, *Mater. Today* **2012**, *15*, 36.

[202] F. Jakubka, M. Heyder, F. Machui, J. Kaschta, D. Eggerath, W. Lövenich, F.C. Krebs, C.J. Brabec, *Sol. Energy Mater. Sol. Cells* **2013**, *109*, 120.

[203] T.-A. Chen, X. Wu, R.D. Rieke, *J. Am. Chem. Soc.* **1995**, *117*, 233.

[204] R.D. McCullough, R.D. Lowe, M. Jayaraman, D.L. Anderson, *J. Org. Chem.* **1993**, *58*, 904.

[205] T.-Y. Chu, S. Alem, S.-W. Tsang, S.-C. Tse, S. Wakim, J. Lu, G. Dennler, D. Waller, R. Gaudiana, Y. Tao, *Appl. Phys. Lett.* **2011**, *98*, 253301.

[206] Y. Zou, A. Najari, P. Berrouard, S. Beaupré, B.R. Aich, Y. Tao, M. Leclerc, *J. Am. Chem. Soc.* **2010**, *132*, 5330.

[207] A. Najari, S. Beaupré, P. Berrouard, Y. Zou, J.-R. Pouliot, C. Lepage-Pérusse, M. Leclerc, *Adv. Funct. Mater.* **2011**, *21*, 718.

[208] B.R. Aïch, J. Lu, S. Beaupré, M. Leclerc, Y. Tao, *Org. Electron.* **2012**, *13*, 1736.

[209] Y. Liang, D. Feng, Y. Wu, S.-T. Tsai, G. Li, C. Ray, L. Yu, *J. Am. Chem. Soc.* **2009**, *131*, 7792.

[210] Y. Liang, Z. Xu, J. Xia, S.-T. Tsai, Y. Wu, G. Li, C. Ray, L. Yu, *Adv. Mater.* **2010**, *22*, E135.

[211] M.C. Scharber, D. Mühlbacher, M. Koppe, P. Denk, C. Waldauf, A.J. Heeger, C.J. Brabec, *Adv. Mater.* **2006**, *18*, 789.

[212] Y.-J. Cheng, C.-H. Hsieh, Y. He, C.-S. Hsu, Y. Li, *J. Am. Chem. Soc.* **2010**, *132*, 17381.

[213] H.W. Kroto, J.R. Heath, S.C. O'Brien, R.F. Curl, R.E. Smalley, *Nature* **1985**, *318*, 162.

[214] W. Krätschmer, L.D. Lamb, K. Fostiropoulos, D.R. Huffman, *Nature* **1990**, *347*, 354.

[215] C.-Z. Li, H.-L. Yip, A.K.-Y. Jen, *J. Mater. Chem.* **2012**, *22*, 4161.

[216] Y. He, Y. Li, *Phys. Chem. Chem. Phys.* **2011**, *13*, 1970.

[217] M.M. Wienk, J.M. Kroon, W.J.H. Verhees, J. Knol, J.C. Hummelen, P.A. van Hal, R.A.J. Janssen, *Angew. Chem. Int. Ed.* **2003**, *42*, 3371.

[218] J.C. Hummelen, B.W. Knight, F. LePeq, F. Wudl, J. Yao, C.L. Wilkins, *J. Org. Chem.* **1995**, *60*, 532.

[219] C.-Y. Chang, C.-E. Wu, S.-Y. Chen, C. Cui, Y.-J. Cheng, C.-S. Hsu, Y.-L. Wang, Y. Li, *Angew. Chem. Int. Ed.* **2011**, *50*, 9386.

[220] P.A. Troshin, H. Hoppe, J. Renz, M. Egginger, J.Y. Mayorova, A.E. Goryachev, A.S. Peregudov, R.N. Lyubovskaya, G. Gobsch, N.S. Sariciftci, V.F. Razumov, *Adv. Funct. Mater.* **2009**, *19*, 779.

[221] S.S. van-Bavel, E. Sourty, G. de With, J. Loos, *Nano Lett.* **2009**, *9*, 507.

[222] Y.S. Eo, H.W. Rhee, B.D. Chin, J.-W. Yu, *Syn. Met.* **2009**, *159*, 1910.

[223] C. Brabec, V. Dyakonov, U. Scherf, *Organic Photovoltaics: Materials, Device Physics, and Manufacturing Technologies*, Wiley-VCH Verlag GmbH & Co., Weinheim, Germany **2008**.

[224] F.C. Krebs, R. Søndergaard, M. Jørgensen, *Sol. Energy Mater. Sol. Cells* **2011**, *95*, 1348.

[225] Y.-F. Lim, S. Lee, D.J. Herman, M.T. Lloyd, J.E. Anthony, G.G. Malliaras, *Appl. Phys. Lett.* **2008**, *93*, 193301.

[226] S.K. Hau, H.-L. Yip, J. Zou, A.K.-Y. Jen, *Org. Electron.* **2009**, *10*, 1401.

[227] S. Sista, Z. Hong, L.-M. Chen, Y. Yang, *Energy Environ. Sci.* **2011**, *4*, 1606.

[228] S. Sista, M.-H. Park, Z. Hong, Y. Wu, J. Hou, W.L. Kwan, G. Li, Y. Yang, *Adv. Mater.* **2010**, *22*, 380.

[229] A. Hadipour, B. de Boer, P.W.M. Blom, *Adv. Funct. Mater.* **2008**, *18*, 169.

[230] T. Ameri, G. Dennler, C. Lungenschmied, C.J. Brabec, *Energy Environ. Sci.* **2009**, *2*, 347.

[231] L. Dou, J. You, J. Yang, C.-C. Chen, Y. He, S. Murase, T. Moriarty, K. Emery, G. Li, Y. Yang, *Nat. Photonics* **2012**, *6*, 180.

[232] G. Dennler, M.C. Scharber, T. Ameri, P. Denk, K. Forberich, C. Waldauf, C.J. Brabec, *Adv. Mater.* **2008**, *20*, 579.

[233] W. Kylberg, F.A. de Castro, P. Chabrecek, U. Sonderegger, B.T.-T. Chu, F. Nüesch, R. Hany, *Adv. Mater.* **2011**, *23*, 1015.

[234] K. Ghaffarzadeh, H. Zervos, R. Das, *Organic Photovoltaics: Technologies, Markets & Players 2012-2022*, **2012**.

[235] F.C. Krebs, T.D. Nielsen, J. Fyenbo, M. Wadstrøm, M.S. Pedersen, *Energy Environ. Sci.* **2010**, *3*, 512.

[236] Nanomarkets, *Opportunities in the Organic Photovoltaics Market – 2012*, **2012**.

[237] Nanomarkets, *Thin-Film, Organic, and Printable Photovoltaic Markets: 2007-2015*, **2007**.

[238] N.S. Sariciftci, L. Smilowitz, A.J. Heeger, F. Wudl, *Science* **1992**, *258*, 1474.

[239] K.M. Coakley, M.D. McGehee, *Chem. Mater.* **2004**, *16*, 4533.

[240] L.J.A. Koster, S.E. Shaheen, J.C. Hummelen, *Adv. Energy Mater.* **2012**, *2*, 1246.

[241] P. Berrouard, A. Najari, A. Pron, D. Gendron, P.-O. Morin, J.-R. Pouliot, J. Veilleux, M. Leclerc, *Angew. Chem. Int. Ed.* **2012**, *51*, 2068.

2

Spray Coated High Conductivity PEDOT:PSS Transparent Electrodes for Stretchable and Mechanically Robust Organic Photovoltaics

2.1 Introduction

2.1.1 Overview

The first layer in organic photovoltaics (OPVs) is a transparent electrode. This material should be transparent across the solar spectrum and have low resistance, properties which are often in conflict. This chapter investigates the use of a conducting polymer: poly(3,4-ethylenedioxythiophene):poly(4-styrenesulfonate) (PEDOT:PSS) as a transparent electrode for both flexible and stretchable OPVs. PEDOT:PSS was spray cast to form transparent electrodes for forward- and inverted-mode OPVs. A multiple solvent ink containing ethylene glycol was developed, and a post-deposition annealing step contributed to a high conductivity of 1070±50 S cm^{-1}. Sheet resistance and transmission at a wavelength of 550 nm were controlled within 24-259 Ω $□^{-1}$ and 71-95%, respectively, which are amongst the best reported combined characteristics. Forward-mode OPVs with spray coated PEDOT:PSS anodes yielded power conversion efficiencies of 3.2%. Mechanical bending and stretching tests demonstrated that the flexibility of these PEDOT:PSS

layers were far superior to that of ITO: elastic moduli were reduced by more than an order of magnitude, and the resistance increased far more slowly under both uniaxial stretching and bending to progressively smaller radii of curvature. With these experiments, the minimum radii of curvature and maximum uniaxial strains at which acceptable performance is maintained were investigated. Collectively, our results illustrate a promising future for the scalable printing of low-cost PEDOT:PSS-based flexible transparent electrodes.

The following subsections will introduce: the transparent electrode market, indium tin oxide, and PEDOT:PSS transparent electrodes.

Chapter 2 was reproduced in part with permission from:

a) J.G. Tait, B.J. Worfolk, S.A. Maloney, T.C. Hauger, A.L. Elias, J.M. Buriak, K.D. Harris, *Sol. Energy Mater. Sol. Cells.* **2013**, *110*, 98-106. Copyright © 2013 Elsevier.

2.1.2 Transparent Electrode Market

Transparent electrodes have many applications including use in OPVs, organic light emitting diodes (OLEDs), liquid crystal displays (LCDs), touch screens, electronic paper, anti-static coatings, and transparent electromagnetic shielding applications.[1–3] The broad uses have resulted in considerable interest in the literature. This has led to the development of a wide range of material solutions from traditional doped metal oxides (such as indium tin oxide [ITO]),[4] to nanomaterials (Ag, and Cu nanowires[NWs]),[5, 6] to conducting carbon allotropes (carbon nanotubes [CNTs], graphene)[7, 8], and conducting polymers.[9] In addition to typical

requirements (i.e., high conductivity and transmissivity), ideal transparent electrodes should be inexpensive, and scalable to mass manufacturing. Flexible and transparent electrodes may offer additional functionality when incorporated into electronic devices.

The market for transparent electrodes was $3 billion USD in 2011, and is expected to grow at a compounded annual growth rate (CAGR) of 20% (from 2010 to 2018).[1] To date, ITO has dominated commercial applications, and in 2011 represented ~85% of the total transparent electrode market.[1] Nanomarkets projects a slow shift to alternative transparent electrodes, as performance improves, and additional functionality (such as flexibility) is required.[1] In 2016, the projected market size of Ag NWs and conducting polymers is estimated to grow to $700 million USD.[1] The breadth of applications and growing market demand make transparent electrodes an important materials science challenge to deliver inexpensive, scalable, and flexible solutions.

2.1.3 Indium Tin Oxide

One application of transparent electrodes is their use in organic photovoltaics (OPVs). ITO is the most commonly used transparent electrode for OPV devices. However, indium is expensive and brittle, limiting the potential for flexible photovoltaic devices.[10–12] ITO is a wide band gap (3.3-4.3 eV) n-type semiconductor with low electrical resistivity of 2-4x10^{-4} Ω cm and high transparency in the visible.[13, 14] ITO is generally fabricated by vacuum deposition and annealed using high temperature processes, each of which are considered expensive.[15, 16] Moreover, the global reserves of indium ore are limited, and the consequential price fluctuations

add uncertainty to OPV manufacturing processes relying on ITO.[17] As seen in Figure 2.1 the average annual price of indium has significantly fluctuated from the 1990's.[18] The price volatility is driven by the increasing demand for ITO and the declining reserves.[19] Flexibility is also a major concern as ITO tends to fail under large or repeated strains.[20, 21]

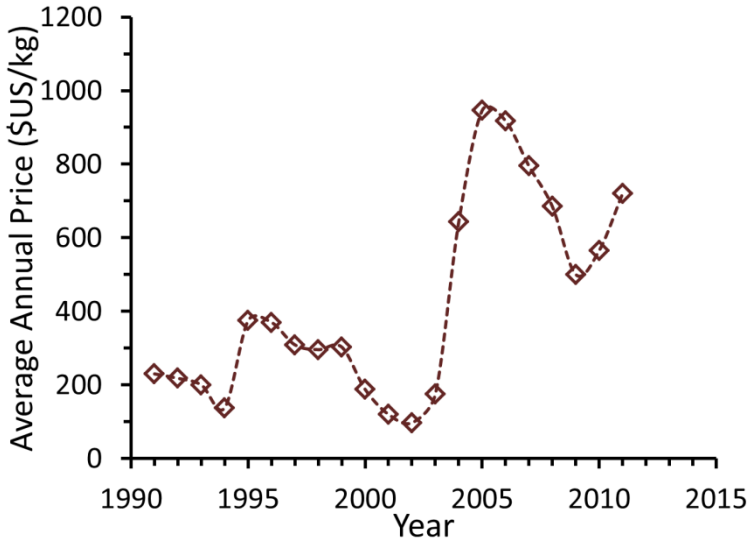

Figure 2.1 The average annual price (in US dollars) of indium from 1991-2011. Data was extracted from the US Geological Survey Mineral Commodity Summaries.[18]

2.1.4 PEDOT:PSS Transparent Electrodes

Replacing ITO, therefore, represents an important research goal, not only for OPVs, but for all technologies requiring transparent conducting layers.[16, 22] As a result, inexpensive, solution-processable conducting polymers such as (PEDOT:PSS) (Figure 2.2) are under intense investigation,[23–30] with key advantages over ITO including greatly improved flexibility,[31, 32] reduced weight, and compatibility with solution-based deposition techniques such as gravure printing, slot die coating, knife-over-edge coating, and spray coating.[12] These solution techniques are considered

inexpensive and industrially scalable, and they have been used to produce OPVs with some success.[12, 23, 33] PEDOT:PSS has also been shown to have an order of magnitude lower embedded energy and production cost than oxide- or metal-based counterparts.[34]

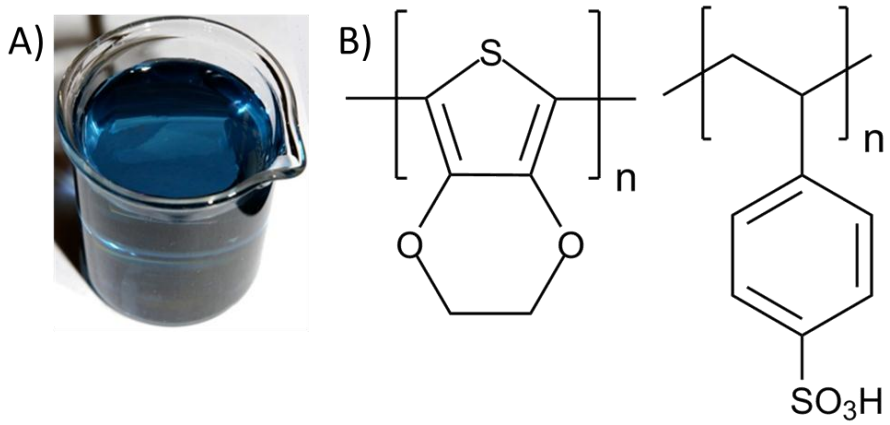

Figure 2.2 A) A picture of a solution of PEDOT:PSS in a beaker. B) Chemical structure of PEDOT:PSS.

Without modifying treatments or additives, PEDOT:PSS has electrical conductivity inferior to ITO, and it is difficult to produce efficient ITO-free OPVs using unmodified PEDOT:PSS films. Many techniques have been developed to improve conductivity, including the integration of metal grids,[11, 35] silver nanowires,[5, 36–39] electrospun copper wires,[40] carbon nanotubes,[7, 41–45] and graphene.[8, 46, 47] High conductivity PEDOT:PSS layers have also been formed by introducing pre- and post-processing steps and various additives,[25–29, 48–56] with Badre, *et al.*[55] and Vosgueritchian, *et al.*[9] demonstrating the best combinations of transmission and sheet resistance to date. PEDOT:PSS films have also recently been incorporated as transparent anodes on stretchable OPVs formed on ultra-thin PDMS substrates, and the flexible devices were found to convert solar energy into electrical current as efficiently as ITO-based cells.[56] These results collectively point toward the ongoing

advantages of characterization and optimization of the electrical, optical and mechanical properties of PEDOT:PSS electrodes.

In this work, we develop and optimize a process for spray coating thin and uniform electrodes of high conductivity PEDOT:PSS, and to the authors' knowledge, we achieve one of the best combinations of transparency and electrical conductivity noted in the literature to date. We realize this by adapting a multiple solvent spray coating technique,[33] and enhance the electrode performance with a post-process annealing step in ethylene glycol to produce sheet resistances comparable to ITO.[49] We thoroughly characterize the resulting materials, focusing considerable attention on mechanical durability, and we construct and characterize both forward- and inverted-mode ITO-free OPVs on glass and poly(ethylene terephthalate) (PET) substrates. The entire PEDOT:PSS spray coating process is performed under ambient conditions, reaches a maximum of 120 °C, uses inexpensive solution based polymers, does not require large quantities of toxic chemicals, and is scalable to mass manufacturing.

2.2 Results and Discussion

2.2.1 PEDOT:PSS Fabrication and Characterization

The process for spray deposition of high conductivity PEDOT:PSS (Heraeus Cleavios PH 1000) is shown in Figure 2.3. PEDOT:PSS in a multiple solvent solution is sprayed from an ultrasonic spray nozzle that is capable of translation across the substrate in two dimensions (Figure 2.3A). Following the spray procedure, individual droplets coalesce (Figure 2.3B), and once the solvent evaporates, an

electrically-conducting film is formed (Figure 2.3C). Critical deposition parameters that govern the properties of the cast films are: the substrate temperature, solvent composition/additives, volumetric spray rate, lateral nozzle speed, and nozzle-to-substrate distance. Substrate temperature controls solution spreading through the rate of solvent evaporation. Greater temperatures lead to reduced spreading, or in extreme cases, droplets that effectively dry on contact, creating thick, rough films. Lower temperatures allow more time for droplet coalescence, but must be controlled to prevent de-wetting. The volumetric spray rate and nozzle speed together control the volume of solution deposited on the substrate and, consequently, the thickness of the dried film. Where much thicker films are required, additional coats of sprayed PEDOT:PSS may also be added. These secondary and tertiary layers are applied to only partially dried films, preventing extended exposure of the initial layers to the atmosphere and the commensurate formation of distinct interfacial energy barriers.

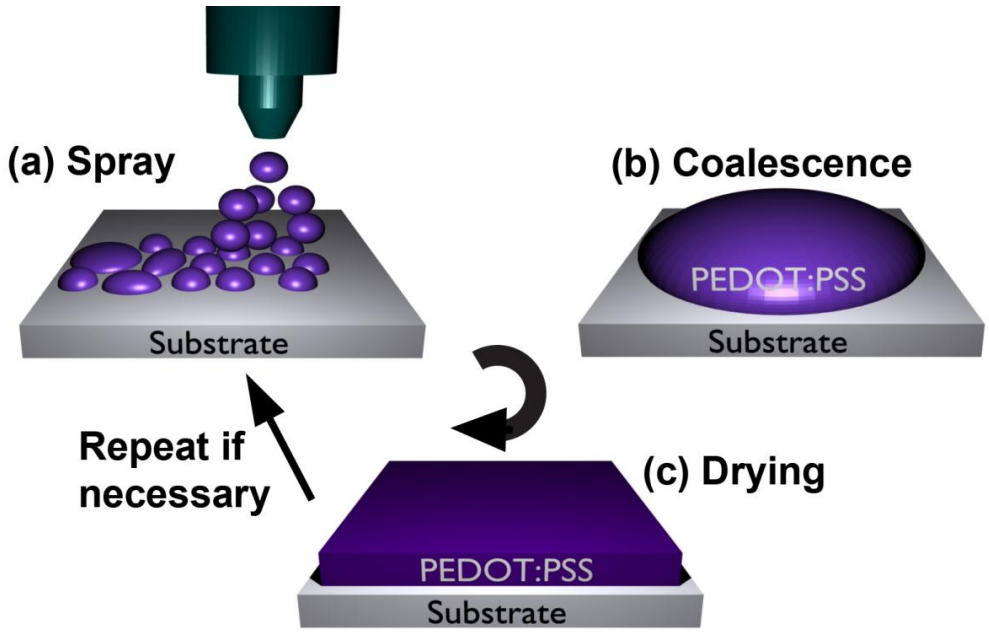

Figure 2.3 Spray coating procedure: A) Nozzle moves at a constant rate over the temperature-controlled substrate, B) the solution coalesces and spreads over the entire substrate, C) the solvent evaporates leaving a thin PEDOT:PSS film. To increase thickness, steps A)-C) can be repeated. Subsequent layers are spin-coated (P3HT:PCBM), dip-coated (PEDOT:PSS/P3(TBP)HT), and thermally evaporated (top interfacial layer and electrode). Reprinted with permission from reference [57]. Copyright © 2013 Elsevier.

To facilitate substrate wetting, a multiple solvent mixture was developed. An ink composition of 19.7 vol.% commercial PEDOT:PSS solution, 6.0 vol.% H_2O, 73.0 vol.% isopropyl alcohol (IPA), and 1.3 vol.% ethylene glycol (EG) [19.7:6.0:73.0:1.3 vol.% (PEDOT:PSS):H_2O:IPA:EG] was found to be the optimal mixture for maximum OPV performance when spray coated as an anodic interfacial modifier in air. This solution composition was used for all spray coated PEDOT:PSS layers. The rationale for this ink composition stems from the work of Girotto *et al.*,[33] where a multiple solvent (PEDOT:PSS):H_2O:IPA ink was developed. Here, the solution was adapted with modified ratios and the inclusion of ethylene glycol. EG is less volatile than water and IPA and tends to remain in cast films once the other solvents have evaporated, leading to films with lower sheet resistances.[26, 49] Soaking PEDOT:PSS

films in EG for 30 minutes followed by a 10 minutes thermal anneal at 120 °C has also been shown to substantially increase conductivity,[49] and hence this procedure was also implemented for all spray coated PEDOT:PSS electrodes.

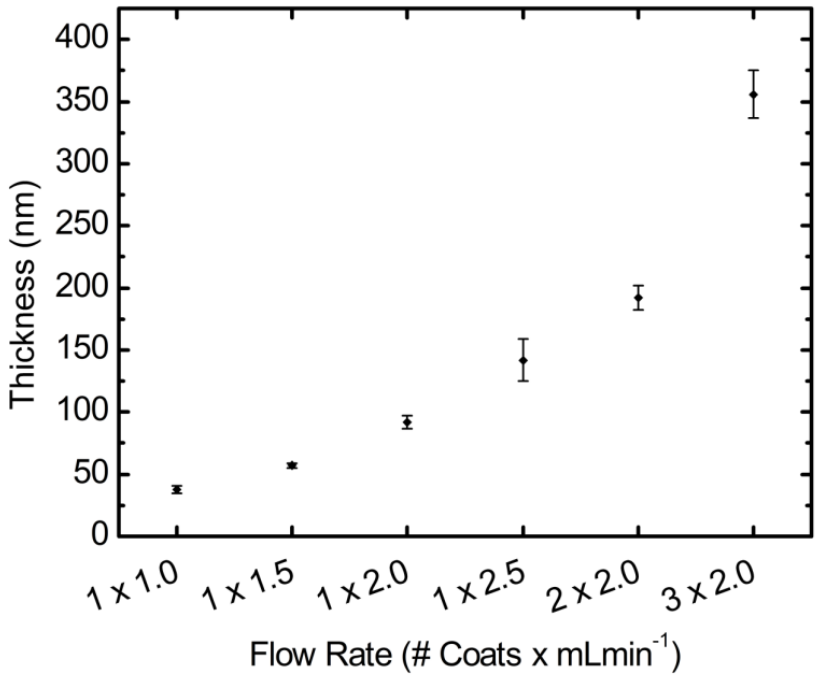

Figure 2.4 Thickness of spray-cast PEDOT:PSS films as a function of solution flow rate through the ultrasonic atomizing nozzle. Reprinted with permission from reference [57]. Copyright © 2013 Elsevier.

To vary the PEDOT:PSS thickness, single nozzle sweeps at volumetric spray rates from 1.0 to 2.5 mL min^{-1} and multiple passes (double and triple) at 2.0 mL min^{-1} were performed on SiO_2-coated Si and quartz substrates for resistance and transparency experiments, respectively. PEDOT:PSS thickness increased with volumetric spray rate (as shown in Figure 2.4), and the root mean square (RMS) roughness measured with tapping mode atomic force microscopy (AFM) was roughly constant at 4±1 nm. The sheet resistances of these PEDOT:PSS films were measured using a four-point probe, and the transmittance across the visible region was analyzed by UV-vis spectroscopy as seen in Figure 2.5A. This data is summarized in Figure 2.6 along

with the reported values for a wide range of alternative fabrication techniques. Conductivities of all our spray cast PEDOT:PSS films were measured to be 1070±50 S cm^{-1}, approaching that of ITO at ~7000 S cm^{-1}.[25, 58] As the film thickness was varied, the measured sheet resistance ranged from 24-259 Ω $□^{-1}$ while the transmission at 550 nm ranged from 71-95%. As noted in Figure 2.6, these values are among the best published for PEDOT:PSS films. To better interpret the viability of this technique for use in transparent OPV electrodes, the solar photon flux-weighted transmissivities[38] were calculated and found to range from 88% to 52% for the 400-800 nm wavelength range (Figure 2.5B). These transmission values are lower than those of ITO, ~94%, and demonstrate the distortion inadvertently introduced by reporting transmission values at only a single wavelength. Comparison between materials intended for solar applications is greatly aided when solar flux weighting is incorporated into the transmission values; however, the majority of the literature does not report these values.

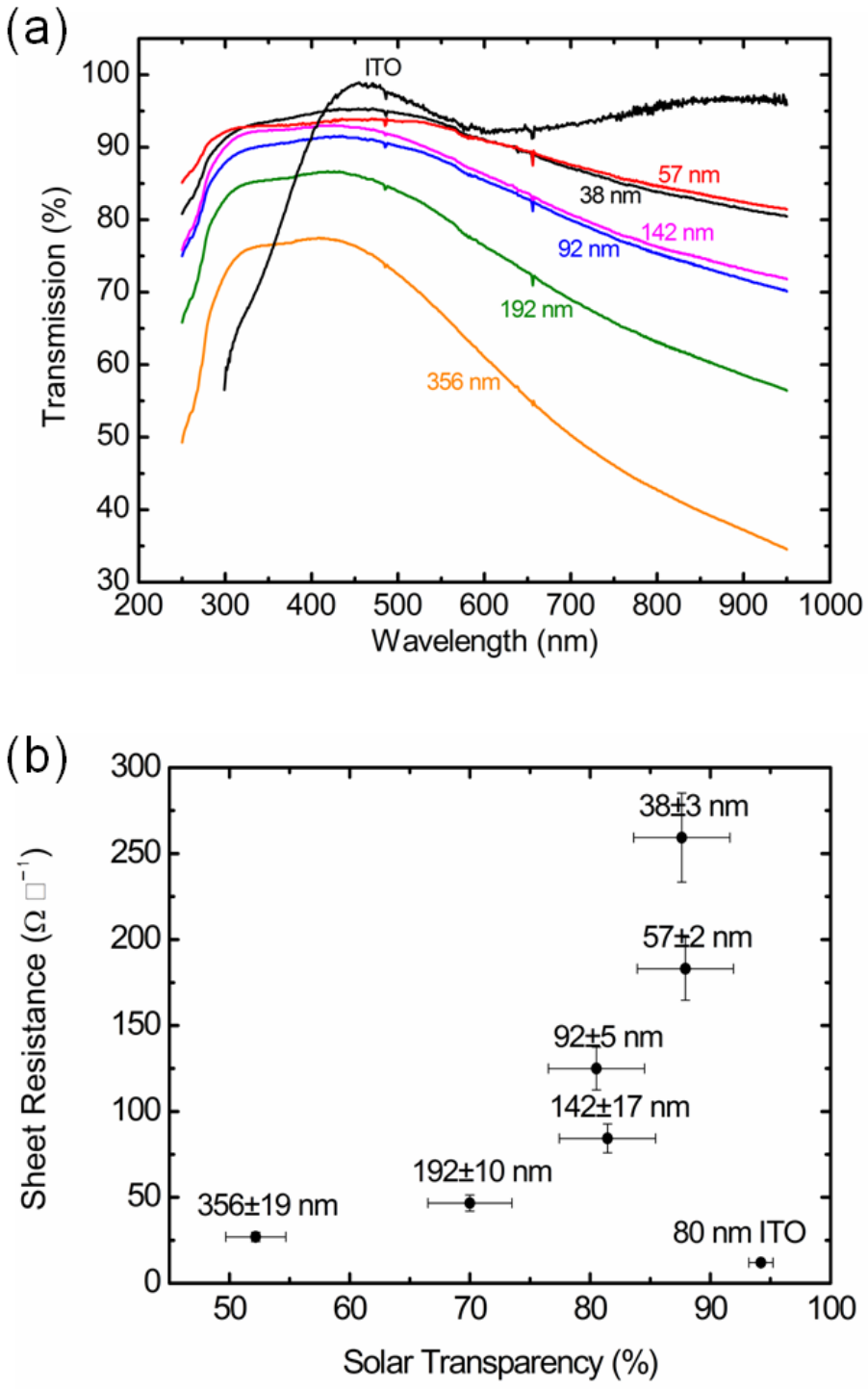

Figure 2.5 A) UV-Vis transmission data for the PEDOT:PSS and ITO films studied in this work. B) Sheet resistance vs. the solar photon flux weighted transparency for PEDOT:PSS electrodes spray coated at various thicknesses. An ITO layer is also included. Reprinted with permission from reference [57]. Copyright © 2013 Elsevier.

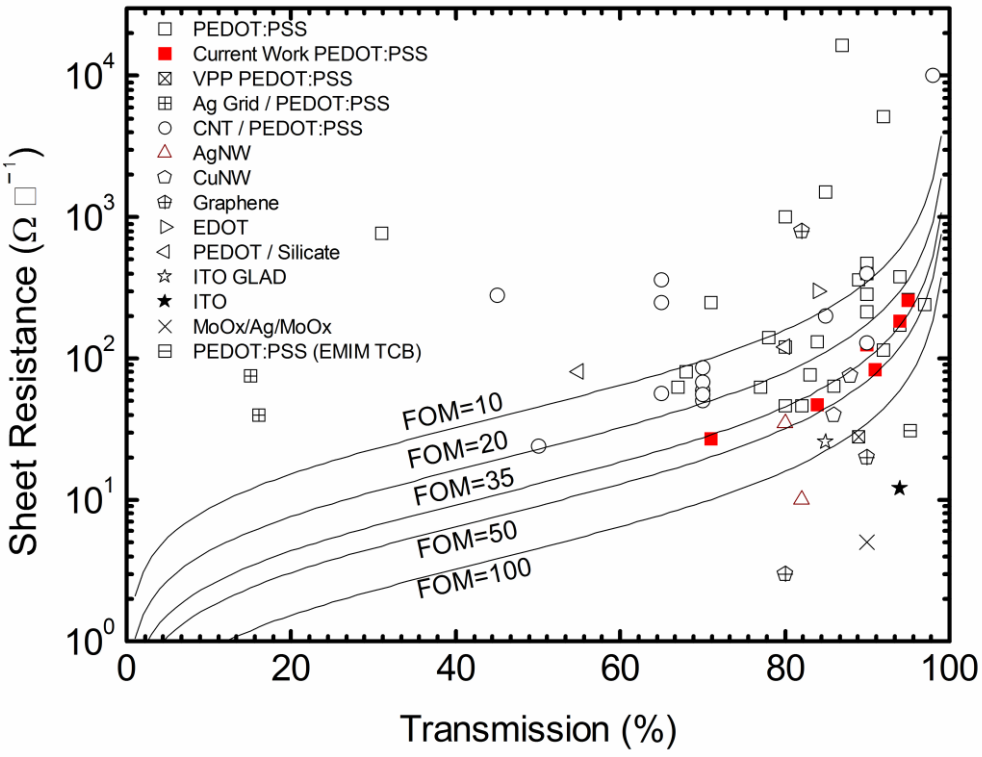

Figure 2.6 Sheet resistance vs. transmission for the spray cast PEDOT:PSS films fabricated in this work and various alternative transparent electrodes reported in literature.[6, 8, 9, 12, 15, 17, 25, 26, 35, 37, 38, 41, 42, 49, 50, 54, 55, 58–79] The literature examples are not exhaustive and were restricted to those with transmission reported at single wavelengths in the limited range 500-550 nm. Solid lines in the plot represent contours of uniform figure of merit (FOM), and optimal transparent electrodes should approach the bottom right corner for highest transmission and lowest sheet resistance. Reprinted with permission from reference [57]. Copyright © 2013 Elsevier.

A figure of merit (FOM), specified by the ratio of DC conductivity to optical conductivity for transparent conducting films, $\frac{\sigma_{DC}}{\sigma_{op}(\lambda)}$, is related to transmission (T), and sheet resistance (R_{SHEET}) through the function:[9]

$$FOM = \frac{\sigma_{DC}}{\sigma_{op}(\lambda)} = \frac{188.5\Omega}{R_{SHEET}\left(T(\lambda)^{-1/2}-1\right)} \qquad (2.1)$$

Contour lines at several FOM values are included in Figure 2.6, and general industrial standards for transparent electrodes specify this FOM must have a

minimum value of 35.[9, 55] The PEDOT:PSS electrodes of this work show a maximum FOM of 46.5 with a sheet resistance of 84 Ω $\square^{-1}$ and a transmission of 91% at a wavelength of 550 nm. To the authors' knowledge, this is near the highest FOM values reported for PEDOT:PSS films.

2.2.2 Mechanical Characterization of PEDOT:PSS

A flexible material bends or stretches reversibly under the action of relatively low applied forces. This property is generally described by the elastic modulus (the ratio of applied stress to induced strain), with more flexible materials having lower moduli. In the context of "flexible electronics," a second definition is also implied; the electrical properties (or any other functional properties) of a flexible material must not deteriorate during deformation. In this paper, we characterize the flexibility of spray cast PEDOT:PSS films under both definitions. Several groups have previously investigated the moduli of PEDOT:PSS films,[23, 56, 80] while others have investigated the performance of PEDOT:PSS electrodes during cyclic bending tests at a fixed radius.[23, 56, 58, 81] These electrodes are typically shown to withstand hundreds of deformation cycles at radii of curvature in the range of 7 to 10 mm before deterioration is seen. To determine the moduli of spray coated PEDOT:PSS electrodes, we performed nanoindentation experiments on thick (>1 μm) spray coated PEDOT:PSS and ~100 nm ITO layers, both on glass.[82] The relatively thick PEDOT:PSS films were utilized to reduce the influence of the substrate over the measurements.[83] The measured moduli for PEDOT:PSS films (7-8 GPa) were much lower than the corresponding values for ITO (100 GPa), suggesting that PEDOT:PSS films are considerably more flexible than their ITO counterparts.

An equally important factor in the mechanical performance of transparent electrodes and flexible OPVs is the impact of the bending radius of curvature (RoC) on film function and OPV performance. The results of a study of sheet resistance vs. RoC for ITO and several thicknesses of PEDOT:PSS are shown in Figure 2.7. PEDOT:PSS layers were spray coated on PET substrates. The coated substrates were wrapped around a cylindrical object of the desired RoC, with the electrode under tensile strain as shown in the inset of Figure 2.7. It was found that bending to any RoC had little effect on the sheet resistance for all thicknesses of PEDOT:PSS. This is in direct contrast to ITO electrodes, which show a measureable increase in sheet resistance starting at only 6 mm RoC, and a ~20x increase by 0.5 mm RoC.

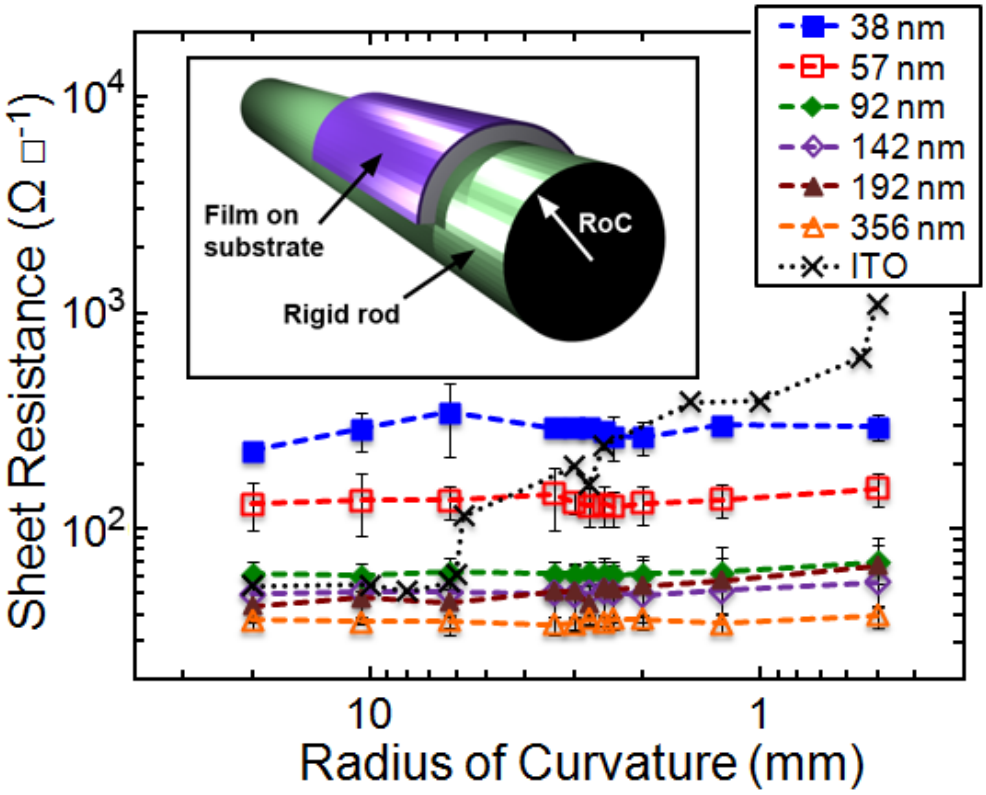

Figure 2.7 Sheet resistance vs. bending radius of curvature for various thicknesses of spray coated PEDOT:PSS and ITO films on PET. The samples were measured flat after bending. Reprinted with permission from reference [57]. Copyright © 2013 Elsevier.

The electrical properties of spray cast PEDOT:PSS films and ITO controls were also assessed as the films were uniaxially stretched under the action of a tensile load. Tests of this nature are uncommonly reported in the literature, but in the future, they may be used as a platform to quantifiably compare the electromechanical properties of prospective transparent conductors against one another. The electrical resistances during deformation for two as-received ITO-on-PET samples and two spray cast PEDOT:PSS films on PET are presented in Figure 2.8, and it is apparent that the two electrode materials perform quite differently under elongation. For the ITO samples, several features can be observed as the strain, ε (i.e., the ratio between the change in length and initial length), is increased. The resistances are relatively stable at low strains ($\varepsilon < 0.03$), but increase sharply thereafter, reaching ~100x their original values by $\varepsilon = 0.045$. The rate of resistance increase begins to slow around $\varepsilon = 0.075$, possibly signifying a reduction in the crack formation rate as seen in literature with multi-stage film cracking,[84, 85] and around $\varepsilon = 0.15$, the measured resistances become unstable but continue to increase rapidly. When this instability is observed, the measured resistances have increased by roughly four orders magnitude. Finally, the measurements cease at $\varepsilon \sim 0.2$ with the resistances increased by ~6 orders of magnitude. It is important to note that the PET substrates have not broken at these strains; instead, the ITO resistances have exceeded the maximum value measurable with our equipment. The corresponding data for PEDOT:PSS films is substantially different: a slow increase in resistance is observed until the PET substrate breaks just below $\varepsilon = 1$ (i.e., when the films have nearly doubled in length). At the point where the ITO resistances become unmeasureable ($\varepsilon \sim 0.2$), the corresponding values for

PEDOT:PSS films have only increased by ~30%, and when the PET substrates break, the PEDOT:PSS resistances are only ~10x-13x their original values.

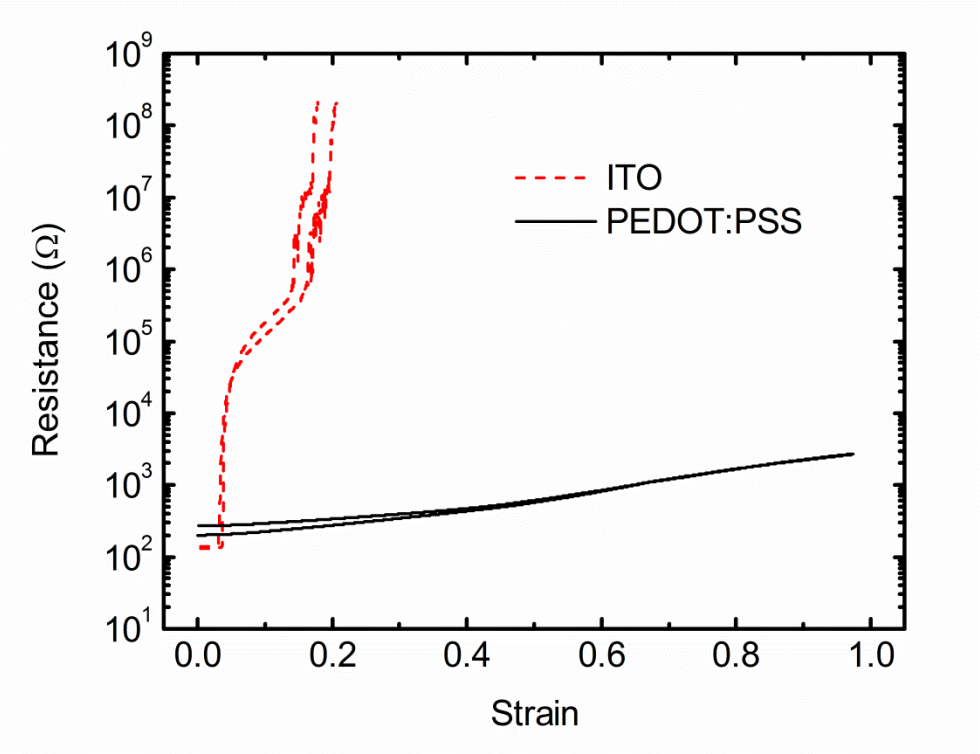

Figure 2.8 Resistance vs. strain for transparent conductors on PET stretched in tension. Data for ITO films are shown in dashed red, and data for PEDOT:PSS films are plotted in solid black. Reprinted with permission from reference [57]. Copyright © 2013 Elsevier.

2.2.3 Organic Photovoltaic Characterization

OPVs can be operated in either of two modes: forward or inverted. Forward-mode OPVs have a transparent anode (commonly ITO), which collects holes from the photoactive layer, on a supporting substrate. Inverted-mode OPVs collect electrons at a transparent cathode (commonly ITO with a modifying layer). This inverted-mode of operation has been shown to lead to longer OPV lifetimes due to higher work function, oxidation-resistant anodes.[86–89] Both forward- and inverted-mode devices (having architectures shown in Figure 2.9A and Figure 2.9B,

respectively) were fabricated to demonstrate OPVs with spray coated PEDOT:PSS electrodes. In each case, five distinct solar cell devices were formed on every substrate, and as depicted in Figure 2.9C, the five devices are numbered based on their proximity to the back contact.

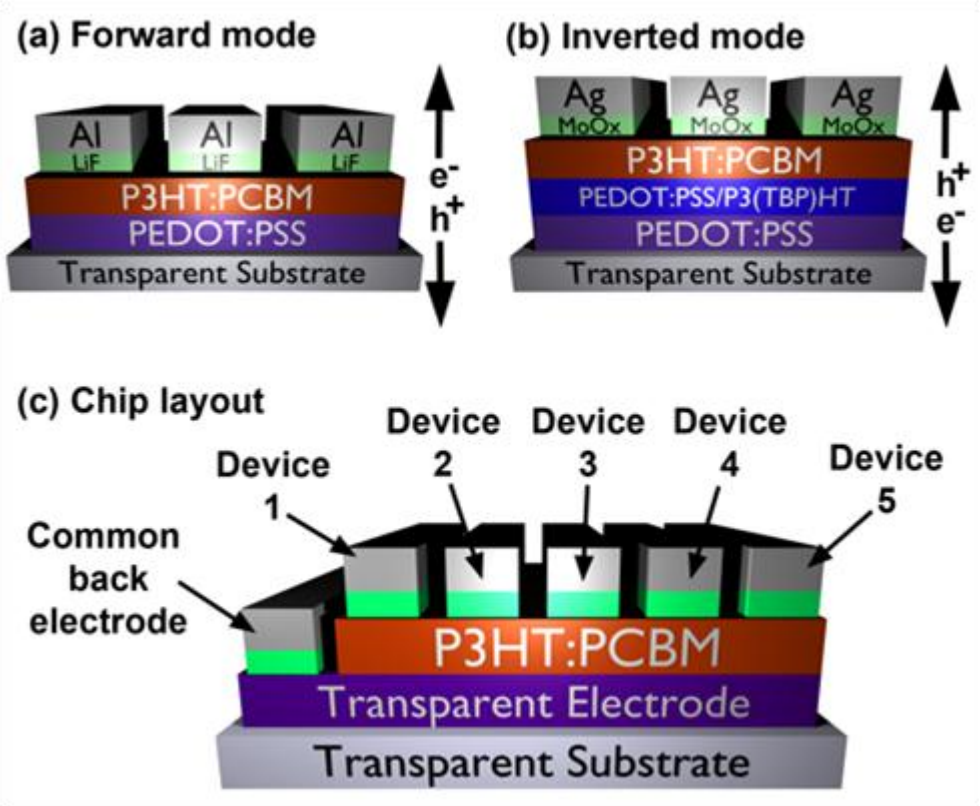

Figure 2.9 Schematics of A) forward and B) inverted-mode OPVs, and C) the overall chip layout with five devices formed on each substrate. P3HT:$PC_{61}BM$ is removed from the vicinity of the bottom electrode prior to top electrode evaporation. Reprinted with permission from reference [57]. Copyright © 2013 Elsevier.

Forward-mode OPVs were fabricated with Borofloat glass as the substrate, spray coated PEDOT:PSS as the transparent anode, spin-coated P3HT:$PC_{61}BM$ (combined 46 mg mL^{-1}, 1:1 weight) as the photoactive layer, lithium fluoride as the cathodic interfacial layer, and aluminum as the reflective cathode. Table 2.1 lists the associated short circuit current density (J_{sc}), open circuit voltage (V_{oc}), power conversion

efficiency (PCE), fill factor (FF), series resistance (R_S), and shunt resistance (R_{SH}) of the highest PCE device for a series of OPVs with varied PEDOT:PSS electrode thicknesses. It should be noted that the best performing (i.e., highest PCE) device on each of the PEDOT:PSS electrode samples was the one nearest to the common electrode (device 1, as shown in Figure 2.9C). The progressively increasing physical distance of each subsequent device from the common electrode adds resistance and leads to increasing R_S. ITO-based OPVs, on the other hand, show only a small increase in R_S with distance from the common electrode, suggesting that if the sheet resistance of PEDOT:PSS can be further decreased, improved photovoltaic performance should result. From the series of PEDOT:PSS-based devices, the highest performance forward-mode solar cell was formed with a 92±5 nm thick PEDOT:PSS anode (R_{SHEET} = 125±9 Ω □$^{-1}$, >90% transmittance, spray cast at 2.0 mL min^{-1}) and had a PCE of 3.2%, J_{sc} of -8.8 mA cm^{-2}, V_{oc} of 590 mV, FF of 0.58, R_S of 4.7 Ω cm^2, and R_{SH} of 0.72 kΩ cm^2. These characteristics place the device amongst the highest performing OPVs based on PEDOT:PSS anodes,[15,62] which is likely the result of improved conductivity and transmittance of the PEDOT:PSS. The PEDOT:PSS-based devices also appear to remain within a fairly small range of performance characteristics despite a large variation in PEDOT:PSS thickness. This property is attractive for mass manufacturing, because high error tolerance has the potential to ease production requirements and reduce costs in the fabrication process.

Table 2.1 Forward-mode photovoltaic performance characteristics for spray coated PEDOT:PSS anodes and ITO anodes with PEDOT:PSS interfacial layers. Reprinted with permission from reference [57]. Copyright © 2013 Elsevier.

Electrode	Thickness (nm)	J_{sc} (mA cm^{-2})	V_{oc} (V)	PCE (%)	FF	R_S (Ω cm^2)	R_{SH} (kΩ cm^2)
PEDOT:PSS	38±3	-8.8	0.60	2.9	0.55	8.1	0.37
PEDOT:PSS	57±2	-8.7	0.60	2.9	0.55	8.6	0.83
PEDOT:PSS	92±5	-8.8	0.59	3.2	0.58	4.7	0.72
PEDOT:PSS	142±17	-8.9	0.59	2.9	0.55	7.6	0.47
PEDOT:PSS	192±10	-8.1	0.60	3.0	0.62	5.2	2.2
PEDOT:PSS	356±19	-6.9	0.59	2.6	0.64	5.5	1.8
ITO/PEDOT:PSS$_{spray}$	35±3	-11	0.57	4.1	0.62	4.5	0.63
ITO/PEDOT:PSS$_{spin}$	30±2	-11	0.56	3.8	0.61	5.6	0.42

The current density vs. voltage (J-V) curves, measured under AM1.5G simulated solar irradiation, for an ITO-free OPV with a PEDOT:PSS electrode of thickness 92±5 nm are shown in Figure 2.10A. Also shown are two control devices with spin and spray coated PEDOT:PSS anodic interfacial layers on ITO electrodes. OPVs incorporating ITO in the anode do perform better (i.e., have greater PCEs) than those with exclusively PEDOT:PSS electrodes. This effect is primarily due to increased J_{sc}, but lower series resistance and higher shunt resistance are also observed. Both ITO- and PEDOT:PSS-based anodes had comparable FF and V_{oc}. This suggests no inherent issues preventing PEDOT:PSS from being employed as the transparent electrode, apart from inferior lifetime stability for PEDOT:PSS anodes (Figure 2.10B).

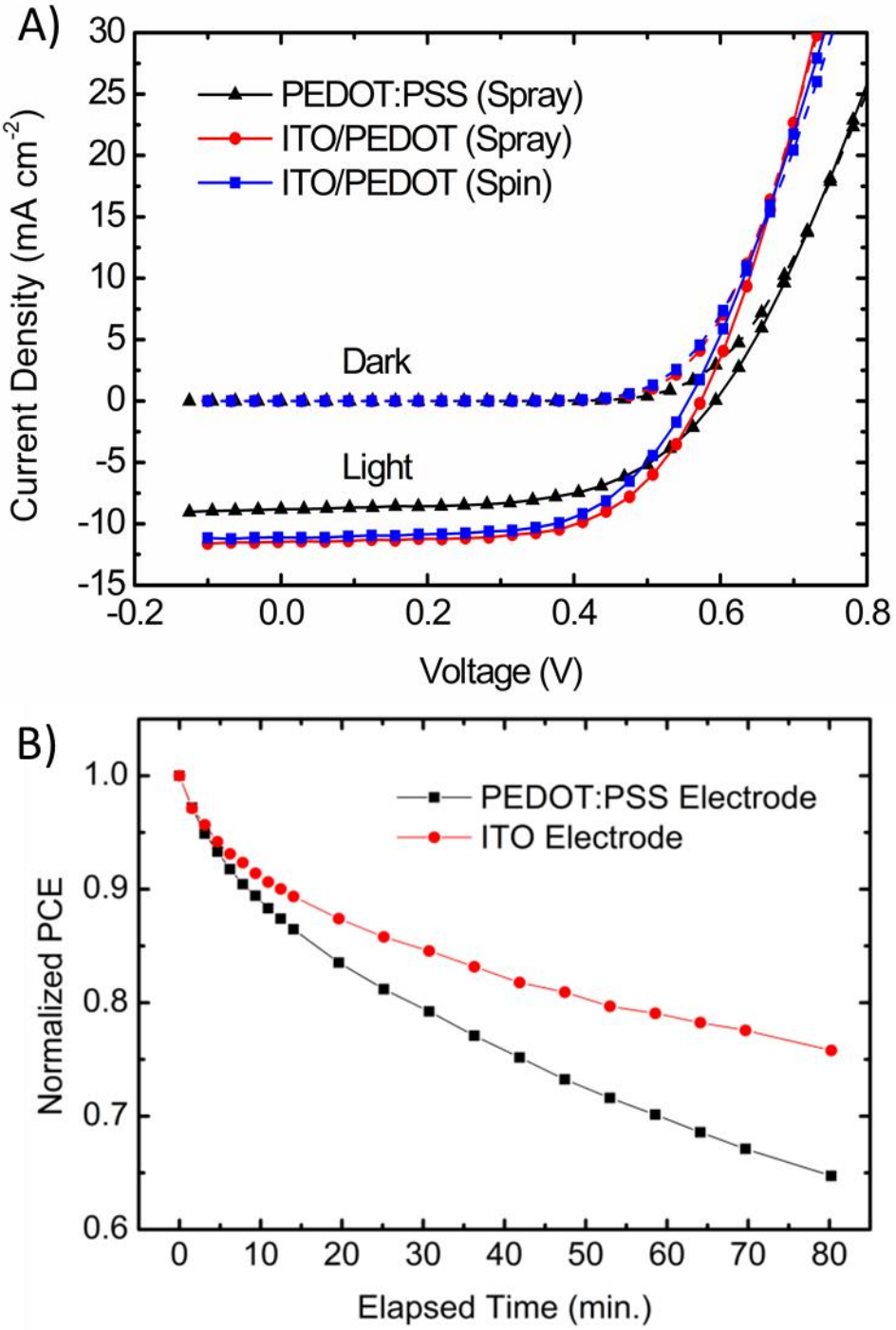

Figure 2.10 A) Dark (dashed lines) and light (solid lines) J-V curves for forward-mode OPVs fabricated from the optimal spray coated PEDOT:PSS anode (92±5 nm thickness) and two ITO-based OPVs with spray coated (35±3 nm) and spin-coated (30±2 nm) PEDOT:PSS interfacial layers. B) The constant illumination OPV lifetimes of ITO and spray-cast PEDOT:PSS anodes. Cells tested started with average PCEs of 3.45% and 2.85%, respectively Reprinted with permission from reference [57]. Copyright © 2013 Elsevier.

To form inverted-mode OPVs, the work function of the transparent electrode must be reduced to allow efficient collection of electrons. We accomplished this by combining PEDOT:PSS with a functionalized P3HT derivative, poly[3-(6-{4-*tert*-butylpyridiniumyl}-hexyl)thiophene-2,5-diyl] [P3(TBP)HT], in an electrostatic layer-by-layer (eLbL) deposition process.[90] eLbL thin films are fabricated by successively submersing an ITO electrode into a solution of cationic P3(TBP)HT, rinsing with water, submersing into a solution of anionic PEDOT:PSS, and rinsing with water a second time. This cycle forms a bilayer thin film on the ITO cathode.[88, 90] This cycle is repeated 5.5 times (ending with P3[TBP]HT) to form 5.5 bilayers. Figure 2.11A shows the ultraviolet photoelectron spectroscopy (UPS) secondary electron cut-off for both ITO and spray coated PEDOT:PSS electrodes, each with and without 5.5 bilayers of [P3(TBP)HT/PEDOT:PSS]. This eLbL deposition of P3(TBP)HT and PEDOT:PSS has been shown in the literature to modify the electrode work function of ITO from 4.6 eV to 3.8 eV,[90] and in the present work a similar reduction in the work function, from 4.9 eV to 4.3 eV, was observed for PEDOT:PSS electrodes modified with the eLbL deposition of $[P3(TBP)HT/PEDOT:PSS]_{5.5}$, as summarized in Table 2.2.

Table 2.2 UPS work function values for the various electrodes and interfaces used in this work. Reprinted with permission from reference [57]. Copyright © 2013 Elsevier.

Film Structure	Work Function (eV)
ITO	4.7
$ITO/[P3(TBP)HT/PEDOT:PSS]_{5.5}$	4.1
PEDOT:PSS	4.9
$PEDOT:PSS/[P3(TBP)HT/PEDOT:PSS]_{5.5}$	4.3

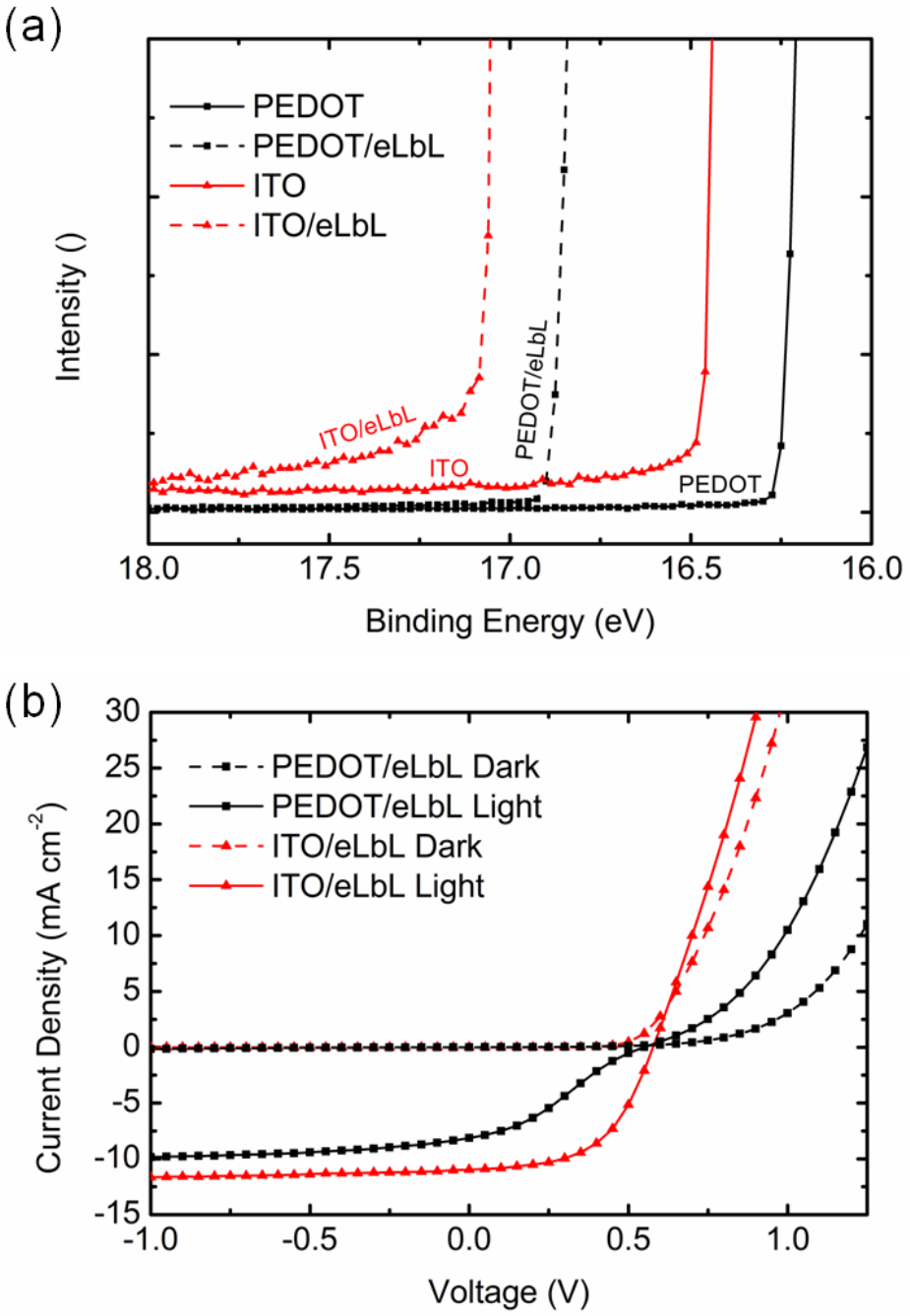

Figure 2.11 A) The secondary electron edges of UPS spectra used to determine work functions. Shown are spectra for PEDOT:PSS and ITO electrodes, both bare and after modification by electrostatic layer-by-layer deposition (eLbL). In eLbL experiments, 5.5 bilayers of P3(TBP)HT/PEDOT:PSS were deposited. B) J-V curves for inverted-mode OPVs with eLbL-modified ITO and spray coated PEDOT:PSS cathodes. Reprinted with permission from reference [57]. Copyright © 2013 Elsevier.

Inverted-mode OPVs were fabricated on the eLbL-modified PEDOT:PSS and ITO electrodes with the layer structure shown in Figure 2.9B. Figure 2.11B presents the J-V curves for these inverted-mode devices, and photovoltaic performance characteristics are presented in Table 2.3. OPVs fabricated with unmodified electrodes were non-functional, acting as open circuits. The PEDOT:PSS-cathode inverted-mode solar cell attained a PCE of 1.4%, which is substantially lower than the ITO-cathode device at 3.5%. The large S-shaped kink in the J-V curve for the spray coated PEDOT:PSS electrode is primarily responsible for the low efficiency compared to the ITO electrode, and is likely due to interfacial dipoles.[91]

Table 2.3 Solar cell performance characteristics for inverted-mode OPVs with eLbL-modified ITO and spray coated PEDOT:PSS cathodes: $[P3(TBP)HT/PEDOT:PSS]_{5.5}$. Reprinted with permission from reference [57]. Copyright © 2013 Elsevier.

Electrode Description	J_{sc} (mA cm^{-2})	V_{oc} (V)	PCE (%)	FF	R_S (Ω cm^2)	R_{SH} (kΩ cm^2)
ITO/eLbL	-11	0.58	3.5	0.54	9.8	1.6
PEDOT:PSS/eLbL	-8.2	0.55	1.4	0.30	13	0.64

2.2.4 Mechanical Characterization of Flexible OPVs

Flexible forward-mode OPVs were fabricated on PET substrates with the architecture shown in Figure 2.9A (PET/anode/P3HT:PCBM/LiF/Al). The cells were bent to progressively smaller RoC and their J-V characteristics were recorded after every bend. J-V curves were measured with the samples flat, both in the dark and under AM1.5G illumination. Figure 2.12 shows the OPV efficiencies, normalized to their independent maxima (i.e., before bending), vs. RoC for devices formed with both PEDOT:PSS and ITO anodes. OPVs of both anode types were also repeatedly tested without bending, and these substrates showed a slight (~10%)

reduction in normalized PCE over the same time period. This indicates that the substantial drop in PCE during bend testing is not the result of degradation unrelated to the bending process for either ITO or PEDOT:PSS anodes.

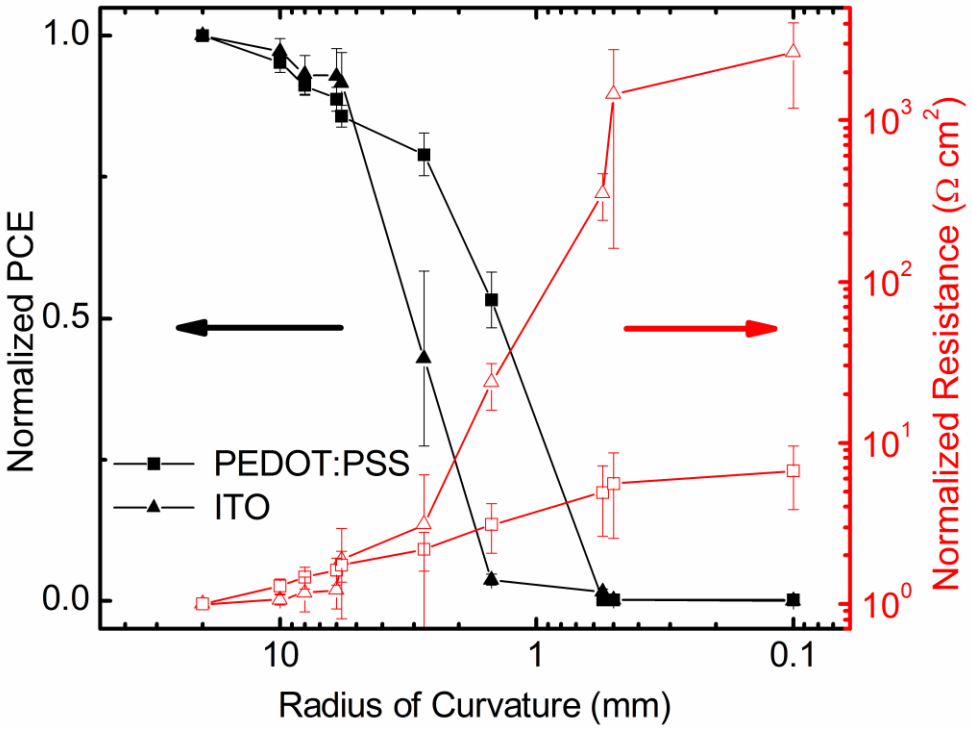

Figure 2.12 Normalized PCE (black, left axis) as a function of bending radius of curvature for flexible solar cells formed with both PEDOT:PSS ($PCE_{starting}$ = 0.56%) and ITO ($PCE_{starting}$ = 0.98%) electrodes on PET substrates. The resistance of similar devices without the photoactive layers are also plotted in red on the right-hand axis. Triangles and squares represent data for devices with ITO and spray coated PEDOT:PSS electrodes, respectively. Reprinted with permission from reference [57]. Copyright © 2013 Elsevier.

During the bend tests, the PCE of the devices based on both PEDOT:PSS and ITO anodes eventually dropped to zero, but the spray coated PEDOT:PSS devices showed a slower reduction. PEDOT:PSS- and ITO-based OCSs stopped functioning at RoCs of 0.5 mm and 2 mm respectively, and different failure modes were observed in the J-V curves: the OPVs with ITO electrodes developed short circuits whereas the devices with PEDOT:PSS electrodes retained a diode-like J-V profile

with J_{sc} falling to near zero. Scanning electron microscopy (SEM) was used to image both PEDOT:PSS and ITO electrode devices before and after bending, and images are shown in Figure 2.13. In these SEM images, cracks are clearly evident in ITO-based devices but not in PEDOT:PSS-based ones. For the ITO-based devices, sections of cracked ITO may be making contact with the Al top electrode and generating the observed short circuits. For the PEDOT:PSS-based devices, on the other hand, failure may actually be occurring via delamination at the active layer/top electrode interface. This has previously been observed in literature with silver electrodes,[9] and in the present case, several pieces of evidence also point toward this conclusion. These include the conservation of the diode-like J-V profile and the observation that LiF/Al films on P3HT:PCBM photoactive layers fail the "scotch tape test", clearly delaminating from the substrate as adhesive tape is removed. To further investigate the mechanical failure mode of flexible OPV devices, purely resistive devices fabricated without photoactive layers (i.e., with a PET/anode/LiF/Al architecture) were also deformed by bending according to the same experimental conditions as the flexible PET/ITO/PEDOT:PSS/P3HT:PCBM/LiF/Al and PET/PEDOT:PSS/P3HT:PCBM/LiF/Al OPVs. Device resistances extracted from this set of experiments are plotted in the right-hand axis of Figure 2.12, and it can be observed that the resistance increases markedly for both ITO- and PEDOT:PSS-based cells once RoC values fall below ~3 mm. The ITO-based cells, however, have ~100x higher normalized resistance at small RoC compared to PEDOT:PSS-based devices. Considering that the bending conditions for this test are identical to those of Figure 2.7 (i.e. the sheet resistance of PEDOT:PSS does not strongly degrade under

bending deformation), it is reasonable to propose that the top metal electrode/interface is responsible for the majority of resistance increase for the devices with PEDOT:PSS anodes.

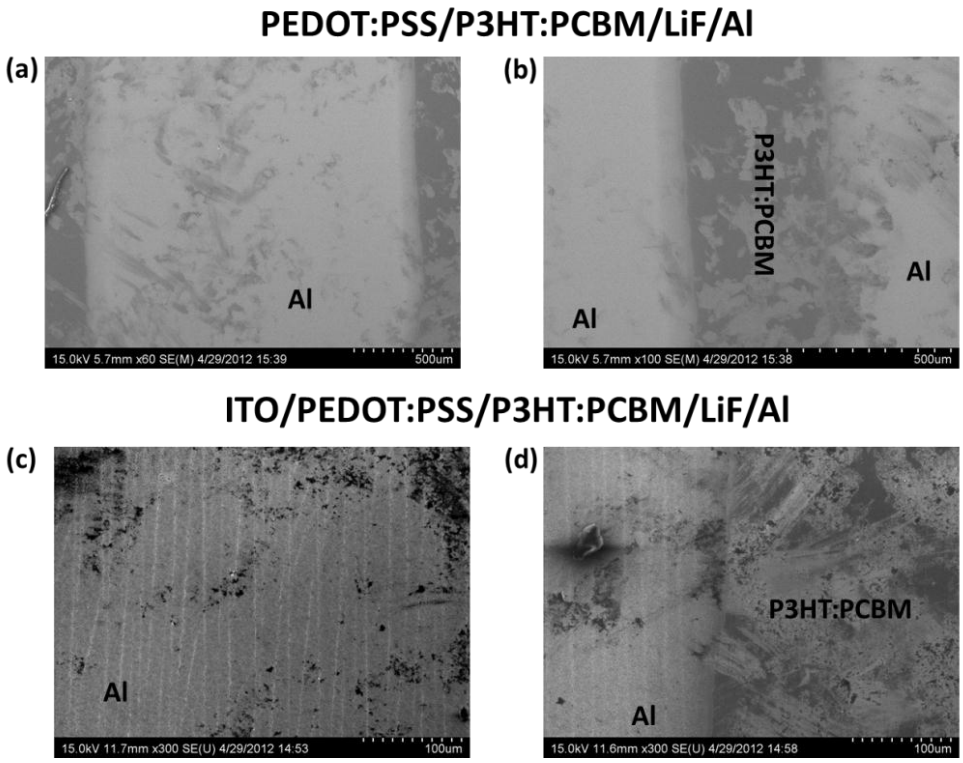

Figure 2.13 Scanning electron microscopy images of OPV devices with A,B) PEDOT:PSS bottom electrodes, C,D) ITO bottom electrodes, and all with LiF/Al top contacts. All images were obtained after bending, where ITO-based devices clearly show cracking visible through the top contact. Reprinted with permission from reference [57]. Copyright © 2013 Elsevier.

2.3 Conclusions

A high-performance spray coating procedure was developed for the deposition and post-treatment of PEDOT:PSS electrodes. The measured PEDOT:PSS conductivity was as large as 1070±50 S cm^{-1}, with sheet resistances varying from 259 to 24 Ω $□^{-1}$ and optical transmission at a wavelength of 550 nm controllable below 95%. Both forward- and inverted-mode OPVs were fabricated using these spray

coated PEDOT:PSS electrodes on glass and PET substrates, and the forward-mode ITO-free OPVs operated with a PCE of 3.2%, which was comparable to ITO-based OPVs.

Several mechanical tests, including stretching, indentation and bending, showed that PEDOT:PSS films and OPVs formed with PEDOT:PSS electrodes were able to withstand far greater mechanical deformation before failure than their ITO-based counterparts. These tests led us to conclude that failure of the ITO-free OPVs occurs by the deterioration or delamination of the cathode rather than failure of the PEDOT:PSS anode. To counter this problem, a polymer based top contact or another robust film could be used as the cathode, which would allow the devices to function at decreasing RoC. Overall, spray coating was demonstrated as a viable fabrication technique for high-performance PEDOT:PSS electrodes and, with future improvements in conductivity and encapsulation, PEDOT:PSS has great potential to become a replacement for the currently ubiquitous ITO.

2.4 Experimental

Materials:

Poly(3,4-ethylenedioxythiophene):poly(4-styrenesulfonate) (PEDOT:PSS) was purchased as an aqueous dispersion from Heraeus (Clevios PH 1000). Regioregular poly[3-(hexyl)thiophene-2,5-diyl] (P3HT) and [6,6]-phenyl-C_{61}-butyric acid methyl ester (PCBM) were purchased from Reike Metals, Inc. and American Dye Source (ADS61BFA) respectively. ITO-coated poly(ethylene terephthalate) (PET) with sheet resistance of 60 $\Omega\ \square^{-1}$ and 79% transmission was purchased from Sigma Aldrich,

ITO-coated glass (~8-12 Ω $\square^{-1}$) from Delta Technologies, Ltd. and quartz substrates from Quartz Scientific (210031010). Methylene chloride and isopropyl alcohol (IPA) from Fisher Scientific, ethylene glycol (EG) from VWR International, LLC, and *ortho*-dichlorobenzene from Sigma-Aldrich were used as received.

PEDOT:PSS Spray Casting and Solar Cell Fabrication:

Glass, quartz and ITO-coated glass substrates were cleaned by sonication for 10 minutes in each of methylene chloride, de-ionized water (18.2 MΩ·cm) and IPA after which they were treated with an air plasma for 10 minutes at 1.0 Torr (Harrick Plasma, PDC 32G, 18W). PET-based substrates were cleaned by sonication for 10 minutes each in de-ionized water and 1:1 IPA:acetone and were treated with an air plasma for 3.5 minutes at 0.5 Torr. The spray coating apparatus consisted of a New Era Pump Systems, Inc. syringe pump connected to a Sonozap Atomizer, set at a power of 5 mW, and with a Velmex, Inc. VXM stepping motor controller (to manage nozzle movement) and a VWR VHP-C10 hot plate (to regulate substrate temperature). Various combinations of deposition parameters were tested while optimizing the properties of the PEDOT:PSS films, but in most cases and unless otherwise noted, the following parameters were utilized: The nozzle to substrate distance was ~30 mm with a glass shroud protecting the mist from ambient airflows (1 mm gap between the shroud bottom and substrate). The lateral nozzle velocity was 25.4 mm s^{-1} over the substrate, and solution spray rates between 1.0 to 2.5 mL min^{-1} were used to control the dried layer thickness. The spray solution consisted of 19.7 vol.% commercial PEDOT:PSS solution, 6.0 vol.% H_2O, 73.0 vol.% IPA, and 1.3 vol.% ethylene glycol, filtered with a 0.45 μm mixed cellulose ester filter prior to

spraying. Sprayed PEDOT:PSS films were deposited on substrates at 50 °C and allowed to dry at this temperature for 5 minutes, followed by annealing at 120 °C for 10 minutes. Once annealed, the films were immediately placed in a bath of ethylene glycol for 30 minutes after which they were removed from the bath and spin dried at 2500 rpm for 30 s before baking for a further 10 minutes at 120 °C.

PEDOT:PSS-based OPVs were fabricated on glass and PET substrates, and ITO-based OPVs were fabricated using commercial ITO-on-glass or ITO-on-PET substrates. Substrates were cleaned and coated with PEDOT:PSS as above. P3HT and PCBM for the photoactive layer were individually dissolved in ortho-dichlorobenzene (each at a concentration of 46 mg mL^{-1} before mixing) and the solutions left to stir for at least 12 hours at 80 °C in an argon environment. The solutions were then combined (1:1 ratio of P3HT:PCBM and a polymer concentration of 23 mg mL^{-1}) and stirred for an additional ~3 hours before being filtered through a 0.2 μm PTFE filter directly onto the substrate. The substrates were then spun at 600 rpm for 60 s, producing an active layer ~210 nm thick. High vacuum (~10^{-4} Pa) thermal evaporation through a shadow mask was used to deposit the LiF and Al top contacts, creating OPV devices with areas of 0.175±0.008 cm^2. In this evaporation process, LiF was deposited to 0.8 nm at a rate of ~0.1 Å s^{-1}, and Al was deposited to 80 nm at a deposition rate that dynamically increased from 1 Å s^{-1} to 2.5 Å s^{-1} during deposition. To form devices without photoactive layers, the thermal evaporation process was performed directly on the ITO or PEDOT:PSS electrodes.

Characterization:

The sheet resistances of commercial ITO and spray cast PEDOT:PSS films were measured using a Lucas Labs four-point probe and a Keithley 2400 Source Meter. The electrically conducting areas were roughly 3 cm x 3 cm for PEDOT:PSS on Si substrates, 2.5 cm diameter for PEDOT:PSS on quartz discs, 3 cm x 3 cm for ITO on PET and 2 cm x 2 cm for PEDOT:PSS on PET. Film thickness was measured by manually scraping trenches into the PEDOT:PSS with a steel razor blade, and then recording the trench depth with an Alpha-Step IQ surface profilometer. An Agilent 8453 UV-Vis Spectrophotometer was used to record absorbance spectra. Atomic force microscopy (AFM) was performed using a Nanoscope IV (Digital Instruments/Veeco) in tapping mode with Si cantilevers (Micromash, 300 kHz). A Kratos Ultra spectrometer with He I ($h\nu$ = 21.2 eV) incident radiation and substrate biasing at -10 V was used to perform ultraviolet photoelectron spectroscopy on PEDOT:PSS films freshly deposited on ITO substrates. Scanning electron microscopy was performed with a Hitachi S-4800 at an accelerating voltage of 15 kV.

A Hysitron Triboindenter fitted with a 1 μm conospherical tip was used for all nanoindentation measurements. Test samples measuring roughly 1 cm x 1 cm were affixed to magnetic steel discs using Instant Krazy Glue and mounted in the Triboindenter. For each sample, a series of 25 indent experiments was performed with a range of indent depths set by adjusting the maximum applied force from 500 μN to 1.75 mN. The sites of all indents were separated from one another by 10 μm according to a 5 x 5 grid pattern. During each indent experiment, the force was linearly increased for 5 s to the specified maximum, held constant for 5 s, and linearly

unloaded for 5 s. The mechanical properties were calculated by the Triboindenter software. A small increase in elastic modulus was observed with increasing indentation depth for the PEDOT:PSS series of samples, indicating that the substrates may have been weakly influencing the mechanical measurements, particularly at larger indentation depths. Therefore for these PEDOT:PSS samples, only indentations to less than 250 nm were included in the modulus calculations.

Resistance vs. strain plots were generated using an Instron 5943 single column testing system in combination with a Keithley 2400 source meter and synchronization software. PET from the same source was used for all experiments, and samples originally measuring 13±1 mm in width and 89±1 mm in length were clamped in the Instron with rubber-insulated grip pads. The sample length between the grips was 25±1 mm (initial length of stretched sample), with 25 mm of sample for each grip pad (this area remains static and unstretched), and the samples extended beyond the grip pads by 7 mm on each end. These ends were connected to the Keithley 2400 with alligator clips. Only the 25 mm portions of the samples between the grip pads were deformed during the experiments, and therefore, the strain-independent portion of the resistance was subtracted from all resistance/time data prior to plotting. The tensile tester and source meter independently collected stress-strain and electrical resistance data, respectively, however the initiation of each test was synchronized using a TTL trigger signal. Strain/time data from the tensile tester was then combined with resistance/time data from the source meter to produce resistance/strain plots.

Measurements of sheet resistance, power conversion efficiency and device resistance (for "OPV devices" without photoactive layers) vs. bending radius of curvature were performed by first fabricating the devices of interest on PET substrates as described above. The sheet resistance (by four point probe), power conversion efficiency (by solar simulator) or device resistance (by Keithley 2400 Source Meter) were always measured before any deformation, then the films/devices were bent to the stated radii of curvature by wrapping them around cylindrical objects. To prevent abrasion of the film/device, substrates were always bent with the PET side against the cylindrical object, and therefore the strain on the film/device was always tensile. The films/devices were then flattened, and the properties re-measured. Repeated bending was performed beginning with large RoC values and moving to progressively smaller values.

Solar Cell Testing:

OPV device performance characteristics were tested at ambient conditions in air under AM 1.5G simulated solar irradiation (OAI TriSOL, class AAA, 300W). A certified Si reference cell with a KG-5 filter (model PVM624, PV Measurements, Inc.) was used to calibrate the testing irradiance before every test, and a Keithley 2400 source meter was used to measure device performance.

2.5 Contributions

The project was conceptualized by B.J. Worfolk. B.J. Worfolk supervised J.G. Tait throughout his undergraduate engineering Capstone project, and as a summer student. B.J. Worfolk and J.G. Tait planned experiments. J.G. Tait optimized the

spraying process, and fabricated photovoltaic devices. S.A. Maloney, assisted with resistance measurements and post-processing optimization. T.C. Hauger, A.L. Elias and K.D. Harris assisted with characterization of mechanical properties data. All authors assisted with analysis and interpretation of data. B.J. Worfolk, J.G. Tait, and K.D. Harris co-wrote the manuscript, and all authors edited the manuscript.

2.6 References

[1] Nanomarkets, *Transparent Conductor Markets 2011*, **2011**.

[2] D.S. Hecht, R.B. Kaner, *MRS Bull.* **2011**, *36*, 749.

[3] D.S. Hecht, L. Hu, G. Irvin, *Adv. Mater.* **2011**, *23*, 1482.

[4] J. Lee, S. Lee, G. Li, M.A. Petruska, D.C. Paine, S. Sun, *J. Am. Chem. Soc.* **2012**, *134*, 13410.

[5] L. Hu, H.S. Kim, J.-Y. Lee, P. Peumans, Y. Cui, *ACS Nano* **2010**, *4*, 2955.

[6] A.R. Rathmell, B.J. Wiley, *Adv. Mater.* **2011**, *23*, 4798.

[7] Z. Wu, Z. Chen, X. Du, J.M. Logan, J. Sippel, M. Nikolou, K. Kamaras, J.R. Reynolds, D.B. Tanner, A.F. Hebard, A.G. Rinzler, *Science* **2004**, *305*, 1273.

[8] J. Wu, M. Agrawal, H.A. Becerril, Z. Bao, Z. Liu, Y. Chen, P. Peumans, *ACS Nano* **2010**, *4*, 43.

[9] M. Vosgueritchian, D.J. Lipomi, Z. Bao, *Adv. Funct. Mater.* **2011**, *22*, 421.

[10] F.C. Krebs, T. Tromholt, M. Jørgensen, *Nanoscale* **2010**, *2*, 873.

[11] Y. Galagan, J.-E. J.M. Rubingh, R. Andriessen, C.-C. Fan, P. W.M. Blom, S. C. Veenstra, J. M. Kroon, *Sol. Energy Mater. Sol. Cells* **2011**, *95*, 1339.

[12] F.C. Krebs, *Sol. Energy Mater. Sol. Cells* **2009**, *93*, 1636.

[13] H. Kim, C.M. Gilmore, A. Piqué, J.S. Horwitz, H. Mattoussi, H. Murata, Z.H. Kafafi, D.B. Chrisey, *J. Appl. Phys.* **1999**, *86*, 6451.

[14] H. Kim, A. Piqué, J.S. Horwitz, H. Mattoussi, H. Murata, Z.H. Kafafi, D.B. Chrisey, *Appl. Phys. Lett.* **1999**, *74*, 3444.

[15] D.A. Rider, R.T. Tucker, B.J. Worfolk, K.M. Krause, A. Lalany, M.J. Brett, J.M. Buriak, K.D. Harris, *Nanotechnology* **2011**, *22*, 085706.

[16] M. Manceau, D. Angmo, M. Jørgensen, F.C. Krebs, *Sol. Energy Mater. Sol. Cells* **2011**, *12*, 566.

[17] R. Po, C. Carbonera, A. Bernardi, F. Tinti, N. Camaioni, *Sol. Energy Mater. Sol. Cells* **2012**, *100*, 97.

[18] J.D. Jorgenson, M.W. George, *Mineral Commodity Profile: Indium*, **2005**.

[19] T. Jansseune, *Comp. Semicond.* **2005**, *11*, 34.

[20] E.-H. Kim, C.-W. Yang, J.-W. Park, *J. Appl. Phys.* **2011**, *109*, 043511.

[21] Y.F. Lan, W.C. Peng, Y.H. Lo, J.L. He, *Org. Electron.* **2010**, *11*, 670.

[22] K. Ellmer, *Nat. Photonics* **2012**, *6*, 809.

[23] C.-K. Cho, W.-J. Hwang, K. Eun, S.-H. Choa, S.-I. Na, H.-K. Kim, *Sol. Energy Mater. Sol. Cells* **2011**, *95*, 3269.

[24] E. Ahlswede, W. Mühleisen, M.W. bin Moh Wahi, J. Hanisch, M. Powalla, *Appl. Phys. Lett.* **2008**, *92*, 143307.

[25] S.-I. Na, G. Wang, S.-S. Kim, T.-W. Kim, S.-H. Oh, B.-K. Yu, T. Lee, D.-Y. Kim, *J. Mater. Chem.* **2009**, *19*, 9045.

[26] Y.-S. Hsiao, W.-T. Whang, C.-P. Chen, Y.-C. Chen, *J. Mater. Chem.* **2008**, *18*, 5948.

[27] Y. Xia, J. Ouyang, *J. Mater. Chem.* **2011**, *21*, 4927.

[28] X. Crispin, F.L.E. Jakobsson, A. Crispin, P.C.M. Grim, P. Andersson, A. Volodin, C. Van Haesendonck, M. Van Der Auweraer, W.R. Salaneck, M. Berggren, *Chem. Mater.* **2006**, *18*, 4354.

[29] J. Ouyang, C.-W. Chu, F.-C. Chen, Q. Xu, Y. Yang, *Adv. Funct. Mater.* **2005**, *15*, 203.

[30] R. Po, C. Carbonera, A. Bernardi, F. Tinti, N. Camaioni, *Sol. Energy Mater. Sol. Cells* **2012**, *100*, 97.

[31] Z. Chen, B. Cotterell, W. Wang, E. Geunther, S.-J. Chua, *Thin Solid Films* **2001**, *394*, 202.

[32] Y. Zhi-nong, X. Fan, L. Yuqiong, X. Wei, in *Asia Optical Fiber Communication and Optoelectronic Exposition and Conference*, Optical Society Of America**2008**, 3.

[33] C. Girotto, D. Moia, B.P. Rand, P. Heremans, *Adv. Funct. Mater.* **2011**, *21*, 64.

[34] C.J.M. Emmott, A. Urbina, J. Nelson, *Sol. Energy Mater. Sol. Cells* **2012**, *97*, 14.

[35] F.C. Krebs, *Org. Electron.* **2009**, *10*, 761.

[36] M.-G. Kang, T. Xu, H.J. Park, X. Luo, L.J. Guo, *Adv. Mater.* **2010**, *22*, 4378.

[37] W. Gaynor, G.F. Burkhard, M.D. McGehee, P. Peumans, *Adv. Mater.* **2011**, *23*, 2905.

[38] J.-Y. Lee, S.T. Connor, Y. Cui, P. Peumans, *Nano Lett.* **2008**, *8*, 689.

[39] S. De, T.M. Higgins, P.E. Lyons, E.M. Doherty, P.N. Nirmalraj, W.J. Blau, J.J. Boland, J.N. Coleman, *ACS Nano* **2009**, *3*, 1767.

[40] H. Wu, L. Hu, M.W. Rowell, D. Kong, J.J. Cha, J.R. McDonough, J. Zhu, Y. Yang, M.D. McGehee, Y. Cui, *Nano Lett.* **2010**, *10*, 4242.

[41] A. Du Pasquier, H.E. Unalan, A. Kanwal, S. Miller, M. Chhowalla, *Appl. Phys. Lett.* **2005**, *87*, 203511.

[42] M.W. Rowell, M.A. Topinka, M.D. McGehee, H.-J. Prall, G. Dennler, N.S. Sariciftci, L. Hu, G. Gruner, *Appl. Phys. Lett.* **2006**, *88*, 233506.

[43] M.H.A. Ng, L.T. Hartadi, H. Tan, C.H.P. Poa, *Nanotechnology* **2008**, *19*, 205703.

[44] Z. Li, H.R. Kandel, E. Dervishi, V. Saini, Y. Xu, A.R. Biris, D. Lupu, G.J. Salamo, A.S. Biris, *Langmuir* **2008**, *24*, 2655.

[45] J.L. Blackburn, T.M. Barnes, M.C. Beard, Y.H. Kim, R.C. Tenent, T.J. McDonald, B. To, T.J. Coutts, M.J. Heben, *ACS Nano* **2008**, *2*, 1266.

[46] D.J. Lipomi, Z. Bao, *Energy Environ. Sci.* **2011**, *4*, 3314.

[47] H.A. Becerril, J. Mao, Z. Liu, R.M. Stoltenberg, Z. Bao, Y. Chen, *ACS Nano* **2008**, *2*, 463.

[48] K. Fehse, K. Walzer, K. Leo, W. Lövenich, A. Elschner, *Adv. Mater.* **2007**, *19*, 441.

[49] Y.H. Kim, C. Sachse, M.L. Machala, C. May, L. Müller-Meskamp, K. Leo, *Adv. Funct. Mater.* **2011**, *21*, 1076.

[50] Y.-H. Ha, N. Nikolov, S.K. Pollack, J. Mastrangelo, B.D. Martin, R. Shashidhar, *Adv. Funct. Mater.* **2004**, *14*, 615.

[51] A.M. Nardes, M. Kemerink, M.M. de Kok, E. Vinken, K. Maturova, R.A.J. Janssen, *Org. Electron.* **2008**, *9*, 727.

[52] B. Peng, X. Guo, C. Cui, Y. Zou, C. Pan, Y. Li, *Appl. Phys. Lett.* **2011**, *98*, 243308.

[53] Y. Zhou, H. Cheun, S. Choi, C. Fuentes-Hernandez, B. Kippelen, *Org. Electron.* **2011**, *12*, 827.

[54] Y. Xia, K. Sun, J. Ouyang, *Energy Environ. Sci.* **2012**, *5*, 5325.

[55] C. Badre, L. Marquant, A.M. Alsayed, L.A. Hough, *Adv. Funct. Mater.* **2012**, *22*, 2723.

[56] M. Kaltenbrunner, M.S. White, E.D. Głowacki, T. Sekitani, T. Someya, N.S. Sariciftci, S. Bauer, *Nat. Commun.* **2012**, *3*, 770.

[57] J.G. Tait, B.J. Worfolk, S.A. Maloney, T.C. Hauger, A.L. Elias, J.M. Buriak, K.D. Harris, *Sol. Energy Mater. Sol. Cells* **2013**,*110*, 98.

[58] S.-I. Na, S.-S. Kim, J. Jo, D.-Y. Kim, *Adv. Mater.* **2008**, *20*, 4061.

[59] S.-I. Na, B.-K. Yu, S.-S. Kim, D. Vak, T.-S. Kim, J.-S. Yeo, D.-Y. Kim, *Sol. Energy Mater. Sol. Cells* **2010**, *94*, 1333.

[60] T. Aernouts, P. Vanlaeke, W. Geens, J. Poortmans, P. Heremans, S. Borghs, R. Mertens, R. Andriessen, L. Leenders, *Thin Solid Films* **2004**, *451-452*, 22.

[61] T. Akter, W. Soo Kim, W.S. Kim, *ACS Appl. Mater. Interfaces* **2012**, *4*, 1855.

[62] V. Scardaci, R. Coull, J.N. Coleman, *Appl. Phys. Lett.* **2010**, *97*, 023114.

[63] Y. Zhu, Z. Sun, Z. Yan, Z. Jin, J.M. Tour, *ACS Nano* **2011**, *5*, 6472.

[64] Y.-M. Chang, L. Wang, W.-F. Su, *Org. Electron.* **2008**, *9*, 968.

[65] A. Colsmann, F. Stenzel, G. Balthasar, H. Do, U. Lemmer, *Thin Solid Films* **2009**, *517*, 1750.

[66] D.J. Lipomi, J.A. Lee, M. Vosgueritchian, B.C.-K. Tee, J.A. Bolander, Z. Bao, *Chem. Mater.* **2012**, *24*, 373.

[67] K. Tvingstedt, O. Inganäs, *Adv. Mater.* **2007**, *19*, 2893.

[68] M.L. Machala, L. Mueller-Meskamp, S. Gang, S. Olthof, K. Leo, *Org. Electron.* **2011**, *12*, 1518.

[69] P.A. Levermore, L. Chen, X. Wang, R. Das, D.D.C. Bradley, *Adv. Mater.* **2007**, *19*, 2379.

[70] N. Cho, H.-L. Yip, J.A. Davies, P.D. Kazarinoff, D.F. Zeigler, M.M. Durban, Y. Segawa, K.M. O'Malley, C.K. Luscombe, A.K.-Y. Jen, *Adv. Energy Mater.* **2011**, *1*, 1148.

[71] Y. Soo Kim, S. Bin Oh, J. Hyeok Park, M. Suk Cho, Y. Lee, *Sol. Energy Mater. Sol. Cells* **2010**, *94*, 471.

[72] H. Jin, C. Tao, M. Velusamy, M. Aljada, Y. Zhang, M. Hambsch, P.L. Burn, P. Meredith, *Adv. Mater.* **2012**, *24*, 2572.

[73] Y. Feng, X. Ju, W. Feng, H. Zhang, Y. Cheng, J. Liu, A. Fujii, M. Ozaki, K. Yoshino, *Appl. Phys. Lett.* **2009**, *94*, 123302.

[74] T.P. Tyler, R.E. Brock, H.J. Karmel, T.J. Marks, M.C. Hersam, *Adv. Energy Mater.* **2011**, *1*, 785.

[75] E. Kymakis, E. Stratakis, E. Koudoumas, *Thin Solid Films* **2007**, *515*, 8598.

[76] R.C. Tenent, T.M. Barnes, J.D. Bergeson, A.J. Ferguson, B. To, L.M. Gedvilas, M.J. Heben, J.L. Blackburn, *Adv. Mater.* **2009**, *21*, 3210.

[77] S. Kim, J. Yim, X. Wang, D.D.C. Bradley, S. Lee, J.C. DeMello, *Adv. Funct. Mater.* **2010**, *20*, 2310.

[78] T.M. Barnes, J.D. Bergeson, R.C. Tenent, B.A. Larsen, G. Teeter, K.M. Jones, J.L. Blackburn, J. van de Lagemaat, *Appl. Phys. Lett.* **2010**, *96*, 243309.

[79] H.E. Unalan, P. Hiralal, D. Kuo, B. Parekh, G. Amaratunga, M. Chhowalla, *J. Mater. Chem.* **2008**, *18*, 5909.

[80] U. Lang, N. Naujoks, J. Dual, *Syn. Met.* **2009**, *159*, 473.

[81] S.K. Hau, H.-L. Yip, J. Zou, A.K.-Y. Jen, *Org. Electron.* **2009**, *10*, 1401.

[82] B.J. Worfolk, D.A. Rider, A.L. Elias, M. Thomas, K.D. Harris, J.M. Buriak, *Adv. Funct. Mater.* **2011**, *21*, 1816.

[83] T.Y. Tsui, W.C. Oliver, G.M. Pharr, in *MRS Proc.*, San Francisco, CA **1996**, 207.

[84] M.M. Hamasha, K. Alzoubi, S. Lu, *IEEE/OSA J. Disp. Technol.* **2011**, *7*, 426.

[85] D.R. Cairns, G.P. Crawford, *Proc. IEEE* **2005**, *93*, 1451.

[86] M. Glatthaar, M. Niggemann, B. Zimmermann, P. Lewer, M.K. Riede, A. Hinsch, J. Luther, *Thin Solid Films* **2005**, *491*, 298.

[87] E. Voroshazi, B. Verreet, A. Buri, R. Müller, D. Di Nuzzo, P. Heremans, *Org. Electron.* **2011**, *12*, 736.

[88] D.A. Rider, B.J. Worfolk, K.D. Harris, A. Lalany, K. Shahbazi, M.D. Fleischauer, M.J. Brett, J.M. Buriak, *Adv. Funct. Mater.* **2010**, *20*, 2404.

[89] Q. Chen, B.J. Worfolk, T.C. Hauger, U. Al-Atar, K.D. Harris, J.M. Buriak, *ACS Appl. Mater. Interfaces* **2011**, *3*, 3962.

[90] B.J. Worfolk, T.C. Hauger, K.D. Harris, D.A. Rider, J.A.M. Fordyce, S. Beaupré, M. Leclerc, J.M. Buriak, *Adv. Energy Mater.* **2012**, *2*, 361.

[91] A. Kumar, S. Sista, Y. Yang, *J. Appl. Phys.* **2009**, *105*, 094512.

3

Work Function Control of Interfacial Buffer Layers for Efficient and Air-Stable Inverted Organic Photovoltaics

3.1 Introduction

3.1.1 Overview

Upon successful fabrication of a transparent electrode (as outlined in Chapter 2), the subsequent layer in an organic photovoltaic device (OPV) is the interfacial buffer layer. Ideal buffer layers should be transparent to allow photons to pass to the photoactive layer (discussed in Chapter 4). Charges generated in the photoactive layer are extracted by the interfacial layers to the electrodes.[1]

This chapter focuses on the introduction of a water-soluble cationic polythiophene derivative poly[3-(6-{4-tert-butylpyridiniumyl}-hexyl)thiophene-2,5-diyl] [P3(TBP)HT]. This semiconducting polymer can be combined with anionic poly(3,4-ethylenedioxythiophene):poly(p-styrenesulfonate) (PEDOT:PSS) on indium tin oxide (ITO) substrates via electrostatic layer-by-layer (eLbL) assembly. By varying the number of eLbL layers, the electrode's work function is lowered from 4.6 to 3.8 eV. These polymeric coatings are used as cathodic interfacial modifiers for efficient inverted-mode OPVs. Notably, these devices demonstrate significant stability

maintaining 83% of their original power conversion efficiency (PCE) after 1 year of storage and 97% of their original PCE after over 1000 h of storage in air.

The following subsections will introduce: the stability of organic photovoltaics, electrostatic layer-by-layer assembly, and conjugated polyelectrolytes for cathodic buffer layers.

Chapter 3 was reproduced in part with permission from:

a) B.J. Worfolk, T.C. Hauger, K.D. Harris, D.A. Rider, J.A.M. Fordyce, S. Beaupré, M. Leclerc, J.M. Buriak, *Adv. Energy Mater.* **2012**, *2*, 361-368. Copyright © 2012 Wiley-VCH Verlag GmbH & Co.

b) D.A. Rider, B.J. Worfolk, K.D. Harris, A. Lalany, K. Shahbazi, M.D. Fleischauer, M.J. Brett, J.M. Buriak, *Adv. Funct. Mater.* **2010**, *20*, 2404-2415. Copyright © 2010 Wiley-VCH Verlag GmbH & Co.

c) Q. Chen, B.J. Worfolk, T.C. Hauger, U. Al-Atar, K.D. Harris, J.M. Buriak, *ACS Appl. Mater. Interfaces* **2011**, *3*, 3962-3970. Copyright © 2011 American Chemical Society.

3.1.2 Stability and Lifetimes of Organic Photovoltaic Devices

Organic photovoltaics have the potential to generate low-cost renewable energy in part due to the potential for solution processing and high throughput roll-to-roll manufacturing.[2–10] In developing the technology, research has focused on improving the device efficiency, lifetimes and fabrication costs. Consequently, new strategies for controlling the morphology of donor and acceptor domains in the photoactive layer and for employing low band gap donor polymers to absorb a larger fraction of the

solar spectrum have led to PCE values of over 7%.[11–14] The lifetime stability of OPVs is often limited, however, and rigorous studies have identified several key degradation mechanisms such as photooxidation and morphology evolution in the structure of the multilayer device.[15–18]

Conventional donor polymers such as P3HT are often prone to oxidation in air when illuminated,[19, 20] while a polymer with a deeper set highest occupied molecular orbital (HOMO) energy level is less prone to oxidation, and in turn contributes to an increased stability in OPVs.[21–26] Additionally, interfacial buffer layers are known to affect the lifetime of OPVs.[27] Specifically, the familiar hole transport interfacial modifier, PEDOT:PSS, can contribute to the degradation of organic light emitting diodes and OPVs as a result of: *i)* its high acidity which can promote ITO etching,[28] and *ii)* an excess hygroscopic of poly(sodium 4-styrenesulfonate) (NaPSS), which can migrate throughout the bulk heterojunction (BHJ) and react with components of the photoactive layer.[27] These factors contribute to the degradation of OPVs in air.

The unencapsulated shelf life of OPVs have been extensively studied in recent years, since it has been recognized as one of the major limitations of the technology.[15, 27, 29] The photovoltaic performance parameters of conventional or forward-mode OPVs, which extract holes at the transparent anode and electrons at the cathode, completely degrade within 40-250 h when stored unencapsulated in air.[29–34] However, the air stability is significantly improved for inverted-mode OPVs, which extract electrons at the transparent cathode and holes at the anode.[35] Because interfacial layers have been shown to influence the device stability (*vide supra*), the effect of using different metals and metal oxides as the cathodic buffer layer has been

investigated. Calcium metal used as the cathodic buffer layer leads to OPV devices that typically degrade ~77% after 720 h,[32] Al_2O_3-based buffer layers lead to ~30% degradation after 278 h,[30] TiO_2 buffer layers lead to ~20% degradation after 500 h,[31, 33, 36] and ZnO utilized as the cathodic buffer layer leads to OPV devices degrading ~13% after 500 h.[20, 37–40]

3.1.3 Electrostatic Layer-by-Layer Assembly

Electrostatic layer-by-layer (eLbL) growth is a versatile and efficient approach to the production of compositionally controlled interfacial structures.[41] Via sequential immersion of the substrate in solutions containing cationic and anionic species (such as nanoparticles, polymers, biological materials, etc.), films of controlled thickness and composition can be built up in an efficient fashion.[42–48] Electrostatic layer-by-layer assembly was developed by G. Decher.[49] One of the first examples of eLbL assembly is the deposition of thin polyelectrolyte films of anionic sodium poly(sodium 4-styrenesulfonate) (PSS) and cationic poly(allylamine hydrochloride) (PAH) as seen in Figure 3.1.[42] The films are typically affected by polyelectrolyte soak time, quality of rinsing, pH and salinity of solutions. The great command of composition and thickness in eLbL assembled films have enabled their use in optoelectronic devices.[50]

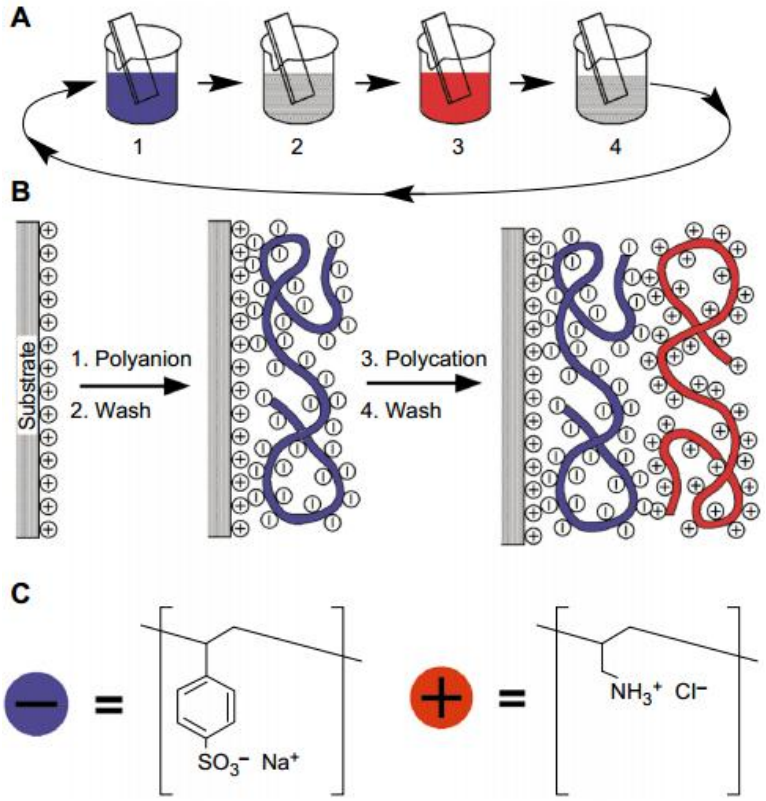

Figure 3.1 Early investigations into electrostatic layer-by-layer assembly by G. Decher. A) A schematic of the LbL assembly process, whereby a substrate is dipped into cationic and anionic polyelectrolyte solutions with rinsing in between each step. B) Schematic of the LbL process at the molecular level, starting with a substrate with a positively charged surface. C) The chemical structures of two commonly used polyelectrolytes: anionic PSS and cationic PAH. Reprinted with permission from reference [42]. Copyright © 1997 American Association for the Advancement of Science.

Sodium poly(3,4-ethylenedioxythiophene):poly(*p*-styrenesulfonate) [(PEDOT:PSS)$^-$Na$^+$] is an organic polymer blend of cationic, conducting PEDOT that is charge over-compensated by anionic and insulating PSSNa, and hence the (PEDOT:PSS)$^-$Na$^+$ complex bears an overall negative charge in aqueous solution. This polymer blend is usually applied in organic electronics (including forward-mode polymer OPVs) as a hole-collecting interfacial modification layer on ITO due to its stable and high work function.[51] Electrostatic LbL assembly using (PEDOT:PSS)$^-$Na$^+$ as an anionic polymer component partnered with various

cationic materials has recently been explored.[52–55] Starting with a substrate that has a charged surface, LbL growth is accomplished by alternating exposure to cationic and anionic polymer solutions. This deposits films of controlled thickness and composition.[43, 44] R.H. Friend and coworkers used eLbL assembly to fabricate thin films of PEDOT:PSS and cationic poly(p-xylylene-α-tetra-hydrothiophenium) (PXT) (see Figure 3.2) to serve as a hole injection layer, controlling electron leakage, for polymer light emitting diodes (PLEDs).[50]

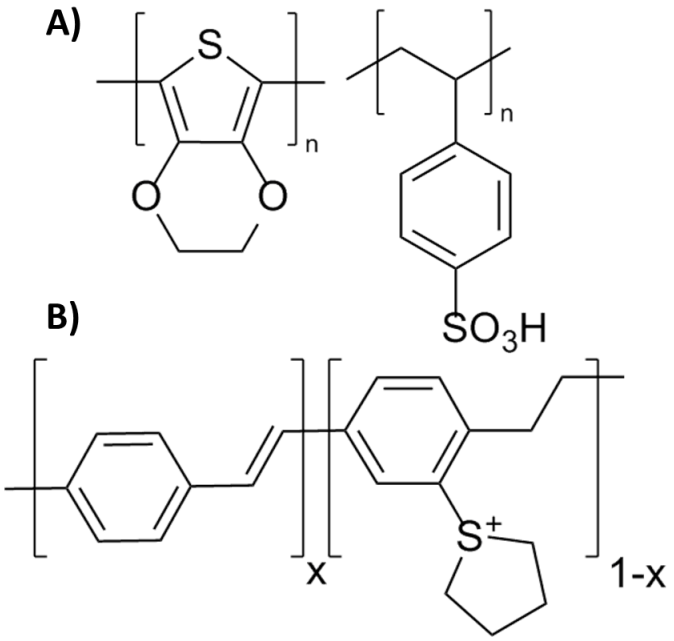

Figure 3.2 The chemical structure of A) PEDOT:PSS and B) PXT, used in eLbL assembly for hole injection layers for PLEDs.[50]

3.1.4 Conjugated Polyelectrolytes as Cathodic Buffer Layers

While $(PEDOT:PSS)^{-}Na^{+}$ is a ubiquitous material in organic electronics, it is not normally applied to ITO in inverted OPVs due to its electron-blocking properties.[56] A low work function alternative is required to successfully modify ITO for use as a cathode in inverted OPVs. Upon submitting this work, surface

modification had been successfully demonstrated using only inorganic or surface-functionalized inorganic materials.[20, 57–63] The reduction of the work function of ITO with purely organic polymer coatings for inverted OPVs had yet to be largely explored. Using organic polymers is attractive from several standpoints. First, many organic polymers can be tailored to match the electronic, morphological and physical requirements for improved device performance. Second, solution-processable polymers are desirable from an industrial perspective as costly vacuum deposition equipment is avoided, and in a further refinement, water-soluble polymers are particularly advantageous as organic solvents are relatively expensive and environmentally harmful. Third, the quality and uniformity of polymer coatings is often higher than those of inorganic counterparts. The electrostatic multilayer assembly of water-soluble interfacial modification polymers on ITO is therefore an attractive complement.

Since publication of our early work on polymeric cathodic interfacial layers,[46] there has been growing interest in low work function organic coatings for cathodic interfacial modifiers.[64–74] Kippelen and coworkers used thin layers of poly(ethyleninimine ethoxylated) (PEIE) and poly(ethylenenimine) (PEI) as universal low work function electrode modifiers for a variety of organic electronic devices including: OPVs, thin film transistors (TFTs), and organic light emitting diodes (OLEDs).[74] The decrease in work function was attributed to the formation of molecular and interfacial dipoles.[74] These polymers can be processed from solution, enabling large-scale fabrication of low work function electrodes through roll-to-roll processing.[74]

Yong Cao and coworkers have also developed a polymeric low work function cathodic modifier, leading to highly efficient OPV devices with a certified power conversion efficiency of 9.2%.[73] Poly[(9,9-bis(3'-(N,N-dimethylamino)propyl)-2,7-fluorene)-alt-2,7-(9,9–dioctylfluorene)] (PFN), soluble in alcohol, is used as a cathodic buffer layer in combination with poly(thieno[3,4-b]thiophene/benzodithiophene) (PTB7) as a low band gap donor in the photoactive layer as seen in Figure 3.3. Devices also exhibited remarkable stability, maintaining 95% of their PCE after 62 days.[73] This work marks a great achievement in both achieving high efficiency and air-stable organic photovoltaics.

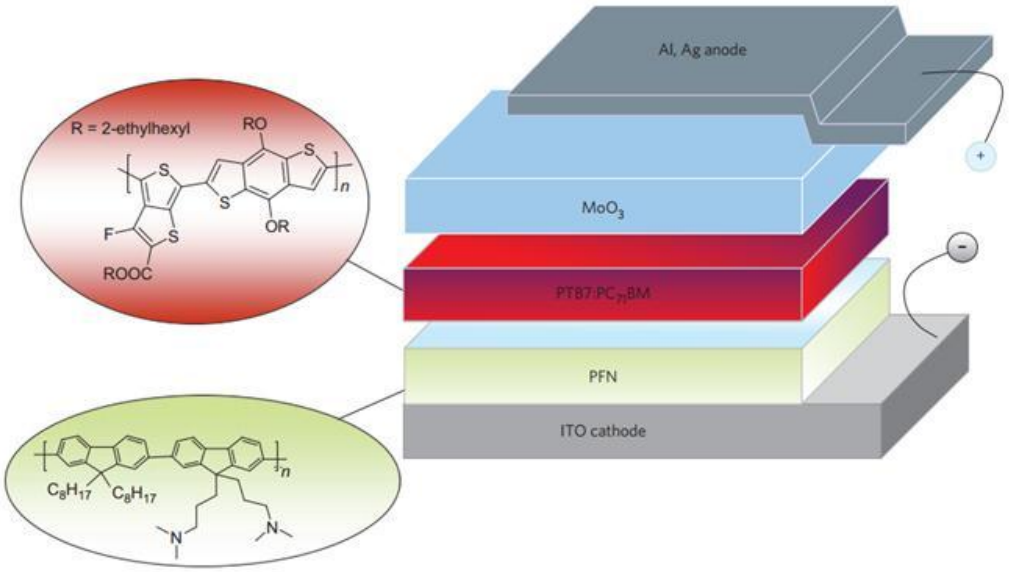

Figure 3.3 Inverted-mode OPV device schematic using a conjugated polyelectrolyte (PFN) as a cathodic interfacial modifier. Reprinted with permission from reference [73]. Copyright © 2012 Macmillan Publishers Limited.

Herein, we describe the synthesis of a cationic and water-soluble polythiophene, poly[3-(6-{4-tert-butylpyridiniumyl}-hexyl)thiophene-2,5-diyl bromide] [P3(TBP)HT^{+}Br^{-}], as shown in Figure 3.4A, combined with anionic PEDOT:PSS through electrostatic layer-by-layer (eLbL) assembly[42, 45, 46] to create a versatile

cathodic buffer layer on ITO. We find that these eLbL-assembled thin films can finely tune the work function of the electrode to better match the electronic band structure of the photoactive layers and consequently affect the OPV performance. In particular, a cathodic interfacial buffer layer of $[P3(TBP)HT:PEDOT:PSS]_{5.5}$ (created by 5.5 iterations of the cycle depicted in Figure 3.4B) leads to an inverted-mode PBDTTPD:$PC_{71}BM$ OPV with PCE of 5.6% and significant air stability, degrading only 3% over 1000 h.

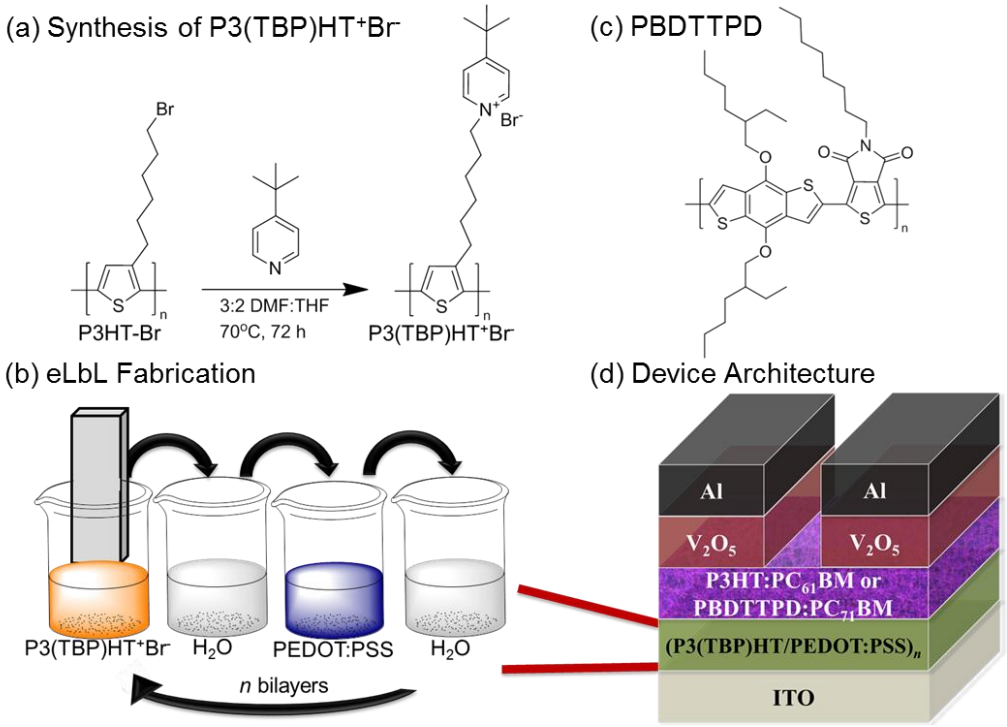

Figure 3.4 A) Synthesis of P3(TBP)HT, B) eLbL fabrication of $(P3(TBP)HT/PEDOT:PSS)_n$, C) chemical structure of PBDTTPD, and D) the PV device architecture of both P3HT:$PC_{61}BM$ and PBDTTPD:$PC_{71}BM$ devices. Reprinted with permission from reference [75]. Copyright © 2012 Wiley-VCH Verlag GmbH & Co.

3.2 Results and Discussion

3.2.1 Synthesis of a Cationic Polythiophene

Water-soluble P3(TBP)HT^{+}Br^{-} was synthesized from a quaternization reaction of poly[3-(6-bromohexyl)thiophene] (M_n = 13.3 kDa, PDI = 1.87) with 4-*tert*-butylpyridine as summarized in Figure 3.4A.[46] P3(TBP)HT^{+}Br^{-} was obtained in good yield with a high degree of quaternization as characterized by ^{1}H NMR spectroscopy (see experimental section 3.4). P3(TBP)HT^{+}Br^{-} is readily soluble in 95:5 (*v*/*v*) H_2O:DMF and has a solution absorption λ_{max} at 424 nm.

3.2.2 Fabrication of Multilayer Thin Films

Multilayer thin films were fabricated using eLbL assembly[42] with cationic P3(TBP)HT^{+}Br^{-} (0.5 mg/mL, 95:5 (*v*/*v*) H_2O:DMF) and anionic PEDOT:PSS (0.8 wt% diluted aqueous solution of Heraeus Clevios P VP AI 4083 PEDOT:PSS) on ITO coated glass substrates. Briefly, a cathodic interfacial buffer layer was fabricated by submerging freshly cleaned ITO (bearing native negative charge) in cationic P3(TBP)HT^{+}Br^{-} solution for 5 min, followed by immersing in anionic PEDOT:PSS solution for 5 min with intermediate rinsing steps. This immersion/rinse cycle was repeated *n* times to build up P3(TBP)HT:PEDOT:PSS films of *n* bilayers as shown in Figure 3.4B. Whole bilayer numbers (*n* = 1, 2, 3, etc.) indicate a final functionalization with PEDOT:PSS, whereas half bilayer numbers (*n* = 0.5, 1.5, 2.5, etc.) indicate a final functionalization with P3(TBP)HT. The electrostatically-bound polyelectrolytes are deposited in a layer-by-layer fashion and lead to a thin film with increasing film thickness as the number of coating cycles increases.

Solid state absorbance spectroscopy was used to characterize the eLbL assembled films of increasing bilayer number, *n*, as seen in Figure 3.5A. The absorbance increases roughly linearly with bilayer number as seen in Figure 3.5B, where the absorbance at λ_{max} = 431 nm is plotted against bilayer number. The absorbance peak is representative of the P3(TBP)HT polymer. eLbL assembly was performed on freshly cleaned Si wafers and the thickness was measured with ellipsometry after each bilayer. From the plot in Figure 3.5C, each bilayer corresponds to ~ 1.2 nm.

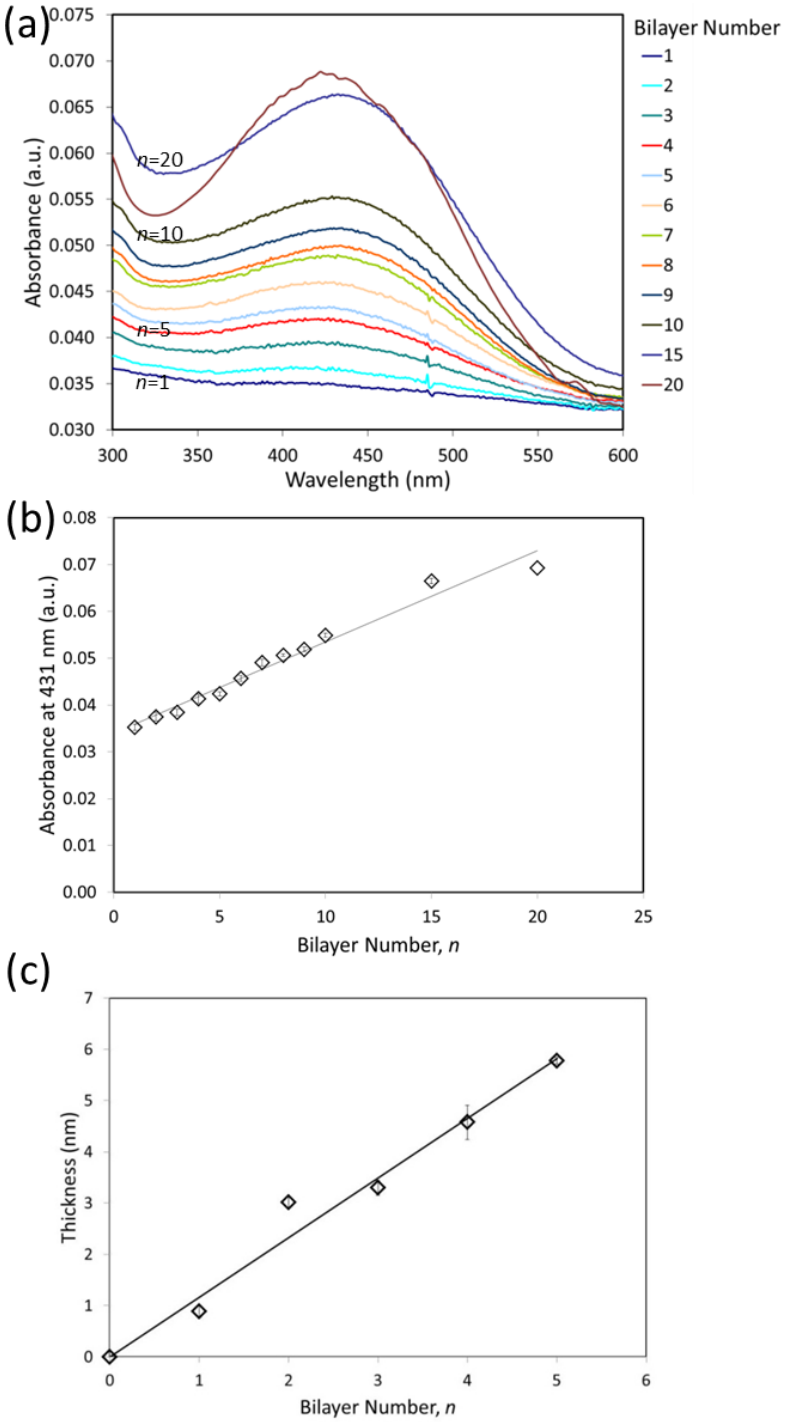

Figure 3.5 A) Solid state UV-vis absorbance spectroscopy of eLbL multilayered films of $[P3(TBPHT):PEDOT:PSS]_n$, where n represent bilayer numbers from n = 1 to 20 bilayers. B) The absorbance at λ_{max} = 431 nm against the bilayer number of the eLbL assembled thin films. C) The thickness of eLbL assembled films of $[P3(TBP)HT:PEDOT:PSS]_n$ measured with ellipsometry. Reprinted with permission from reference [75]. Copyright © 2012 Wiley-VCH Verlag GmbH & Co.

The multilayered thin films were chemically characterized with X-ray photoelectron spectroscopy (XPS). High resolution XPS spectra were acquired for the S(2p), N(1s), Br(3d) and Na(1s) regions of $[P3(TBP)HT:PEDOT:PSS]_n$ thin films, where n = 4.5, 5, 5.5 and 6 bilayers as seen in Figure 3.6. The S(2p) region consists of two peaks, which are characteristic of both $(PEDOT:PSS)^-$ and $P3(TBP)HT^+$ components. The peak at ~ 165 eV corresponds to the thiophene group in PEDOT and $P3(TBP)HT^+$, while the higher binding energy peak at ~ 168.5 eV corresponds to the sulfonate group in PSS^-. There are two prominent peaks in the N(1s) spectra at ~ 399.9 and 402.5 eV. The peak at higher binding energy corresponds to the N from the pyridinium group in $P3(TBP)HT^+$. The lower binding energy peak is present in the original PEDOT:PSS formulation.[46, 76] The broad peak at ~ 71.2 eV in the Br(3d) spectra results from the bromide in $P3(TBP)HT^+Br^-$. The presence of this peak indicates that either some of the cationic polythiophene exists unbound to $(PEDOT:PSS)^-$ or that NaBr is present as a salt. The absence of Na in the Na(1s) spectra indicates the prior. Formulations of PEDOT:PSS typically consist of an excess of NaPSS (1:6 ratio of PEDOT:PSS in Heraeus Clevios P VP AI 4083).[77] This excess NaPSS has been shown to lead to the degradation of OPV devices as NaPSS is mobile and can react with components in the photoactive layer.[27] The absence of Na, as characterized with XPS, indicates the removal of NaPSS, likely during the rinse cycles, which may aid in improving the stability of these devices.

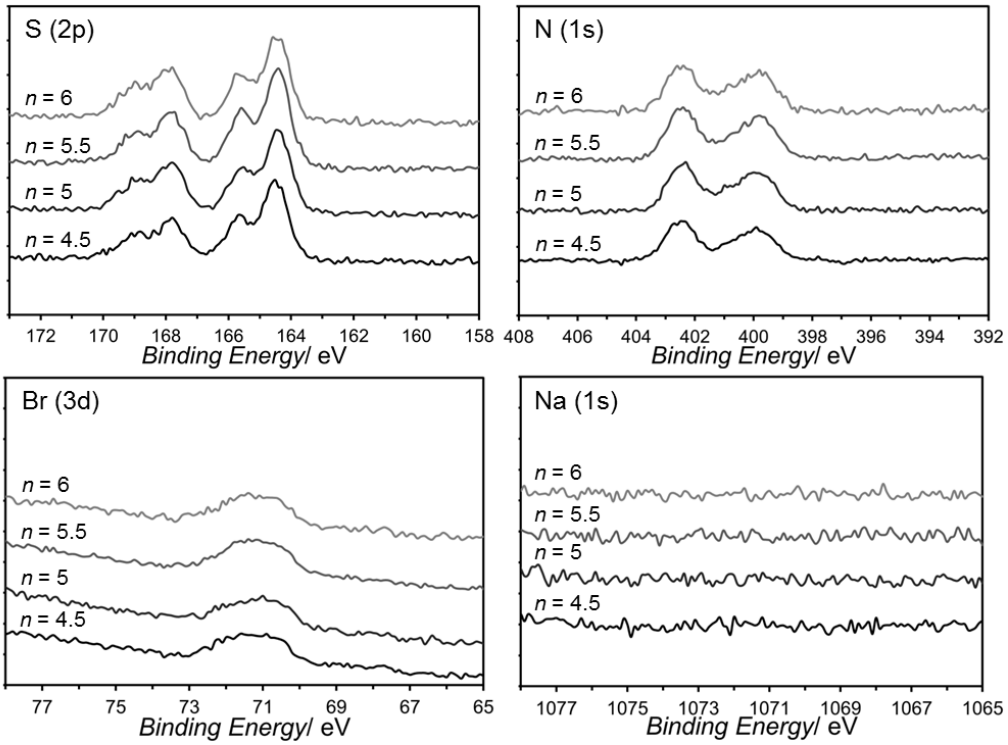

Figure 3.6 High resolution X-ray photoelectron spectra of multilayered films of $[P3(TBP)HT:PEDOT:PSS]_n$ of the S(2p), N(1s), Br(3d) and the Na(1s) regions where n = 4.5, 5, 5.5 and 6 bilayers. Reprinted with permission from reference [75]. Copyright © 2012 Wiley-VCH Verlag GmbH & Co.

3.2.3 Work Function of Films

For efficient extraction of electrons and holes, the work function of interfacial buffer layers must be carefully aligned with the ITO electrode and the active layer.[78, 79] The work functions of the $[P3(TBP)HT:PEDOT:PSS]_n$ films were measured by ultraviolet photoelectron spectroscopy (UPS) (He I line, $h\nu$ = 21.2 eV) and are presented in Figure 3.7. The unmodified ITO work function (n = 0) was 4.60 ± 0.02 eV, similar to previously reported values.[80] After the deposition of the P3(TBP)HT n = 0.5 layer, the work function decreased to 3.93 ± 0.01 eV followed by an increase to 4.25 ± 0.06 eV after completing the first bilayer (n = 1) with subsequent PEDOT:PSS functionalization. As deposition of the eLbL interfacial buffer layer is continued for the range of n = 0 to 3, an overall decrease in the work function is

observed and is presumed to arise from the decreasing influence of the ITO substrate on the measurement (the penetration depth of UPS is ~0.5 to 2 nm). Beyond n = 3, the work function of the buffer layer was found to oscillate predictably between approximately 3.8 eV and 4.0 eV for half-integer bilayer values [i.e., P3(TBP)HT-terminated films] and integer values (i.e., PEDOT:PSS-terminated films), respectively. This oscillation phenomenon has been previously observed in small molecule:polyelectrolyte[81, 82] and nanoparticle hybrid multilayered films and is attributed to the modulation of the electron affinity of ITO.[83]

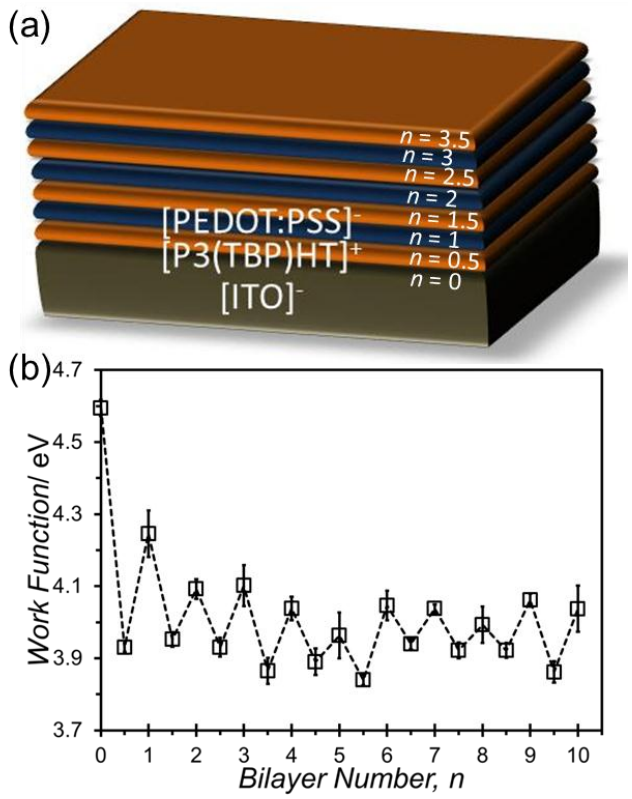

Figure 3.7 A) A schematic of the multilayered thin films of [P3(TBP)HT:PEDOT:PSS]$_n$. B) The work function of eLbL-assembled [P3(TBP)HT:PEDOT:PSS]$_n$ thin films on an ITO electrode measured with UPS. Reprinted with permission from reference [75]. Copyright © 2012 Wiley-VCH Verlag GmbH & Co.

3.2.4 Photovoltaic Devices

The UPS data illustrates the successful formation of lower work function electrode modifiers, which could be applied as cathodic interfacial buffer layers for inverted-mode OPVs.[79] For photovoltaic device fabrication, we employed P3HT and the low band gap polymer [poly({4,8-di(2-ethylhexyloxyl)benzo[1,2-b:4,5-b']dithiophene}-2,6-diyl)-alt-({5-octylthieno[3,4-c]pyrrole-4,6-dione}-1,3-diyl) (PBDTTPD)] (Figure 3.4C), which has a deep HOMO energy level of -5.6 eV imparting resistance to oxidation.[84] Typically, a forward-mode OPV incorporating a PBDTTPD:$PC_{71}BM$ BHJ photoactive layer operates in air with a PCE of 5.5% with a device area of 1.0 cm^2[85–87] and up to 6.8% with a device area of 0.03 cm^2,[84, 86] while inverted-mode devices have achieved a PCE of 4.2% with a C_{70}-based self-assembled monolayer (SAM) on ZnO as the interfacial modifier.[85] Our OPV devices consist of a ~90 nm thick PBDTTPD:$PC_{71}BM$ (1:1.5 wt:wt) bulk heterojunction photoactive layer spin cast from *o*-dichlorobenzene with V_2O_5 and Al as the hole transport layer and anode respectively, as depicted in Figure 3.4D. The architecture of the series of inverted-mode OPVs that are constructed to assess the utility of the eLbL interfacial buffer layer is: ITO/[P3(TBP)HT:PEDOT:PSS]$_n$/PBDTTPD:$PC_{71}BM$/V_2O_5/Al with a device area of 0.155 ± 0.008 cm^2.

We investigated the relationship between the eLbL interfacial buffer bilayer number and the photoresponse of the OPV devices for the PBDTTPD:$PC_{71}BM$ photoactive layer as seen in Figure 3.8. All photovoltaic parameters rapidly improve for increasing bilayers $n = 0$ to 2 with increasing surface coverage of the thin eLbL film on the ITO cathode and the commensurate adjustment of the electrode work function to lower values (Figure 3.7). With greater bilayer numbers, the PCE and fill

factor (FF) then subtly oscillate with bilayer number, where improved performance occurs with larger half-integer bilayer numbers [i.e. multilayer films terminated with P3(TBP)HT]. This result agrees with the work function data as half-integer layers were found to have a lower work function. The open-circuit voltage (V_{OC}) levels out after n = 2 bilayers, while the short-circuit current density (J_{SC}) stabilizes from n = 2 to 4.5 bilayers and increases ~1.1 mA/cm^2 at n = 5.5 bilayers, corresponding to an increase in FF from 0.51 to 0.55. By changing from n = 5 to 5.5 bilayers, the thickness of the film increases by ~0.6 nm, while the PCE significantly improves from 4.5 ± 0.3% to 5.5 ± 0.1%. This large increase in PCE with a very thin additional half bilayer, suggests a limited role for optical interference and demonstrates the important role of interfacial surface energy on photovoltaic performance. The work function is reduced as the result of an interfacial dipole between the ITO substrate and cationic P3(TBP)HT. At n = 5.5 bilayers, the magnitude of the dipole is 0.76 eV relative to the substrate work function. This reduces the energy barrier between the lowest unoccupied molecular orbital (LUMO) of PCBM and the work function of the cathode, allowing improved extraction of electrons. For maximum initial PCE, the optimal bilayer number was n = 5.5, which corresponds to an interfacial buffer layer with the lowest work function (i.e. 3.84 ± 0.01 eV, see Figure 3.7. These results are consistent with the literature, as a lower work function buffer layer improves PV performance for inverted-mode OPVs.[1, 57]

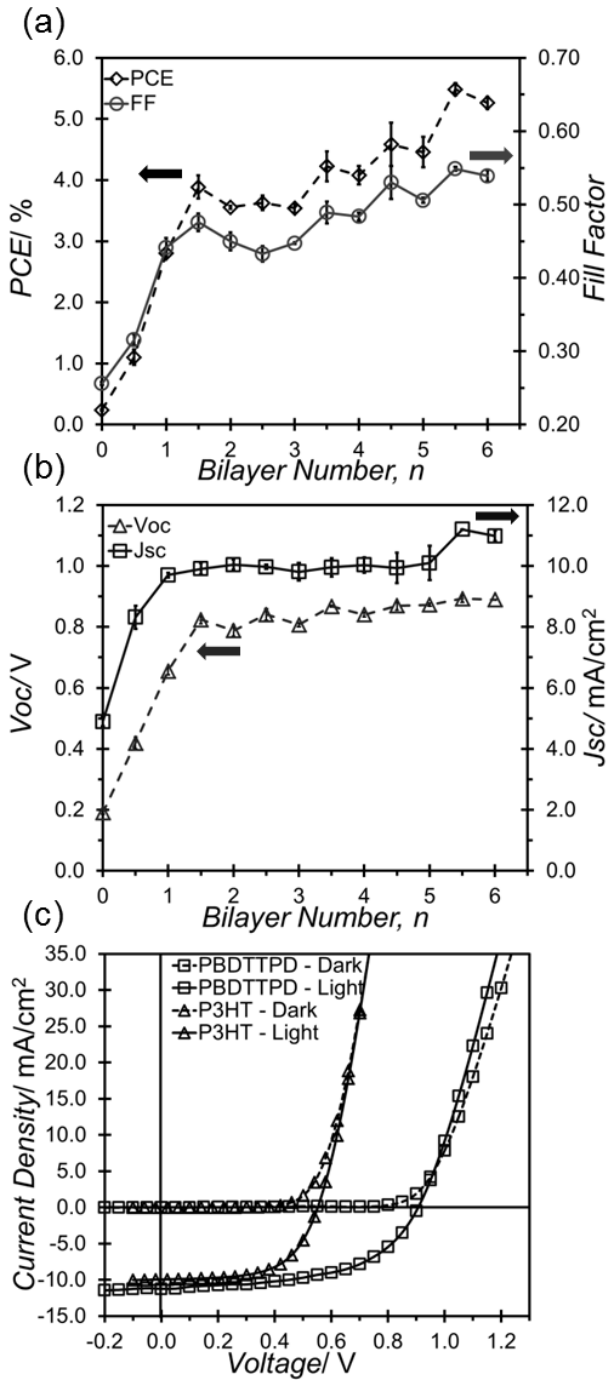

Figure 3.8 The A) PCE and FF and B) the V_{OC} and J_{SC} for different bilayer numbers, *n*, with the device architecture: ITO/[P3(TBP)HT:PEDOT:PSS]$_n$/PBDTTPD:$PC_{71}BM$/V_2O_5/Al. Each data point represents the average of three devices and the error bars (very small) represent the standard deviation. C) *J-V* curves for the optimal devices with 5.5 bilayers of P3(TBP)HT:PEDOT:PSS as the cathodic interfacial layer for both P3HT:$PC_{61}BM$ and PBDTTPD:$PC_{71}BM$ devices. Reprinted with permission from reference [75]. Copyright © 2012 Wiley-VCH Verlag GmbH & Co.

The current density – voltage (*J-V*) curve of the optimal inverted-mode PBDTTPD:$PC_{71}BM$ OPV fabricated in this study is depicted in Figure 3.8C and photovoltaic characteristics summarized in Table 3.1. These efficient devices have a J_{SC} of -11.2 mA/cm^2, V_{OC} of 0.91 V, FF of 0.55, and a PCE of 5.6%. These devices represent the highest PCE obtained for inverted-mode OPVs using PBDTTPD in the photoactive layer. OPV devices with a P3HT:$PC_{61}BM$ photoactive layer obtained a J_{SC} of -9.9 mA/cm^2, V_{OC} of 0.55 V, a FF of 0.60 and a PCE of 3.8%. The low band gap polymer OPVs have larger J_{SC} and V_{OC} values, which can be attributed to absorption of a larger portion of the solar spectrum and better energy alignment of the HOMO of PBDTTPD with the LUMO of $PC_{71}BM$, respectively.[84]

Table 3.1 Photovoltaic characteristics of the P3HT:$PC_{61}BM$ and PBDTTPD:$PC_{71}BM$ photoactive layers. Reprinted with permission from reference [75]. Copyright © 2012 Wiley-VCH Verlag GmbH & Co.

Photoactive Layer	Jsc (mA/cm^2)	Voc (V)	FF	PCE (%)
P3HT:$PC_{61}BM$	-9.9	0.55	0.60	3.8
PBDTTPD:$PC_{71}BM$	-11.2	0.91	0.55	5.6

Control devices were fabricated with complementary insulating polyelectrolytes as a control to determine the roles of both P3(TBP)HT and PEDOT:PSS components in eLbL multilayer films. Cationic poly(diallyldimethylammonium chloride) (PDDA) and anionic sodium polystyrene sulfonate (PSS) were selected as control polyelectrolytes. Table 3.2 illustrates the reduced performance of both $[PDDA:PEDOT:PSS]_{5.5}$ and $[P3(TBP)HT:PSS]_{5.5}$ cathodic interfaces with P3HT:$PC_{61}BM$ OPV devices compared to $[P3(TBP)HT:PEDOT:PSS]_{5.5}$ devices in Table 3.1. Both the J_{SC} and the FF are significantly reduced. This indicates that both components are required to improve the cathodic buffer layer performance.

Table 3.2 Control experiment of different multilayer compositions including $[PDDA:PEDOT:PSS]_{5.5}$ and $[P3(TBP)HT:PSS]_{5.5}$ cathodic buffer layers for P3HT:$PC_{61}BM$ devices. Reprinted with permission from reference [75]. Copyright © 2012 Wiley-VCH Verlag GmbH & Co.

Multilayer Composition	Jsc (mA/cm^2)	Voc (V)	PCE (%)	FF
$[PDDA:PEDOT:PSS]_{5.5}$	-8.47	0.54	2.04	0.45
$[P3(TBP)HT:PSS]_{5.5}$	-8.98	0.52	2.08	0.44

3.2.5 Shelf Life of Organic Photovoltaics

The stability of P3HT:$PC_{61}BM$ devices were studied by obtaining *J-V* curves in air over the course of one year as seen in Figure 3.9A. Between testing procedures, the devices were stored in N_2. The V_{OC} of the devices was found to be remarkably stable over the course of the year. While the J_{SC} initially increases and the FF decreases, these parameters were observed to nearly stabilize over time at ~110% and ~80% of their original values, respectively. Overall, the devices maintained 83% of their original PCE after one year and 47% after 1.7 years. Devices with Cs_2CO_3 as the cathodic buffer layer (standard in the literature)[57] significantly degraded to 20% of their original PCE within 500 h.

The stability of the PBDTTPD:$PC_{71}BM$ devices was studied for over 1500 hours, while the devices were stored in ambient air between testing according to ISOS-D-1 protocol.[88] The results are shown in Figure 3.9B. The normalized PCE of the devices maintains 97% of its original performance after 1080 hours and then decreases 13% as the devices approach 1500 hours exposure to air (39% of original PCE after 1.4 years). For comparison a Cs_2CO_3 cathodic buffer layer with the same photoactive layer and electrodes was fabricated. These devices exhibited significant instability, degrading to 28% of its original PCE in 480 hours. The

P3(TBP)HT:PEDOT:PSS multilayers lead to stability exceeding other reports of Ca, Al_2O_3, TiO_2 or ZnO cathodic buffer layers stored under similar conditions (*vide supra*).[20, 30–33, 36–40] Because OPVs typically degrade in air, encapsulation is necessary in order to improve lifetimes. To achieve long-term stability of OPVs, flexible barrier films with very low oxygen transmission rate (OTRs) and water vapor transmission rates (WVTRs) of 10^{-3} cm^3 m^{-2} day^{-1} atm^{-1} and 10^{-6} g m^{-2} $day^{-1}$are required.[89, 90] Glass encapsulation has been utilized, leading to OPV lifetimes of 3 to 7 years,[23, 91] however this sacrifices the flexibility of device modules. Flexible poly(ethylene naphthalate) (PEN) based barrier films were used to significantly improve the stability of OPVs compared to unencapsulated devices.[92] With this barrier film, the devices degraded ~25% of their original photovoltaic performance after 1000 h storage in air and darkness.[92, 93] While this encapsulated performance is among the best recorded to date for flexible barrier layers, the stability must continue to improve for full market acceptance. This emphasizes the requirement for air stable OPVs, particularly for modules with flexible barrier layers. In comparison, our devices have enhanced air stability without further encapsulation.

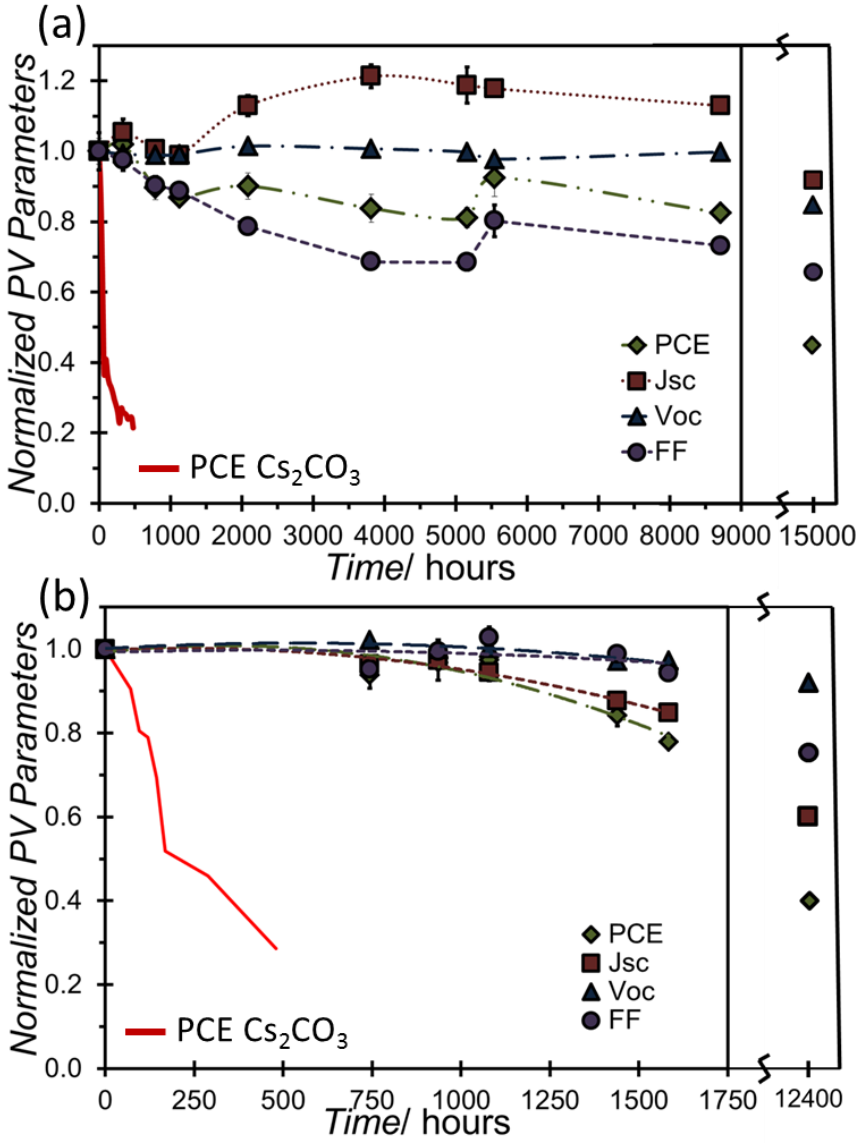

Figure 3.9 A) Normalized power conversion efficiency of the ITO/(P3(TBP)HT/PEDOT:PSS)$_{5.5}$/P3HT:PC$_{61}$BM/V_2O_5/Al devices stored for 1 year under nitrogen and tested in air. B) Normalized power conversion efficiency of the ITO/(P3(TBP)HT/PEDOT:PSS)$_{5.5}$/PBDTTPD:PC$_{71}$BM/V_2O_5/Al devices stored in air for over 1500 hours. Each data point represents the average of 4 devices and the error bars (very small) represent the standard deviations. Both plots include devices with Cs_2CO_3 as a cathodic buffer layer for comparison (solid red line). Reprinted with permission from reference [75]. Copyright © 2012 Wiley-VCH Verlag GmbH & Co.

We attribute the lengthened device lifetime to a combination of two main factors: *i)* an improved architecture in the modifying layer and *ii)* the use of a low band gap polymer with a deep HOMO energy level.[15] Since the first layer deposited on the

ITO coated substrate is P3(TBP)HT and not acidic PEDOT:PSS, we propose that a thin protective barrier of P3(TBP)HT is formed, reducing etching of the ITO electrode by PEDOT:PSS. The effect of inserting a SAM before depositing PEDOT:PSS has previously been studied and leads to a 98% decrease in the In content in PEDOT:PSS films[94] and a 60% increase in the lifetime of an electroluminescent device.[95] In our case, anionic PSS^- segments are also electrostatically tethered in the multilayer while excess NaPSS is removed, as confirmed by the absence of sodium signals in the X-ray photoelectron spectroscopy spectra (*vide supra*). The combination of these two features thus stabilizes this interface, which is commonly prone to degradation.[27] Future work will involve enhanced constant illumination tests using flexible barrier films with higher work function anodes.

3.3 Conclusions

In conclusion, we have synthesized a new water-soluble and cationic polythiophene which can be combined with anionic PEDOT:PSS *via* eLbL assembly. The nanoscale control over film thickness and surface work function demonstrates tuning of the electronic level of the electrode and enables tailoring of the energetic interface between the photoactive layer and ITO. This environmentally friendly solution processing method also reduces costs, health and safety issues commonly associated with organic solvents. The eLbL assembled thin films can function as cathodic buffer layers in inverted-mode BHJ OPVs, where the bilayer number allows for tuning of the PV performance. OPVs with P3HT:$PC_{61}BM$ photoactive layers exhibited a PCE of 3.8% and maintained >80% of their original performance over

the course of a year, while PBDTTPD:$PC_{71}BM$ devices achieved a record high PCE of 5.6% for inverted-mode devices with PBDTTPD as the donor and long-term air stability for over 1000 hours. Improving efficiencies with longer device lifetimes will increase the commercial viability and acceptance of OPVs in the future.

3.4 Experimental

Chemicals:

Tetrahydrofuran (THF), dimethylformamide (DMF), methylene chloride, isopropyl alcohol, methanol and *o*-dichlorobenzene (*o*-DCB) were used without further purification from Sigma-Aldrich. Regioregular head-to-tail poly[3-(6-bromohexyl)thiophene] (P3HT-Br) (M_n = 13300 Da, PDI = 1.87) was obtained from Polymer Source. Commercially available poly(3,4-ethylenedioxythiophene):poly(*p*-styrenesulfonate) (PEDOT:PSS) was used as received from Hereaus Clevios (P VP AI 4083). Poly({4,8-di(2-ethylhexyloxyl)benzo[1,2-b:4,5-b']dithiophene}-2,6-diyl)-alt-({5-octylthieno[3,4-c]pyrrole-4,6-dione}-1,3-diyl) (PBDTTPD) was synthesized according to Zou *et al.*[84], poly[(3-hexylthiophene)-2,5-diyl] (P3HT) from Rieke Metals, Inc. and the fullerene acceptors [6,6-phenyl-C_{71}-butyric acid methyl ester ($PC_{71}BM$)] and [6,6-phenyl-C_{61}-butyric acid methyl ester ($PC_{61}BM$)] were obtained from American Dye Source and used without further purification. ITO coated glass was obtained from Delta Technologies (8-12 Ω sq^{-1}). V_2O_5 (99.99%) and Al (99.99%) were obtained from Sigma-Aldrich and Kurt J. Lesker, respectively.

Instrumentation:

Absorbance spectroscopy was performed with an Agilent UV-vis spectrometer. Nuclear magnetic resonance (NMR) spectroscopy was performed with a Varian Inova two-channel 400 MHz system. Ellipsometry was used to estimate the thin film thickness for the electrostatic layer-by-layer (eLbL) multilayered films and was performed with a Gaertner multiangle ellipsometer and assumed negligible absorption from the 633 nm wavelength incident laser. X-ray photoelectron spectroscopy (XPS) of the eLBL multilayer films on ITO substrates was characterized with a Kratos Ultra spectrometer with a monochromatic Al Kα ($h\nu$ = 1486.71 eV) radiation source. The spectra are referenced to the 84.0 eV binding energy of Au $4f_{7/2}$, referenced to the Fermi level and corrected to the C(1s) peak at 284.8 eV, and under vacuum of base pressure of less than $5x10^{-10}$ Torr before radiation. Ultraviolet photoelectron spectroscopy (UPS) was performed on freshly prepared multilayer thin films on ITO biased at -10 V during analysis with a Kratos Ultra spectrometer with He I ($h\nu$ = 21.2 eV) incident radiation. The average and standard deviation of three spots on the same sample were analyzed. The photoactive layer thickness was characterized with a Zygo white light optical profilometer after sections of film were scrapped away with a metal scalpel.

Synthesis of P3(TBP)HT:

The synthesis of P3(TBP)HT is similar to a procedure recently published by Rider *et al.*[46] 0.1 g of P3HT-Br was dissolved in 10 mL of THF and stirred for 2 hours. 15 mL of DMF and 0.32 g of 4-*tert*-butylpyridine were added and the solution was stirred for 72 hours at 70 °C under Ar and in darkness. The solvent was evaporated

and the obtained solid was washed with copious amounts of methanol to remove unreacted 4-*tert*-butylpyridine. The dark-red solid (0.135 g, 95% yield) was dried under vacuum at 70 °C for 5 hours to remove remaining solvent. ^{1}H-NMR (400 MHz, [D_7]-DMF, 25°C, TMS) δ=9.33 (m, 2H), 8.23 (m, 2H), 7.25 (m, 1H), 4.82 (m, 2H), 2.04 (m, 2H), 1.89-0.93 (br, 17H); *UV-Vis (95:5 v/v H_2O:DMF): λ_{max} = 424 nm.*

eLbL Assembly of Multilayer Films:

ITO coated glass substrates were cleaned in sequential 10 min ultrasonication in methylene chloride, distilled water and isopropyl alcohol, followed by a 10 min air plasma with a Harrick plasma cleaner (~0.1 mTorr, PDC 32G, 18W). Both P3(TBP)HT and PEDOT:PSS solutions were filtered with a 0.45 μm mixed cellulose esters filter before use. For eLbL assembly, freshly cleaned ITO substrates were immersed in a 0.5 mg/mL solution of P3(TBP)HT in 95:5 (v/v) H_2O:DMF for 5 min, rinsed with a copious amount of distilled water, submersed in a 0.8 wt% aqueous solution of PEDOT:PSS for 5 min and rinsed with copious amounts of distilled water. This cycle constitutes one bilayer. This eLbL process can be repeated forming *n* bilayers on an ITO substrate. Half-integer bilayer numbers indicate P3(TBP)HT as the last deposited layer, while whole integer bilayer numbers indicate PEDOT:PSS as the last deposited layer. After the formation of the polymeric multilayer thin films, the coated ITO glass substrate was spin dry at 3000 rpm for 1 min and annealed at 120 °C under Ar and in darkness. For ellipsometry measurements, the above eLbL process was performed on a freshly cleaned silicon wafer, and for solid-state absorbance, on a glass substrate.

OPV Device Fabrication and Testing:

OPV devices consisted of the following architecture: ITO/[P3(TBP)HT:PEDOT:PSS]$_n$/photoactive layer/V_2O_5/Al, where the photoactive layer consists of a bulk heterojunction (BHJ) of either P3HT:$PC_{61}BM$ or PBDTTPD:$PC_{71}BM$. The cathodic buffer layer consisted of eLbL assembled [P3(TBP)HT:PEDOT:PSS]$_n$ multilayer films on freshly cleaned ITO coated glass substrates as described above. The photoactive layer solution was prepared under an inert environment. For P3HT:$PC_{61}BM$ photoactive layers, seperate solutions of P3HT and $PC_{61}BM$ in *o*-DCB were stirred at 80 °C for 8 hours then mixed in a 1:1 P3HT:$PC_{61}BM$ ratio forming a combined 46 mg/mL solution. This solution was left to mix at 80 °C for 2 hours before filtering with a 0.45 μm polytetrafluoroethylene (PTFE) filter and spin casting in air directly on top of the eLbL assembled cathodic buffer layer. The spin cast was performed at 600 rpm for 1 minute, forming a ~220 nm thick layer as determined with optical profilometry. Films were immediately transfered to a covered Petri dish and left to dry in air for 20-25 min. For the PBDTTPD:$PC_{71}BM$ photoactive layer, separate solutions of PBDTTPD and $PC_{71}BM$ in *o*-DCB were stirred at 80 °C for 8 hours then mixed in a 1:1.5 PBDTTPD:$PC_{71}BM$ ratio. This formed a 15 mg/mL solution, which was left to stir at 80 °C for 2 hours. A heated spin casting method was used to coat the photoactive layer. The eLbL-modified ITO substrates and the PBDTTPD:$PC_{71}BM$ solution were heated to 90 °C in air, and pipette tips were heated to 80 °C. Immediately before coating, a heated ITO/[P3(TBP)HT:PEDOT:PSS]$_n$ substrate was transferred to the spin-coated chuck. 100 μL of the photoactive layer solution was quickly dispensed and spin-cast at 600 rpm for 1 min in air, forming a ~90 nm thick layer as

determined with optical profilometry. The films were covered with a Petri dish and stored in air and darkness for 18 hours. Afterwhich, a 20 nm V_2O_5 hole transport layer and 80-100 nm aluminum anode were thermally evaporated on all films at ~5 Å s^{-1} under high vacuum (~10^{-4} Pa) defining a device area of 0.155 ± 0.008 cm^2. The PV characteristics of the OPV devices were characterized at 25-30 °C in air under simulated AM1.5 G conditions (xenon source from Oriel 91191 1000W) and calibrated to a certified Si reference cell with a KG-5 filter (PV Measurements, PVM624). *J-V* characteristics were recorded using a computer-controlled Keithley 2400 source meter. Three devices were average for each data point.

Stability Testing:

The P3HT:PC_{61}BM devices were fabricated and periodically tested in air over the course of one year. Between tests, the devices were stored under N_2 at 25 °C. For PBDTTPD:PC_{71}BM devices, stability testing was performed according to ISOS-D-1 (shelf) protocol,[88] whereby unencapsulated devices were stored in air at 25 °C in vials wrapped in Al foil between tests with the above conditions. The average of four devices represents each data point.

3.5 Contributions

B.J. Worfolk planned and executed most experiments. T.C. Hauger assisted with device fabrication and characterization. J.A.M. Fordyce assisted with the synthesis and purification of P3(TBP)HT. PBDTTPD was synthesized by S. Beaupré and M. Leclerc. All authors assisted with analysis and interpretation of data. B.J. Worfolk wrote the manuscript, and all authors edited the manuscript.

3.6 References

[1] R. Steim, F.R. Kogler, C.J. Brabec, *J. Mater. Chem.* **2010**, *20*, 2499.

[2] G. Yu, J. Gao, J.C. Hummelen, F. Wudl, A.J. Heeger, *Science* **1995**, *270*, 1789.

[3] N.S. Sariciftci, L. Smilowitz, A.J. Heeger, F. Wudl, *Science* **1992**, *258*, 1474.

[4] J.J.M. Halls, C.A. Walsh, N.C. Greenham, E.A. Marseglia, R.H. Friend, S.C. Moratti, A.B. Holmes, *Nature* **1995**, *376*, 498.

[5] K.M. Coakley, M.D. McGehee, *Chem. Mater.* **2004**, *16*, 4533.

[6] M. Helgesen, R. Søndergaard, F.C. Krebs, *J. Mater. Chem.* **2010**, *20*, 36.

[7] F.C. Krebs, T. Tromholt, M. Jørgensen, *Nanoscale* **2010**, *2*, 873.

[8] T.D. Nielsen, C. Cruickshank, S. Foged, J. Thorsen, F.C. Krebs, *Sol. Energy Mater. Sol. Cells* **2010**, *94*, 1553.

[9] F.C. Krebs, *Sol. Energy Mater. Sol. Cells* **2009**, *93*, 1636.

[10] Y. Zhu, X. Xu, L. Zhang, J. Chen, Y. Cao, *Sol. Energy Mater. Sol. Cells* **2012**, *97*, 83.

[11] M.-S. Su, C.-Y. Kuo, M.-C. Yuan, U.-S. Jeng, C.-J. Su, K.-H. Wei, *Adv. Mater.* **2011**, *23*, 3315.

[12] C.M. Amb, S. Chen, K.R. Graham, J. Subbiah, C.E. Small, F. So, J.R. Reynolds, *J. Am. Chem. Soc.* **2011**, *133*, 10062.

[13] Y. Liang, Z. Xu, J. Xia, S.-T. Tsai, Y. Wu, G. Li, C. Ray, L. Yu, *Adv. Mater.* **2010**, *22*, E135.

[14] T.-Y. Chu, J. Lu, S. Beaupré, Y. Zhang, J.-R. Pouliot, S. Wakim, J. Zhou, M. Leclerc, Z. Li, J. Ding, Y. Tao, *J. Am. Chem. Soc.* **2011**, *133*, 4250.

[15] M. Jørgensen, K. Norrman, F.C. Krebs, *Sol. Energy Mater. Sol. Cells* **2008**, *92*, 686.

[16] K. Kawano, R. Pacios, D. Poplavskyy, J. Nelson, D. Bradley, J. Durrant, *Sol. Energy Mater. Sol. Cells* **2006**, *90*, 3520.

[17] K. Norrman, S.A. Gevorgyan, F.C. Krebs, *ACS Appl. Mater. Interfaces* **2009**, *1*, 102.

[18] H. Neugebauer, C. Brabec, J.C. Hummelen, N.S. Sariciftci, *Sol. Energy Mater. Sol. Cells* **2000**, *61*, 35.

[19] E. Voroshazi, B. Verreet, T. Aernouts, P. Heremans, *Sol. Energy Mater. Sol. Cells* **2010**, *95*, 1303.

[20] S.K. Hau, H.-L. Yip, N.S. Baek, J. Zou, K. O'Malley, A.K.-Y. Jen, *Appl. Phys. Lett.* **2008**, *92*, 253301.

[21] N. Blouin, A. Michaud, M. Leclerc, *Adv. Mater.* **2007**, *19*, 2295.

[22] N. Blouin, A. Michaud, D. Gendron, S. Wakim, E. Blair, R. Neagu-Plesu, M. Belletête, G. Durocher, Y. Tao, M. Leclerc, *J. Am. Chem. Soc.* **2008**, *130*, 732.

[23] C.H. Peters, I.T. Sachs-Quitana, J.P. Kastrop, S. Beaupré, M. Leclerc, M.D. McGehee, *Adv. Energy Mater.* **2011**, *1*, 491.

[24] Y. Sun, J.H. Seo, C.J. Takacs, J. Seifter, A.J. Heeger, *Adv. Mater.* **2011**, *23*, 1679.

[25] S. Cho, J.H. Seo, S.H. Park, S. Beaupré, M. Leclerc, A.J. Heeger, *Adv. Mater.* **2010**, *22*, 1253.

[26] Y. Sun, C.J. Takacs, S.R. Cowan, J.H. Seo, X. Gong, A. Roy, A.J. Heeger, *Adv. Mater.* **2011**, *23*, 2226.

[27] K. Norrman, N. Larsen, F.C. Krebs, *Sol. Energy Mater. Sol. Cells* **2006**, *90*, 2793.

[28] M.P. de Jong, L.J. van IJzendoorn, M.J.A. de Voigt, *Appl. Phys. Lett.* **2000**, *77*, 2255.

[29] J.W. Jung, J.W. Jo, W.H. Jo, *Adv. Mater.* **2011**, *23*, 1782.

[30] Y. Zhou, H. Cheun, W.J. Potscavage, Jr, C. Fuentes-Hernandez, S.-J. Kim, B. Kippelen, *J. Mater. Chem.* **2010**, *20*, 6189.

[31] J.-H. Huang, H.-Y. Wei, K.-C. Huang, C.-L. Chen, R.-R. Wang, F.-C. Chen, K.-C. Ho, C.-W. Chu, *Energy Environ. Sci.* **2010**, *3*, 654.

[32] C.Y. Jiang, X.W. Sun, D.W. Zhao, A.K.K. Kyaw, Y.N. Li, *Sol. Energy Mater. Sol. Cells* **2010**, *94*, 1618.

[33] C.-Y. Li, T.-C. Wen, T.-H. Lee, T.-F. Guo, J.-C.-A. Huang, Y.-C. Lin, Y.-J. Hsu, *J. Mater. Chem.* **2009**, *19*, 1643.

[34] R. Betancur, M. Maymó, X. Elias, L.T. Vuong, J. Martorell, *Sol. Energy Mater. Sol. Cells* **2011**, *95*, 735.

[35] S. Hau, H.-L. Yip, A.K.-Y. Jen, *Polym. Rev.* **2010**, *50*, 474.

[36] J. Bandara, K. Shankar, C.A. Grimes,, M. Thelakkat, *Thin Solid Films* **2011**, *520*, 582.

[37] Y. Sun, X. Gong, B.B.Y. Hsu, H.-L. Yip, A.K.-Y. Jen, A.J. Heeger, *Appl. Phys. Lett.* **2010**, *97*, 193310.

[38] Y.-J. Cheng, C.-H. Hsieh, Y. He, C.-S. Hsu, Y. Li, *J. Am. Chem. Soc.* **2010**, *132*, 17381.

[39] J.-S. Huang, C.-Y. Chou, C.-F. Lin, *IEEE Electron Device Lett.* **2010**, *31*, 332.

[40] T.-Y. Chu, S.-W. Tsang, J. Zhou, P.G. Verly, J. Lu, S. Beaupré, M. Leclerc, Y. Tao, *Sol. Energy Mater. Sol. Cells* **2011**, *96*, 155.

[41] K. Ariga, J.P. Hill, Q. Ji, *Phys. Chem. Chem. Phys.* **2007**, *9*, 2319.

[42] G. Decher, *Science* **1997**, *277*, 1232.

[43] F. Schreiber, *Prog. Surf. Sci.* **2000**, *65*, 151.

[44] F. Caruso, *Adv. Mater.* **2001**, *13*, 11.

[45] S.A. McClure, B.J. Worfolk, D.A. Rider, R.T. Tucker, J.A.M. Fordyce, M.D. Fleischauer, K.D. Harris, M.J. Brett, J.M. Buriak, *ACS Appl. Mater. Interfaces* **2010**, *2*, 219.

[46] D.A. Rider, B.J. Worfolk, K.D. Harris, A. Lalany, K. Shahbazi, M.D. Fleischauer, M.J. Brett, J.M. Buriak, *Adv. Funct. Mater.* **2010**, *20*, 2404.

[47] P.J. Yoo, K.T. Nam, J. Qi, S.-K. Lee, J. Park, A.M. Belcher, P.T. Hammond, *Nat. Mater.* **2006**, *5*, 234.

[48] A.P.R. Johnston, E.S. Read, F. Caruso, *Nano Lett.* **2005**, *5*, 953.

[49] G. Decher, J.-D. Hong, *Makromol. Chem. Macromol. Symp.* **1991**, *46*, 321.

[50] P. Ho, J. Kim, J. Burroughes, H. Becker, S. Li, T. Brown, F. Cacialli, R. Friend, *Nature* **2000**, *404*, 481.

[51] B.-Y. Yu, W.-C. Lin, W.-B. Wang, S.-I. Iida, S.-Z. Chen, C.-Y. Liu, C.-H. Kuo, S.-H. Lee, W.-L. Kao, G.-J. Yen, Y.-W. You, C.-P. Liu, J.-H. Jou, J.-J. Shyue, *ACS Nano* **2010**, *4*, 833.

[52] D.M. DeLongchamp, M. Kastantin, P.T. Hammond, *Chem. Mater.* **2003**, *15*, 1575.

[53] D. Wakizaka, T. Fushimi, H. Ohkita, S. Ito, *Polymer* **2004**, *45*, 8561.

[54] N. Sakai, G.K. Prasad, Y. Ebina, K. Takada, T. Sasaki, *Chem. Mater.* **2006**, *18*, 3596.

[55] D. DeLongchamp, P.T. Hammond, *Adv. Mater.* **2001**, *13*, 1455.

[56] L.S. Roman, W. Mammo, L.A.A. Pettersson, M.R. Andersson, O. Inganäs, *Adv. Mater.* **1998**, *10*, 774.

[57] H.-H. Liao, L.-M. Chen, Z. Xu, G. Li, Y. Yang, *Appl. Phys. Lett.* **2008**, *92*, 173303.

[58] V. Shrotriya, G. Li, Y. Yao, C.-W. Chu, Y. Yang, *Appl. Phys. Lett.* **2006**, *88*, 073508.

[59] M.S. White, D.C. Olson, S.E. Shaheen, N. Kopidakis, D.S. Ginley, *Appl. Phys. Lett.* **2006**, *89*, 143517.

[60] C. Waldauf, M. Morana, P. Denk, P. Schilinsky, K. Coakley, S.A. Choulis, C.J. Brabec, *Appl. Phys. Lett.* **2006**, *89*, 233517.

[61] R. Steim, S.A. Choulis, P. Schilinsky, C.J. Brabec, *Applied Physics Letters* **2008**, *92*, 93303.

[62] S.K. Hau, H.-L. Yip, O. Acton, N.S. Baek, H. Ma, A.K.-Y. Jen, *J. Mater. Chem.* **2008**, *18*, 5113.

[63] W. Gaynor, J.-Y. Lee, P. Peumans, *ACS Nano* **2010**, *4*, 30.

[64] K. Sun, B. Zhao, V. Murugesan, A. Kumar, K. Zeng, J. Subbiah, W.W.H. Wong, D.J. Jones, J. Ouyang, *J. Mater. Chem.* **2012**, *22*, 24155.

[65] C. He, C. Zhong, H. Wu, R. Yang, W. Yang, F. Huang, G.C. Bazan, Y. Cao, *J. Mater. Chem.* **2010**, *20*, 2617.

[66] C. V. Hoven, A. Garcia, G.C. Bazan, T.-Q. Nguyen, *Adv. Mater.* **2008**, *20*, 3793.

[67] J.H. Seo, A. Gutacker, Y. Sun, H. Wu, F. Huang, Y. Cao, U. Scherf, A.J. Heeger, G.C. Bazan, *J. Am. Chem. Soc.* **2011**, *133*, 8416.

[68] T. V. Pho, H. Kim, J.H. Seo, A.J. Heeger, F. Wudl, *Adv. Funct. Mater.* **2011**, *21*, 4338.

[69] H. Kang, S. Hong, J. Lee, K. Lee, *Adv. Mater.* **2012**, *24*, 3005.

[70] T. Shi, X. Zhu, D. Yang, Y. Xie, J. Zhang, G. Tu, *Appl. Phys. Lett.* **2012**, *101*, 161602.

[71] Y.-M. Chang, R. Zhu, E. Richard, C.-C. Chen, G. Li, Y. Yang, *Adv. Funct. Mater.* **2012**, *22*, 3284.

[72] Z. Tang, L.M. Andersson, Z. George, K. Vandewal, K. Tvingstedt, P. Heriksson, R. Kroon, M.R. Andersson, O. Inganäs, *Adv. Mater.* **2012**, *24*, 554.

[73] Z. He, C. Zhong, S. Su, M. Xu, H. Wu, Y. Cao, *Nat. Photonics* **2012**, *6*, 593.

[74] Y. Zhou, C. Fuentes-Hernandez, J. Shim, J. Meyer, A.J. Giordano, H. Li, P. Winget, T. Papadopoulos, H. Cheun, J. Kim, M. Fenoll, A. Dindar, W. Haske, E. Najafabadi, T.M. Khan, H. Sojoudi, S. Barlow, S. Graham, J.-L. Brédas, S.R. Marder, A. Kahn, B. Kippelen, *Science* **2012**, *336*, 327.

[75] B.J. Worfolk, T.C. Hauger, K.D. Harris, D.A. Rider, J.A.M. Fordyce, S. Beaupré, M. Leclerc, J.M. Buriak, *Adv. Energy Mater.* **2012**, *2*, 361.

[76] K.-P. Kim, A.M. Hussain, D.-K. Hwang, S.-H. Woo, H.-K. Lyu, S.-H. Baek, Y. Jang, J.-H. Kim, *Jpn. J. Appl. Phys.* **2009**, *48*, 021601.

[77] L.S.C. Pingree, B.A. MacLeod, D.S. Ginger, *J. Phys. Chem. C* **2008**, *112*, 7922.

[78] H. Ma, M.S. Liu, A.K.-Y. Jen, *Polym. Int.* **2009**, *58*, 594.

[79] H. Ma, H.-L. Yip, F. Huang, A.K.-Y. Jen, *Adv. Funct. Mater.* **2010**, *20*, 1371.

[80] K. Sugiyama, H. Ishii, Y. Ouchi, K. Seki, *J. Appl. Phys.* **2000**, *87*, 295.

[81] L.S. Li, R. Wang, M. Fitzsimmons, D. Li, *J. Phys. Chem. B* **2000**, *104*, 11195.

[82] Q. Chen, B.J. Worfolk, C. Hauger, Tate, U. Al-Atar, K.D. Harris, J.M. Buriak, *ACS Appl. Mater. Interfaces* **2011**, *3*, 3962.

[83] M. Carrara, J.J. Kakkassery, J.-P. Abid, D.J. Fermín, *ChemPhysChem* **2004**, *5*, 571.

[84] Y. Zou, A. Najari, P. Berrouard, S. Beaupré, B.R. Aich, Y. Tao, M. Leclerc, *J. Am. Chem. Soc.* **2010**, *132*, 5330.

[85] Y. Zhang, S.K. Hau, H.-L. Yip, Y. Sun, O. Acton, A.K.-Y. Jen, *Chem. Mater.* **2010**, *22*, 2696.

[86] C. Piliego, T.W. Holcombe, J.D. Douglas, C.H. Woo, P.M. Beaujuge, J.M.J. Fréchet, *J. Am. Chem. Soc.* **2010**, *132*, 7595.

[87] A. Najari, S. Beaupré, P. Berrouard, Y. Zou, J.-R. Pouliot, C. Lepage-Pérusse, M. Leclerc, *Adv. Funct. Mater.* **2011**, *21*, 718.

[88] F.C. Reese, M.O.; Gevorgyan, S.A.; Jørgensen, M.; Bundgaard, E.; Kurtz, S.R.; Ginley, D.S.; Olsen, D.C.; Lloyd, M.T.; Morvillo, P.; Katz, E.A.; Elschner, A.; Haillant, O.; Currier, T.R.; Shrotriya, V.; Hermenau, M.; Riede, M.; Kirov, K.R.; Trimmel, G.; Rath, T, *Sol. Energy Mater. Sol. Cells* **2011**, *95*, 1253.

[89] C. Brabec, V. Dyakonov, U. Scherf, *Organic Photovoltaics: Materials, Device Physics, and Manufacturing Technologies*, Wiley-VCH Verlag GmbH & Co., Weinheim, Germany **2008**.

[90] J. Lewis, *Mater. Today* **2006**, *9*, 38.

[91] R. Tipnis, J. Bernkopf, S. Jia, J. Krieg, S. Li, M. Storch, D. Laird, *Sol. Energy Mater. Sol. Cells* **2009**, *93*, 442.

[92] G. Dennler, C. Lungenschmied, H. Neugebauer, N. Sariciftci, M. Latreche, G. Czeremuszkin, M. Wertheimer, *Thin Solid Films* **2006**, *511-512*, 349.

[93] C. Lungenschmied, G. Dennler, H. Neugebauer, S.N. Sariciftci, M. Glatthaar, T. Meyer, A. Meyer, *Sol. Energy Mater. Sol. Cells* **2007**, *91*, 379.

[94] K.W. Wong, H.L. Yip, Y. Luo, K.Y. Wong, W.M. Lau, K.H. Low, H.F. Chow, Z.Q. Gao, W.L. Yeung, C.C. Chang, *Appl. Phys. Lett.* **2002**, *80*, 2788.

[95] Y. Kim, S. Lee, J. Noh, S. Han, *Thin Solid Films* **2006**, *510*, 305.

4

Flexible Bulk Heterojunction Organic Photovoltaics Based on Carboxylated Polythiophenes and PCBM

4.1 Introduction

4.1.1 Overview

Upon successful fabrication of a transparent electrode (as outlined in Chapter 2), and the interfacial buffer layer (discussed in Chapter 3), the subsequent layer in typical organic photovoltaics (OPVs) is the photoactive layer (introduced in Chapter 1). This chapter focuses on the introduction of regioregular poly[3-(carboxyalkyl)thiophene-2,5-diyl] (P3CAT) p-type semiconductors with different carboxyalkyl chain lengths (propylene to hexylene). Each P3CAT was combined with [6,6]-phenyl-C_{61}-butyric acid methyl ester ($PC_{61}BM$) to form the photoactive bulk heterojunction layer for OPV devices. The extent of hydrogen bonding, blend morphology, and mechanical properties of the films were characterized. These measurements suggest that P3CATs are suitable for use in flexible devices. Power conversion efficiencies of up to 2.6% and 1.6% were obtained for devices fabricated in air, and supported on glass and flexible poly(ethylene terephthalate) substrates, respectively.

The following subsections will introduce the photoactive layer, strategies for controlling the morphology of the photoactive layer, the use of hydrogen bonding in the photoactive layer, and an overview of carboxylated polythiophenes.

Chapter 4 was reproduced in part with permission from:

a) B.J. Worfolk, D.A. Rider, A.L. Elias, M. Thomas, K.D. Harris, J.M. Buriak, *Adv. Funct. Mater.* **2011**, *21*, 1816-1826. Copyright © 2011 Wiley-VCH Verlag GmbH & Co.

b) B.J. Worfolk, W. Li, P. Li, T.C. Hauger, K.D. Harris, J.M. Buriak, *J. Mater. Chem.* **2012**, *22*, 11354-11363. Copyright © 2012 The Royal Society of Chemistry.

4.1.2 Photoactive Layer

The photoactive layer of excitonic OPVs typically consists of a mixture of a light-absorbing, electron-donating semiconducting polymer, such as a regioregular poly[3-(alkyl)thiophene] (P3AT), and an electron-accepting fullerene, commonly [6,6]-phenyl-C_{61}-butyric acid methyl ester (PCBM).[1–9] This donor-acceptor mixture is most often employed in a phase-separated and disordered bicontinuous interpenetrating network known as the bulk heterojunction (BHJ), and the arrangement has been intensely studied and optimized in recent years for the efficient generation and extraction of charges.[8, 10–16]

The photoactive layer is responsible for the absorption of photons creating bound excitons, dissociation of the excitons, and transport of charges to the interfacial buffer layers.[17] The absorption of photons depends on the optoelectronic properties of the blend film. The absorption of the photoactive layer should overlap the solar

emission spectrum. Both the dissociation of excitons and transport of charges to the interfacial buffer layers are controlled by both the physical properties of the semiconducting materials as well as the film morphology. Investigating strategies to control the morphology in bulk heterojunction films has been identified as a key factor to improve the photovoltaic performance and stability of OPVs.[17]

4.1.3 Morphological Control of the Photoactive Layer

The morphology of the BHJ photoactive layer affects exciton dissociation and charge transport of holes and electrons in the donor and acceptor, respectively. The exciton diffusion length of conjugated polymers is typically 4-20 nm.[18] If an exciton does not reach a donor/acceptor interface within this distance, the exciton will recombine leading to a reduction in the extracted charges in the device. The recombination can be limited if there is a large interfacial surface area between donor and acceptor components. Upon exciton dissociation, the next challenge is efficient transport of charges within the BHJ. The photoactive layer should consist of a bicontinuous network of donor and acceptor components allowing transport of electrons and holes to the interfacial buffer layers.[19] Thus requirements for an ideal bulk heterojunction include a high donor/acceptor interfacial surface area and bicontinuous networks of both components.

There are many ways to control to morphology of the BHJ layer both synthetically and with post-processing of deposited films. Key strategies include solvent and/or thermal annealing, surface energy control in the interfacial buffer layer and photocrosslinkable polymers.

Post-processing of the BHJ layer typically consists of solvent and/or thermal annealing.[13] Solvent annealing involves extending the drying time of as-cast films by sealing them in Petri dishes. This reduces the solvent evaporation rate, which allows ordering of polymer domains, resulting in a larger polymer crystallite size.[20] Thermal annealing at 150 °C increases the polymer crystallite size as seen in Figure 4.1, and improves contact with the cathode.[10] This leads to higher short-circuit current densities (J_{SC}) and fill factors (FF). These increase the power conversion efficiency (PCE) of devices from 0.82% to 3.2%.[10] Careful tuning of both solvent and thermal annealing are critical in optimizing the morphology of the BHJ, and improving the PCE of photovoltaic devices.

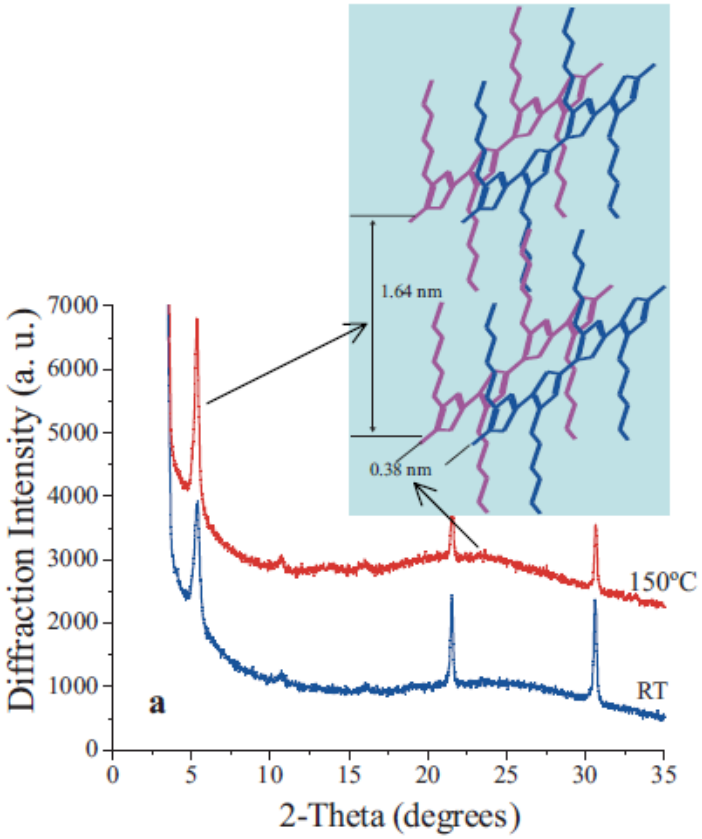

Figure 4.1 The X-ray diffraction spectra of a P3HT:PCBM film drop-cast on a PEDOT:PSS/ITO substrate with and without annealing at 150 °C for 30 minutes. The inset shows the P3HT crystal structure with the d = 1.64 nm (100) interdigitation of alkyl side chains and d = 0.38 nm (010) π-π stacking of the thiophene backbone. Reprinted with permission from reference [10]. Copyright © 2005 Wiley-VCH Verlag GmbH & Co.

The surface energy of substrates has considerable influence over concentration gradients in BHJ photoactive layers and hence influences the OPV device performance.[21, 22] Because P3HT has a lower surface energy than PCBM, when hydrophilic PEDOT:PSS is used as the hole transport layer (HTL), P3HT tends to accumulate near the air/BHJ interface while PCBM accumulates closer to the hydrophilic PEDOT:PSS HTLs.[21] This surface-induced concentration of PCBM near the anode is detrimental to forward mode OPV operation as a more uniform distribution of P3HT and PCBM (or, possibly even more advantageous, a greater P3HT content near the anode) would be preferred to reduce recombination.[21,22]

Gradient formation occurs during the solvent evaporation step following spin-coating. Decreasing the surface energy of the anode tends to reduce the magnitude of concentration gradients. For example, a thin lower surface energy film of poly[3-(5-carboxypentyl) thiophene-2,5-diyl] (P3CPenT), can be used in place of PEDOT:PSS, which led to a homogeneous distribution of P3HT and PCBM throughout the film.[23] This improved morphology leads to improved FF and PCE over conventional PEDOT:PSS HTLs.

Control of the BHJ morphology through post-processing techniques and tuning the interfacial surface energy of the HTL can lead to optimum performance. Most BHJ systems have poor stability, and this peak photovoltaic performance is not maintained. Donor and acceptor components often continue to migrate leading to macrophase segregation.[24] A potential strategy to circumvent this is to photocrosslink the polymer domains to stabilize the nanoscale BHJ morphology. Light sensitive bromoalkyl side chains can be introduced into semiconducting polymers which photocrosslink upon exposure to ultraviolet light. Devices with photocrosslinked polymers maintain their photovoltaic performance with annealing at 150 °C for 70 h, while non-photocrosslinked polymers see a reduction in PCE.[24] Controlling the morphology of BHJ photoactive layers can improve exciton dissociation, facilitate efficient charge transport, and increase the stability of organic photovoltaics.

4.1.4 Hydrogen Bonding in the Photoactive Layer

Another way to control the morphology of BHJ films is to incorporate hydrogen bonding moieties in the photoactive layer components. With careful control over the

blend morphology, the photovoltaic performance can be improved.[25–29] It has been proposed that hydrogen bonding encourages greater molecular level ordering, increases molecular rigidity, promotes interfacial electron transfer, reduces charge trap sites and extends device lifetime.[25, 27, 30–34] For example, Watkins and coworkers investigated the cooperative hydrogen bonding between a semiconducting diblock copolythiophene: poly(3-hexylthiophene)-block-poly[3-(2,5,8,11-tetraoxadodecane)thiophene] (P3HTb-P3TODT) with bis-[6, 6]-phenyl C_{61}-butyric acid (bis-PCBA) as seen in Figure 4.2.[35] Favourable self-assembly between components stabilizes the morphology of the photoactive layer leading to improved photovoltaic performance with ageing experiments.[35] It is therefore a fruitful approach to investigate the effect of hydrogen bonding in the photoactive layer of BHJ OPVs.

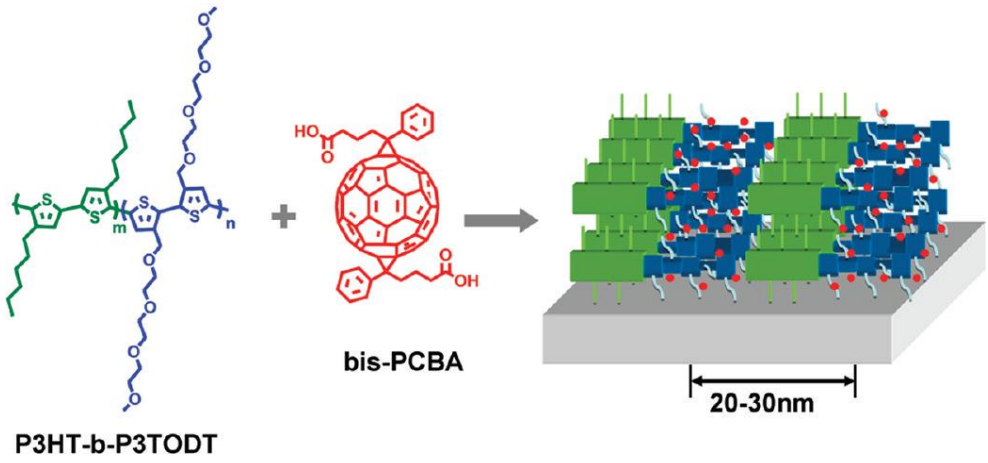

Figure 4.2 Chemical structures of P3HT-b-P3TODT and bis-PCBA and schematic of the ordered, photoactive layer blend. Reprinted with permission from reference [35]. Copyright © 2012 American Chemical Society.

4.1.5 Carboxylated Polythiophenes

The side chains of polythiophenes are important for the formation of crystallites and influence the solubility of the polymer. Polythiophenes with alkyl side chains,

such as P3HT, are soluble in chlorinated solvents such as chloroform and dichlorobenzene. Adding a carboxylic acid to the end of an alkyl side chain alters the physical properties, where the carboxylated polythiophene will now be soluble in solvents such as pyridine and dimethyl sulfoxide. These solvents are an improvement compared to the chlorinated analogues when solution processing is conducted on a large scale. The carboxylic acid also introduces additional chemical functionality, which could be used to control the morphology of films through hydrogen bonding.

The synthesis of carboxylated polythiophenes involves a CuO-modifed Stille coupling as seen in Figure 4.3.[36–38] The carboxylic acid is masked by an oxazoline, which can be hydrolyzed to give carboxylated polythiophenes.[36] Subsequent deprotonation with a base yields a water-soluble derivative which can be used as a chemoselective ionchromatic sensor in water.[36]

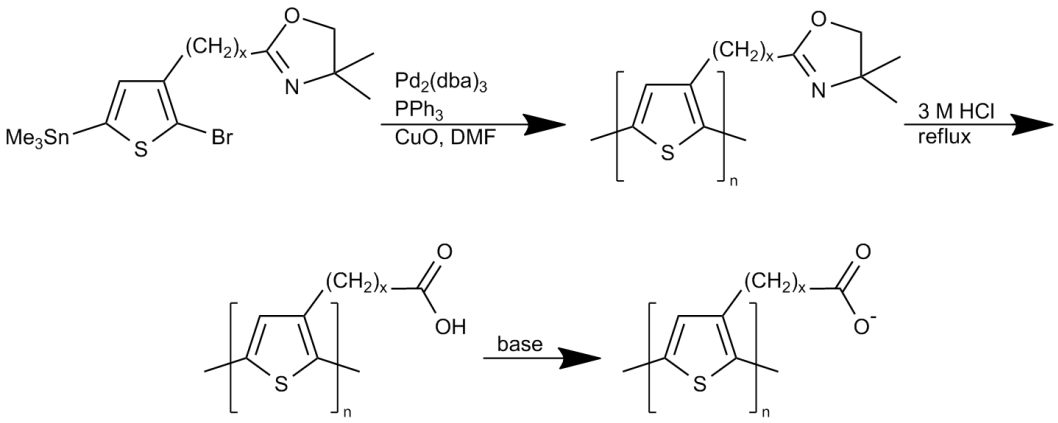

Figure 4.3 The synthesis of carboxylated polythiophenes, where x = alkyl chain length.[36]

Carboxylated polythiophenes or poly[3-(carboxyalkyl)thiophene-2,5-diyl] (P3CAT) have recently been used in dye-sensitized solar cells where the free carboxylic acid served as an anchoring group to TiO_2.[39–46] The suitable optical and electronic properties, and the potential for hydrogen bonding and further

derivatization of the P3CAT series has been recognized, and has led to other applications in chemical[36, 37, 47, 48] and biological sensors,[49] field-effect transistors[38] and single-walled carbon nanotube/polymer nanohybrids.[50]

In an effort to establish poly[3-(carboxyalkyl)thiophene-2,5-diyl]s (P3CATs) as suitable donor materials for BHJ OPVs, we investigated the polymer series containing carboxyalkyl side chains [-$(CH_2)_x$COOH; for x ranging from 3 to 6]. The series includes poly[3-(3-carboxypropyl)thiophene-2,5-diyl] (P3CProT), poly[3-(4-carboxybutyl)thiophene-2,5-diyl] (P3CButT), poly[3-(5-carboxypentyl)thiophene-2,5-diyl] (P3CPenT) and poly[3-(6-carboxyhexyl)thiophene-2,5-diyl] (P3CHexT).

4.2 Results and Discussion

We report the optoelectronic and mechanical properties of this carboxyl-functionalized polythiophene series. Despite numerous statements of mechanical flexibility as a driving factor in OPV research,[51–57] measurement of OPV mechanical properties is uncommon in the literature,[53] and thus we devote attention to this aspect of characterization. P3CAT:PCBM films are incorporated into BHJ OPVs with a device architecture of ITO/PEDOT:PSS/P3CAT:PCBM/Al on both borosilicate glass and flexible poly(ethylene terephthalate) (PET) substrates (Figure 4.4).

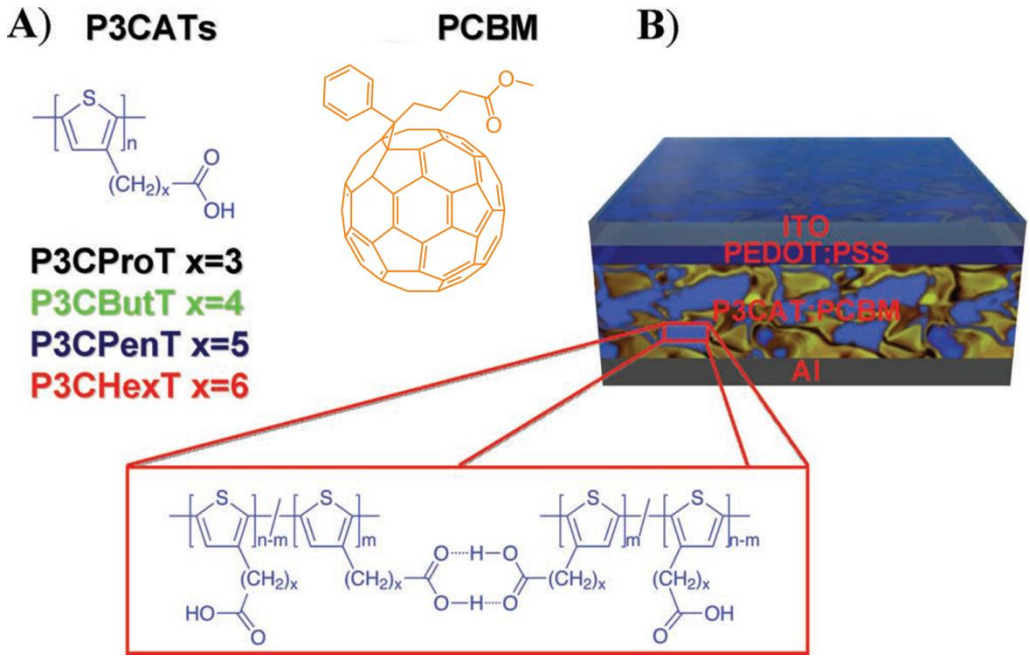

Figure 4.4 A) The chemical structures of P3CATs with carboxyalkyl chain lengths, x , ranging from 3–6 as well as PCBM. B) A schematic representation of the OPV device architecture consisting of: ITO/PEDOT:PSS/P3CAT:PCBM/Al and the depiction of the hydrogen bonding in P3CATs. Reprinted with permission from reference [58]. Copyright © 2011 Wiley-VCH Verlag GmbH & Co.

4.2.1 Optoelectronic Properties of Carboxylated Polythiophenes

To determine and contrast the behaviour of regioregular P3CATs in the context of OPVs, the optoelectronic properties were studied. The P3CAT derivatives were found to be highly soluble in pyridine and appeared orange to red in colour. Solution-phase absorbance and photoluminescence (PL) spectra for the P3CATs dissolved in pyridine are shown in Figure 4.5A. The wavelengths of maximum absorption, $\lambda_{max\text{-}abs}$, red-shift slightly (from 430 nm to 457 nm) as the carboxyalkyl chain length [-$(CH_2)_x$COOH] increases from propylene to hexylene (x = 3-6), while the wavelengths of maximum photoluminescence, $\lambda_{max\text{-}PL}$, in the solution fluorescence spectra are approximately the same for all P3CATs. The $\lambda_{max\text{-}PL}$ of the spectra are in close agreement with the wavelength corresponding to the onset of absorption for

the polymers. The P3CAT pyridine solutions were spin-cast on quartz substrates, and the solid-state absorbance spectra from the resulting films are shown in Figure 4.5B. The optical bandgaps of the P3CATs in the solid state were calculated from the absorbance onsets and were similar across the series (Table 4.1). The bandgap invariance around ~1.9 eV with increasing carboxyalkyl chain length is similar to the alkyl-substituted P3AT series.[7, 59, 60]

The absorbance and photoluminescence spectra for the P3CATs consist of broad peaks. The peak broadening is the result of the Franck-Condon principle. The absorption or emission of light is the result of an electronic transition between the ground (E_0) and excited (E_1) states of the polymer. Each electronic level has a number of vibrational states associated with it. The probability of an electronic transition is dependent on the optimal overlap of vibrational wavefunctions (since electronic transitions are much quicker). If the polymer is in the vibrational level, $\nu = 0$ of the electronic ground state, a number of electronic transitions are possible: $\nu = 0 \rightarrow 0$, $0 \rightarrow 1$, $0 \rightarrow 2$, $0 \rightarrow 3$, $0 \rightarrow 4$, $0 \rightarrow 5$, etc. The energy related with each transition is different. Since there are a number of vibrational states associated with each electronic level, a large number of transitions are possible, leading to peak broadening in both absorbance and photoluminescence spectra as seen in Figure 4.5.

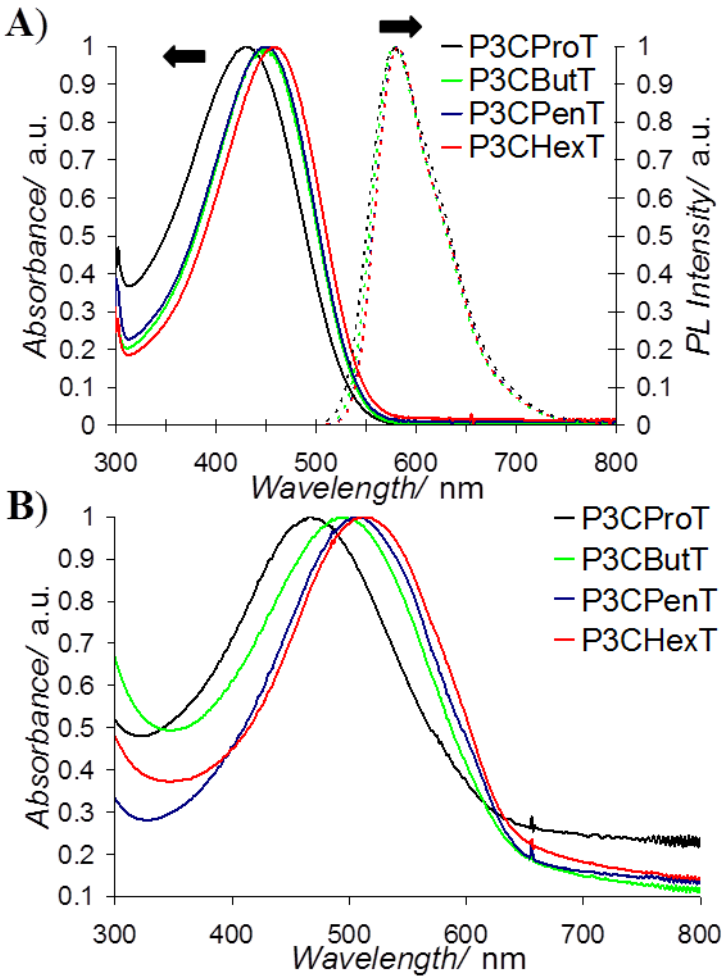

Figure 4.5 A) Normalized solution UV–vis absorbance and photoluminescence of P3CATs in pyridine. B) Normalized solid-state UV–vis spectra of P3CATs cast from pyridine on quartz substrates. Reprinted with permission from reference [58]. Copyright © 2011 Wiley-VCH Verlag GmbH & Co.

The energies of the highest occupied molecular orbital (HOMO) and lowest unoccupied molecular orbital (LUMO) of the P3CAT series were determined using cyclic voltammetry (CV) and from solid-state absorbance spectra. Cyclic voltammetry was performed in a standard three electrode electrochemical cell with a Ag/Ag^+ reference electrode in acetonitrile. Films of P3CATs were cast from pyridine directly onto a Pt disc working electrode. The onset of oxidation for the P3CATs ranged

from 0.27 to 0.34 V, corresponding to HOMO energies ranging from -5.19 to -5.12 eV.[7, 60] The corresponding LUMO energies for the P3CAT series were calculated by adding the measured optical bandgap energy to the CV-determined HOMO energy. The results are reported in Table 4.1.

Table 4.1 A summary of oxidation potentials from the cyclic voltammetry scans of the P3CATs, and associated calculation of the energies of the HOMO and LUMO bands and the optical bandgap. Reprinted with permission from reference [58]. Copyright © 2011 Wiley-VCH Verlag GmbH & Co.

P3CAT	E_{ox} [V] [i]	E_{HOMO} [eV] [ii]	E_{LUMO} [eV] [iii]	E_g [eV] [iv]
P3CProT	0.27	-5.12	-3.08	2.04
P3CButT	0.34	-5.19	-3.25	1.94
P3CPenT	0.28	-5.13	-3.20	1.93
P3CHexT	0.31	-5.16	-3.23	1.93

[i] The onset of oxidation from the cyclic voltammetry scans versus Ag/Ag^+ reference electrode.
[ii] The energy of the HOMO band calculated from the potential of the onset of oxidation, calibrated to a ferrocene redox couple and corrected to vacuum.
[iii] The energy of the LUMO band calculated by addition of the optical bandgap to the E_{HOMO}.
[iv] Calculated from the onset of absorption from P3CAT films.

Figure 4.6 depicts the band energies of the P3CATs, PCBM, poly(3,4-ethylenedioxythiophene):poly(*p*-styrenesulfonate) (PEDOT:PSS) and ITO and Al electrodes. All donor P3CATs form type-II heterojunctions with PCBM, and have appropriate band edge offsets (acceptor LUMO - donor HOMO) and exciton dissociation energies for use in OPVs.[61–64] It is interesting to note that the HOMO energies of the P3CATs are lower in energy compared to P3HT (-4.8 eV), which suggests that a higher V_{oc} for P3CAT:PCBM BHJs may be possible.[65]

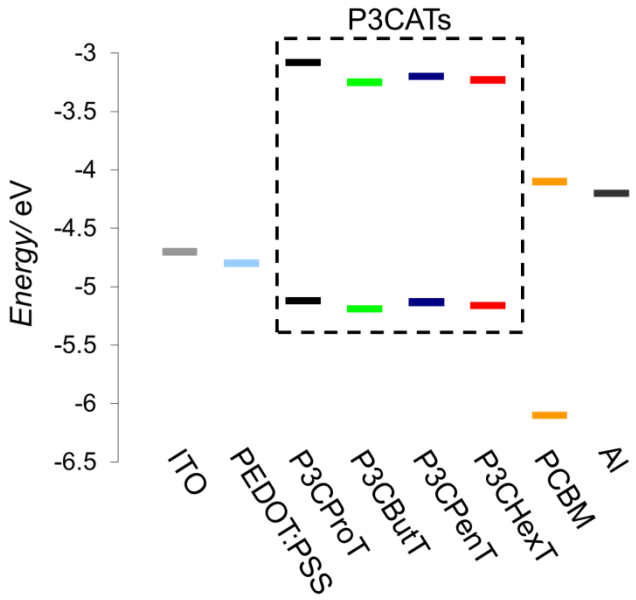

Figure 4.6 Energy level diagram of components used in OPV devices including P3CATs, PCBM, hole-transporting PEDOT:PSS, ITO and Al electrodes. Reprinted with permission from reference [58]. Copyright © 2011 Wiley-VCH Verlag GmbH & Co.

4.2.2 Properties of Bulk Heterojunction Films

To probe the charge transfer between the polythiophene donor and fullerene acceptor in thin films, photoluminescence (PL) spectroscopy was performed. Thin films of P3CAT-only and P3CAT:PCBM were cast from optimized solvent compositions onto quartz substrates and excited at 442 nm with a He-Cd laser. Figure 4.7 shows PL spectra of the films. Quenching of the P3CAT PL signal was visible in all cases, with P3CHexT:PCBM films undergoing near complete quenching. This behaviour is strong evidence for efficient charge transfer from the photoexcited P3CATs to PCBM.[66–69] Since all P3CAT films are highly quenched in the presence of PCBM, donor-acceptor charge transfer is not likely to limit device performance.

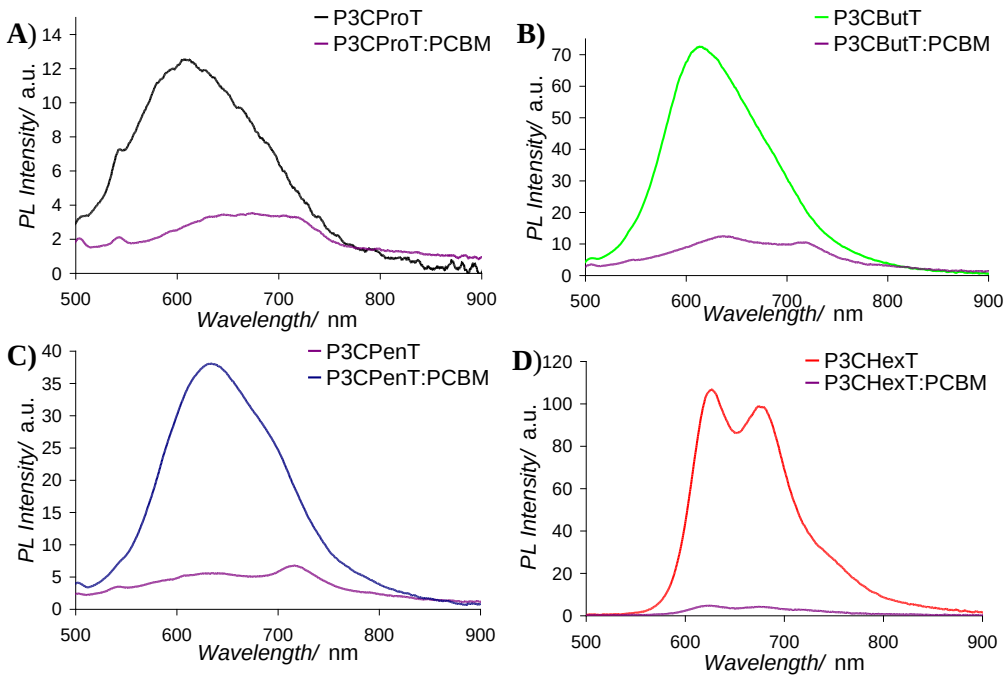

Figure 4.7 Photoluminescence spectra of P3CAT thin films and BHJ films (1:1 by weight) with PCBM spin-cast on quartz substrates, excited at 442 nm. Reprinted with permission from reference [58]. Copyright © 2011 Wiley-VCH Verlag GmbH & Co.

To cater to the solubility requirements of both components, a mixed solvent system was selected. P3CATs are soluble in pyridine, dimethylformamide (DMF) and dimethyl sulfoxide (DMSO),[37, 38] and sparingly soluble in chlorobenzene and dichlorobenzene. Conversely, PCBM is highly soluble in chlorobenzene and dichlorobenzene and only marginally soluble in pyridine, dimethylformamide and dimethyl sulfoxide. Pyridine and chlorobenzene were selected as co-solvents for P3CAT:PCBM mixtures as their boiling points (115 °C and 130 °C, respectively) and enthalpies of vaporization (40.2 kJ/mol and 41.0 kJ/mol, respectively) are similar and are consequently volatilized at similar rates during casting procedures.[70, 71] Initial solubility experiments revealed that PCBM precipitates in mixtures with high pyridine content, which therefore limits the solvent composition to include no more than 25% v/v pyridine. Characterization of P3CAT:PCBM solutions or cast films

was always performed using solvent ratios empirically determined to produce the optimum power conversion efficiency in completed OPV devices (*vide infra*). For the distinct P3CAT:PCBM combinations, the optimum solvent ratios were identified as 1:7, 1:8, 1:6 and 1:7 pyridine:chlorobenzene for alkyl chain lengths x = 3, 4, 5 and 6, respectively.

The extent of hydrogen bonding in P3CATs, in both solid and solution phases, can be assessed with infrared (IR) spectroscopy.[29, 37, 47, 72, 73] The polymers were cast from the optimized solvent compositions onto KBr discs, and the carbonyl regions of the IR spectra are shown in Figure 4.8. The carbonyl regions for all spectra consist of two peaks corresponding to free C=O stretches at higher energy (~1733 cm^{-1}) and hydrogen bonded C=O vibrations at lower energy (~1700 cm^{-1}).[73] All P3CATs have significant hydrogen bonded C=O vibrational modes, pointing to interchain cross-linking of the polymers. The hydrogen bonded C=O peaks for P3CButT and P3CHexT are shifted to higher energy compared to P3CProT and P3CPenT by approximately 14 cm^{-1}, indicating weaker hydrogen bonding interactions in the carboxyalkyl chains of these polymers.[74] The extent of hydrogen bonding can be assessed from the relative peak areas of the free and hydrogen bonded C=O vibrational modes. By this analysis, P3CPenT has a significantly larger degree of hydrogen bonding, while P3CProT exhibits the least hydrogen bonded molecular interactions. It is important to note that the IR spectra of BHJ films were further complicated by an overlap of the hydrogen bonded C=O stretch with the ester stretch in PCBM (~1736 cm^{-1}) and prevented complete quantification of the extent of hydrogen bonding in these BHJ films.

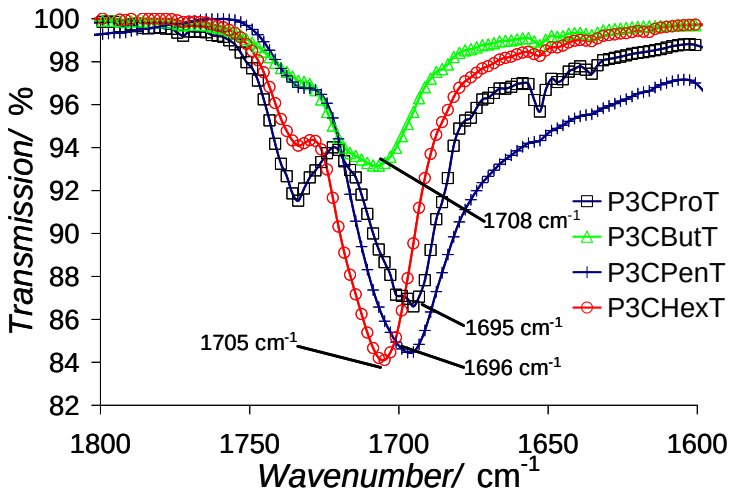

Figure 4.8 The IR spectra of P3CAT films cast from their optimized solvent compositions on a KBr disc. Reprinted with permission from reference [58]. Copyright © 2011 Wiley-VCH Verlag GmbH & Co.

To better understand the structure and morphology of P3CATs in BHJ films, glancing angle X-ray diffraction (XRD) analysis was performed on P3CAT:PCBM samples cast on silicon wafers using the optimized casting conditions. Figure 4.9A shows the XRD spectra of the four P3CAT:PCBM films, offset for clarity. A distinct peak corresponding to the interdigitation of the carboxyalkyl chains (100) was evident for all films, and as expected, this peak shifted to higher d-spacings with increasing alkyl chain length as previously observed with P3ATs.[75] For P3CProT, P3CButT, P3CPenT and P3CHexT, the d-spacings were 12.1 Å, 14.1 Å, 16.8 Å and 19.0 Å respectively, and this trend is summarized in Figure 4.9B. This figure also includes the (100) d-spacings previously reported for alkyl chain lengths of 2 and 7.[37, 38] An obvious linear relationship exists between (100) d-spacing and carboxyalkyl chain length. The (200) peak was also present in all spectra, and the corresponding d-spacing also increased with lengthening of the carboxyalkyl chain. Other characteristic peaks were detected in the XRD spectra at $2\theta = 19.7^{o}$ which

correspond to d-spacings of 4.5 Å in all films. This peak has been previously observed, and represents dense stacking of PCBM molecules normal to the film plane.[76, 77] It is interesting to note that the intensity of this $2\theta = 19.7^{o}$ peak is significantly stronger in P3CProT and P3CButT samples, suggesting a greater degree of complex molecular arrangement of PCBM in these BHJ films. Similarly, an additional PCBM peak was observed in the P3CProT:PCBM and P3CButT:PCBM spectra at $2\theta = 10.2^{o}$ (indicating a d-spacing of 8.7 Å), which also corresponds to the packing of PCBM molecules.[76] The size of polymer crystallites can be calculated from the Scherrer equation for the (100) diffraction peaks.[78, 79] Using this equation, the crystallite sizes for P3CProT, P3CButT, P3CPenT and P3CHexT BHJ films were determined to be 4.2 nm, 4.7 nm, 9.2 nm and 4.0 nm respectively. In the P3CPenT:PCBM BHJ films, the polymer P3CAT crystallite size is approximately double that of the other polymers.

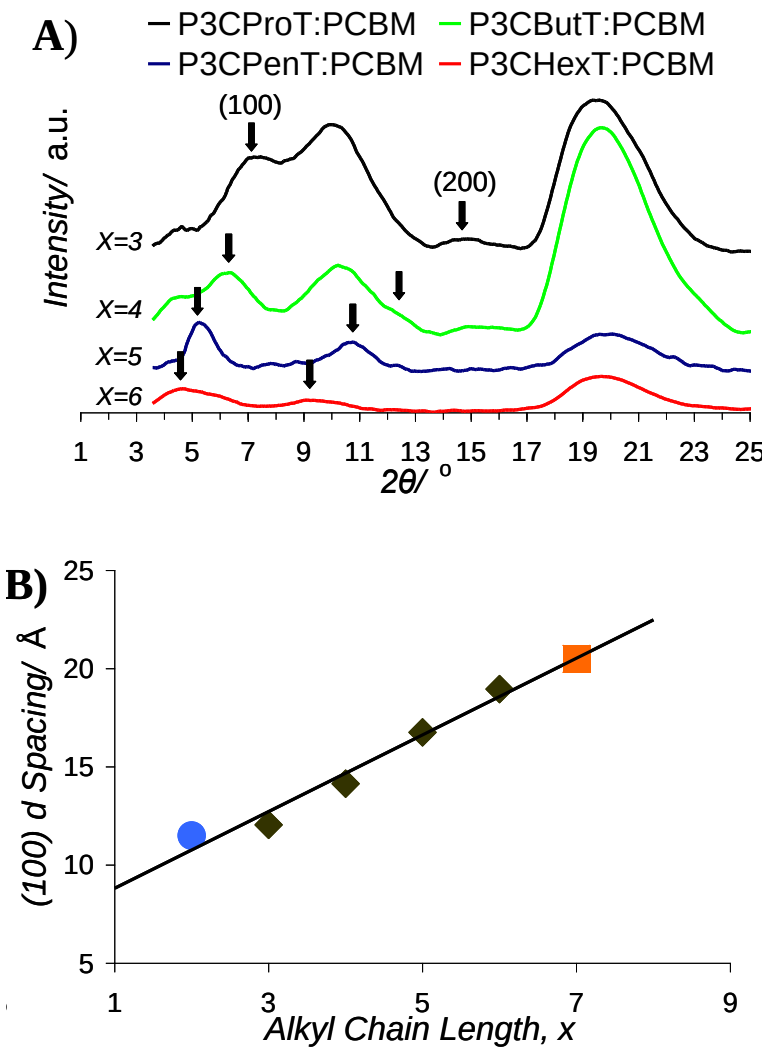

Figure 4.9 A) XRD spectra of P3CAT:PCBM BHJ films spin-cast on Si substrates. B) The d-spacing of the (100) crystal plane of the P3CATs with increasing carboxyalkyl chain length. The circle ($x = 2$) was reported by Bao and Lovinger[38] while the square ($x = 7$) was reported by Ewbank et al .[37] Reprinted with permission from reference [58]. Copyright © 2011 Wiley-VCH Verlag GmbH & Co.

The charge carrier mobility of holes in the P3CAT-only films was investigated by fabricating "hole-only" devices and fitting the current density – voltage (*J-V*) characteristics to a space charge limited current (SCLC) model. Anodes and donor layers were fabricated (*vide supra*), followed by the addition of 80 nm aluminum as a

top contact. *J-V* curves were measured under dark conditions. The SCLC is commonly modelled using the field-corrected Mott-Gurney equation:

$$J = \frac{9}{8}\varepsilon_r\varepsilon_0\mu_{h0}e^{0.89\gamma\sqrt{E}}\frac{V^2}{L^3} \quad (4.1)$$

where J is the current density, ε_r is the dielectric constant of the polymer, ε_0 is the permittivity of free space, μ_{h0} is the zero-field mobility, γ is the electric field activation factor, E is the electric field, V is the voltage drop across the device and L is the film thickness.[80–85] We assume a dielectric constant of 3, as values near this are commonly measured for conjugated polymers.[83] The experimental *J-V* data is fit using μ_{h0} and γ as fitting parameters. The experimentally-determined *J-V* data and the associated curve fits for the P3CAT devices are presented in Figure 4.10. The calculated mobilities of the P3CAT films range from $7.5\text{x}10^{-5}$ cm^2 /(V s) to $3.9\text{x}10^{-4}$ cm^2 /(V s) and are shown in Table 4.2. The hole mobility of P3CPenT was higher than that of the other polymers. The increased hole mobility for P3CPenT is likely the result of larger crystallites as evidenced by XRD.[86] These mobility values were similar to those reported by Bao and Lovinger for DMSO- and DMF-cast P3CAT films with a carboxyalkyl chain length of $x = 2$ [$8.0\text{x}10^{-5}$ and $2.9\text{x}10^{-4}$ cm^2/(V s), respectively].[38] The results of the hole mobility study suggest that the P3CPenT:PCBM BHJ may be the optimal system for this family of polymers in OPVs.

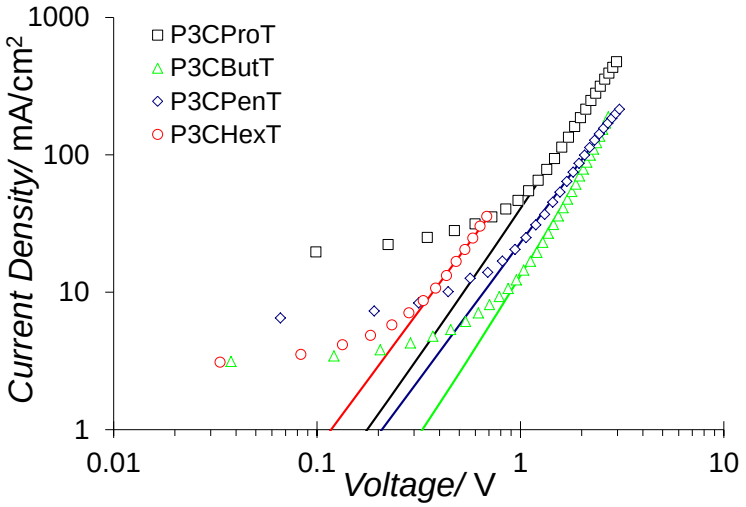

Figure 4.10 The measured (points) and modelled (lines) dark *J–V* curves for hole-only P3CAT devices. Data for P3CProT is shown in black using squares to mark measured points, data for P3CButT is shown in green with triangles denoting measured points, data for P3CPenT is shown in blue with diamonds marking measured points, and data for P3CHexT is shown in red with circles marking measured data points. Reprinted with permission from reference [58].

Table 4.2 Summary of PV characteristics of the BHJ OPVs including zero-field hole mobility (μ_{h0}) and averages [i] and standard deviations of the short circuit current density (J_{sc}), open circuit potential (V_{oc}), fill factor (*FF*) and power conversion efficiency (η) fabricated on ITO coated borosilicate glass and flexible PET substrates. Reprinted with permission from reference [58]. Copyright © 2011 Wiley-VCH Verlag GmbH & Co.

Polymer	Solvent Composition (Pyridine:CB)	Hole Mobility μ_{h0}	J_{sc} (std. dev.)	V_{oc} (std. dev.)	FF (std. dev.)	η (std. dev.)	Best η
P3CProT	1:7	$7.5x10^{-5}$ $cm^2/(V\ s)$	-2.69 mA/cm^2 (0.44)	0.59 V (0.01)	0.48 (0.04)	0.79% (0.08)	0.9%
P3CButT	1:8	$1.5x10^{-4}$ $cm^2/(V\ s)$	-2.57 mA/cm^2 (0.05)	0.60 V (0.01)	0.55 (0.01)	0.88% (0.02)	0.9%
P3CPenT	1:6	$3.9x10^{-4}$ $cm^2/(V\ s)$	-6.26 mA/cm^2 (0.24)	0.56 V (0.02)	0.64 (0.07)	2.43% (0.10)	2.6%
P3CHexT	1:7	$8.4x10^{-5}$ $cm^2/(V\ s)$	-5.86 mA/cm^2 (0.01)	0.64 V (0.01)	0.46 (0.01)	1.99% (0.01)	2.0%
P3HT on PET-ITO	DCB		-7.14 mA/cm^2	0.55 V	0.34	1.57%	
P3CHexT on PET-ITO	1:7		-4.69 mA/cm^2	0.62 V	0.48	1.62%	

[i] Device statistics represent the average of 4 devices on one ITO chip.

4.2.3 Mechanical Properties

In an "ideal" OPV material, the mechanical properties would reflect a balance of durability, flexibility and stability. This balance is required to satisfy the needs of both long-term device operation and implementation of fabrication techniques such as roll-to-roll processing. Despite this, specific mechanical criteria for OPV materials have not been clearly established, particularly as the mechanical properties of many leading candidates remain completely unknown, and reports of mechanical studies on OPV active layer materials are uncommon.[56, 87–90] Tabulating these properties for donors, acceptors, and BHJ blends will assist in establishing acceptable ranges, and understanding how variations in chemical functionalization and morphology affect

mechanical behaviour. Two measurable parameters are Young's modulus and hardness. A higher modulus is generally indicative of a lower flexibility, and as such lower values are preferable. Hardness characterizes the resistance of a material to plastic deformation and is therefore linked to durability.

One method of characterizing the mechanical properties of thin films and coatings is nanoindentation. This technique entails driving a hard tip into a material while recording the load-displacement curves; from these experiments, the Young's modulus and hardness of the layer can be determined.[91, 92] Nanoindentation is routinely used to characterize the mechanical properties of polymer films[93] including poly(ethylene terephthalate) (PET),[94] poly(methyl methacrylate),[95] shape memory polymers,[96] polyfluorene derivatives,[97] poly(*p*-phenylene vinylene),[98] PEDOT:PSS,[99] as well as hybrid CdSe/polymer,[100] and fullerene films.[101, 102]

The Young's modulus of cast P3HT has been measured by other techniques, and values of ~0.7 GPa[87, 88] and 1.3 GPa[89, 90] were reported. We substantiated these values for P3HT with nanoindentation, observing a Young's modulus of 1.4 GPa, and a hardness of 0.08 GPa. The P3HT:PCBM system has also been studied, and the BHJ film was found to have an elastic modulus of ~6.2 GPa, approximately five times larger than pure P3HT.[89]

For P3CAT-only films, we measured average indentation moduli in the range from 3.8 to 1.5 GPa, and hardness values from 0.17 to 0.09 GPa, as shown in Table 4.3. Shorter carboxyalkyl chain lengths lead to greater moduli and hardness, and, in each case, the values for P3CAT films exceed those measured for P3HT. In OPV devices, P3CATs are blended with PCBM, and therefore, the mechanical properties

of the combined BHJ films are of the greatest interest in the context of OPV devices. In the case of P3CProT:PCBM and P3CButT:PCBM mixtures, rough surfaces were observed optically, and inconsistent nanoindentation data was recorded as the measurement spot was varied over the sample. Consistent measurements were collected for P3CPenT:PCBM, P3CHexT:PCBM and P3HT:PCBM films, and these samples appeared smoother by optical microscopy. In each case, the introduction of PCBM significantly increased the Young's modulus of the films, with moduli ranging from 5.3 to 4.0 GPa and hardness ranging from 0.26 to 0.19 GPa for P3CPenT:PCBM, P3CHexT:PCBM and P3HT:PCBM, respectively (Table 4.3). These increased values are consistent with the literature, as the "filler effect" routinely leads to increased mechanical properties, i.e. larger modulus and hardness, in particle-loaded polymer films.[103, 104]

Table 4.3 Summary of the Young's moduli and hardness values from the nanoindentation of the polymer only and combined polymer:PCBM films. Reprinted with permission from reference [58]. Copyright © 2011 Wiley-VCH Verlag GmbH & Co.

Material	Polymer Only		Polymer:PCBM	
	Young's Modulus [GPa]	Hardness [GPa]	Young's Modulus [GPa]	Hardness [GPa]
P3CProT	3.8	0.17	-	-
P3CButT	2.7	0.15	-	-
P3CPenT	2.2	0.12	5.3	0.26
P3CHexT	1.5	0.09	4.9	0.22
P3HT	1.4	0.08	4.0	0.19

Materials with high elastic moduli and hardness tend to be more resistant to plastic deformation and creep than softer counterparts, and in the past, hydrogen bonding in polymer films has been shown to significantly increase moduli and hardness.[105–107] Hydrogen-bonded P3CATs reflect this trend, as each material measured showed greater indentation modulus and hardness than non-hydrogen

bonded P3HT. Less variation in mechanical properties was observed in the series of measurements of P3CATs in the presence of PCBM, but both P3CAT:PCBM mixtures were harder than P3HT:PCBM. This may lead to improved durability. The moduli and hardness of P3CAT and P3HT films are on-par with reported values for common flexible substrates, include poly(ethylene terephthalate) (PET) and poly(ethylene naphthalate) (PEN), which have Young's moduli of 2.3 and 3.3 GPa and hardnesses of 0.27 and 0.65 GPa, respectively.[57, 108] The BHJs, however, have larger moduli than the substrate layers, suggesting that PCBM will dominate the overall mechanical properties of the photoactive layer.

4.2.4 Photovoltaic Devices

The optoelectronic and photophysical properties of the P3CATs were found to be appropriate for incorporation into BHJ OPVs. Devices were fabricated on ITO substrates coated with a 20 nm hole-transporting interfacial layer of PEDOT:PSS. This layer enhances hole collection and increases open-circuit potential (V_{oc}) due to improved ohmic contact with the photoactive layer.[109–111] The active layer, 1:1 P3CAT:PCBM, was spin-cast in air on top of annealed PEDOT:PSS films and Al was thermally deposited to complete the cell. The photovoltaic performance of cells was tested in air under simulated AM 1.5 G conditions with power calibrated to a NREL certified KG-5 reference Si cell, which typically minimizes spectral mismatch.[112] Four 0.155 cm^2 devices at each solvent composition were fabricated and their short-circuit current density (J_{sc}), open-circuit potential (V_{oc}), fill factor (*FF*) and power conversion efficiency (η) were calculated from *J-V* curves. Figure 4.11A depicts the relationship between photovoltaic parameters and the pyridine composition (in chlorobenzene) for P3CPenT:PCBM. The

ITO/PEDOT:PSS/P3CPenT:PCBM/Al device architecture exhibited favourable PV performance at ~14% pyridine in the casting solvent, or a 1:6 pyridine:chlorobenzene ratio. The J_{sc}, FF and η exhibit similar trends of decreasing performance with increasing pyridine content. The V_{oc} increases, however, with higher pyridine fractions. These trends are attributed to the formation of PCBM nanoclusters as a result of large scale phase separation occurring in mixtures with greater pyridine content as evidenced by roughness in the cross-sectional scanning electron micrographs (SEMs). Clusters of PCBM in unoptimized BHJs have also been previously reported and have been shown to significantly reduce measured photocurrent.[11, 113, 114] Figure 4.11B illustrates the different device components in cross-sectional SEMs. As evidenced from the SEM image, the photoactive layer thickness for P3CPenT:PCBM cast from 1:6 pyridine:chlorobenzene was approximately 200 nm, and no large PCBM clusters were visible.

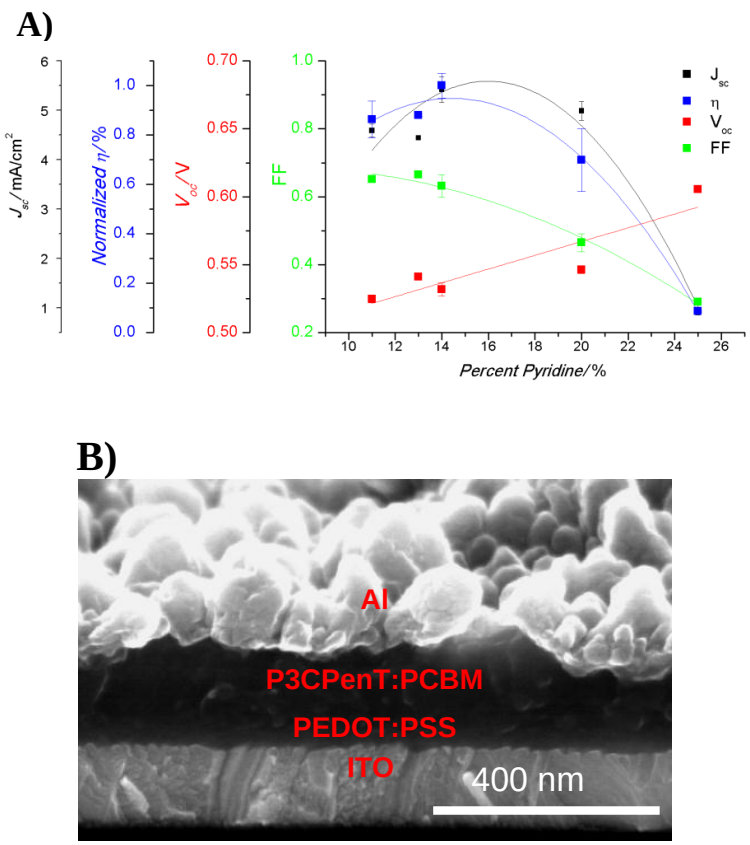

Figure 4.11 A) PV characteristics of a series of P3PenT:PCBM devices with different pyridine contents in a mixed pyridine:chlorobenzene solvent system. Each point represents the average of 4 PV devices. B) A cross-sectional SEM image illustrating the device architecture: ITO/PEDOT:PSS/P3CPenT:PCBM/Al with the active layer cast from the optimized solvent ratio of 1:6 pyridine:chlorobenzene. Reprinted with permission from reference [58]. Copyright © 2011 Wiley-VCH Verlag GmbH & Co.

OPV devices were fabricated using the optimized solvent composition for each P3CAT:PCBM mixture, and the performance parameters of these devices are displayed in Table 4.2, with light and dark *J-V* curves presented in Figure 4.12A. Within the P3CAT series, there does not appear to be a direct trend between photovoltaic performance and carboxyalkyl chain length, and the only measured PV parameter which varies greatly is the short-circuit current, which may be the determining factor in device performance. The V_{oc} can be predicted from the band

offset between the acceptor LUMO and donor HOMO. From the energy level diagram in Figure 4.6, the V_{oc} is expected to be slightly smaller for P3CProT and P3CPenT compared to P3CButT and P3CHexT, and this effect is clear in Table 4.2. P3CProT (x = 3) and P3CButT (x = 4) have modest power conversion efficiencies (η) mainly due to low short-circuit current densities. This can be explained by suboptimal morphology in the bulk heterojunction as a result of the larger PCBM aggregates observed by XRD for both P3CProT:PCBM and P3CButT:PCBM films (Figure 4.9A). The optimal power conversion efficiencies for P3CProT and P3CButT were both 0.9%. P3CHexT (x = 6) reached a greater power conversion efficiency of 2.0%, with the improved performance primarily a result of the higher J_{sc}. The best photovoltaic performance was measured for P3CPenT (x = 5) which achieved η = 2.6% due to increased J_{sc} and a high fill factor of 0.64, indicative of favourable morphology in the bulk heterojunction.[115, 116] The P3CPenT devices exhibit superior PV performance due to larger polymer crystallite sizes, relatively high hole mobilities and a larger extent of hydrogen bonding molecular interactions, compared to the other carboxylated polythiophenes. The P3CPenT:PCBM films also have a bathochromic shift from the absorbance spectroscopy of films, while the other P3CATs are blue-shifted. This indicates longer conjugation lengths for the P3CPenT blend films.

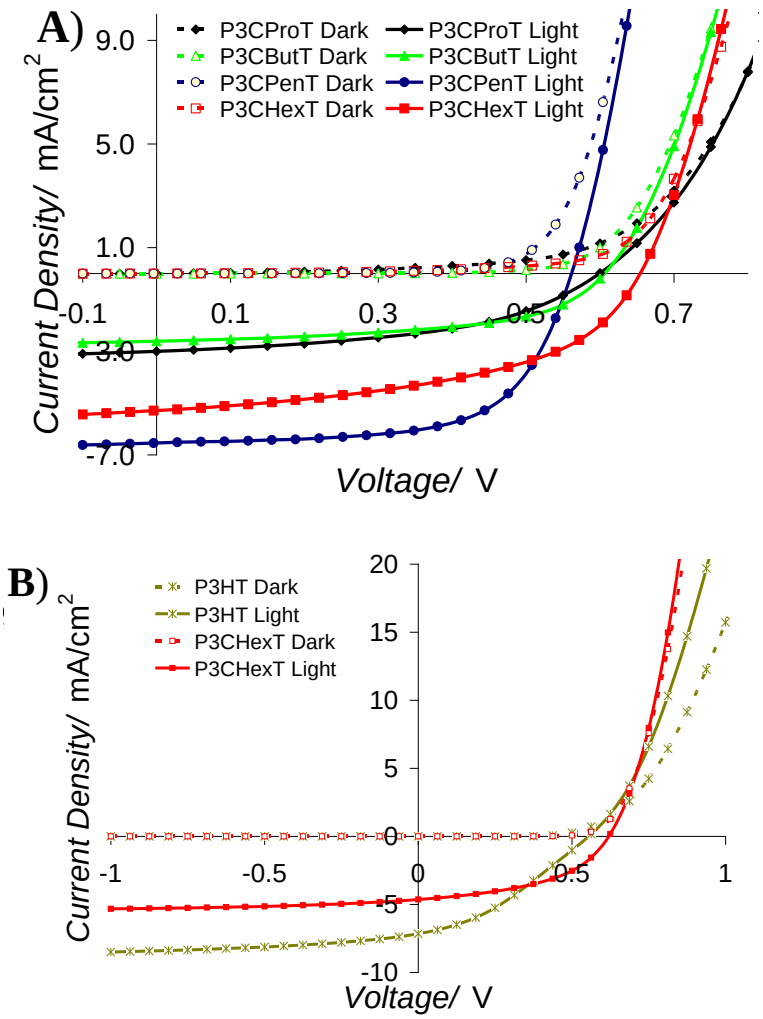

Figure 4.12 A) Dark and light *J–V* curves for the series of BHJ OPVs (P3CProT:PCBM), (P3CButT:PCBM), (P3CPenT:PCBM) and (P3CHexT:PCBM) with device architecture: ITO/PEDOT:PSS/P3CAT:PCBM/Al. B) Dark and light *J–V* curves for BHJ OPVs on flexible PET–ITO for P3HT:PCBM and P3CHexT:PCBM. Reprinted with permission from reference [58]. Copyright © 2011 Wiley-VCH Verlag GmbH & Co.

In order to test these materials in flexible BHJ OPV devices, assembly was carried out on ITO-coated PET substrates for P3CHexT:PCBM and P3HT:PCBM and the resultant *J-V* curves and PV parameters are summarized in Figure 4.12B and Table 4.2. The photovoltaic characteristics of the P3HT:PCBM device on PET-ITO was very similar to Al-Ibrahim *et al.* who report PCEs of 1.54%, with a J_{sc} of 6.61

mA/cm^2 and a fill factor of 0.39.[117] The P3CHexT:PCBM device had comparable performance to the P3HT:PCBM device with a lower J_{sc} but higher V_{oc} and fill factor. In comparing the P3CHexT:PCBM BHJ on borosilicate and flexible PET-ITO, most PV parameters are similar with the exception of a slightly lower J_{sc}, which may be attributed to decreased transmission in PET-ITO films.[118] These results are comparable to similar reported flexible organic solar cells in the literature.[55, 119–122] The nanoindentation results of the combined polymer:PCBM films suggests that the carboxy-functionalized polythiophenes are suitable for use on flexible substrates. However, a major limitation in the device architecture is the far larger modulus of ITO (100 GPa),[123] which is more prone to cracking than P3HT and the P3CAT series. If ITO can be replaced with a mechanically robust material, the carboxy-functionalized polythiophenes would have similar mechanical stability as P3HT but would be more resistant to deformation.

4.3 Conclusions

We investigated the optoelectronic and photophysical properties of a series of poly[3-(carboxyalkyl)thiophenes] with alkyl length, *x*, ranging from 3-6, and it was determined that absorption coefficients and band offsets were appropriate for incorporation into bulk heterojunction photovoltaics with PCBM. OPV devices were fabricated, and the highest power conversion efficiency of 2.6% was observed for the P3CPenT:PCBM film. This particular blend film had significantly larger polymer crystallite size and hole mobility aiding in charge transport through the OPV device. The superior performance of the P3CPenT member of this family of polymers may

be the result of a delicate balance between solubility and BHJ morphology resulting from its solid-state properties.

4.4 Experimental

Materials:

Regioregular poly[3-(3-carboxypropyl)thiophene-2,5-diyl] (P3CProT), poly[3-(4-carboxybutyl)thiophene-2,5-diyl] (P3CButT), poly[3-(5-carboxypentyl)thiophene-2,5-diyl] (P3CPenT), poly[3-(6-carboxyhexyl)thiophene-2,5-diyl] (P3CHexT) and poly[3-(hexyl)thiophene-2,5-diyl] (P3HT) were purchased from Rieke Metals, Inc. PCBM, PEDOT:PSS and Al (99.99%) were purchased from American Dye Source (ADS61BFA), Heraues (Clevios P VP AI 4083) and Kurt J. Lesker respectively. ITO coated glass substrates (8-12 Ω/□) were purchased from Delta Technologies, Ltd. Methylene chloride, 2-propanol, acetone, anhydrous pyridine, chlorobenzene and ortho-dichlorobenzene were used as received from Sigma-Aldrich.

Characterization:

Absorbance spectra were measured on an Agilent UV-vis spectrometer, and spectra were normalized to the intensity of $\lambda_{max\text{-}abs}$. Solution photoluminescence (PL) spectra were recorded with a Photon Technology International fluorescence spectrophotometer excited at 500 nm with a 75 W Xe lamp. SEM cross-section images were acquired using a Hitachi S-4800 FE-SEM tilted at 10°, with an accelerating voltage of 10 keV. Profilometry was performed on thin films using a Zygo white light optical profilometer. The thickness of the film was measured relative to silicon substrates, where part of the film had been removed with a razor to

create a step. Films were analyzed using a 10x lens with fine control set to 0.4x. Three scans were collected and averaged using a vertical scan range of 2 μm and the resulting surface profile was averaged along a 0.5 mm wide line perpendicular to the film edge.

Solid-state Photoluminescence Spectroscopy:

Solid-state photoluminescence spectroscopy was performed at room temperature, excited at 442 nm with a He-Cd laser. Irradiance was filtered with a 475 nm light pass filter and detected using a USB2000 Ocean Optics charge coupled detector (range 300-1050 nm). The spectral response was normalized using a standard blackbody radiator with a dark spectrum subtracted from all spectra with an integration time of 500 ms except for the P3CHexT and P3CHexT:PCBM films, which were measured with an integration time of 100 ms. To account for differences in film thickness between the polymer-only and combined films, the polymer-only absorbance spectra were normalized to the combined BHJ film and the thickness normalization factors were applied to PL spectra of P3CAT-only films.

Cyclic Voltammetry:

Cyclic voltammetry was performed with a Princeton Applied Research Potentiostat model 2273 in a standard three-electrode electrochemical cell with all potentials referenced to a Ag/Ag^+ electrode. A Pt counter electrode was used, and the working electrode was a Pt disc (0.071 cm^2) coated with the dried film of interest. The electrolyte solution contained 0.1 mol L^{-1} tetra(*n*-butyl)ammonium hexafluorophosphate (nBu_4NPF_6) in acetonitrile. All scans were performed at a scan

rate of 100 mV/s, and the reference potential was calibrated to a ferrocene redox couple.

Infrared Spectroscopy:

Fourier transform infrared (FTIR) spectroscopy was performed using a Nicolet Nexus 760 spectrometer with a DTGS detector and a nitrogen-purged sample chamber. All acquisitions were obtained using 32 scans with 4 cm^{-1} resolution. KBr pellets of P3CAT powder were prepared by grinding KBr and the P3CAT and forming a pellet with a press. Solution FTIR samples were prepared by drop-casting a solution of either P3CAT-only or P3CAT:PCBM from the optimized solvent composition (*vide infra*) between two KBr pellets before the solvent evaporated. FTIR films were prepared by drying the aforementioned FTIR solution samples.

X-ray Diffraction:

X-ray diffraction (XRD) was performed using a Bruker D8 Discover instrument with a Cu K_α beam (40 kV, 40 mA; λ = 1.54184 Å) and operated at a glancing angle, $\omega = 2°$. P3CAT:PCBM films were spin-cast on cleaned Si wafers. Peaks in the X-ray diffraction pattern were identified in terms of the Bragg angle, 2θ, and calibrated to a LaB_6 NIST standard (SRM-660b). Integration time for all samples was 1 hour.

Hole Mobilities:

The hole mobility in P3CAT materials was determined in devices with the following architecture: ITO/PEDOT:PSS(20 nm)/P3CAT(~120 nm)/Al (80 nm). The device input voltage was swept from 0 V to 4 V under dark conditions, while

measuring the output current density using a Keithley 2400 source meter. The results were fit to the modified Mott-Gurney theory.[82]

Nanoindentation:

P3CAT-only devices were spin-cast from 100 mg/mL pyridine solutions at 600 rpm for 60 s, and P3CAT:PCBM films were drop-cast from mixed (total 34 mg/mL) pyridine/chlorobenzene solutions having proportions optimized for maximum photovoltaic performance (*vide infra*). In both cases, ITO-coated glass was used as a substrate, and test pieces measuring approximately 1 cm x 1 cm were mounted on aluminum sample holders using Instant Krazy Glue (Columbus, OH). Nanoindentation was performed using a Hysitron Triboindenter with a 1 μm cono-spherical tip. For each test sample, a series of indents was performed as the maximum applied force was varied from 10 μN to a value between 290 μN and 450 μN depending on the desired indent depth. Each indent was performed at a different position on the sample with a minimum spacing of 5 μm between indentations. For every indent experiment, a time-dependent load function was used: the load was linearly increased to the desired maximum over 5 s, held for 2 s, and unloaded over 5 s. The modulus and hardness were calculated by the Triboscanner software v.8, which uses the method developed by Oliver and Pharr.[91] The tip area function was calibrated over the range from 5 nm to 155 nm against a quartz substrate (using 100 indents of varying force/depth). The results were averaged over all points from a contact depth of 70 nm to 155 nm; values collected at lower depth were discarded due the difficultly of making precise measurements with a 1 μm tip below 70 nm, and values collected at greater depths were discarded because the tip area function

could not be measured at these depths with the force available (8000 μN). In the profiles, an "indentation size effect" was observed at low contact depths,[92] and no marked increase in hardness or elastic modulus was observed with increasing contact depth, indicating no appreciable substrate effect.

Device Fabrication:

Devices were fabricated on ITO-coated glass substrates which were cleaned by successive 10 min ultrasonications in methylene chloride, Millipore water (18 MΩ·cm) and 2-propanol followed by a 10 min air plasma at ~0.1 mTorr (Harrick Plasma, PDC 32G, 18W). PEDOT:PSS was filtered with a 0.2 μm cellulose acetate filter directly onto the freshly cleaned ITO substrates and spin-cast at 3000 rpm for 1 min to form a ~20 nm thick layer which was annealed in air for 15 min at 140°C. Solutions of P3CATs (34 mg/mL) in pyridine and chlorobenzene and PCBM (34 mg/mL) in chlorobenzene were prepared and left to stir for 15 hours at 45°C. Optimized total pyridine:chlorobenzene solvent mixtures for the P3CAT:PCBM were 1:7, 1:8, 1:6 and 1:7 for P3CProT, P3CButT, P3CPenT and P3CHexT respectively. P3CAT and PCBM solutions were combined (1:1 by weight) and left to stir for ~1 hour at 45°C before being filtered with a 0.45 μm PTFE filter directly onto the freshly annealed PEDOT:PSS layer. The active layer was spin-cast at 600 rpm for 1 minute in air. The active layer thickness for P3CProT:PCBM, P3CButT:PCBM, P3CPenT:PCBM and P3CHexT:PCBM was 170 nm, 180 nm, 200 nm and 230 nm respectively measured by optical profilometry. The top aluminum cathode (70-80 nm) was deposited by thermal evaporation under high vacuum conditions (~10^{-4} Pa) at a rate of ~5 Å/s. The device area was 0.155±0.008 cm^2.

Flexible PET-ITO Device Fabrication:

ITO coated poly(ethylene terephthalate) (PET) substrates from Solutia Inc. (OFD10) were washed in successive 10 min sonications in Millipore water (18 MΩ·cm) and 1:1 acetone:2-propanol followed by a 3.5 min air plasma at ~0.1 mTorr (Harrick Plasma, PDC 32G, 18W). PEDOT:PSS and P3CHexT were spin-cast as usual. Equal volume solutions of poly[3-hexylthiophene] (P3HT) (34 mg/mL) and PCBM (34 mg/mL) were prepared in *o*-dichlorobenzene and left to stir for 15 hours at 45°C. After which, the solutions were combined and left to stir for ~1 hour at 45°C before filtering with a 0.2 μm PTFE filter directly onto the freshly annealed PEDOT:PSS layer. The P3HT:PCBM photoactive layer was spin-cast at 600 rpm for 1 min in air and covered with a Petri dish to dry over the course of 15-20 minutes. Devices were completed by the thermal evaporation of 50 nm of aluminum forming a device area of 0.08 cm^2.

Device Testing:

Photovoltaic performance was assessed at ambient temperature in air under AM 1.5 G simulated irradiation with a xenon solar simulator (Oriel 91191 1000W). The testing irradiance was calibrated against a certified Si reference cell fitted with a KG-5 filter (model PVM624, PV Measurements, Inc.). Device characterization was performed with a Keithley 2400 source meter. The total irradiance was 140 mW/cm^2 (200 nm to 20 μm wavelength), 130 mW/cm^2 (200 nm to 1360 nm wavelength), and 40 mW/cm^2 (300 nm to 700 nm wavelength, KG-5 filter), resulting in testing temperatures of 25 - 30 °C.

4.5 Contributions

B.J. Worfolk planned and executed most experiments. A.L. Elias assisted with mechanical property measurements and interpretation. M. Thomas assisted with absorption coefficient analysis. K.D. Harris assisted with hole mobility measurements. All authors assisted with analysis and interpretation of data. B.J. Worfolk wrote the manuscript, and all authors edited the manuscript.

4.6 References

[1] D.A. Rider, K.D. Harris, D. Wang, J. Bruce, M.D. Fleischauer, R.T. Tucker, M.J. Brett, J.M. Buriak, *ACS Appl. Mater. Interfaces* **2009**, *1*, 279.

[2] G. Li, V. Shrotriya, Y. Yao, J. Huang, Y. Yang, *J. Mater. Chem.* **2007**, *17*, 3126.

[3] A.C. Mayer, S.R. Scully, B.E. Hardin, M.W. Rowell, M.D. McGehee, *Renewable Energy* **2007**, *10*, 28.

[4] D.A. Rider, B.J. Worfolk, K.D. Harris, A. Lalany, K. Shahbazi, M.D. Fleischauer, M.J. Brett, J.M. Buriak, *Adv. Funct. Mater.* **2010**, *20*, 2404.

[5] L.H. Nguyen, H. Hoppe, T. Erb, S. Günes, G. Gobsch, N.S. Sariciftci, *Adv. Funct. Mater.* **2007**, *17*, 1071.

[6] W.D. Oosterbaan, V. Vrindts, S. Berson, S. Guillerez, O. Douhéret, B. Ruttens, J. D'Haen, P. Adriaensens, J. Manca, L. Lutsen, D. Vanderzande, *J. Mater. Chem.* **2009**, *19*, 5424.

[7] M. Al-Ibrahim, H. Roth, M. Schroedner, A. Konkin, U. Zhokhavets, G. Gobsch, P. Scharff, S. Sensfuss, *Org. Electron.* **2005**, *6*, 65.

[8] H. Xin, F.S. Kim, S.A. Jenekhe, *J. Am. Chem. Soc.* **2008**, *130*, 5424.

[9] H. Xin, G. Ren, F.S. Kim, S.A. Jenekhe, *Chem. Mater.* **2008**, *20*, 6199.

[10] W. Ma, C. Yang, X. Gong, K. Lee, A.J. Heeger, *Adv. Funct. Mater.* **2005**, *15*, 1617.

[11] H. Hoppe, N.S. Sariciftci, *J. Mater. Chem.* **2006**, *16*, 45.

[12] M. Campoy-Quiles, T. Ferenczi, T. Agostinelli, P.G. Etchegoin, Y. Kim, T.D. Anthopoulos, P.N. Stavrinou, D.D.C. Bradley, J. Nelson, *Nat. Mater.* **2008**, *7*, 158.

[13] G. Li, V. Shrotriya, J. Huang, Y. Yao, T. Moriarty, K. Emery, Y. Yang, *Nat. Mater.* **2005**, *4*, 864.

[14] S.E. Gledhill, B. Scott, B.A. Gregg, *J. Mater. Res.* **2005**, *20*, 3167.

[15] Y. Yao, J. Hou, Z. Xu, G. Li, Y. Yang, *Adv. Funct. Mater.* **2008**, *18*, 1783.

[16] Y. Kim, S. Cook, S.M. Tuladhar, S.A. Choulis, J. Nelson, J.R. Durrant, D.D.C. Bradley, M. Giles, I. McCulloch, C.-S. Ha, M. Ree, *Nat. Mater.* **2006**, *5*, 197.

[17] G. Nagarjuna, D. Venkataraman, *J. Polym. Sci., Part B: Polym. Phys.* **2012**, *50*, 1045.

[18] K.M. Coakley, M.D. McGehee, *Chem. Mater.* **2004**, *16*, 4533.

[19] J. Nelson, *Mater. Today* **2011**, *14*, 462.

[20] G. Li, Y. Yao, H. Yang, V. Shrotriya, G. Yang, Y. Yang, *Adv. Funct. Mater.* **2007**, *17*, 1636.

[21] Z. Xu, L.-M. Chen, G. Yang, C.-H. Huang, J. Hou, Y. Wu, G. Li, C.-S. Hsu, Y. Yang, *Adv. Funct. Mater.* **2009**, *19*, 1227.

[22] A.S. Anselmo, L. Lindgren, J. Rysz, A. Bernasik, A. Budkowski, M. R. Andersson, K. Svensson, J. van Stam, E. Moons, *Chem. Mater.* **2011**, *23*, 2295.

[23] B.J. Worfolk, W. Li, P. Li, T.C. Hauger, K.D. Harris, J.M. Buriak, *J. Mater. Chem.* **2012**, 11354.

[24] G. Griffini, J.D. Douglas, C. Piliego, T.W. Holcombe, S. Turri, J.M.J. Fréchet, J.L. Mynar, *Adv. Mater.* **2011**, *23*, 1660.

[25] C.-H. Huang, N.D. McClenaghan, A. Kuhn, G. Bravic, D.M. Bassani, *Tetrahedron* **2006**, *62*, 2050.

[26] C.-H. Huang, N.D. McClenaghan, A. Kuhn, J.W. Hofstraat, D.M. Bassani, *Org. Lett.* **2005**, *7*, 3409.

[27] P. Liu, J. Huang, W. Pan, M. Huang, W. Deng, Y. Mai, A. Luan, *Chin. Chem. Lett.* **2007**, *18*, 437.

[28] C. Jiang, P. Liu, W. Deng, *Synth. Commun.* **2009**, *39*, 2360.

[29] A. Kira, M. Tanaka, T. Umeyama, Y. Matano, N. Yoshimoto, Y. Zhang, S. Ye, H. Lehtivuori, N.V. Tkachenko, H. Lemmetyinen, H. Imahori, *J. Phys. Chem. C* **2007**, *111*, 13618.

[30] M. Helgesen, R. Søndergaard, F.C. Krebs, *J. Mater. Chem.* **2010**, *20*, 36.

[31] F.C. Krebs, H. Spanggaard, *Chem. Mater.* **2005**, *17*, 5235.

[32] M. Bjerring, J.S. Nielsen, A. Siu, N.C. Nielsen, F.C. Krebs, *Sol. Energy Mater. Sol. Cells* **2008**, *92*, 772.

[33] J. Liu, E.N. Kadnikova, Y. Liu, M.D. McGehee, J.M.J. Fréchet, *J. Am. Chem. Soc.* **2004**, *126*, 9486.

[34] F.C. Krebs, H. Spanggaard, *Chem. Mater.* **2005**, *17*, 5235.

[35] Y. Lin, J. Ah Lim, Q. Wei, S.C.B. Mannsfeld, A.L. Briseno, J.J. Watkins, *Chem. Mater.* **2012**, *24*, 622.

[36] R.D. McCullough, P.C. Ewbank, R.S. Loewe, *J. Am. Chem. Soc.* **1997**, *119*, 633.

[37] P.C. Ewbank, R.S. Loewe, L. Zhai, J. Reddinger, G. Sauvé, R.D. McCullough, *Tetrahedron* **2004**, *60*, 11269.

[38] Z. Bao, A.J. Lovinger, *Chem. Mater.* **1999**, 2607.

[39] K. Shankar, G.K. Mor, H.E. Prakasam, O.K. Varghese, C.A. Grimes, *Langmuir* **2007**, *23*, 12445.

[40] J.K. Mwaura, X. Zhao, H. Jiang, K.S. Schanze, J.R. Reynolds, *Chem. Mater.* **2006**, *18*, 6109.

[41] R. Senadeera, N. Fukuri, Y. Saito, T. Kitamura, Y. Wada, S. Yanagida, *Chem. Commun.* **2005**, 2259.

[42] C.J. Bhongale, M. Thelakkat, *Sol. Energy Mater. Sol. Cells* **2010**, *94*, 817.

[43] Y. Liu, S.R. Scully, M.D. McGehee, J. Liu, C.K. Luscombe, J.M.J. Fréchet, S.E. Shaheen, D.S. Ginley, *J. Phys. Chem. B* **2006**, *110*, 3257.

[44] R.H. Lohwasser, J. Bandara, M. Thelakkat, *J. Mater. Chem.* **2009**, *19*, 4126.

[45] Y.-G. Kim, J. Walker, L.A. Samuelson, J. Kumar, *Nano Lett.* **2003**, *3*, 523.

[46] S. Yanagida, G.K.R. Senadeera, K. Nakamura, T. Kitamura, Y. Wada, *J. Photochem. Photobiol., A* **2004**, *166*, 75.

[47] B. Kim, L. Chen, J. Gong, Y. Osada, *Macromolecules* **1999**, *32*, 3964.

[48] C.-N. Hou, M.-Y. Hua, S.-A. Chen, *Mater. Chem. Phys.* **1994**, *36*, 359.

[49] Y.-G. Kim, L. Samuelson, J. Kumar, S. Tripathy, *J. Macromol. Sci. Part A Pure Appl. Chem.* **2002**, *A39*, 1127.

[50] G.M.A. Rahman, D.M. Guldi, R. Cagnoli, A. Mucci, L. Schenetti, L. Vaccari, M. Prato, *J. Am. Chem. Soc.* **2005**, *127*, 10051.

[51] L. Blankenburg, K. Schultheis, H. Schache, S. Sensfuss, M. Schrödner, *Sol. Energy Mater. Sol. Cells* **2009**, *93*, 476.

[52] F.C. Krebs, S.A. Gevorgyan, J. Alstrup, *J. Mater. Chem.* **2009**, *19*, 5442.

[53] F.C. Krebs, T. Tromholt, M. Jørgensen, *Nanoscale* **2010**, *2*, 873.

[54] F.C. Krebs, K. Norrman, *ACS Appl. Mater. Interfaces* **2010**, *2*, 877.

[55] C. Lungenschmied, G. Dennler, H. Neugebauer, S.N. Sariciftci, M. Glatthaar, T. Meyer, A. Meyer, *Sol. Energy Mater. Sol. Cells* **2007**, *91*, 379.

[56] B. O'Connor, E.P. Chan, C. Chan, B.R. Conrad, L.J. Richter, R.J. Kline, M. Heeney, I. McCulloch, C.L. Soles, D.M. Delongchamp, *ACS Nano* **2010**, *4*, 7538.

[57] K.A. Sierros, D.R. Cairns, J.S. Abell, S.N. Kukureka, *Thin Solid Films* **2010**, *518*, 2623.

[58] B.J. Worfolk, D.A. Rider, A.L. Elias, M. Thomas, K.D. Harris, J.M. Buriak, *Adv. Funct. Mater.* **2011**, *21*, 1816.

[59] S. Günes, H. Neugebauer, N.S. Sariciftci, *Chem. Rev.* **2007**, *107*, 1324.

[60] B. Friedel, C.R. McNeill, N.C. Greenham, *Chem. Mater.* **2010**, 3389.

[61] J.-L. Brédas, D. Beljonne, V. Coropceanu, J. Cornil, *Chem. Rev.* **2004**, *104*, 4971.

[62] M.C. Scharber, D. Mühlbacher, M. Koppe, P. Denk, C. Waldauf, A.J. Heeger, C.J. Brabec, *Adv. Mater.* **2006**, *18*, 789.

[63] N. Blouin, A. Michaud, D. Gendron, S. Wakim, E. Blair, R. Neagu-Plesu, M. Belletête, G. Durocher, Y. Tao, M. Leclerc, *J. Am. Chem. Soc.* **2008**, *130*, 732.

[64] V. Cleave, G. Yahioglu, P. Le Barny, D.H. Hwang, A.B. Holmes, R.H. Friend, N. Tessler, *Adv. Mater.* **2001**, *13*, 44.

[65] L.J.A. Koster, V.D. Mihailetchi, P.W.M. Blom, *Appl. Phys. Lett.* **2006**, *88*, 093511.

[66] Y. Kim, S.A. Choulis, J. Nelson, D.D.C. Bradley, S. Cook, J.R. Durrant, *J. Mater. Sci.* **2005**, *40*, 1371.

[67] J. Gao, F. Hide, H. Wang, *Syn. Met.* **1997**, *84*, 979.

[68] C. Lee, G. Yu, D. Moses, K. Pakbaz, C. Zhang, N. Sariciftci, A. Heeger, F. Wudl, *Phys. Rev. B* **1993**, *48*, 15425.

[69] L. Smilowitz, N.S. Sariciftci, R. Wu, C. Gettinger, A.J. Heeger, F. Wudl, *Phys. Rev. B* **1993**, *47*, 13835.

[70] D. Lipkind, J.S. Chickos, J.F. Liebman, *Struct. Chem.* **2009**, *20*, 617.

[71] S.P. Verevkin, V.N. Emel'yanenko, A. Klamt, *J. Chem. Eng. Data* **2007**, *52*, 499.

[72] T. Kato, T. Uryu, F. Kaneuchi, C. Jin, J. Fréchet, *Liq. Cryst.* **1993**, *14*, 1311.

[73] J. Casanovas, O. Bertran, E. Armelin, J. Torras, F. Estrany, C. Alemán, *J. Phys. Chem. A* **2008**, *112*, 10650.

[74] R.M. Silverstein, F.X. Webster, *Spectrometric Identification of Organic Compounds*, John Wiley & Sons, Inc.**1998**.

[75] P.-T. Wu, H. Xin, F.S. Kim, G. Ren, S.A. Jenekhe, *Macromolecules* **2009**, *42*, 8817.

[76] X. Yang, J.K.J. van Duren, M.T. Rispens, J.C. Hummelen, R.A.J. Janssen, M.A.J. Michels, J. Loos, *Adv. Mater.* **2004**, *16*, 802.

[77] Y. Kim, J. Nelson, T. Zhang, S. Cook, J.R. Durrant, H. Kim, J. Park, M. Shin, S. Nam, M. Heeney, I. McCulloch, C.-S. Ha, D.D.C. Bradley, *ACS Nano* **2009**, *3*, 2557.

[78] H.-G. Flesch, R. Resel, C.R. McNeill, *Org. Electron.* **2009**, *10*, 1549.

[79] T. Erb, U. Zhokhavets, G. Gobsch, S. Raleva, B. Stühn, P. Schilinsky, C. Waldauf, C.J. Brabec, *Adv. Funct. Mater.* **2005**, *15*, 1193.

[80] N.F. Mott, R.W. Gurney, *Electronic Processes in Ionic Crystals*, Oxford Univeristy Press, London **1940**.

[81] P.W.M. Blom, M.J.M. De Jong, J.J.M. Vleggaar, *Appl. Phys. Lett.* **1996**, *68*, 3308.

[82] P.W.M. Blom, M.J.M. de Jong, M.G. van Munster, *Phys. Rev. B* **1997**, *55*, R656.

[83] C. Goh, R.J. Kline, M.D. McGehee, E.N. Kadnikova, J.M.J. Fréchet, *Appl. Phys. Lett.* **2005**, *86*, 122110.

[84] P.N. Murgatroyd, *J. Phys. D: Appl. Phys.* **1970**, *3*, 151.

[85] J. Frenkel, *Phys. Rev.* **1938**, *54*, 647.

[86] T. Savenije, J. Kroeze, X. Yang, J. Loos, *Thin Solid Films* **2006**, *511-512*, 2.

[87] B.K. Kuila, A.K. Nandi, *J. Phys. Chem. B* **2006**, *110*, 1621.

[88] S. Miyauchi, T. Kondo, K. Oshima, T. Yamauchi, M. Shimomura, H. Mitomo, *J. Appl. Polym. Sci.* **2002**, *85*, 1429.

[89] D. Tahk, H.H. Lee, D.-Y. Khang, *Macromolecules* **2009**, *42*, 7079.

[90] D.-Y. Khang, J.A. Rogers, H.H. Lee, *Adv. Funct. Mater.* **2009**, *19*, 1526.

[91] W.C. Oliver, G.M. Pharr, *J. Mater. Res.* **2004**, *19*, 3.

[92] A. Gouldstone, N. Chollacoop, M. Dao, J. Li, A. Minor, Y. Shen, *Acta Mater.* **2007**, *55*, 4015.

[93] X. Li, B. Bhushan, *Mater. Charact.* **2002**, *48*, 11.

[94] D. Tranchida, S. Piccarolo, *Macromol. Rapid Commun.* **2005**, *26*, 1800.

[95] D. Tranchida, S. Piccarolo, M. Soliman, *Macromolecules* **2006**, *39*, 4547.

[96] E. Wornyo, K. Gall, F. Yang, W. King, *Polymer* **2007**, *48*, 3213.

[97] K. Zeng, Z. Chen, L. Shen, B. Liu, *Thin Solid Films* **2005**, *477*, 111.

[98] E. Tekin, D.A.M. Egbe, J.M. Kranenburg, C. Ulbricht, S. Rathgeber, E. Birckner, N. Rehmann, K. Meerholz, U.S. Schubert, *Chem. Mater* **2008**, *20*, 2727.

[99] S. Shanmugham, J. Jeong, A. Alkhateeb, D.E. Aston, *Langmuir* **2005**, *21*, 10214.

[100] E.J. McCumiskey, N. Chandrasekhar, C.R. Taylor, *Nanotechnology* **2010**, *21*, 225703.

[101] A. Richter, R. Ries, R. Smith, M. Henkel, B. Wolf, *Diamond Relat. Mater.* **2000**, *9*, 170.

[102] H. Vaez Taghavi, A. Hirata, *Mater. Lett.* **2010**, *64*, 83.

[103] D. Ciprari, K. Jacob, R. Tannenbaum, *Macromolecules* **2006**, *39*, 6565.

[104] E.J. McCumiskey, N. Chandrasekhar, C.R. Taylor, *Nanotechnology* **2010**, *21*, 225703.

[105] L. Ge, X. Wang, L. Ba, Z. Gu, *J. Nanosci. Nanotechnol.* **2008**, *8*, 2996.

[106] Y.I. Tien, K.H. Wei, *Macromolecules* **2001**, *34*, 9045.

[107] S.W. Shang, J.W. Williams, K.J.M. Soderholm, *J. Mater. Sci.* **1994**, *29*, 2406.

[108] F.C. Krebs, *Org. Electron.* **2009**, *10*, 761.

[109] P. Peumans, S.R. Forrest, *Appl. Phys. Lett.* **2001**, *79*, 126.

[110] M. Granstroum, K. Petritsch, A.C. Arias, A. Lux, M.R. Andersson, R.H. Friend, *Nature* **1998**, *395*, 257.

[111] C.J. Brabec, S.E. Shaheen, C. Winder, N.S. Sariciftci, P. Denk, *Appl. Phys. Lett.* **2002**, *80*, 1288.

[112] V. Shrotriya, G. Li, Y. Yao, T. Moriarty, K. Emery, Y. Yang, *Adv. Funct. Mater.* **2006**, *16*, 2016.

[113] H. Hoppe, T. Glatzel, M. Niggemann, W. Schwinger, F. Schaeffler, A. Hinsch, M. Luxsteiner, N. Sariciftci, *Thin Solid Films* **2006**, *511-512*, 587.

[114] H. Hoppe, M. Niggemann, C. Winder, J. Kraut, R. Hiesgen, A. Hinsch, D. Meissner, N.S. Sariciftci, *Adv. Funct. Mater.* **2004**, *14*, 1005.

[115] M.-S. Kim, B.-G. Kim, J. Kim, *ACS Appl. Mater. Interfaces* **2009**, *1*, 1264.

[116] M. Jørgensen, K. Norrman, F.C. Krebs, *Sol. Energy Mater. Sol. Cells* **2008**, *92*, 686.

[117] M. Alibrahim, S. Sensfuss, J. Uziel, G. Ecke, O. Ambacher, *Sol. Energy Mater. Sol. Cells* **2005**, *85*, 277.

[118] S. Hau, H.-L. Yip, A.K.-Y. Jen, *Polym. Rev.* **2010**, *50*, 474.

[119] Y.-T. Cheng, J.-J. Ho, C.-K. Wang, W. Lee, C.-C. Lu, B.-S. Yau, J.-L. Nain, S.-H. Chang, C.-C. Chang, K.L. Wang, *Appl. Surf. Sci.* **2010**, *256*, 7606.

[120] T. Ameri, G. Dennler, C. Waldauf, H. Azimi, A. Seemann, K. Forberich, J. Hauch, M. Scharber, K. Hingerl, C.J. Brabec, *Adv. Funct. Mater.* **2010**, *20*, 1592.

[121] N. Sun, G. Fang, P. Qin, Q. Zheng, M. Wang, X. Fan, F. Cheng, J. Wan, X. Zhao, J. Liu, D.L. Carroll, J. Ye, *J. Phys. D: Appl. Phys.* **2010**, *43*, 445101.

[122] S.K. Hau, H.-L. Yip, N.S. Baek, J. Zou, K. O'Malley, A.K.-Y. Jen, *Appl. Phys. Lett.* **2008**, *92*, 253301.

[123] K. Zeng, F. Zhu, J. Hu, L. Shen, K. Zhang, H. Gong, *Thin Solid Films* **2003**, *443*, 60.

5

Conclusions

This thesis examined an integrative approach to organic photovoltaics (OPVs) through the use of new materials and architectures. This section summarizes each chapter, and presents potential research directions for the future.

5.1 Chapter Summaries

5.1.1 Chapter 1

The first chapter introduced semiconducting polymers as a key enabler for organic electronics. The development of OPVs was discussed starting from the observation of the photovoltaic effect to organic single bilayer devices and complex tandem OPVs. The characterization of photovoltaic devices was introduced under simulated solar radiation conditions. Components of OPV devices were deconstructed and thoroughly discussed, while highlighting significant advances in the field. The chapter concluded with a market assessment and future outlook of OPVs. Flexible OPVs have great potential as a low-cost power source. However, further advances in efficiency, lifetimes and understanding the processing of components are required to reach commercial viability.

5.1.2 Chapter 2

Chapter 2 discussed the development of spray-coated polymer transparent conductors. Materials for transparent electrodes combine low sheet resistance with high transmissivity. Poly(3,4-ethylenedioxythiophene) : poly(4-styrenesulfonate) (PEDOT:PSS) was selected due to its promising film conductivity and low absorption in the visible spectrum. A PEDOT:PSS ink was formulated, consisting of water, isopropyl alcohol, and ethylene glycol. Spray-coated films exhibited high conductivities of 1070±50 S cm^{-1}. Sheet resistances ranged from 24-259 Ω $□^{-1}$, while the transmission varied from 71-95%, depending on the PEDOT:PSS film thickness. PEDOT:PSS films deposited on poly(ethylene terephthalate) (PET) substrates exhibited superior flexibility and stretchability compared to commonly used indium tin oxide (ITO) films. OPV devices obtained comparable power conversion efficiencies (PCEs) and had superior photovoltaic performance when flexing, compared to ITO. Since one of the major functional advantages of OPVs is the potential for flexible modules, mechanically robust devices are required. The scalable fabrication of PEDOT:PSS transparent electrodes shows promise in enabling both flexible and stretchable organic electronic applications.

5.1.3 Chapter 3

In this chapter, a blended polymeric cathodic interfacial buffer layer improved the air stability of high efficiency OPVs. A water-soluble cationic polythiophene derivative: poly[3-(6-{4-tert-butylpyridiniumyl}-hexyl)thiophene-2,5-diyl] [P3(TBP)HT] was synthesized, and used to fabricate thin films with anionic PEDOT:PSS via electrostatic layer-by-layer (eLbL) assembly. The eLbL process enabled control of thickness and composition of blended films, permitting precise

control of the work function. Tunable work functions are advantages in interfacial buffer layers allowing optimal energetic alignment with the photoactive layer. The assembled multilayered films were applied as a cathodic modifying layer, resulting in high efficiency photovoltaic performance. These OPV devices exhibited superior air stability compared to standard Cs_2CO_3 cathodic buffer layers. The stability of OPVs has been a long-standing issue. Increasing the stability of efficient OPVs promises to aid in the commercial feasibility of this technology.

5.1.4 Chapter 4

The morphology of the photoactive layer in OPVs is critical for efficient exciton dissociation and charge collection. Chapter 4 investigated the role of hydrogen bonding in the photoactive layer upon introduction of a series of carboxylated polythiophenes (P3CATs) with [6,6]-phenyl-C_{61}-butyric acid methyl ester ($PC_{61}BM$). Bulk heterojunction films containing poly[3-(5-carboxypentyl)thiophene-2,5-diyl] (P3CPenT) had the largest extent of hydrogen bonding, crystallite size, and hole mobility, resulting in superior photovoltaic performance. Hydrogen bonding in P3CAT films increased both the Young's modulus and hardness compared to poly(3-hexylthiophene) (P3HT). This signified increased resistance to deformation in P3CAT films, which may lead to improved durability of carboxylated polythiophene-based OPVs.

5.2 Proposed Research Directions

5.2.1 Self-Healing Hybrid Transparent Conductors

Recently there has been interest in electronic applications using self-healing materials.[1–4] These have taken the form of electronic skin,[5] as well as transparent conductors.[6] There are exciting future applications such as transparent displays or touch screens which could be cut and scarred, but would self-heal themselves like human skin, and not affect device integrity. An interesting approach to self-healing transparent conductors was reported by Sun and coworkers.[7] They utilizes a polyelectrolyte membrane (PEM) as a template for self-healing in the presence of water.[7] Branched poly(ethylenimine) (bPEI) and poly(acrylic acid) (PAA) are used via electrostatic layer-by-layer (eLbL) assembly to fabricate multilayer thin films.[7] The chemical structures are shown in Figure 5.1. The film increases in thickness with repeated exposure to aqueous bPEI and PAA solutions, as seen in Figure 5.2. The thickness of the eLbL assembled film after 30 deposition cycles is ~30.4 μm. After a 50 μm width cut, the free-standing films are exposed to water and self-heal within 5 minutes.[7] The self-healing is a result of swelling, high flowability and interdiffusion of polyelectrolytes in the film.[7]

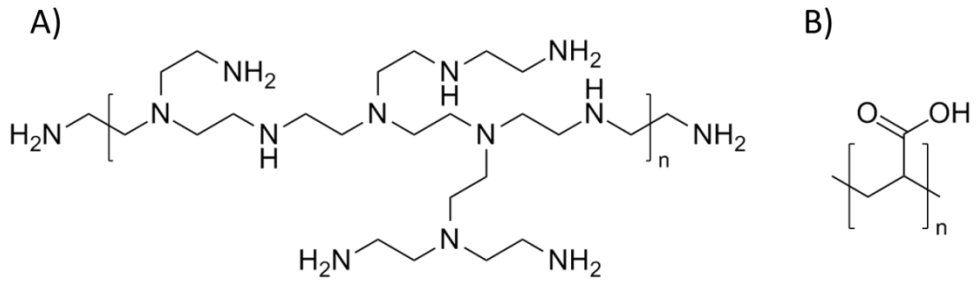

Figure 5.1 The chemical structures of A) branched poly(ethylenimine) and B) poly(acrylic acid) used in the eLbL assembly of PEM films.

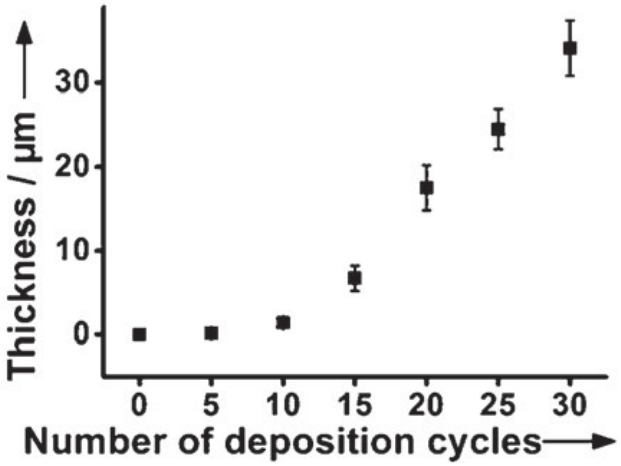

Figure 5.2 The thickness of eLbL assembled (bPEI/PAA) multilayer films with increasing deposition cycles. Reprinted with permission from reference [7]. Copyright © 2011 Wiley-VCH Verlag GmbH & Co.

In order to adapt the previous PEM for transparent conductors, highly hygroscopic poly(acrylic acid)–hyaluronic acid (PAA–HA) is used with PEI via eLbL assembly to fabricate PEM films on PET substrates. This leads to smoother films with higher optical transmission.[6] Ag NWs are drop-cast on top of the PEM films, where the concentration of solution changes the NW coverage on the substrate. A conductive coating with sheet resistance of 7 $\Omega\ \square^{-1}$ is obtained with a transmissivity of 56%. After the Ag NW coated PEM is cut, water can swell the underlying multilayer film restoring the electrical conductivity of the Ag NWs. This results in a sheet resistance of 14 $\Omega\ \square^{-1}$. The scanning electron microscope (SEM) images in

Figure 5.3 show the cut film in A) and the PEM/Ag NW film after healing in B). This technique represents a general strategy for self-healing of transparent conductive films.

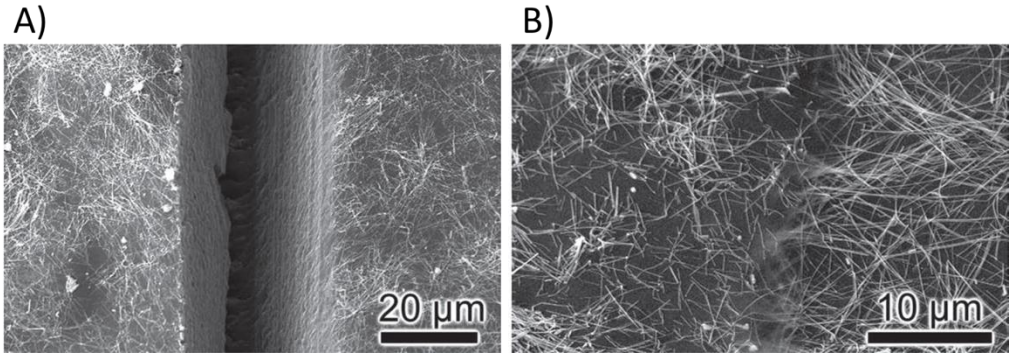

Figure 5.3 SEM images of A) a cut (bPEI/PAA-HA) film coated with Ag NWs, and B) the healed film after exposure to water. Reprinted with permission from reference [6]. Copyright © 2012 Wiley-VCH Verlag GmbH & Co.

The previous self-healing strategy remarkably restores electrical conductivity in scarred or cut Ag NW films.[6] However, the PEM/Ag NW composites have low optical transmission and the repeatability of self-healing was not demonstrated. A potential strategy to circumvent poor transmission, and improve the mechanical properties of the film is to combine Ag NWs with flexible and smooth PEDOT:PSS coatings. Hybrid polymer-metal NW coatings for transparent electrodes were introduced by Peumans and coworkers as a means to decrease the surface roughness of Ag NWs.[8] Ag NWs may also help to decrease the sheet resistance of composite films, useful for large area applications.[9]

Building on the previously discussed work of PEM/Ag NW films, our PEDOT:PSS spray-coating method could be used to deposit a conductive polymer film on top of the healable template (Figure 5.4B). Since we have previously shown that PEDOT:PSS films lose hydrophilicity after our post-processing steps, water is

not expected to significantly resolubilize the PEDOT:PSS coating.[10] After spray-deposition of PEDOT:PSS on top of the PEM/Ag NW films, pressure can be applied to press the PEDOT:PSS into the Ag NWs (Figure 5.4C).[8] By combining PEM/Ag NWs with high conductivity PEDOT:PSS, the thickness (concentration) of Ag NWs could be reduced, improving the transmission of films. The concentration of Ag NWs and thickness of PEDOT:PSS will have to be optimized finding a careful balance between low resistance and high transmittance.

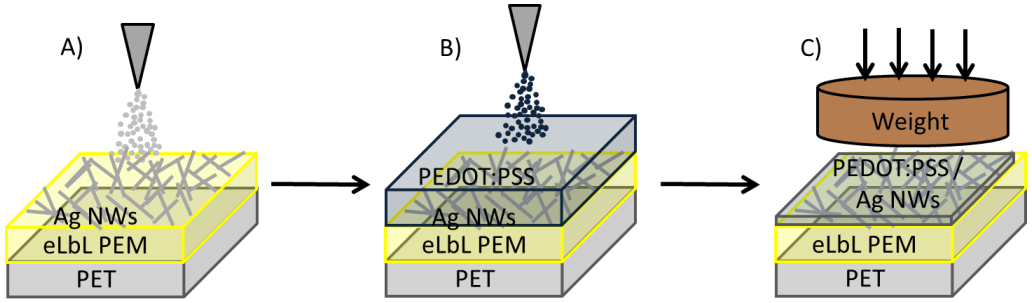

Figure 5.4 Schematic illustrating the proposed fabrication of healable PEM/Ag NW/PEDOT:PSS films. A) Using previously established techniques, PEM multilayers are fabricated on PET. Ag NWs are sprayed on top of the PEM multilayered film. B) PEDOT:PSS is sprayed on top of the Ag NW film. C) A weight is used to compress the PEDOT:PSS into the Ag NW layer, forming a hybrid PEDOT:PSS/Ag NW film.

The next step would be to evaluate the healability of PEM/Ag NW/PEDOT:PSS films. Excess poly(4-styrenesulfonate) (PSS) can swell in water, aiding in the healability of scarred or cut films. In addition, flexible PEDOT:PSS may aid in demonstrating multiple cycles of self-healing. Since the underlying PEM films are highly hygroscopic, the (bPEI/PAA-HA) multilayers may compete for water absorption with PEDOT:PSS. Since the hygroscopicity of PEDOT:PSS has been detrimental to the lifetimes of OPVs,[11] reducing the absorption of water by PEDOT:PSS should improve stability of devices.

The fabrication of PEM/Ag NW/PEDOT:PSS composites may lead to highly flexible, transparent, and self-healing electrodes. This may be an important step to realizing self-healing in organic electronic devices.

5.2.2 Stability of Cathodic Interfacial Layer

In Chapter 3, we reported a new polymeric cathodic interfacial modifier for stable OPVs. This consisted of building films of cationic poly[3-(6-{4-tert-butylpyridiniumyl}-hexyl)thiophene-2,5-diyl bromide] [P3(TBP)HT^{+}Br^{-}] and anionic (PEDOT:PSS) via eLbL assembly. The stability of OPV devices with the polymeric multilayer architecture out-performed commonly-used Cs_2CO_3 cathodic buffer layers. However, it is unconfirmed what led to enhanced stability of the devices. At first, one might expect inferior stability as a result of PEDOT:PSS's hygroscopicity and the common air and light sensitivity of polymers.

A hint at the reasoning for increased stability of polymeric multilayered films was found in further analysis of the X-ray photoelectron spectroscopy (XPS) spectra as previously presented in Chapter 3, Figure 3.6. Fitting the XPS spectra of [P3(TBP)HT:PEDOT:PSS]$_n$ (where n = number of bilayers) films in the S(2p) region provides further insight into the composition of the films. The S(2p) regions consists of two sets of peaks. The peaks at ~ 165 eV correspond to the thiophene moiety, while the peaks at ~ 168.5 eV correspond to the PSS sulfonate group. This allows calculation of the ratio between PSS and thiophene. More importantly, the ratio of PEDOT to PSS can be extracted. In films cast from colloidal (unmodified) PEDOT:PSS, we have previously shown the PSS to PEDOT ratio is 6:1.[12, 13] In the multilayered film architecture, the PSS to PEDOT ratio decreases to ~ 1.4:1. This

represents about a four times decrease in PSS content of the multilayered films. The PSS moiety is responsible for the water absorption of PEDOT:PSS films.[14] Removing PSS from the multilayered films should reduce the hygroscopicity, and extend the lifetime of OPV devices.

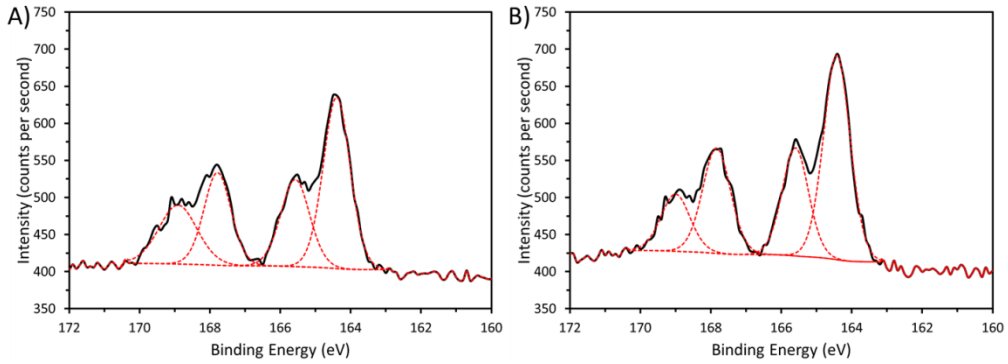

Figure 5.5 The X-ray photoelectron spectra of the S (2p) region of $[P3(TBP)HT:PEDOT:PSS]_n$ films on ITO with A) 5 bilayers, and B) 5.5 bilayers.

To test this hypothesis, the hygroscopicity of regular PEDOT:PSS films and eLbL multilayered films should be tested and compared. This would ideally require an environmental chamber, with control over humidity, coupled with an in-situ mass balance. Considerably thicker multilayered and PEDOT:PSS films may be required to obtain accurate mass determination. It would also be valuable to measure the film resistance under different humidity conditions.

Previous research indicates that the long-term resistance of PEDOT:PSS films increases with higher PSS content.[13] Leo and coworkers fabricated a series of PEDOT:PSS films and treated them to different soak times in ethylene glycol (EG).[13] The longer PEDOT:PSS films soaked in EG, the lower the concentration of PSS. The resistance of films with no EG treatment, and 1 min, 5 min, and 30 min EG soaking was measured in air as seen in Figure 5.6. Films with lower PSS content

(30 min EG soak) resulted in stabilized resistance compared to unprocessed PEDOT:PSS films. The authors attributed lower PSS concentrations with reduced water absorption, resulting in improved stability of resistance over time.[13]

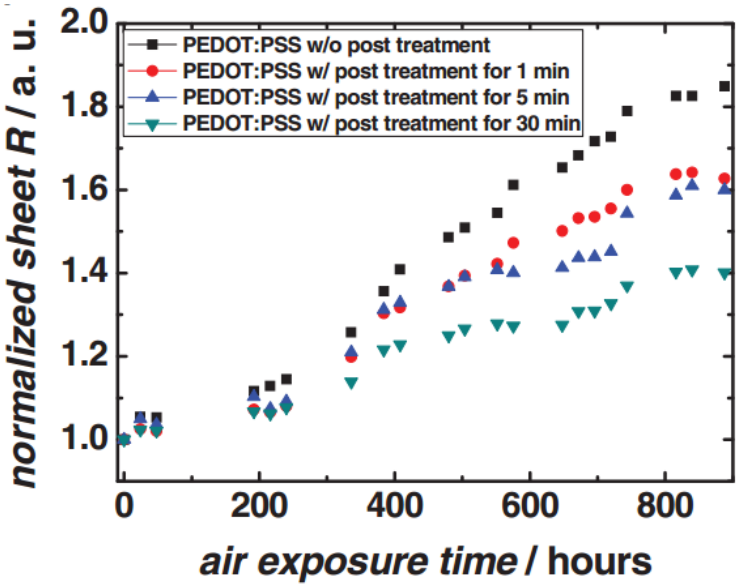

Figure 5.6 The normalized sheet resistance of PEDOT:PSS films with air exposure. Less PSS in films stabilizes the resistance. The PSS content decreases through the series: squares, circles, up triangles, and down triangles. Reprinted with permission from reference [13]. Copyright © 2011 Wiley-VCH Verlag GmbH & Co.

Another degradation mode of PEDOT:PSS, is its high acidity, which can etch ITO electrodes. This can decrease the electrode resistance over time.[15] Excess PSS in PEDOT:PSS films can act as a weak acid and decrease the pH when deprotonated in water. Rutherford backscattering revealed increasing indium content in PEDOT:PSS film over time as seen in Figure 5.7.[15] As previously discussed, the multilayered [P3(TBP)HT:PEDOT:PSS]$_n$ films have reduced PSS content, which decreases water absorption and should reduce etching of the ITO electrode.

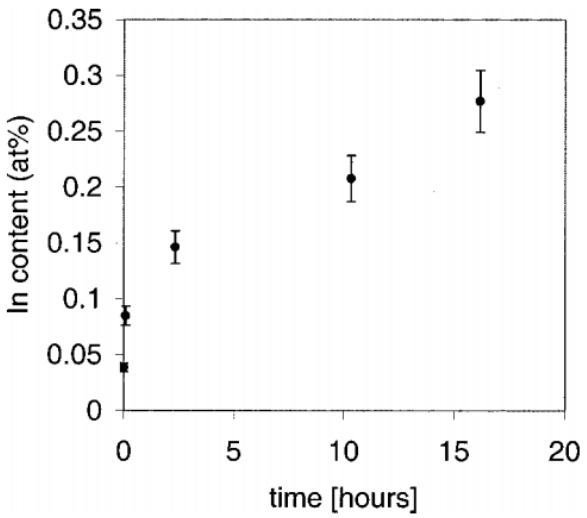

Figure 5.7 The indium content in PEDOT:PSS films with exposure to air as characterized with Rutherford backscattering. Reprinted with permission from reference [15]. Copyright © 2000 American Institute of Physics.

Previous studies have shown that inserting self-assembled monolayers between ITO and PEDOT:PSS have resulted in a 98% decrease of indium in PEDOT:PSS films,[16] and improved stability of electroluminescent devices.[17] Since the first-deposited layer is cationic P3(TBP)HT, it may act as a thin protective barrier between the PEDOT:PSS and ITO, reducing etching. X-ray photoelectron spectroscopy could be used to test the potential for etching ITO in our multilayered films. Multilayered eLbL films can be fabricated with thickness > 10 nm to minimize the underlying ITO substrate signal. These films can be exposed to air for a range of times, while characterizing the indium concentration with XPS. The indium content over time can be compared to control films of spin-cast PEDOT:PSS on ITO.

The increased stability of $[P3(TBP)HT:PEDOT:PSS]_n$ based devices need to be better understood in order to develop strategies to further improve their lifetimes. Excess PSS in PEDOT:PSS has been shown to be a major contributor to the

degradation of OPVs. Understanding the role of PSS in the multilayered films may help elucidate reasons for enhanced stability.

5.2.3 Carboxylated Polythiophenes

Carboxylated functionalized polythiophenes were used as the donor material in bulk heterojunction OPVs in Chapter 4. The carboxylic acid functional group enabled hydrogen bonded assembly via interdigitation of carboxyalkyl chains, leading to average crystallite sizes of 10 nm for poly[3-(5-carboxypentyl)thiophene-2,5-diyl] (P3CPenT). P3CPenT also had the highest hole mobility of the series at 3.9×10^{-4} $cm^2/(V\ s)$. In order to optimize the photovoltaic performance of the carboxylated polythiophene-based devices, the hole mobilities should be improved. This will allow better transport of charges within the polymer, and result in higher short-circuit current densities (J_{SC}).

The hole mobility of semiconducting polymers can be improved by optimizing the polymer morphology in films. Intermolecular charge transport is a limiting factor in the mobility of polymers, which can be improved with shorter π-π stacking distances.[18, 19] Common π-π stacking distances in regioregular polythiophenes are 3.5-3.8 Å. Approaches to optimizing the morphology in polymer films include: annealing,[20] solvent assisted annealing,[21][22] and preassembling polymer nanowires.[23–28]

The self-assembly of regioregular poly[3-(alkyl)thiophene] (P3AT) NWs has been extensively studied by Jenekhe and coworkers.[26–28] P3ATs can be self-assembled in solution by heating them to 100 °C and slowly cooling to room temperature in a dark, vibrationless environment.[28] The solution self-assembly of poly(3-

butylthiophene) (P3BT) leads to widths of 8-10 nm and 5-10 μm lengths as seen in the scanning electron microscope (SEM) and atomic force microscope (AFM) images in Figure 5.8.[28] The hole mobility improved more than two orders of magnitude going from 3.8×10^{-5} $cm^2/(V\ s)$ to 8.0×10^{-3} $cm^2/(V\ s)$ when P3BT was preassembled in solution. This resulted in higher J_{SC} and more than doubling of the power conversion efficiency (PCE).

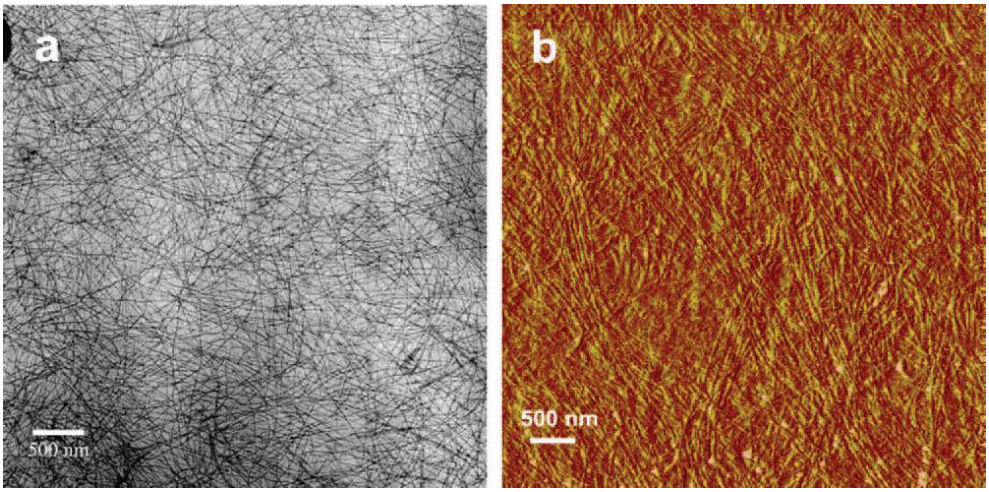

Figure 5.8 A) SEM and B) AFM images of self-assembled P3BT NWs : $PC_{61}BM$ (1:1 by weight) composites. Reprinted with permission from reference [28]. © 2008 American Chemical Society.

Recently we have shown a similar self-assembly motif as Jenekhe with carboxylated polythiophenes.[29] P3CPenT NWs can be formed in dimethyl sulfoxide (DMSO) by heating solutions above 90 °C and cooling to room temperature. Upon cooling, the solutions turn from orange to deep purple. The P3CPenT NW solutions shown significant red-shifting absorption peaks compared to non-nanowire pyridine solutions (Figure 5.9A).[29] In addition, the X-ray diffraction (XRD) spectra in Figure 5.9B show considerably sharper peaks for films cast from P3CPenT NW solutions in DMSO. The crystallite size doubles for the preassembled NW films.[29]

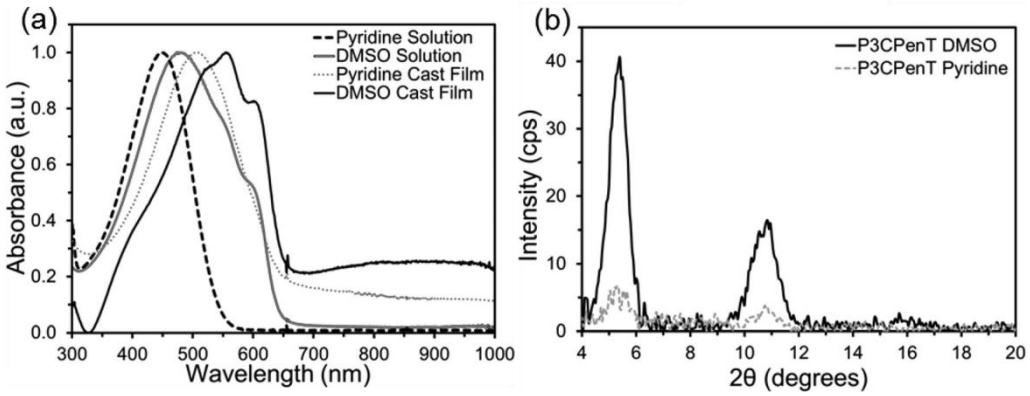

Figure 5.9 A) The solution and solid-state absorption spectra of P3CPenT in and cast from pyridine and DMSO solutions. B) The XRD of P3CPenT films cast from pyridine and DMSO. Reprinted with permission from reference [29]. © 2012 The Royal Society of Chemistry.

The morphology of the P3CPenT NW films should be thoroughly characterized with selected area electron diffraction and X-ray diffraction (with thicker films), in order to determine the π-π stacking distance. In addition, the role of hydrogen bonding in the self-assembled NWs should be assessed with infrared spectroscopy. The hole mobility should be characterized and compared to P3CPenT films cast from pyridine. In addition, the effect of annealing and solvent assisted annealing should be determined by evaluating changes in the absorption spectra and hole mobilities. A better understanding of the polymer morphology and improved hole mobilities may enable the investigation of P3CPenT NWs incorporated into the photoactive layer of OPVs, which may lead to improved photovoltaic performance.

5.3 References

[1] B. Aïssa, D. Therriault, E. Haddad, W. Jamroz, *Adv. Mater. Sci. Eng.* **2012**, *2012*, 854203.

[2] S.R. Baliga, M. Ren, M.N. Kozicki, *Thin Solid Films* **2011**, *519*, 2339.

[3] S.A. Odom, S. Chayanupatkul, B.J. Blaiszik, O. Zhao, A.C. Jackson, P. V Braun, N.R. Sottos, S.R. White, J.S. Moore, *Adv. Mater.* **2012**, *24*, 2578.

[4] K.A. Williams, A.J. Boydston, C.W. Bielawski, *J. R. Soc. Interface* **2007**, *4*, 359.

[5] B.C.-K. Tee, C. Wang, R. Allen, Z. Bao, *Nat. Nanotechnol.* **2012**, *7*, 825.

[6] Y. Li, S. Chen, M. Wu, J. Sun, *Adv. Mater.* **2012**, *24*, 4578.

[7] X. Wang, F. Liu, X. Zheng, J. Sun, *Angew. Chem. Int. Ed.* **2011**, *50*, 11378.

[8] Z. Yu, L. Li, Q. Zhang, W. Hu, Q. Pei, *Adv. Mater.* **2011**, *23*, 4453.

[9] R. Po, C. Carbonera, A. Bernardi, F. Tinti, N. Camaioni, *Sol. Energy Mater. Sol. Cells* **2012**, *100*, 97.

[10] J.G. Tait, B.J. Worfolk, S.A. Maloney, T.C. Hauger, A.L. Elias, J.M. Buriak, K.D. Harris, *Sol. Energy Mater. Sol. Cells* **2013**, *110*, 98.

[11] E. Voroshazi, B. Verreet, A. Buri, R. Müller, D. Di Nuzzo, P. Heremans, *Org. Electron.* **2011**, *12*, 736.

[12] D.A. Rider, B.J. Worfolk, K.D. Harris, A. Lalany, K. Shahbazi, M.D. Fleischauer, M.J. Brett, J.M. Buriak, *Adv. Funct. Mater.* **2010**, *20*, 2404.

[13] Y.H. Kim, C. Sachse, M.L. Machala, C. May, L. Müller-Meskamp, K. Leo, *Adv. Funct. Mater.* **2011**, *21*, 1076.

[14] Y. Hyun Kim, C. Sachse, M. Hermenau, K. Fehse, M. Riede, L. Müller-Meskamp, K. Leo, *Appl. Phys. Lett.* **2011**, *99*, 113305.

[15] M.P. de Jong, L.J. van IJzendoorn, M.J.A. de Voigt, *Appl. Phys. Lett.* **2000**, *77*, 2255.

[16] K.W. Wong, H.L. Yip, Y. Luo, K.Y. Wong, W.M. Lau, K.H. Low, H.F. Chow, Z.Q. Gao, W.L. Yeung, C.C. Chang, *Appl. Phys. Lett.* **2002**, *80*, 2788.

[17] Y. Kim, S. Lee, J. Noh, S. Han, *Thin Solid Films* **2006**, *510*, 305.

[18] A.R. Murphy, J. Liu, C. Luscombe, D. Kavulak, J.M.J. Fréchet, R.J. Kline, M.D. McGehee, *Chem. Mater* **2005**, *17*, 4892.

[19] A.J. Heeger, *Chem. Soc. Rev.* **2010**, *39*, 2354.

[20] T. Savenije, J. Kroeze, X. Yang, J. Loos, *Thin Solid Films* **2006**, *511-512*, 2.

[21] S.S. van-Bavel, E. Sourty, G. de With, J. Loos, *Nano Lett.* **2009**, *9*, 507.

[22] J. Peet, M.L. Senatore, A.J. Heeger, G.C. Bazan, *Adv. Mater.* **2009**, *21*, 1521.

[23] P.-T. Wu, G. Ren, C. Li, R. Mezzenga, S.A. Jenekhe, *Macromolecules* **2009**, *42*, 2317.

[24] H. Xin, O.G. Reid, G. Ren, F.S. Kim, D.S. Ginger, S.A. Jenekhe, *ACS Nano* **2010**, *4*, 1861.

[25] G. Ren, P.-T. Wu, S.A. Jenekhe, *ACS Nano* **2011**, *5*, 376.

[26] H. Xin, G. Ren, F.S. Kim, S.A. Jenekhe, *Chem. Mater.* **2008**, *20*, 6199.

[27] P.-T. Wu, H. Xin, F.S. Kim, G. Ren, S.A. Jenekhe, *Macromolecules* **2009**, *42*, 8817.

[28] H. Xin, F.S. Kim, S.A. Jenekhe, *J. Am. Chem. Soc.* **2008**, *130*, 5424.

[29] B.J. Worfolk, W. Li, P. Li, T.C. Hauger, K.D. Harris, J.M. Buriak, *J. Mater. Chem.* **2012**, 11354.